Albert–Ludwigs–Universität Freiburg

Doctoral Thesis

Charge Multiplication detectors for use in the HL-LHC and Measurement of the production cross-section in pp collisions of a W boson in association with a charm quark at $\sqrt{s} = 8$ TeV with the ATLAS detector

Author:
Christopher Betancourt

Supervisor:
Dr. Karl Jakobs

Dissertation
zur Erlangung des Doktorgrades
der Fakultät für Mathematik und Physik
der Albert–Ludwigs–Universität Freiburg im Breisgau

January 2016

"Es gibt keinen Gott und Dirac ist sein Prophet."

Wolfgang Pauli

Dekan:	Prof. Dr. Dietmar Kröner
Referent:	Prof. Dr. Karl Jakobs
Koreferent:	Prof. Dr. Markus Schumacher
Tag der mündlichen Prüfung:	1 April 2016

Declaration of Authorship

I, Christopher BETANCOURT, declare that this thesis titled, 'Charge Multiplication detectors for use in the HL-LHC and Measurement of the production cross-section in pp collisions of a W boson in association with a charm quark at $\sqrt{s} = 8$ TeV with the ATLAS detector' and the work presented in it are my own. I confirm that:

- This work was done wholly or mainly while in candidature for a research degree at this University.
- Where any part of this thesis has previously been submitted for a degree or any other qualification at this University or any other institution, this has been clearly stated.
- Where I have consulted the published work of others, this is always clearly attributed.
- Where I have quoted from the work of others, the source is always given. With the exception of such quotations, this thesis is entirely my own work.
- I have acknowledged all main sources of help.

Signed: _____

Date: _____

This thesis is dedicated to Emily, my best friend, my wife, and the love of my life.

Contents

List of Figures

List of Tables

Chapter 1

Introduction

The unification of the electromagnetic and weak nuclear forces into a single theory is one of the greatest scientific achievements of the last century. It provided the starting point for the theoretical framework known as the Standard Model. Not only has the Standard Model resulted in a profound understanding of physics at the subatomic level, it has also enjoyed unprecedented experimental verification, often regarded as the most precise scientific theory in history.

The exploration into the subatomic world has lead to particle accelerators of every increasing size. The Large Hadron Collider (LHC), currently the world's largest particle accelerator and machine, was built with the primary goal of discovering the Higgs boson, the last ingredient of the Standard Model, and to search for new physics beyond the Standard Model's predictions. The discovery of the Higgs boson in 2012 at the LHC by the ATLAS and CMS collaborations has been a triumph for human ingenuity. Although its discovery is an important milestone in understanding the fundamental workings of nature, the search for a full unified theory describing all natural phenomena is far from over. Physicists know the Standard Model is not the end game, as it fails to account for various observed phenomena, which include dark matter, dark energy, and perhaps most embarrassingly, gravity.

The search for new physics requires precise knowledge of several parameters in the Standard Model. This includes the distribution of quarks and gluons inside the proton, usually in terms of parton distribution functions, or PDFs. These PDFs cannot be calculated exactly from theory, and require experimental measurements as inputs. Therefore, besides searching for new physics, the LHC physics program includes performing precision measurements on various Standard Model processes to better constrain the PDFs.

The strange quark PDF is currently not very well constrained. Measurements of the production of a W boson in association with a charm quark at hadron colliders is known to be sensitive to the strange quark content of the proton, and serve as a way to constrain the strange quark PDF. Work in this thesis presents such a measurement, measuring the production cross section of a W boson in association with a charm quark using proton-proton collisions with a center-of-mass energy of $\sqrt{s} = 8$ TeV, taken with the ATLAS detector. The measurement presented here serves to compliment previous measurements taken at lower energies.

The LHC requires the latest and most novel technologies in its search for new

physics. Of particular importance are silicon detectors. They represent a large instrumental volume in the inner layers of experiments such as ATLAS and CMS, and provide the primary means of momentum measurement and track reconstruction for charged particles. A key concern for such devices is radiation damage stemming from the high particle fluxes near the collision point.

The LHC will need a major upgrade in the 2020s to increase its longevity and extend its discovery potential. The High Luminosity LHC, or simply the HL-LHC, is a planned luminosity upgrade of the machine which will increase the integrated luminosity ten fold. By the time of the upgrade, the current machine components will have aged considerably, and the silicon tracking detectors in ATLAS and CMS will have already undergone severe radiation damage. The more extreme radiation environment in the HL-LHC will present unique challenges that must be overcome, not just to the silicon detectors, but also to the electronics and physics analyses, which will have to cope with increased data volumes and pileup conditions.

The CERN RD50 collaboration has been investigating radiation hard semiconductor materials, with the main driver being radiation damage posed by the HL-LHC conditions. Several designs have been proposed to replace the silicon trackers in ATLAS and CMS, with one such option being charge multiplication detectors.

Charge multiplication detectors aim to mitigate the radiation induced signal loss in silicon detectors by means of impact ionization. The electric fields in such devices must reach a critical point for multiplication of the signal to occur. This can be achieved in a variety of ways, from simple geometrical designs to changes in the wafer processing. An open question has been the stability of this charge multiplication mode under large bias voltages and long time scales, as would be relevant in operational conditions at the LHC. The work in this thesis aims to address this, with emphasis on the feasibility of such devices as radiation-hard detectors for use in the HL-LHC.

This thesis is presented as follows. Chapter 2 gives a theoretical overview of the Standard Model, presenting a formal description of electromagnetic, weak, and strong forces. The parton model and the physics of proton-proton collisions is outlined in chapter 3. Chapter 4 reviews the properties of silicon and gives an overview of silicon detectors. The LHC and the ATLAS detector are described in chapter 5, which also outlines the HL-LHC and physical object reconstruction in ATLAS. The measurement strategy, including background estimation, for the $W+c$ cross section measurement is presented in chapter 6 and the results in chapter 7. Different detectors studied in this work, and a description of the measurements performed on them can be found in chapter 8. Chapter 9 gives the results on detector measurements. Finally, a summary is given in chapter 10.

Chapter 2

The Standard Model

The Standard Model is a quantum field theory incorporating internal symmetries of the gauge group;

$$SU(3) \times SU(2) \times U(1) \tag{2.1}$$

where $SU(N)$ is the *special unitary group* consisting of all $N \times N$ unitary matrices with determinant equal to 1, and $U(N)$ the group of all $N \times N$ unitary matrices[1]. This non-Abelian[2] symmetry group provides a theoretical explanation for three of the four known fundamental forces of nature; the strong force, the weak force, and the electromagnetic force. The symmetry group $SU(3)$ describes the strong sector; the interaction between quarks and gluons. The electromagnetic and weak sectors are unified and described by the $SU(2) \times U(1)$ group. There is currently no satisfactory quantum theory for the fourth force, gravity, and it is thus not part of the Standard Model. The exclusion of gravity is justified on practical grounds due to its extremely small couplings relative to the other three forces, even if this exclusion is unsatisfactory from a theoretical point of view.

Each particle is characterized by its spin, mass and charge. Spin 1/2 particles are known as *fermions*, which constitute the matter content of the model. Spin 1 particles are known as *bosons*, and make up the interaction forces between particles. The fermions of the Standard Model are listed in table 2.1 and the bosons in table 2.2.

The fermions are differentiated into *leptons*, which participate in electroweak interactions and *quarks*, which additionally interact through the strong force. The fermions are arranged into three copies, or *generations*. Each generation consists of two leptons, a charged electron type particle and a corresponding neutral neutrino, and two quarks which come as either isospin "up" or isospin "down" flavors. The three generations differ only by the mass of their particles.

The bosons are classified by the internal gauge-symmetries of the model. The generators of each group correspond to different force carrier particles, known as *gauge bosons*. In general, the number of generators for the group $SU(N)$ is $N^2 - 1$. Thus there are eight gauge-bosons for $SU(3)$, corresponding to eight different gluons in the strong sector. Likewise, the electroweak sector has four generators; one from the $U(1)$ symmetry and three from the $SU(2)$ symmetry.

[1] A matrix U is unitary if $UU^* = I$.

[2] A group is non-Abelian if at least one pair of elements do not commute.

Leptons

Name	Symbol	Charge	Mass[2]
Electron	e	-1	0.511 MeV
Electron Neutrino	ν_e	0	0
Muon	μ	-1	105.66 MeV
Muon Neutrino	ν_μ	0	0
Tau	τ	-1	1776.82 MeV
Tau Neutrino	ν_τ	0	0

Quarks

Name	Symbol	Charge	Mass[2]
Up	u	+2/3	$\approx$ 2.3 MeV
Down	d	-1/3	$\approx$ 4.8 MeV
Strange	s	+2/3	$\approx$ 95 MeV
Charm	c	-1/3	$\approx$ 1.275 GeV
Bottom	b	+2/3	$\approx$ 4.18 GeV
Top	t	-1/3	$\approx$ 173.07 GeV

TABLE 2.1: The fermionic content of the Standard Model. The quarks and leptons are repeated in three generations of increasing mass.

Gauge bosons

Interaction	Name	Symbol	Charge	Mass[2]
Weak	W boson	$W^\pm$	±1	80.385 $\pm$ 0.015 GeV
Weak	Z boson	Z	0	91.1876 $\pm$ 0.0021 GeV
Electromagnetic	Photon	γ	0	0
Strong	Gluons	g	0	0

TABLE 2.2: The gauge bosons of the Standard Model.

The four gauge bosons from $SU(2) \times U(1)$ correspond to the W^+, W^-, Z bosons and the photon[3].

2.1 The electroweak sector and the Higgs mechanism

This section introduces the formalism of electroweak interactions. It begins with a brief overview of quantum electrodynamics (QED) before moving on to a description of the Higgs mechanism. It ends with the Glashow-Weinberg-Salam theory of weak interactions. The following description closely follows that of *Peskin* and *Schroeder* [3].

[3]The gauge-bosons of $SU(2) \times U(1)$ are actually massless, and the W^+, W^-, Z bosons only acquire mass via the Higgs mechanism [1].

2.1.1 Quantum electrodynamics

Consider the Lagrangian density of a free Dirac particle

$$\mathcal{L}_0 = i\bar{\psi}(x)\gamma^\mu\partial_\mu\psi(x) - m\bar{\psi}(x)\psi(x) \tag{2.2}$$

which is invariant under *global* $U(1)$ transformations. These take the form

$$\psi(x) \to \psi'(x) = e^{i\theta}\psi(x) \tag{2.3}$$

where θ is an arbitrary real constant. We can move from a *global* to a *local* transformation by performing the transformation separately for each point in spacetime, that is by taking $\theta = \theta(x)$. The price to pay is that now $\mathcal{L}_0$ not invariant under these local transformations. In order to restore invariance of equation (2.2) under local $U(1)$ transformations, we must introduce a new spin-1 field A_μ which transforms as

$$A_\mu(x) \to A'_\mu(x) = A_\mu(x) + \frac{1}{e}\partial_\mu\theta(x) \tag{2.4}$$

and define the *covariant derivative*

$$D_\mu \equiv \partial_\mu - ieA_\mu(x) \tag{2.5}$$

with the following transformation

$$D_\mu\psi(x) \to (D_\mu\psi(x))' = e^{i\theta}D_\mu\psi(x). \tag{2.6}$$

The following Lagrangian

$$\mathcal{L} = i\bar{\psi}(x)\gamma^\mu D_\mu\psi(x) - m\bar{\psi}(x)\psi(x) = \mathcal{L}_0 + eA_\mu\bar{\psi}(x)\gamma^\mu\psi(x) \tag{2.7}$$

is now invariant under local $U(1)$ transformations.

Imposing local gauge invariance under $U(1)$ transformation has generated an interaction term of the form $eA_\mu\bar{\psi}\gamma^\mu\psi$, which corresponds to the electromagnetic interaction with charge e. In order to write down the full QED Lagrangian, we need one last step. Namely, we would like the field A_μ to be able to propagate through spacetime, and so we thus need a kinetic term which is also gauge invariant. The term

$$\mathcal{L}_{KE} = -\frac{1}{4}F_{\mu\nu}F^{\mu\nu} \tag{2.8}$$

does the trick. $F_{\mu\nu} = \partial_\mu A_\nu - \partial_\nu A_\mu$ is the electromagnetic field strength. Combining equations (2.7) and (2.8) leads to the full Lagrangian of QED

$$\mathcal{L}_{QED} = i\bar{\psi}(x)\gamma^\mu D_\mu\psi(x) - m\bar{\psi}(x)\psi(x) - \frac{1}{4}F_{\mu\nu}F^{\mu\nu} \tag{2.9}$$

which is fully renormalizable[4] and reproduces the full set of Maxwell equations.

[4] A theory is said to be renormalizable if infinities arising in calculations can be eliminated in a systematic way.

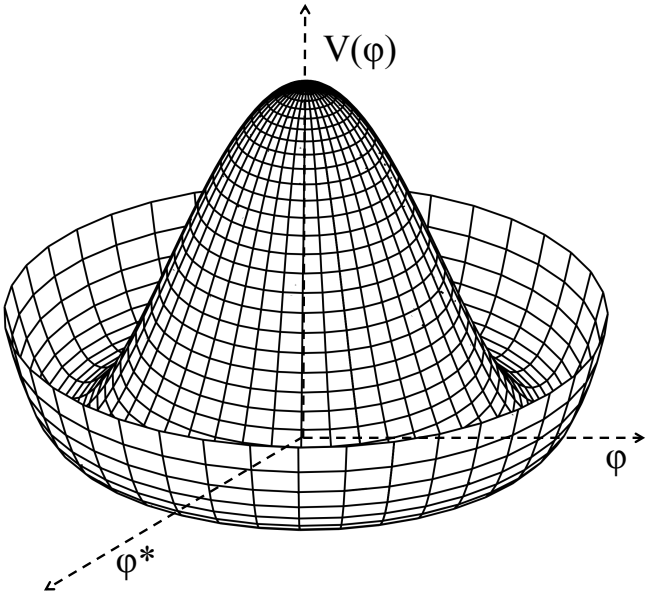

FIGURE 2.1: Sketch of the $V(\phi) = -\mu^2\phi^*\phi + \frac{\lambda}{2}(\phi^*\phi)^2$ potential.

2.1.2 The Higgs mechanism and the Higgs boson

Our discussion of the Higgs mechanism begins by considering a complex scalar field ϕ that is coupled to itself and the electromagnetic field

$$\mathcal{L} = |D_\mu\phi| - \frac{1}{4}F_{\mu\nu}F^{\mu\nu} - V(\phi) \tag{2.10}$$

where D_μ is the covariant derivative and $F_{\mu\nu}$ is the electromagnetic field strength. This Lagrangian exhibits symmetry under local $U(1)$ transformations. If the potential $V(\phi)$ is taken to be

$$V(\phi) = -\mu^2\phi^*\phi + \frac{\lambda}{2}(\phi^*\phi)^2 \tag{2.11}$$

with $\mu^2 > 0$, then the minimum of this potential, as seen in figure 2.1, will occur at

$$\phi_0 = \left(\frac{\mu^2}{\lambda}\right)^{1/2} \equiv v \tag{2.12}$$

and the $U(1)$ symmetry will be spontaneously broken. We have defined the *vacuum expectation value* (VEV), v, to be the minimum of this potential. Expanding the field $\phi(x)$ about this minimum and separating the real and imaginary parts reads

$$\phi(x) = \phi_0 + \frac{1}{\sqrt{2}}\left(\phi_1(x) + i\phi_2(x)\right). \tag{2.13}$$

The potential $V(\phi)$ now reads

$$V(\phi) = -\frac{1}{2\lambda}\mu^4 + \mu^2\phi_1^2 + \mathcal{O}(\phi_1^3, \phi_2^3) \tag{2.14}$$

so that the field ϕ_1 gets a mass term $m = \sqrt{2}\mu$ and the field ϕ_2 remains massless. The appearance of massless fields arising from spontaneous symmetry breaking is known as *Goldstone's theorem*, and the massless particles known as *Goldstone's bosons* [4]. The kinetic term $|D_\mu\phi|$ can also be expanded and gains an additional mass term for the photon

$$\Delta\mathcal{L} = \frac{1}{2}m_A^2 A_\mu A^\mu \tag{2.15}$$

where the mass $m_a^2 = 2e^2\phi_0^2$. The act of massless gauge bosons acquiring a mass term from spontaneous symmetry breaking is known as the *Higgs mechanism*, and will be of utmost importance when discussing a unified theory of electroweak interaction in the following section.

The field ϕ responsible for spontaneous symmetry breaking also has a more physical manifestation. Let us move from a theory with $U(1)$ gauge invariance to one exhibiting $SU(2)$ symmetry. A scalar field in the spinor representation of $SU(2)$ produces no massless gauge bosons, so we direct our attention to $SU(2) \times U(1)$. Such a field has a gauge transformation of the form

$$\phi \to e^{i\alpha^a\tau^a}e^{i\beta/2}\phi. \tag{2.16}$$

Where $\tau^a = \sigma^a/2$ and σ^a are the *Pauli matrices*. Choosing $\alpha^1 = \alpha^2 = 0$ and $\alpha^3 = \beta$ leads to

$$\langle\phi\rangle = \frac{1}{\sqrt{2}}\begin{pmatrix}0\\v\end{pmatrix} \tag{2.17}$$

which is invariant under 2.16. We can parameterize the field by

$$\phi(x) = \frac{1}{\sqrt{2}}\begin{pmatrix}0\\v+h(x)\end{pmatrix} \tag{2.18}$$

where $h(x)$ is a real-valued field fluctuating around v with $\langle h(x)\rangle = 0$. The following Lagrangian

$$\mathcal{L} = |D_\mu\phi| + \mu^2\phi^\dagger\phi - \lambda\left(\phi^\dagger\phi\right)^2 \tag{2.19}$$

leads to a VEV for ϕ

$$v = \left(\frac{\mu^2}{\lambda}\right)^{1/2}. \tag{2.20}$$

The potential energy term now reads

$$\mathcal{L} = -\frac{1}{2}m_h^2h^2 - \sqrt{\frac{\lambda}{2}}m_h h^3 - \frac{1}{4}\lambda h^4 \tag{2.21}$$

so that the field $h(x)$ corresponds to a scalar particle with a mass

$$m_h = \sqrt{2\lambda}v. \tag{2.22}$$

This particle is known as the *Higgs boson*. A particle consistent with the Standard Model Higgs boson was discovered in 2012 by the ATLAS and CMS collaborations [5, 6]. The combined ATLAS and CMS data yield a mass of m_h =125.09±0.21(stat.) ±0.11(syst.) GeV/c^2 [7].

2.1.3 The Glashow-Weinberg-Salam theory of weak interactions

The Glashow-Weinberg-Salam (GWS) theory unifies the electromagnetic and weak interactions. It is a $SU(2) \times U(1)$ theory that is spontaneously broken down by the Higgs mechanism to produce massive gauge-bosons. We start with introducing the covariant derivative for $SU(2) \times U(1)$

$$D_\mu \phi = \left(\partial_\mu - igA^a_\mu \tau^a - \frac{i}{2} g' B_\mu \right) \phi \tag{2.23}$$

where A^a_μ and B_μ are the gauge bosons corresponding to $SU(2)$ and $U(1)$ respectively. The field ϕ is the complex scalar field corresponding to $SU(2)$. Through Higgs mechanism, the field acquires a vacuum expectation value of

$$\langle \phi \rangle = \frac{1}{\sqrt{2}} \begin{pmatrix} 0 \\ v \end{pmatrix}. \tag{2.24}$$

Following the recipe from the last section, we can write down the mass terms of the Lagrangian evaluated at $\langle \phi \rangle$

$$\Delta \mathcal{L} = \frac{1}{2} \begin{pmatrix} 0 & v \end{pmatrix} \left(gA^a_\mu \tau^a + \frac{1}{2} g' B_\mu \right) \left(gA^{b\mu} \tau^b + \frac{1}{2} g' B^\mu \right) \begin{pmatrix} 0 \\ v \end{pmatrix}. \tag{2.25}$$

Evaluating this term with $\tau^a = \sigma^a/2$ leads to

$$\Delta \mathcal{L} = \frac{1}{2} \frac{v^2}{4} \left[g^2 (A^1_\mu)^2 + g^2 (A^2_\mu)^2 + (-gA^3_\mu + g' B_\mu)^2 \right] \tag{2.26}$$

which naturally gives rise to three massive gauge bosons, and one massless one. These mass eigenstates are denoted as

$$W^\pm_\mu = \frac{1}{\sqrt{2}} \left(A^1_\mu \mp i A^2_\mu \right) \tag{2.27}$$

with mass $m_W = gv/2$,

$$Z^0_\mu = \frac{1}{\sqrt{g^2 + g'^2}} \left(gA^3_\mu - g' B_\mu \right) \tag{2.28}$$

with mass $m_Z = \sqrt{g^2 + g'^2} v/2$, and finally

$$A_\mu = \frac{1}{\sqrt{g^2 + g'^2}} \left(g' A^3_\mu + g B_\mu \right) \tag{2.29}$$

which remains massless and is identified as the electromagnetic vector potential.

Taking a general fermion field belonging to the $SU(2)$ representation and having a charge Y under $U(1)$, we can write the covariant derivative in terms of

the mass eigenstates

$$\begin{aligned} D_\mu &= \partial_\mu - igA^a_\mu T^a - ig'YB_\mu \\ &= \partial_\mu - i\frac{g}{\sqrt{2}}\left(W^+_\mu T^+ + W^-_\mu T^-\right) - i\frac{1}{\sqrt{g^2+g'^2}}Z_\mu\left(g^2T^3 - g'^2Y\right) \\ &\quad - i\frac{gg'}{\sqrt{g^2+g'^2}}A_\mu\left(T^3+Y\right) \end{aligned} \tag{2.30}$$

where $T^\pm = \frac{1}{2}(\sigma^1 \pm i\sigma^2)$. We can write equation (2.30) in a more compact and suggestive form by identifying the electron charge e

$$e = \frac{gg'}{\sqrt{g^2+g'^2}} \tag{2.31}$$

which has the quantum number $Q = T^3 + Y$. Setting $Q = -1$ then leads to the normal coupling of the electromagnetic field derived earlier.

The *weak mixing angle*, θ_w, can be introduced to further simplify equation (2.30) through

$$\begin{pmatrix} Z^0 \\ A \end{pmatrix} = \begin{pmatrix} cos\theta_w & -sin\theta_w \\ sin\theta_w & cos\theta_w \end{pmatrix}\begin{pmatrix} A^3 \\ B \end{pmatrix} \tag{2.32}$$

so that

$$cos\theta_w = \frac{g}{\sqrt{g^2+g'^2}}, \quad sin\theta_w = \frac{g'}{\sqrt{g^2+g'^2}}. \tag{2.33}$$

The covariant derivative can now be written as

$$D_\mu = \partial_\mu - i\frac{g}{\sqrt{2}}\left(W^+_\mu T^+ + W^-_\mu T^-\right) - i\frac{g}{cos\theta_w}Z_\mu\left(T^3 - sin^2\theta_w Q\right) - ieA_\mu Q \tag{2.34}$$

where

$$g = \frac{e}{sin\theta_w}. \tag{2.35}$$

At tree level all processes involving exchange of a W or Z boson can be described by three parameters e, θ_w, and m_W. Furthermore, the ratio W and Z boson masses is uniquely determined by

$$cos\theta_w = \frac{m_W}{m_Z}. \tag{2.36}$$

In practice, the value of $sin^2\theta_w$ is more often used. The *weak neutral currents*, mediated by the exchange of a Z boson, were first discovered in 1973 [8], and the W and Z bosons were discovered in 1983 by the UA1 and UA2 experiments [9–12].

Just as the Higgs mechanism leads to massive gauge bosons, the fermions can acquire mass in a similar fashion. Consider the kinetic term for fermions $\bar{\psi}i\gamma^\mu\partial_\mu\psi$ which can be decomposed into right- and left-handed fields

$$\bar{\psi}i\gamma^\mu\partial_\mu\psi = \bar{\psi}_L i\gamma^\mu\partial_\mu\psi_L + \bar{\psi}_R i\gamma^\nu\partial_\nu\psi_R. \tag{2.37}$$

We can use the GWS theory to assign left-handed fermion fields to doublets of $SU(2)$, and assign the right-handed fields to singlets. For the right-handed fields $T^3 = 0$ so that $Q = Y$, that is Y becomes the electric charge. Considering the left handed leptons,

$$\psi = \begin{pmatrix} \nu_e \\ e^- \end{pmatrix} \tag{2.38}$$

we assign $Y = -1/2$ in order to reproduce the correct pattern of gauge bosons, and $T^3 = 1/2$ in order to get the correct electric charge for the electron. If ϕ acquires a VEV via the Higgs mechanism, then the Lagrangian will have mass terms

$$\Delta\mathcal{L}_e = -\frac{1}{\sqrt{2}}\lambda_e \bar{e}_L e_R + h.c. + \dots \tag{2.39}$$

with the electron mass reading

$$m_e = \frac{1}{\sqrt{2}}\lambda_e v \tag{2.40}$$

where λ_e is a new dimensionless coupling constant. The quark masses can be written down in the same way

$$m_d = \frac{1}{\sqrt{2}}\lambda_d v, \qquad m_u = \frac{1}{\sqrt{2}}\lambda_u v. \tag{2.41}$$

While the leptons exchange W bosons only within the same generation, the quarks can couple to quarks from different generations. This implies that the mass eigenstates of quarks are not equal to the weak isospin states. The mixing of the different quark flavors is described by the Cabibbo-Kobayashi-Maskawa (CKM) matrix [13, 14],

$$V_{CKM} = \begin{pmatrix} V_{ud} & V_{us} & V_{ub} \\ V_{cd} & V_{cs} & V_{cb} \\ V_{td} & V_{ts} & V_{tb} \end{pmatrix} = \begin{pmatrix} c_{12}c_{13} & s_{12}c_{13} & s_{13}e^{-i\delta} \\ -s_{12}c_{23} - c_{12}s_{23}s_{13}ei\delta & c_{12}c_{23} - s_{12}s_{23}s_{13}e^{i\delta} & s_{23}c_{13} \\ s_{12}s_{23} - c_{12}c_{23}s_{13}e^{i\delta} & -c_{12}s_{23} - s_{12}c_{23}s_{13}e^{i\delta} & c_{23}c_{13} \end{pmatrix} \tag{2.42}$$

which transforms from the mass basis to the weak isospin basis and the coupling to quarks takes the form

$$\frac{-g}{\sqrt{2}}\left(\bar{u}_L \bar{c}_L \bar{t}_L\right)\gamma^\mu W^+_\mu V_{CKM}\begin{pmatrix} d_L \\ s_L \\ b_L \end{pmatrix} + h.c.$$

The $c_{ij} = cos(\theta_{ij})$, $s_{ij} = sin(\theta_{ij})$ and δ is a phase that governs all CP-violating terms in flavor-changing processes. Flavor-Changing Neutral Currents (FCNCs), whose interactions happen via exchange of a Z boson, are not allowed in the SM.

2.2 The strong sector

This section provides an overview of strong interactions. It begins with a review of the full quantum field theory of strong interactions under the local gauge $SU(3)$,

known as quantum chromodynamics (QCD). The quark model and the classification of different hadrons is then presented.

2.2.1 Quantum chromodynamics

The strong force is described by quantum chromodynamics. It is a non-Abelian gauge theory with the local gauge group $SU(3)$. Quarks are assigned to the fundamental representation $SU(3)$, which gives rise to a quantum number known as *color*, of which there are 3 states labeled *red*, *green*, and *blue*. The gauge fields corresponding to $SU(3)$ are known as *gluons*, and describe interaction between colored particles. The quark fields transform under $SU(3)$ in the following way

$$q(x) \to q'(x) = e^{\frac{1}{2}\theta_a(x)\lambda_a} q(x) \tag{2.43}$$

where q represents a quark of one of three color states and $\frac{1}{2}\lambda_a$ are the eight generators of $SU(3)$, known as the Gell-Mann matrices. The matrices satisfy the following relation

$$[\lambda_a/2, \lambda_b/2] = i f_{abc} \lambda_c/2 \tag{2.44}$$

where f_{abc} are the non-zero structure functions.

In order to construct a Lagrangian that is invariant under local $SU(3)$ transformations, we introduce the gauge fields $G^a_\mu(x)$ and follow the recipe from QED to get the transformation

$$G^a_\mu(x) \to G^a_\mu(x)' = G^a_\mu(x) - \frac{1}{g}\partial_\mu \theta_a(x) \tag{2.45}$$

and to define a covariant derivative

$$D_\mu = \partial_\mu - ig\frac{\lambda_\alpha}{2} G^\alpha_\mu(x) \tag{2.46}$$

where g represents the coupling constant between quarks and gluons. The field strength reads

$$G^a_{\mu\nu} = \partial_\mu G^a_\nu - \partial_\nu G^a_\mu + g f^{abc} G^b_\mu G^c_\nu. \tag{2.47}$$

which leads us to the full QCD Lagrangian

$$\mathcal{L}_{QCD} = i\bar{q}(x)\gamma^\mu D_\mu q(x) - m\bar{q}(x)q(x) - \frac{1}{4} G^a_{\mu\nu} G^{\mu\nu,a} \tag{2.48}$$

The addition of terms involving f^{abc} have no analogue in QED, and leads to self interaction terms of the gluon fields $G^a_\mu(x)$.

2.2.2 The quark model

Hadrons are particle composed of quarks and the gluons that bind them. The quark model was first proposed independently by Gell-Mann [15] and Zweig [16] as a way to classify the growing list of different hadrons known at the time. It classifies the different hadrons according to their valence quarks, which give rise to the quantum numbers of the hadrons. The quarks have a baryon number of

Quantum number	d	u	s	c	b	t
Q - electric charge	-1/3	+2/3	-1/3	+2/3	-1/3	+2/3
I - isospin	1/2	1/2	0	0	0	0
I_z - isospin z-component	-1/2	+1/2	0	0	0	0
S - strangeness	0	0	-1	0	0	0
C - charm	0	0	0	+1	0	0
B' - bottomness	0	0	0	0	-1	0
T - topness	0	0	0	0	0	+1

TABLE 2.3: Additive quantum numbers of the different quark flavors

.

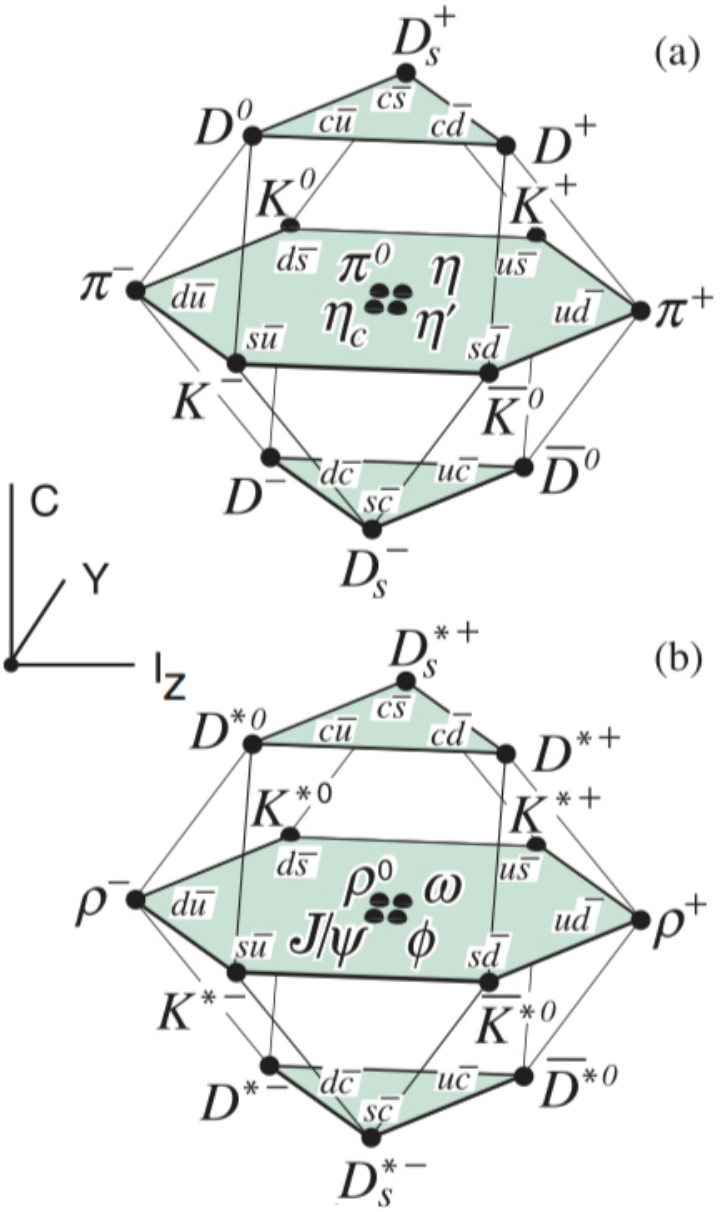

FIGURE 2.2: The 16-plet of $SU(4)$ for the (a) the psudoscalar and (b) the vector mesons composed of u, d, s and c quarks [2].

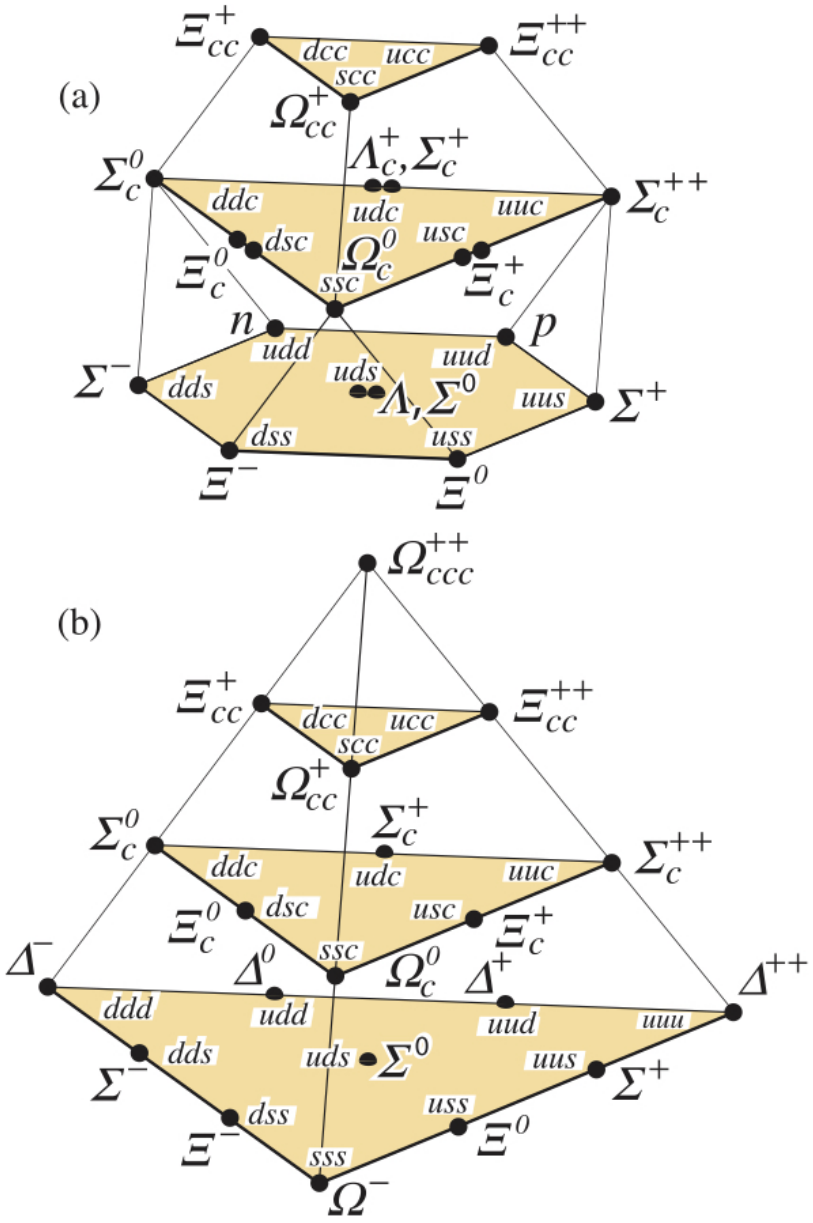

FIGURE 2.3: Multiplets of $SU(4)$ for the baryons composed of u, d, s and c for the (a) The 20-plet with an $SU(3)$ octet and (b) the 20-plet with an $SU(3)$ decuplet [2].

+1/3 while the anti-quarks have a baryon of -1/3. The quantum numbers for the quarks are listed in section 2.2.2. The quantum numbers are related via the Gell-Mann-Nishijima formula

$$Q = I_z + \frac{B + S + C + B' + T}{2} \tag{2.49}$$

where Q is the electric charge, I_z the third component of the isospin[5], B is the baryon number, S is the strangeness, C is the charmness, B' is the bottomness and T is the topness. The *hypercharge* is defined as

$$Y = B + S + \frac{C - B' + T}{3}. \tag{2.50}$$

The hypercharge Y is 1/3 for the U and d quarks, -2/3 for the strange quark, and 0 for all the rest.

The *Mesons* are hadrons containing one quark and one anti-quark, and thus have a baryon number $B = 0$. Furthermore, mesons are bosons. They are J^{PC} multiplets; the $\ell = 0$ states are the psudoscalars (0^{-+}) and the vectors (1^{--}), while the $\ell = 1$ states are the scalars (0^{++}), the axial vectors (1^{++}) and (1^{+1}) and the tensors (2^{++}). All mesons are unstable with the longest living meson having a lifetime of about 10^{-8} seconds.

The nine possible $q\bar{q}'$ combinations of the u, d and s quarks can be grouped into an octet and a singlet of mesons under $SU(3)$,

$$\mathbf{3} \otimes \bar{\mathbf{3}} = \mathbf{8} \oplus \mathbf{1} \tag{2.51}$$

which can be extended to $SU(4)$ by including combinations containing c quarks to give a 15-plet and a singlet,

$$\mathbf{4} \otimes \bar{\mathbf{4}} = \mathbf{15} \oplus \mathbf{1}. \tag{2.52}$$

The psudoscalar and vector mesons *weight diagrams* are depicted in figure 2.2. Of particular relevance to the $pp \to W + c$ cross-section presented later will be the charmed mesons D^+, D^0 and D_s.

The *Baryons* are hadrons containing three quarks plus any number of quark and anti-quark pairs. Thus their baryon number is always equal to 1. Because they are composed of three quarks, baryons are fermions. The proton and neutron belong to this family of particles.

The different qqq combinations of the u, d and s quarks can be decomposed as

$$\mathbf{3} \otimes \mathbf{3} \otimes \mathbf{3} = \mathbf{10} \oplus \mathbf{8} \oplus \mathbf{8} \oplus \mathbf{1}. \tag{2.53}$$

Adding c quarks extends this to $SU(4)$. The $SU(4)$ multiplet of baryons made up of u, d, and c quarks is shown in figure 2.3.

[5]To be distinguished from the weak isospin of electroweak theory.

Chapter 3

Physics of proton-proton collisions

3.1 The parton model

Deep inelastic electron-proton scattering experiments, like those carried out at SLAC in the late sixties [17, 18], give strong indications of the composite structure of the proton. At low to modest energies, electron-proton scattering is elastic: $e+p \rightarrow e+p$. If the incident electron carries enough energy though, the scattering becomes inelastic: $e+p \rightarrow e+X$, where X represents outgoing hadronic material from the exploded proton. This fragmentation of the proton in such scattering experiment provided concrete proof of the composite nature of the proton.

The differential cross-section for inelastic scattering of an electron with an energy between E' and $E'+dE'$ off of a proton into a solid angle $d\Omega$ is given by

$$\frac{d^2\sigma}{d\Omega dE'} = \frac{4\alpha^2 E'^2}{Q^4}\left[W_2(Q^2,\nu)cos^2\left(\frac{\theta}{2}\right) + 2W_1(Q^2,\nu)sin^2\left(\frac{\theta}{2}\right)\right] \tag{3.1}$$

$W_1(Q^2,\nu)$ and $W_2(Q^2,\nu)$ are called *structure functions* and depend on two independent variables $Q^2 = -q^2$ and $\nu = q^2/M$, where q^2 represents the momentum transfer and M the mass of the proton. Assuming that the scattering is taking place between electrons and point-like constituents of mass m_i inside the proton, the structure functions should have the form [19]

$$2m_i W_1^i(Q^2,\nu) = \frac{Q^2}{2m_i\nu}\delta\left(1-\frac{Q^2}{2m_i\nu}\right) \tag{3.2}$$

$$\nu W_2^i(Q^2,\nu) = \delta\left(\frac{Q^2}{2m_i\nu}\right) \tag{3.3}$$

The structure functions are no longer functions of Q^2 and ν separately, which appear only in the dimensionless ratio $x = Q^2/2m_i\nu$. This is known as *Bjorken scaling* [20].

Feynman was the first to give a physical interpretation to the scaling variable x [21]. He postulated that each constituent, or *parton*, carries only a fraction, x, of the total proton. The four-momentum of a parton is given by $p_i = xp$, where p

is the four-momentum of the proton, and has a mass of $m_i \approx xM$. Let $f_i(x)$ be the probability that a given parton of type i carries a momentum fraction x and e_i be the corresponding fractional charge of the parton. The contribution to the individual partons to the total inelastic electron-proton differential cross-section can be summed and written as

$$W_1(Q^2, \nu) = \sum_i \int e_i^2 \frac{Q^2}{4M^2x^2} f_i(x) \delta \left(\nu - \frac{Q^2}{2Mx} \right) dx \tag{3.4}$$

$$W_2(Q^2, \nu) = \sum_i \int e_i^2 f_i(x) \delta \left(\nu - \frac{Q^2}{2Mx} \right) dx \tag{3.5}$$

which reduce to

$$MW_1(Q^2, \nu) = \sum_i \frac{e_i^2}{2} f_i(x) \equiv F_1(x) \tag{3.6}$$

$$\nu W_2(Q^2, \nu) = \sum_i e_i^2 x f_i(x) \equiv F_2(x). \tag{3.7}$$

The quantity $xf_i(x)$ is known as a *parton distribution function* (PDF), and there is a different one for each parton. Comparing these last two relations leads to the Callan-Gross relation [22]

$$2xF_1(x) = F_2(x) \tag{3.8}$$

which is valid for spin 1/2 partons only.

The Bjorken scaling hypothesis and the Callan-Gross relation provide for a straightforward test of the parton model. Deep inelastic scattering experiments at SLAC [17, 18] provided support for such a model; protons are composite particles whose constituents act as point-like spin 1/2 Dirac particles, which are identified as quarks. The lightest and most stable of the quarks are the u and d quarks, which are ideal candidates for the quarks within protons. Since the proton is itself a spin 1/2 particle, the minimum number of quarks needed would be three. Moreover, the charge of the proton indicates that the quarks needed are uud, which add up to give a charge of +1.

While the model of the proton consisting of quarks is a good starting point, it is not the end of the picture. So far the quarks have been assumed to behave as free particles within the proton. While this is a good assumption when dealing with their interactions on short time scales with virtual photons, on larger time scales this assumption breaks down. After all, the quarks are bound to each other, so it would be a gross simplification that the proton consist of only quarks. Indeed, if one computes the average total momentum of the proton carried by the quarks, one finds that it only accounts for 54% of the total proton's momentum. The missing momentum can be accounted for by *gluons*, which are the force carriers that bind the quarks together. They do not carry electric charge, so are not directly seen in inelastic scattering experiments discussed thus far, but can be indirectly inferred from the momentum contribution of the charged quarks within the proton.

The departure from a picture in where the quarks are free to one where the quarks are bound together by the gluon fields leads scaling violations not predicted by Bjorken scaling. This leads to a dependence of the PDFs on Q^2

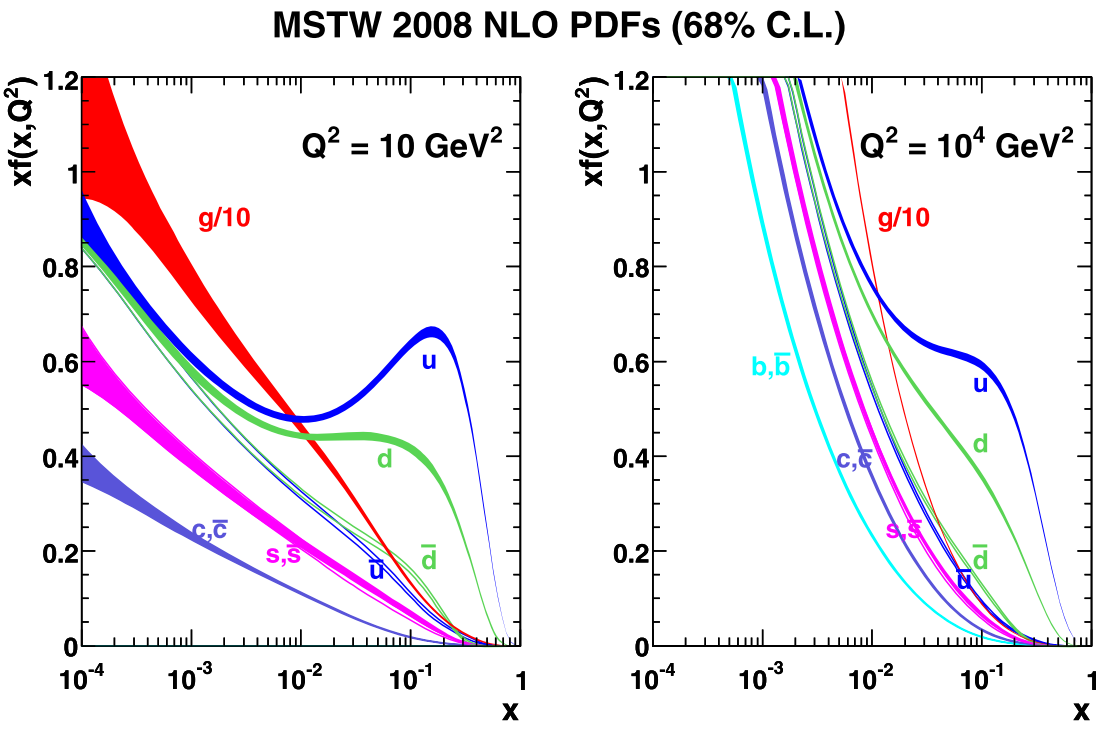

FIGURE 3.1: Parton distribution functions as determined from the MSTW group [26] for $Q^2 = 10$ GeV and $Q^2 = 10^4$ GeV.

at higher energy interactions so that $f_i(x) \to f_i(x, Q^2)$. The dependence on Q^2 cannot be calculated, but the x dependence can be taken from some experiment at a particular Q^2, and then calculated at another value of Q^2 through the QCD evolution equations of Dokshitzer, Gribov, Lipatov, Altarelli and Parisi (DGLAP equations) [23–25].

The *uud* quarks that make up the proton's charge and spin are know as *valence quarks*. The term is used to differentiate them from *sea quarks*, which arise from the gluons splitting into quark-antiquark pairs. Thus, in addition to the PDFs for the valence quarks, there are also PDFs associated with each sea quark. The PDFs for the proton as determined by the MSTW group are shown in figure 3.1 [26]. While the term PDF in this thesis refers to PDF sets of the proton, there are different PDF sets for each hadron depending on the quantum numbers of the system.

3.2 Proton-Proton collisions

The collision of protons is dominated by strong interactions. During inelastic pp collisions, the hard scattering occurs between two partons, q_i and q_j, while softer interactions occur between the constituents of the proton remnants. A typical example of two protons colliding is illustrated in figure 3.3.

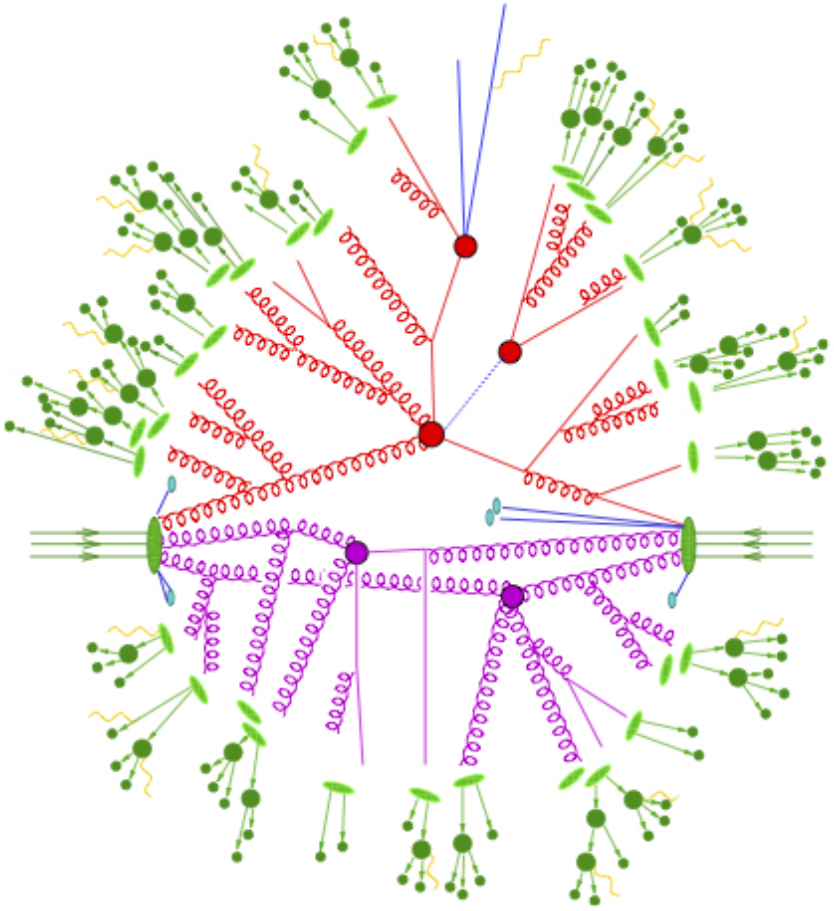

FIGURE 3.2: Illustration of a pp collision. The hard interaction is seen in red and secondary interactions (pileup) are indicated by purple [27].

3.2.1 Cross-section for pp collisions

Perturbative QCD calculations can be used to determine the cross-section from the collision of two partons. The *factorization theorem* allows the cross-section for deep inelastic to be decomposed as a convolution of two terms: a calculable hard term and a non-perturbative PDF. Thus the cross-section for $pp \to X + Y$ can be written as

$$\sigma(pp \to X + Y) = \sum_{i,j} \int dx_i dx_j f_i(x_i, Q^2) f_j(x_j, Q^2) \sigma(q_i q_j \to +Y) \tag{3.9}$$

where X is any final hadronic state, $\sigma(q_i q_j \to +Y)$ is the cross-section for the partons q_i and q_j scattering into a final state Y and the sum runs over all parton types.

3.2.2 Parton showers

The partons stemming from the hard interaction typically have very large momentum, and can produce shower of secondary low momentum partons. Examples

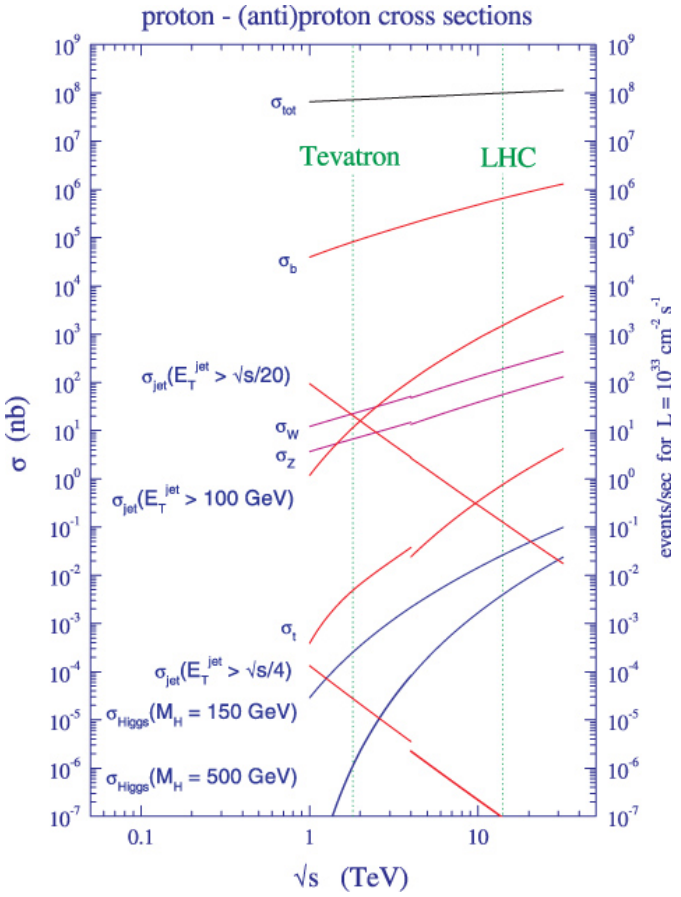

FIGURE 3.3: Standard Model cross sections for pp collisions as a function of the center-of-mass energy [28].

include gluon splitting ($g \to q\bar{q}$) and gluon radiation ($q \to gq$). The shower of secondary soft-material is known as a *parton shower*.

Perturbative QCD can be used to determine the evolution of any given parton, but the large number of possible final state partons make calculation of the entire parton shower nearly impossible. Further complicating things is the fact that some processes lead to divergences, such as soft-emission of a gluon or collinear gluon emission. Alternative approaches to the calculation make use of iterative procedures based on various phenomenological models. Such calculations are parameterized by Sudakov form factors [29] and make use of *splitting functions*, which give the probability that a given parton originates from a parton with a higher momentum.

3.2.3 Hadronization

The process in which hadrons are formed from quarks and gluons is called *hadronization*. Color confinement does not allow for color-charged particles to exist individually, so that quarks and gluons will combine with other quarks and anti-quarks created from the vacuum to form hadrons which are then color neutral. The process of hadronization is not fully understood as there are no perturbative QCD

techniques that can be employed to calculate such processes with such low momentum transfer. Hadronization is therefore studied and parameterized by a series of phenomenological models, such as the Lund-String-Model [30].

Typically several hadrons are formed from the hadronization processes. This spray of hadrons, and the collinear emission of gluons, will form a cone of particles, known as *jets*, which will have the same general direction as the original parton. Thus, hadrons are typically observed within these collimated jets.

3.2.4 Underlying event and pileup

Besides the hard-scatter interaction of typical interest, there are many soft-scatter interactions between other partons from the proton remnants which form a background to the hard-scattering process. These secondary interactions form what is known as the *underlying event*. Soft-particles from the underlying event can have a large effect on the calculation of the missing transverse energy and calibration of the jet energy. The underlying event arises from low energy QCD which cannot be calculated perturbatively and rely on various phenomenological using experimental data.

Multiple proton-proton interactions within the same bunch crossing presents another challenging aspect when analyzing collisions. These multiple interactions are termed *pileup*, and can easily exceed an average number of 20 collisions per bunch crossing. Pileup is modeled by overlaying inclusive samples of pp collisions over the hard-scattering process. The number of these overlaid events is varied and reweighted to match the number of crossings seen in data.

3.2.5 Monte Carlo generators

To adequately model detector response to various physics processes, precise theoretical models are needed. These typically take the form of Monte Carlo[1] generators, which take into account the parton showering, hadronization of quarks, underlying events and decay of unstable hadrons. Each generator treats each step differently, and typically perform calculations to Leading Order (LO) or Next to Leading Order (NLO). A few different generators are outlined here:

- `PYTHIA` [31, 32] calculates hard-scattering processing to LO. Parton showers are added on-top, the accuracy of which becomes limited at large jet multiplicities. Hadronization of quarks and gluons are simulated using phenomenological models.

- `HERWIG` [33] calculates the hard-scatter to LO in the same way as `PYTHIA`. The difference between the two generators comes from different implementation of the parton shower and modeling of hadronization. The simulation underlying event is normally performed separately using `Jimmy` [34].

[1] Monte Carlo algorithms are a large class of probabilistic algorithms relying on repeated random sampling to get numerical results.

- `HERWIG++` [35] is similar to `HERWIG`, but implemented separately. The main difference comes from switching from Fortran to C++, as well as improvements in the modeling of the parton shower hadronization.

- `SHERPA` [27, 36] is a LO generator which includes additional partons in the hard-scattering calculations. It provides a more accurate picture for high jet multiplicities than `PYTHIA` and `HERWIG` allowing for a treatment of heavy flavor quarks such as c and b quarks.

- `ALPGEN` [37] is a LO generator focusing on final states with many jets. It is typically interfaced with `PYTHIA` or `HERWIG` for parton showering and hadronization modeling.

- `MADGRAPH` [38] is a LO generator similar to `ALPGEN` but with simpler implementation. It is usually interfaced with `HERWIG` or `PYTHIA`.

- `AcerMC` [39] is a generator dedicated to simulating Standard Model processes for the LHC. It makes use of an internal library of matrix element calculations from `MADGRAPH` for hard-scattering process. It is usually interfaced with `HERWIG` or `PYTHIA`.

- `McAtNLO` [40] is a NLO generator, providing a more accurate description of hard-scattering processes and kinematic distributions. It is typically interfaced with `HERWIG` for parton showering, hadronization and underlying event modeling.

- `POWHEG` [41] calculates hard-interactions at NLO. It can be interfaced with any parton shower generator.

- `EvtGen` [42] is specifically designed to simulate complex decay chains, and it is typically interfaced with other generators after the hadronization process.

The cross sections obtained from Monte Carlo are corrected to NLO or NNLO calculations by the use of multiplicative factors called *k-factors*. The k-factor correction for going from LO to NLO is

$$k = \frac{\sigma_{NLO}}{\sigma_{LO}} \tag{3.10}$$

where σ_{NLO} is the NLO cross section and σ_{LO} the LO one. It is important to note that k-factors can in general be different for different kinematic phase spaces for a given process.

Chapter 4

Silicon and Silicon Detectors

4.1 Silicon

Silicon is the most abundant element within the Earth's crust. It is typically found in a compound state of Silicon dioxide, due to its reaction with oxygen at high temperatures. Its abundance means that it has been well studied and its properties are well know.

Dominating today's electronics technology, silicon's importance to modern society cannot be overstated. It is not only the primary component of most semiconductor devices, such as integrated circuits, computer chips and solar cells, but is also the principle component in stone, glass and concrete which makes it invaluable to the construction industry.

Silicon is a semiconductor, and we will begin our discussion by outlining the most important concepts of semiconductor physics.

4.1.1 Band structure

Semiconductors are crystalline or amorphous solids, which are characterized by their electrical properties. Crystalline solids, which include silicon, can be described by three primary basis vectors, **a**, **b** and **c**. The crystal structure remains invariant under translations by a vector which is an integral sum of any of these three vectors so that direct lattice sites are defined by the set

$$\mathbf{R} = m\mathbf{a} + b\mathbf{b} + p\mathbf{c} \tag{4.1}$$

where m, n, and p are arbitrary integers. The crystalline structure of silicon is that of a diamond lattice, which is shown in figure 4.1.

Perhaps the most important theorem in semiconductor physics is that of *Bloch's theorem* [44]. It states that given a periodic potential $V(\mathbf{r})$, the solutions to Schrödinger's equation will be of the form

$$\psi_k(\mathbf{r}) = e^{i\mathbf{k}\cdot\mathbf{r}} u_k(\mathbf{r}) \tag{4.2}$$

where $\mathbf{k}$ is the wave vector, $\mathbf{r}$ is the position, and $u_k(\mathbf{r})$ is a function that is periodic in $\mathbf{r}$. The energy levels calculated using equation (4.2) will form semi-continuous energy bands. Furthermore, there will be energy levels for which there are no

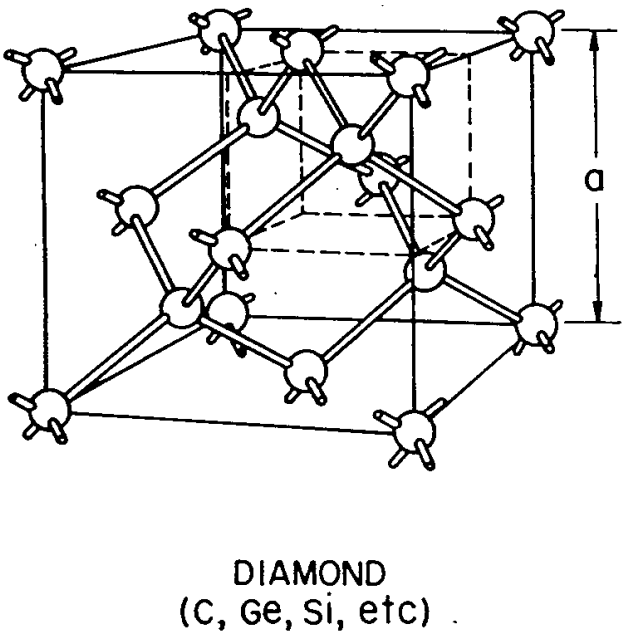

FIGURE 4.1: The diamond lattice structure, where a is the lattice constant [43].

solutions to Schrödinger's equation of the form equation (4.2). These forbidden energy solutions will form gaps within the bands, and are referred as *band gaps*. Thus, silicon, with its periodic diamond lattice structure, will also have a band structure characterized by its band gap. The band gap of silicon at a temperature of $T = 300$ K is $E_g = 1.12$ eV. The band structures for three of the most important semiconductors, germanium (Ge), silicon (Si) and gallium arsenide (GaAs), are shown in figure 4.2.

The lower band is known as the *valence band*, and represents the energy of valence electrons bound to their parent atoms, while the upper band is known as the *conduction band*, and represents quasi-free states where electrons are free to move throughout the crystal. At $T = 0$ K, the valence band will be completely occupied by valence electrons while the conduction band will be empty.

The bands are not constant, but vary with the wave vector. Semiconductors where the maximum of the valence band and minimum of the conduction band occur at the same $\mathbf{k}$ are known as *direct* semiconductors, while ones who's valence band has a maximum and conduction band has minimum at different $\mathbf{k}$ are known as *indirect* semiconductors. Silicon is an indirect semiconductor, but for most practical purposes it is useful to consider a simplified band picture where the bands are constant, as seen in figure 4.3. Here the valence band is denoted E_V and the conduction band E_C.

The electrical conductivity of a material will depend on the size of the band gap. *Insulators* are materials who's band gap is very large, typically several eV, which lead to very low electrical conductivity. *Conductors* are materials whose energy bands overlap or where partial filling of the conduction band is seen already at $T = 0$ K, and will have very high electrical conductivity. Semiconductors are then materials whose bands do not overlap, but have a band gap smaller than that of insulators, typically on the order of an eV.

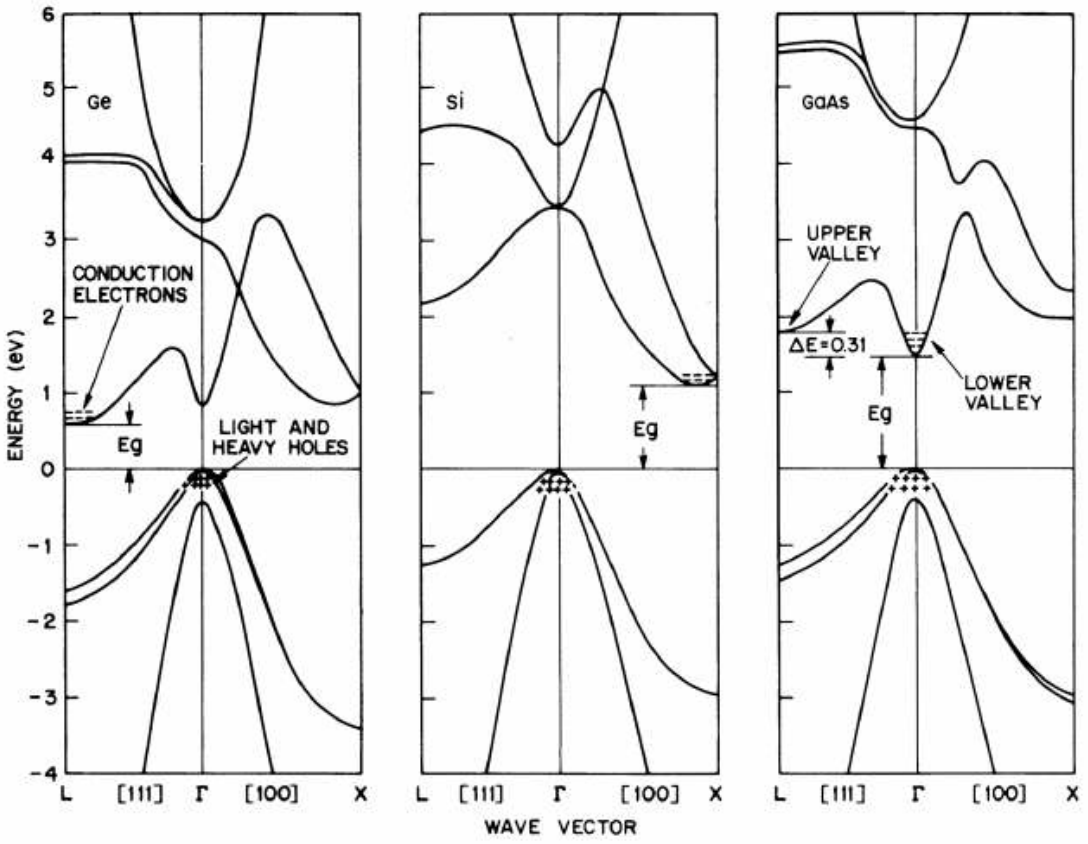

FIGURE 4.2: The band structure as a function of the wave vector for Ge, Si, and GeAs, where E_g is the band gap energy [43].

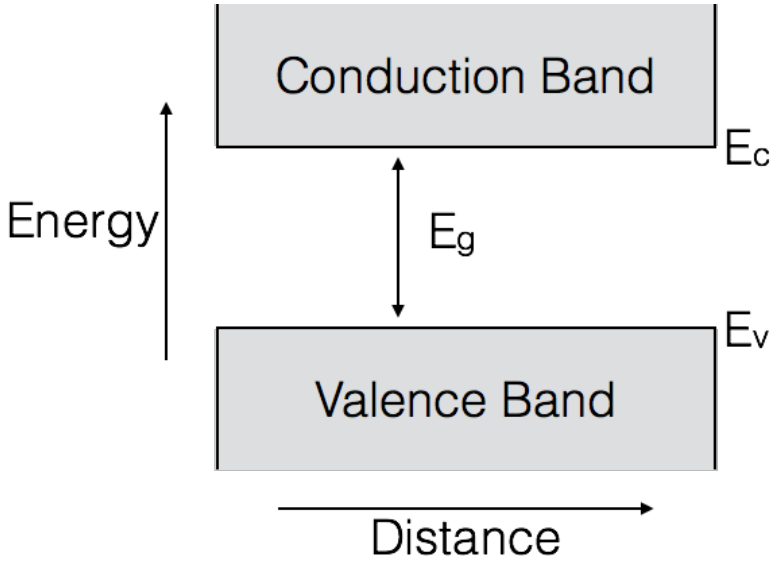

FIGURE 4.3: A simplified band diagram of a semiconductor.

4.1.2 Extrinsic silicon

The real advantage of semiconductors is their ability to change electrical conductivity by introduction of impurity atoms, called *dopants*. These dopants replace atoms of the original material at lattice sites, and typically have more or less valence electrons in their outer shell, depending on the specific type of dopant. They will introduce additional energy states that may lie within the band gap region of the semiconductor. Semiconductors with little to no dopants are termed *intrinsic* while semiconductors which have had dopants added are termed *extrinsic*.

Each silicon atom shares four valence electrons with its neighbors, forming covalent bonds. Replacing one of these atoms by a phosphorus atom, which has five valence electrons, will lead to an extra electron that does not form a covalent bond. These loosely bound electrons are easily excited into the conduction band, and can contribute to the electric conductivity of the device. In this way negative charge electrons are donated to the conduction band, and the impurities in this case are called *donors*. Conversely, one can substitute a boron atom, which has three valence electrons, leading to an electron being accepted from other atoms to form four covalent bonds with the boron atom. This leaves a positive charged *hole* in the valence band, and such impurities are known as *acceptors*. Semiconductors with a larger number of donors than acceptors are called *n-type*, while those with a larger number of acceptors than donors are called *p-type*.

The dominant charge carriers type in n-type materials are electrons, while for p-type materials they are holes. These are known as *majority carriers*. Likewise, *minority carriers* are the opposite type of charge carriers from the majority carriers, that is electrons in p-type material and holes in n-type material.

4.1.3 The space charge

Dopants refer to purposefully added impurities, typically forming energy states near the band edges which are readily ionized. *Defects* are more general, encompassing impurities which can also appear from uncontrolled processes, such as during crystal growing procedures or radiation damage. These states can be very shallow, i.e. near the band edges, or deep within the band gap. These defect states have the potential to significantly alter the electrical properties of extrinsic silicon, and care must be taken to account and control such states.

Donors will be electrically neutral when occupied by an electron and positively charged when occupied by a hole while acceptors will be electrically neutral when occupied by a hole and negatively charged when occupied by an electron. The probability that a given defect state at an energy E is filled in thermal equilibrium is given by Fermi-Dirac statistics

$$f(E) = \frac{1}{1 + e^{(E-E_F)/kT}} \tag{4.3}$$

where E_F is the Fermi Energy, k is Boltzmann's constant and T the temperature. For a defect with a concentration N_t at an energy E_t, the concentration of trapped

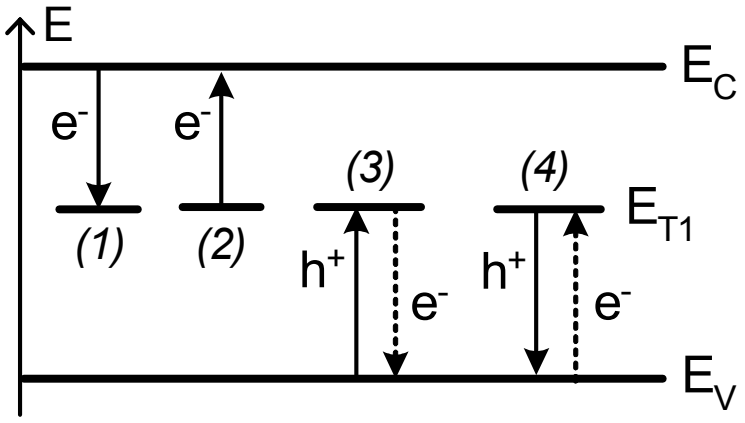

FIGURE 4.4: An illustration of the four competing processes governing the occupancy of defect states [45].

electrons is then determined by

$$n_t = N_t f(E_t) = \frac{N_t}{1 + e^{(E_t - E_F)/kT}} \tag{4.4}$$

and that of trapped holes

$$p_t = N_t \left(1 - f(E_t)\right) = \frac{N_t}{1 + e^{-(E_t - E_F)/kT}}. \tag{4.5}$$

In general[1], the charge state of defects will depend on four competing processes as seen in figure 4.4 [46, 47]

1. capture of an electron from the conduction band: $r_1 = e_n n_t$
2. emission of an electron into the conduction band: $r_2 = c_n n p_t$
3. capture of a hole from a valence band: $r_3 = c_p p n_t$
4. emission of a hole into the valence band: $r_4 = e_p p_t$

Here r_i represents the rate for process i, n and p are the respective concentration of free electrons and holes in the conduction and valence bands, e_n and e_p are the *emission rates* for electrons and holes, and c_n and c_p are the *capture coefficients* for electrons and holes. The emission rates and capture coefficients are related by

$$e_{n,p} = c_{n,p} e^{\pm\left(E_{C,V} - E_t\right)/kT} N_{C,V} \tag{4.6}$$

where $N_{C,V}$ represents the number of free states in the conduction and valence bands. The *capture cross section* for electrons and holes can be defined as

$$\sigma_{n,p} = c_{n,p} / \bar{v}_{n,p} \tag{4.7}$$

[1]This means not necessarily in thermal equilibrium, such as in a steady state or high injection conditions.

where $\bar{v}$ is the thermal velocity of the carriers. This can be used to define the minority carrier lifetime for holes in n-type material

$$\tau_p = \frac{1}{\sigma_p \bar{v}_p N_t} \tag{4.8}$$

and for eletrons in p-type material

$$\tau_n = \frac{1}{\sigma_n \bar{v}_n N_t}. \tag{4.9}$$

The electric field within a semiconductor can then be determined from Poisson's equation

$$\nabla^2 V = -\frac{\rho}{\epsilon} = -\frac{q\left(N_{eff} + p - n\right)}{\epsilon} \tag{4.10}$$

where V is the electric potential, q represents the electron charge, ϵ the dielectric constant of the material, p the concentration of free holes in the valence band, and n the concentration of free electrons in the conduction band. The effective doping concentration N_{eff} is determined by the number of charged donor and acceptor states and reads

$$N_{eff} = \sum_{donors} p_t + \sum_{acceptors} n_t. \tag{4.11}$$

The effective doping concentration is generally referred to as the *space charge*, and represents the overall charge density in the device.

4.1.4 Carrier transport

The movement of electrons or holes within a semiconductor is not a straightforward affair. In the absence of an electric field, electrons will move randomly within the material due to thermal vibrations, and the average velocity will be zero. Under the influence of an electric field, the electrons will be accelerated. Unlike the case of a vacuum, electrons will not be constantly accelerated but will instead move with an average velocity, called the *drift velocity*, due to scattering in the crystal by defect states, atoms within the lattice, phonons and other electrons. The complicated motion of the electron is therefore included in a constant, known as the *mobility*, which depends on the particular material of the semiconductor. The drift velocity is given by

$$\mathbf{v} = \mathbf{E}\mu \tag{4.12}$$

where μ is the mobility[2] of electrons for a given material and $\mathbf{E}$ is the electric field.

The movement of holes in a semiconductor is a bit more complicated. Unlike electrons, which really are localized particles which move through the crystal, holes are really an absence of an electron. The movement of holes requires valence electrons jumping from one atom to another, each filling the absence as they do so. Therefore the mobility of electrons and holes will in general be different, owing

[2]The mobility is in general dependent on the electric field through $\mu = \frac{\mu_0}{1+bE}$ where μ_0 is the mobility at $E = 0$ and b a constant depending on the material choice. This expression for the mobility leads to velocity saturation at large electric fields.

to the different nature of their movement, and we denote the hole mobility as μ_p and the electron mobility as μ_n. For intrinsic silicon at $T = 300$ K the mobility of electrons is $\mu_n = 1350$ cm^2/Vs, while that of holes is roughly a third and is $\mu_p = 480$ cm^2/Vs.

Diffusion will also play a role in the movement of charges due to gradients in the carrier concentration and Brownian motion. This type of movement is determine by the *diffusion coefficient* and is related to the mobility by the Einstein relation [48]

$$D = \frac{kT}{q}\mu \tag{4.13}$$

where k is Boltzmann's constant, T the temperature and q the electron charge. Owing to different mobilities, there will be two separate diffusion constants; D_n for electrons and D_p for holes.

The current in semiconductors due to mobile charge carries will be the sum of drift and diffusion components. The current density for electrons will read

$$\mathbf{J}_n = q\mu_n \mathbf{E} + qD_n \nabla n \tag{4.14}$$

and for holes

$$\mathbf{J}_p = q\mu_p \mathbf{E} - qD_p \nabla p \tag{4.15}$$

where n is the concentration of free electrons in the conduction band and p the concentration of free holes in the valence band. The total current density will be the sum of electron and hole components

$$\mathbf{J} = \mathbf{J}_n + \mathbf{J}_p. \tag{4.16}$$

The above equations neglect effects from external applied magnetic fields. This will lead to a transverse component to the current and is known as the *Hall effect* [49], which will not be covered here.

Finally, the current must satisfy the continuity equations

$$\frac{\partial n}{\partial t} = G_n - U_n + \frac{1}{q}\nabla \cdot \mathbf{j}_n \tag{4.17}$$

$$\frac{\partial p}{\partial t} = G_p - U_p - \frac{1}{q}\nabla \cdot \mathbf{j}_p \tag{4.18}$$

where G_n is the generation rate for electrons, G_p the generation rate for holes, U_n the recombination rate for electrons and U_p the recombination rate for holes. Under steady state conditions we have

$$\frac{\partial n}{\partial t} = \frac{\partial p}{\partial t} = 0. \tag{4.19}$$

4.1.5 The p-n junction

We are now ready to discuss one of the most important devices in semiconductor physics; the *p-n junction*. As their name implies, p-n junctions are two terminal devices made when p-type material comes into contact with n-type material.

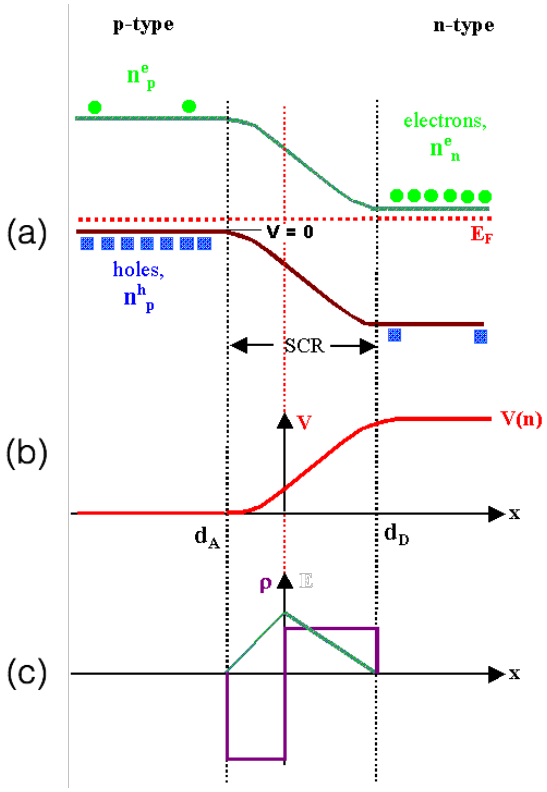

FIGURE 4.5: An illustration of a p-n junction showing (a) the energy band diagram, (b) the resulting built-in voltage and (c) the charge density within the space charge region.

Let us first consider the case of an intrinsic semiconductor. For such a material, the Fermi energy E_F will lie in the middle of the band gap, half way between the valence and conduction bands. As donors are added, the Fermi energy will shift upwards towards the conduction band. Conversely, adding acceptors will shift the Fermi energy down towards the valence band. So for n-type material, the Fermi energy lies near the conduction band, and for p-type material it lies close to the valence band. When the two materials come into contact, their Fermi energy of the two will not match. In order for the system to be in thermal equilibrium, a constant Fermi energy throughout the whole system is required. This leads to electrons from the n-type material diffusing into the p-type material and holes from the p-type material diffusing into the n-type material until a constant Fermi energy is achieved throughout. The bands will be shifted with respect to each other in the two materials, and the region around the junction being depleted of free charge carriers. This region is known as the *depletion region*, or more appropriately the *space charge region*, and consists of fixed ionized impurities stripped of their quasi-free charge carriers. The space charge region constitutes the active region of the device. The shift in bands also leads to a potential drop called the built-in voltage. The entire process is illustrated in figure 4.5.

The current-voltage characteristics of a p-n junction were first derived by Shockley[3] [50]. The current in a p-n junction as a function of the applied external

[3]The derivation depends on four main assumptions: (1) the junction is abrupt; (2) the Boltzmann relation holds in the depletion region; (3) the injected concentration of minority carries is

voltage can be approximated by

$$J = J_s \left(e^{qV/kT} - 1\right) \tag{4.20}$$

where J_s is the saturation current and V is the applied bias voltage. This is known as the Shockley diode equation, or simply the Shockley equation, and gives the current-voltage relationship of an ideal diode. Two modes of operation are defined from equation (4.20); the region $V < 0$ is known as *reverse* bias and the current saturates at J_s, while the region $V > 0$ is known as *forward* bias and the current rises exponentially with V.

In the reverse bias mode, the space charge region increases with increasing $|V|$. The size of this region, W, can be determined by solving Poisson's equation with the appropriate boundary conditions. For the sake of simplicity, let us assume a 1-D abrupt junction at $x = 0$, and consider only one side of the junction. Also, we assume low injection conditions so that $p \approx n \approx 0$. From here on we will refer to the applied bias voltage as V_{bias} and $V = V(x)$ will be the potential as a function of x. In this case, Poisson's equation reads

$$\frac{d^2V}{d^2x} = \frac{qN_{eff}}{\epsilon} \tag{4.21}$$

which upon integration and with the following boundary conditions

$$\frac{dV}{dx}|_{x=W} = -E(W) = 0 \tag{4.22}$$

$$V(W) = V_{bias} \tag{4.23}$$

leads to the following relation

$$W = \left(\frac{2\epsilon}{qN_{eff}} V_{bias}\right)^{1/2} \tag{4.24}$$

where here N_{eff} is equal to the doping concentration.

4.1.6 The Si-SiO$_2$ interface

Before directing our attention to an overview of silicon detectors, we will review the interface between silicon and silicon dioxide, or Si-SiO$_2$. The Si-SiO$_2$ interface plays an important role in the operation of silicon detectors. We will quickly summarize the main concepts here[4].

The bandgap of SiO$_2$ is very large, with $E_g = 8.8$ eV. Furthermore, the hole density is quite large at the interface and detrapping rates for holes very slow. This leads to an accumulation of a fixed positive charge. This fixed positive oxide charge represent states that do not exchange electrons or holes with the lattice. If the silicon side is made of p-type material, the positive oxide charge will result in an inverted layer of mobile electrons, which make the interface highly conductive.

small compared to that of majority carriers; (4) there is no generation of current in the depletion region.

[4]For a more detailed discussion, please see [45, 51].

The interface represents an abrupt termination of the lattice structure. This results in the interruption of covalent bonds, leading to "dangling bonds", where the valence electrons are not satisfied. These dangling bonds result in additional states located at the interface, termed *interface states*, and can readily capture or emit electrons or holes. Interface states can arise from avalanche multiplication, radiation damage, oxidation during the fabrication process or from internal photo emission.

4.2 Silicon detectors

Silicon detectors are essential components of many high energy physics experiments, providing the primary means of momentum determination of charged particles. Segmented silicon detectors are capable of resolving the primary and secondary vertices in experiments such as ATLAS and CMS with high accuracy where the large particle fluxes require readout fast readout.

4.2.1 Basic design

Silicon detectors are complicated diode structures, consisting of many segmented p-n junctions biased in parallel. In the case of silicon strip detectors (SSDs), they consist of several n^+ (or p^+) strips implanted on a p-type (or n-type) substrate. Reverse biasing leads to establishment of a depletion region and electric field in the detector's volume, where electron-hole pairs generated by traversing particles form a signal. A layer of SiO_2 couples the signal from the strip implants to aluminum strips, which are connected to readout electronics where generated signals can be further processed and analyzed. Detectors are biased from the backplane, where the strip implants are held to ground through a bias ring near the detector surface, typically via a polysilicon resistor[5]. Guard rings typically surround the bias ring, which act to slowly drop the voltage between the backplane and surface, so as not to cause damage from large voltage differences. The entire sensor is typically passivated with a layer of SiO_2 to protect the sensor from environmental effects, with small opening on the strips and bias ring for electrical contact. A schematic with the basic features of a typical silicon detectors is shown in figure 4.6.

4.2.2 Signal formation and acquisition

The basic principal of all tracking detectors is to turn energy deposited from charged particles into electrical signals. For silicon detectors, this takes the form of creation of electron-hole pairs from traversing particles, which then move towards readout electronics under the influence of an electric field within the sensor volume. The number of electron-hole pairs created depends on the energy of the incoming particle. The average energy loss of charged particles in a material is determined

[5]Other forms of biasing include punch-through biasing and Field Oxide FET (FOXFET) biasing.

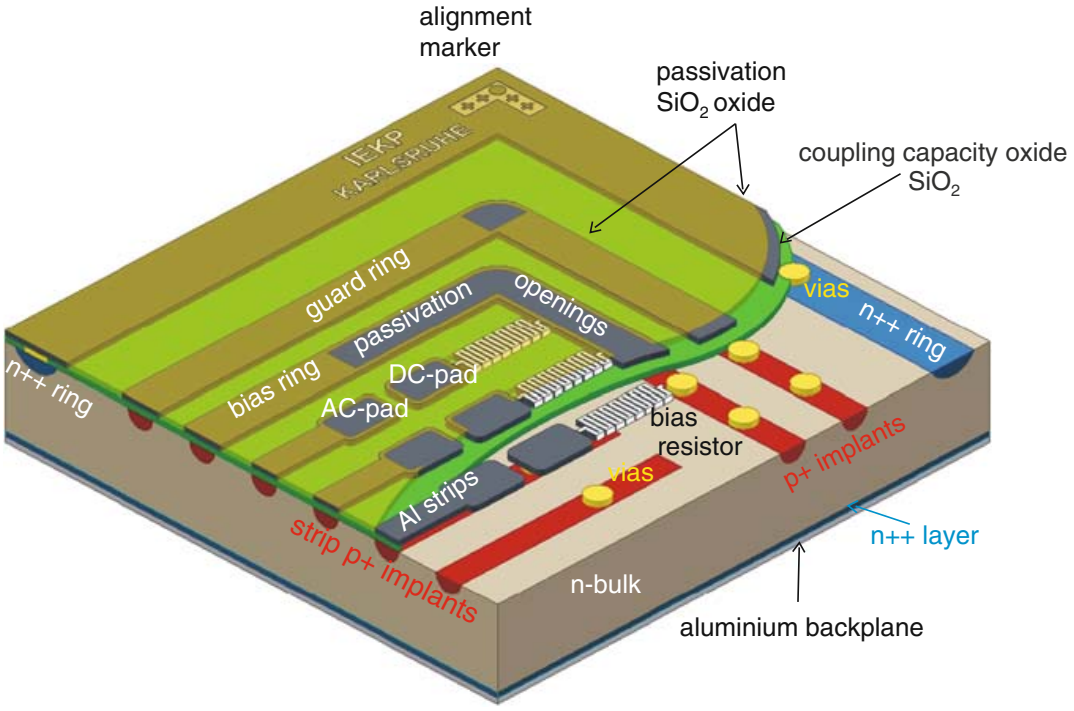

FIGURE 4.6: A schematic of a typical silicon strip detector [52].

by the Bethe-Bloch formula

$$-\frac{dE}{dx} = 4\pi N_A r_e^2 m_e c^2 z^2 \frac{Z}{A}\frac{1}{\beta}\left[\frac{1}{2}ln\left(\frac{2m_e c^2\beta^2\gamma^2 T_{max}}{I^2}\right) - \beta^2 - \frac{\delta(\gamma)}{2}\right] \tag{4.25}$$

where z is the charge of the incoming particle, T_{max} the maximum kinetic energy that can be imparted to an electron during a collision, I the average excitation energy, Z the atomic number, A the atomic mass, N_A Avogadro's number, m_e the mass of the electron, c the speed of light, r_e the classical electron radius, $\beta = v/c$, $\gamma = 1/\sqrt{1-\beta^2}$ and δ the density effect correction. The full function for the case muons traversing copper is shown in figure 4.7. The most important part of the curve occurs at the minimum, which represents the minimum ionization energy in the material. Particles with an energy at the minimum are termed Minimum Ionizing Particles (MIPs). For silicon, the average energy loss is 390 $\frac{eV}{\mu m}$, which, given that the energy needed to create an electron-hole pair is 3.6 eV, leads to an average number of 108 electron-hole pairs being created for each μm. The full function of the Bethe-Bloch formula is shown in figure 4.7.

The most probable value (MPV) of the deposited charge is less than the average due to statistical fluctuations that can be described by *straggling functions*. These straggling functions are described by a Landau distribution, which also takes into account noise contributions which tend to broaden the spectrum, which can be seen in figure 4.8. For silicon, the MPV for a MIP leads to 76 electron-hole pairs for each μm.

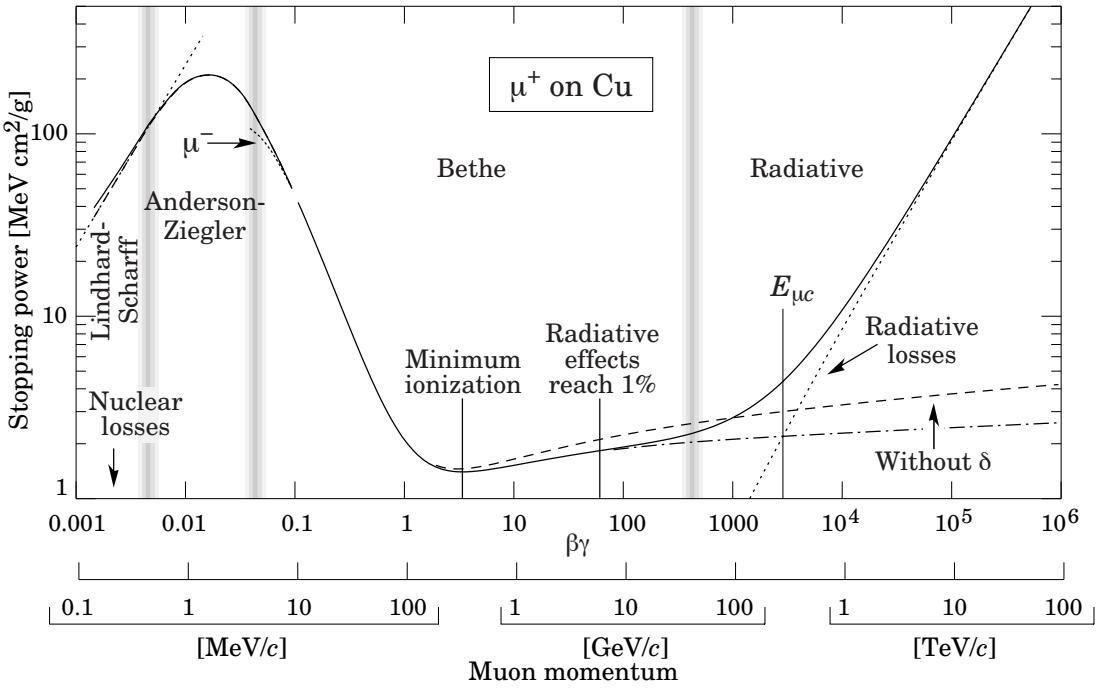

FIGURE 4.7: The stopping power dE/dx of copper for muons [2].

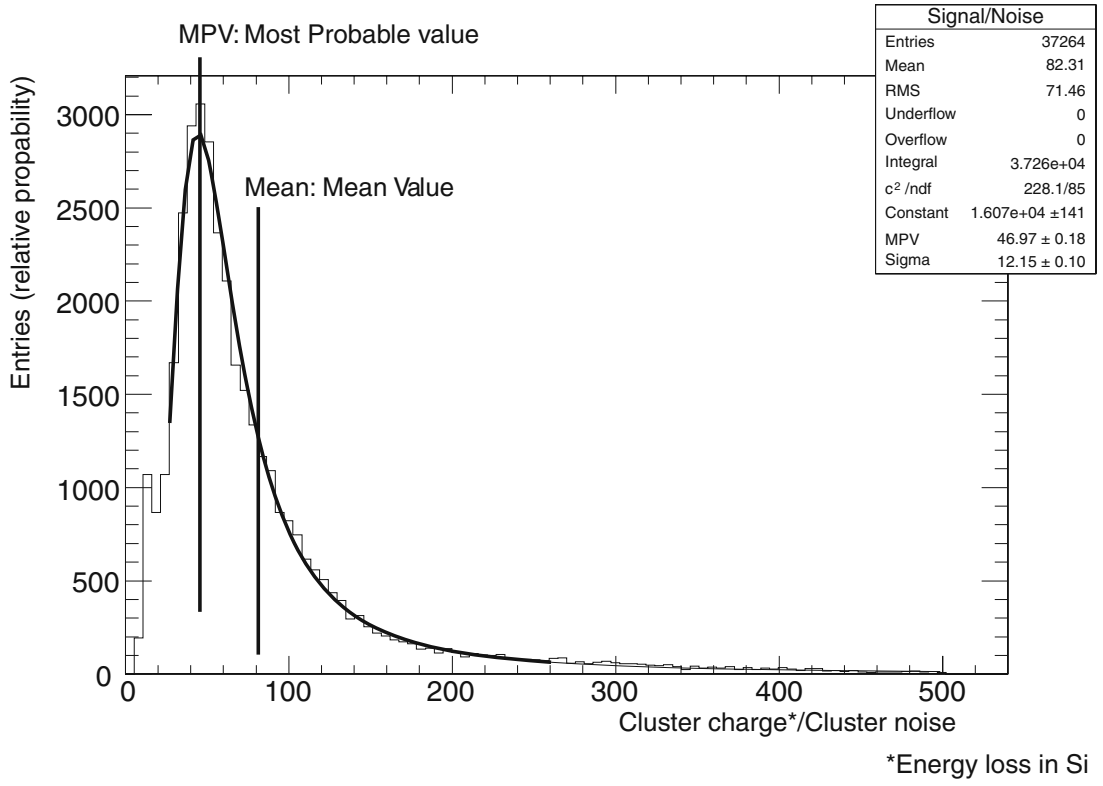

FIGURE 4.8: Landau distribution showing the differences in the Most Probable Value (MPV) and the mean energy loss in silicon [52].

4.2.3 Leakage current

The leakage current is one of the main consideration in the design of and proper functionality of silicon detectors. It represents a source of noise in the final signal, and must be kept as low as possible. It consists of a bulk current, generated within the device and determined to first order by equation (4.20), and surface current, stemming from imperfection on the surface such as scratches, mishaps in processing, or poor oxides. The two types of current can be differentiated by their temperature dependence; bulk current has a strong temperature dependence, while surface current only weakly depends on temperature.

An additional effect, referred to as *thermal runaway*, arises from self heating of the device. High current leads to a higher internal temperature, which in turn to a higher current. This is an uncontrolled positive feedback effect, and is most pronounced in irradiated devices. This requires sensors to not only be operated at cold temperatures, but also for the temperature to be held constant by a sufficient heat sink.

4.2.4 Detector capacitance

The total capacitance of a device comes from several sources. Depending on the source, it can be either beneficial or detrimental to the proper operation of a detector.

The coupling capacitance is defined between the strip implants and the aluminum readout strips. A large coupling capacitance leads to better coupling of the signal to the readout electronics. It can be increased by thinning the layer of SiO_2 between the implants and Al layer. This can be difficult to achieve, as thin oxides can lead to shorts between the implants and readout.

The interstrip capacitance is measured between strips. It contributes to the capacitive load into the readout electronics, and typically represents a significant source of noise. It should also be kept low to reduce charge sharing between strips. Increasing the distance between strips can lead to a lower interstrip capacitance, but this also leads to a lower spatial resolution of the device.

The bulk capacitance is defined between the strip implants and the backplane. It is also a contributor to the noise of a device, but is typically less than the contribution from other source, such as the interstrip capacitance, parasitic capacitance, and the internal capacitance of the readout electronics. For a 1D simple diode, the bulk capacitance is related to the width of the depletion region W by the expression for the capacitance of a parallel plate capacitor

$$C = \epsilon A/W \tag{4.26}$$

where ϵ is the dielectric constant and A the area of the device. For a complicated strip geometry, the bulk capacitance can be approximated by that of the 1D case only when the width of the depletion region becomes larger than the pitch, where bending of the electric field lines toward the strip edges becomes "washed out" [53]. The bulk capacitance is also used as the main measurement of the depletion voltage, the voltage in which the depletion region width becomes equal to the total

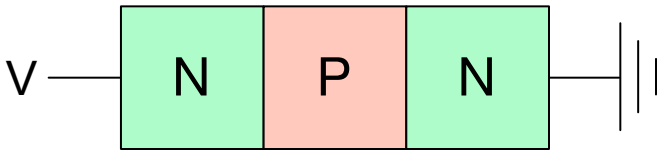

FIGURE 4.9: An n-p-n sandwich structure. Applying a voltage leads to one junction being forward biased, while the other becomes reverse biased.

thickness of the device. Combining equations (4.24) and (4.26) leads to

$$\frac{1}{C^2} = 2\frac{V_{bias}}{q\epsilon A N_{eff}} \tag{4.27}$$

so that N_{eff} can be determined from the slope if the reciprocal squared of the capacitance as a function the bias voltage. Even more information can be extracted by examining the capacitance as a function of the frequency of the applied AC signal used to measure the capacitance[6] [51, 54, 55]. Defect states with different emission rates will contribute to the total capacitance at different frequencies; if the frequency is sufficiently small a defect state will have time to contribute to the capacitance through a change in charge state, while if the frequency is too large then the defect states will not have time to change charge states and thus not contribute to the total capacitance. Furthermore, measurements at different temperatures will lead to a shift of the capacitance vs. frequency curves, allowing one to determine the energy of the various defect states. Indeed, capacitance measurements are able to reveal more information about the internal details of silicon detectors than any other type of measurement.

4.2.5 The punch-through effect

The punch-through, or reach-through, effect can cause significant current flow in semiconductor devices [56–58]. Consider a n-p-n (or p-n-p) sandwich structure, as seen in figure 4.9. When an external voltage is applied to such a structure, one of the junctions will become forward biased, while the other will become reverse biased. As the voltage is increased, the reverse biased junction will grow, until eventually the the two junctions come into contact. The voltage when the two junctions touch is known as the *punch-through* voltage. Past this voltage, the current will grow exponentially across the device, as the forward region is able to inject charge carriers into the reverse region. Full depletion occurs at the so called *flatband voltage*[7], called so because at this point $dV/dx = 0$ at one end of the device. Eventually the density of free carriers becomes comparable to the space charge density, causing free carriers to modify the electric field so as to limit any additional charges being injected into the device, and this is know as *space charge limited*.

[6] The capacitance is typically measured by applying a small alternating voltage on top of the DC bias voltage, and measuring the complex impedance or admittance. Separating the real and imaginary components lets one determine resistive and capacitive components of the device.

[7] Not to be confused with the flatband voltage when referring to MOS capacitors.

The punch-through effect is often useful in detector operation [59]. The region between the strip implants and the bias ring represents such a npn sandwich structure, where the bulk wafer acts as the intermediate material creating the double sided junction. The short created after reaching the punch-through voltage can be used to tie voltage of the bias ring to the strip implants, allowing for biasing without the need of a polysilicon biasing resistor. The effect can also be used to limit excess voltages on the strip implants, which can cause damage to the coupling capacitor if larger than the specified hold off voltage, in turn causing damage to the readout electronics. Such a scenario can occur during beam accidents, where significant charge can be deposited in a small area of a sensor, flooding the detector with charge and collapsing the electric field within and resulting in large voltages on the implants which are limited only by the total bias voltage [60–62].

4.2.6 Impact ionization and charge multiplication

At large electric fields, charge carriers can be multiplied through *impact ionization* [43, 63, 64]. Such multiplication can be beneficial in silicon detectors, compensating for signal loss due to radiation induced trapping. Furthermore, they can be used in fast timing detectors to significantly increase the signal, where the small thickness of such devices leads to a very low signal-to-noise ratio (SNR). This increase, or multiplication, of the original signal is colloquially known as *charge multiplication* (CM).

Large electric fields can accelerate charge carriers to sufficient energies that collisions within the lattice lead to the creation of additional electron hole pairs. These additional charges will in turn have sufficient energy to create additional electron-hole pairs. The number of electron-hole pairs created is expressed as an ionization rate α. Since the electric field is dependent on position, so is α, which can be parameterized by

$$\alpha = Ae^{-(B+TC)/E} \tag{4.28}$$

where A, B and C are parameters to be fitted for, T is the temperature, and E is the strength of the electric field. The α for electrons in silicon reads [63]

$$\alpha_n = 6.2 \times 10^5 exp\left(-\frac{1.40 \times 10^6 + 1.3 \times 10^3 T}{E}\right) \qquad (E < 24V/\mu m) \tag{4.29}$$

$$\alpha_n = 6.2 \times 10^5 exp\left(-\frac{1.05 \times 10^6 + 1.3 \times 10^3 T}{E}\right) \qquad (E > 24V/\mu m) \tag{4.30}$$

and for holes

$$\alpha_p = 2.0 \times 10^6 exp\left(-\frac{1.95 \times 10^6 + 1.1 \times 10^3 T}{E}\right) \qquad (E > 24V/\mu m). \tag{4.31}$$

The values of α_n and α_p as a function of the electric field are shown in figure 4.10. CM typically begins around 10-15 V/μm. The *multiplication factor* defines the strength of multiplication, and for electrons is given by [43]

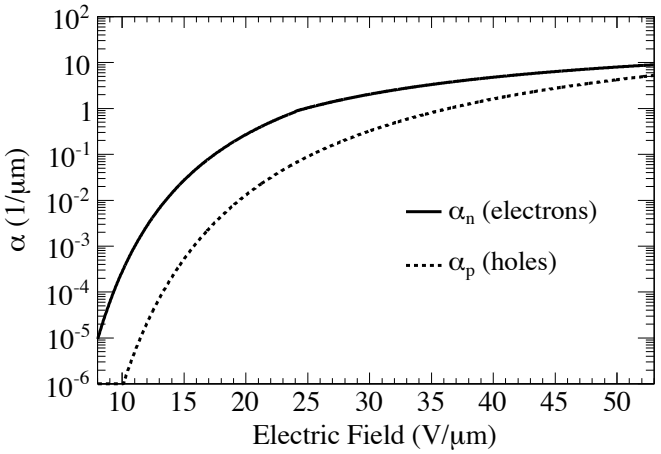

FIGURE 4.10: The ionization rates for electron and holes in silicon as a function of the electric field [65].

$$M = \left(1 - \int_0^W dx\, e^{-\int_0^x dx'(\alpha_n - \alpha_p)}\right)^{-1} \tag{4.32}$$

where W is the size of the multiplication region. Breakdown of the device can occur if $M \to \infty$. Not only is the signal multiplied by CM, but the noise will also tend to become larger through the same process. Hence, while CM can be beneficial in certain cases, care must be taken to ensure that the noise remains low and breakdown voltage remains high.

4.3 Radiation damage

Detectors in the inner layers of experiments such as ATLAS and CMS are exposed to very large particle fluxes. This leads to those sensors being exposed to large amounts of radiation, which will tend to degrade detector performance over time. The damage due to radiation in such devices can be separated into two types; bulk damage and surface damage, with the former representing the main limiting effect in irradiated detectors. Radiation damage in semiconductor detectors has been intensely studied by the CERN RD50 collaboration [66].

4.3.1 Bulk damage

Bulk damage result from the displacement of atoms from lattice sites through *non-ionizing energy loss* (NIEL). The displaced atoms leave behind energy states which are categorized as *interstitials* (I), or *vacancies* (V), which is illustrated in figure 4.11. Interstitials are the displaced atoms themselves, which move throughout the crystal and can interact with other impurities or defects while vacancies are the empty lattice sites where the displaced atoms use to reside, and can be migrate and interact with the rest of the crystal. Higher energy collisions between the lattice and incoming radiation can cause a recoil at the lattice sites, which can cause further displacements. These recoils lead to a decrease in the incident particle energy, and at the end of the path large number of defects are present.

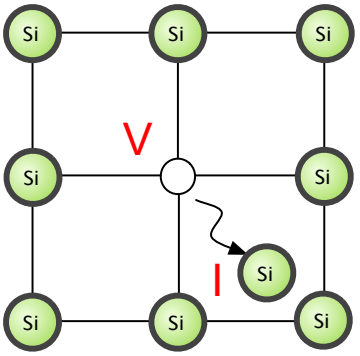

FIGURE 4.11: Illustration of a vacancy and interstitial within a silicon lattice.

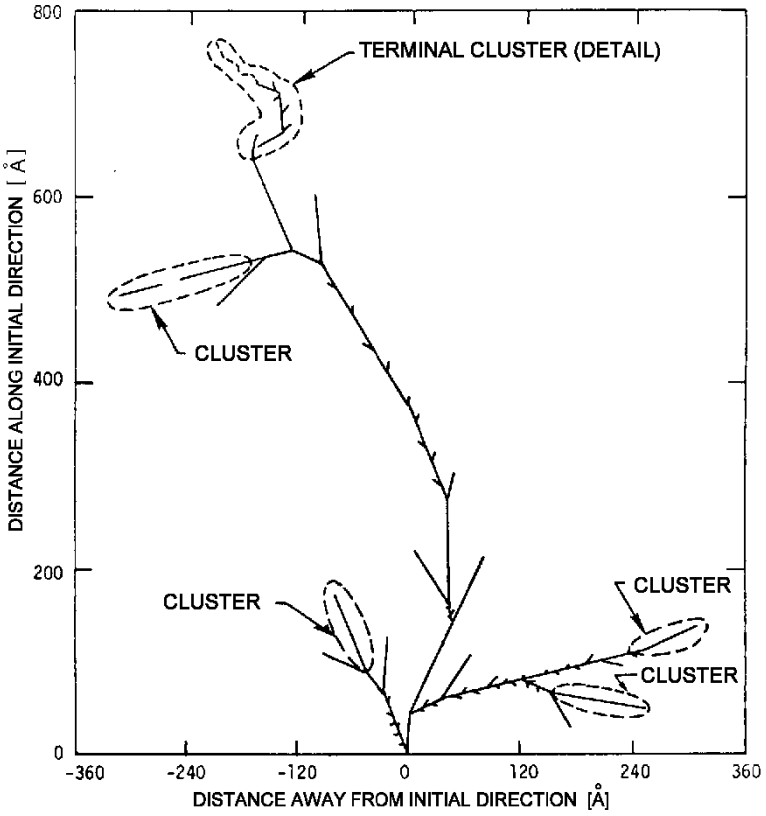

FIGURE 4.12: A monte Carlo simulation showing the creation of clusters by recoil atoms [67].

Areas where there are large numbers of defects states created through such damage are called *clusters*, whereas individual displacements are called *point defects*. A Monte Carlo simulation of such a recoil-atom track is shown in figure 4.12

The energy states created from radiation induced defects significantly alter the electrical properties and operation of silicon detectors. On a macroscopic level these manifest themselves in

- Increase of the leakage current through additional generation from defect states near the midgap.

- Change in the depletion or operating voltage of the device through changes occurring in the effective doping concentration or space charge.
- Loss of signal and detector efficiency due to trapping by defect states.

The NIEL hypothesis allows normalization of the displacement damage due to different radiation particle species with differing energies. The displacement damage can be calculated as

$$D(E) = \sum_i \sigma_i(E_{kin}) \int_0^{E_{R,max}} f_i(E_{kin}, E_R) P(E_R) dE_R \tag{4.33}$$

where the sum runs over all possible interactions, σ_i is the cross section for process i, $f_i(E, E_R)$ is the probability of a particle of energy E_{kin} transferring a recoil energy E_R, and $P(E_R)$ is the Lindhard partition function [68] describing the fraction of energy displacing a silicon atom. The function is plotted in figure 4.13. A standard 1 MeV *neutron equivalent fluence*, or n_{eq}/cm^2 (or simply just n_{eq}) is used which corresponds to $D_{neutron}(1\text{MeV})/\text{cm}^2 = 95$ MeV mb/cm^2. The damage can then be scaled by a multiplicative factor κ so as to make comparison from different radiation species and normalize to 1 MeV n_{eq} by

$$\kappa = \frac{\int D(E)\phi(E)dE}{95 MeV mb \cdot \Phi} = \frac{\Phi_{eq}}{\Phi} \tag{4.34}$$

where $\Phi = \int \phi(E)dE$ is the radiation fluence and Φ_{eq} is the corresponding 1 MeV neutron equivalent fluence, which is easily determined from the above expression

$$\Phi_{eq} = \kappa\Phi. \tag{4.35}$$

Radiation induced defects near the midgap will be produced at a constant rate with the radiation fluence. The midgap states will readily generate electron-hole pairs, leading to an increase in the observed leakage current of the device. This scales linearly with fluence so the change in leakage current ΔI can be expressed as

$$\Delta I = \alpha \Phi_{eq} V \tag{4.36}$$

where V represents the total volume of the device and α is a current related damage constant. The linear behavior of the leakage current with fluence can be seen in figure 4.14.

The introduction of donor and acceptor type defects from irradiation will lead to changes in N_{eff}. This inevitably leads to a change in the depletion voltage of the device[8]. In general, more acceptor like states are introduced than donor like states, so that the overall material becomes more p-type with increasing fluence,

[8]The term "depletion" is actually a misnomer when discussing irradiated detectors. While for unirradiated devices, there is a clear region with an active electric field and the term is appropriate, irradiated detectors exhibit a space charge that extends across the entire device. This space charge also changes its spatial distribution in response to an applied voltage, and trapping of the leakage current and phenomena such as formation double junctions further complicate the picture. Nevertheless, the concept is still used as a useful picture in the practical characterization of devices after irradiation.

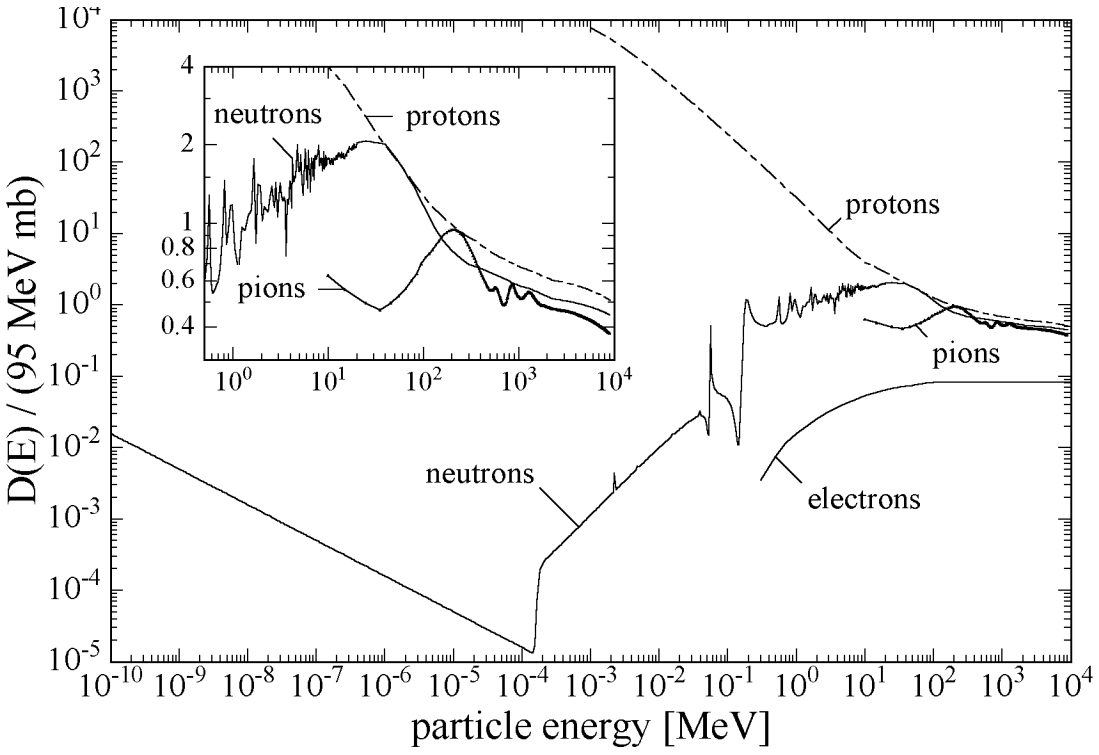

FIGURE 4.13: The displacement damage function $D(E)$ as a function of the particle energy, normalized to 95 MeVmb for neutrons, protons, pions and electrons. The inserted graph shows a zoom-in of the figure [67].

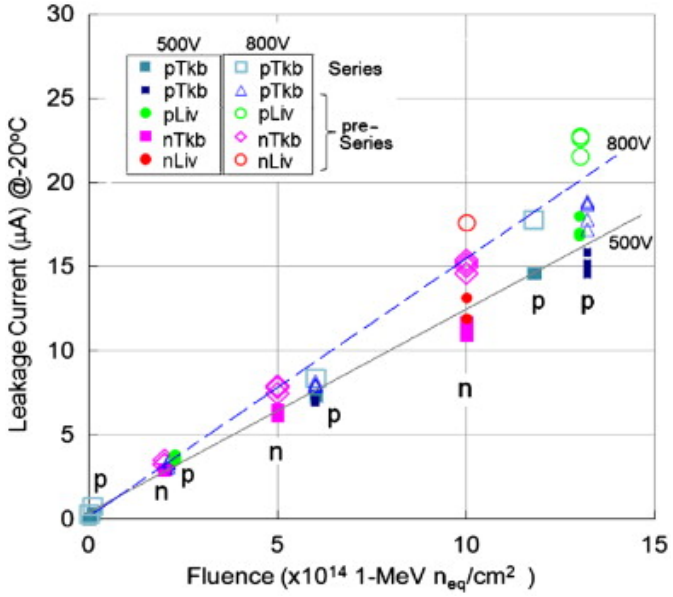

FIGURE 4.14: The observed leakage current as a function of the radiation fluence for several irradiated sensors. The labels n and p stand for irradiation with neutrons and protons, respectively. Lines are drawn to guide the eye [69].

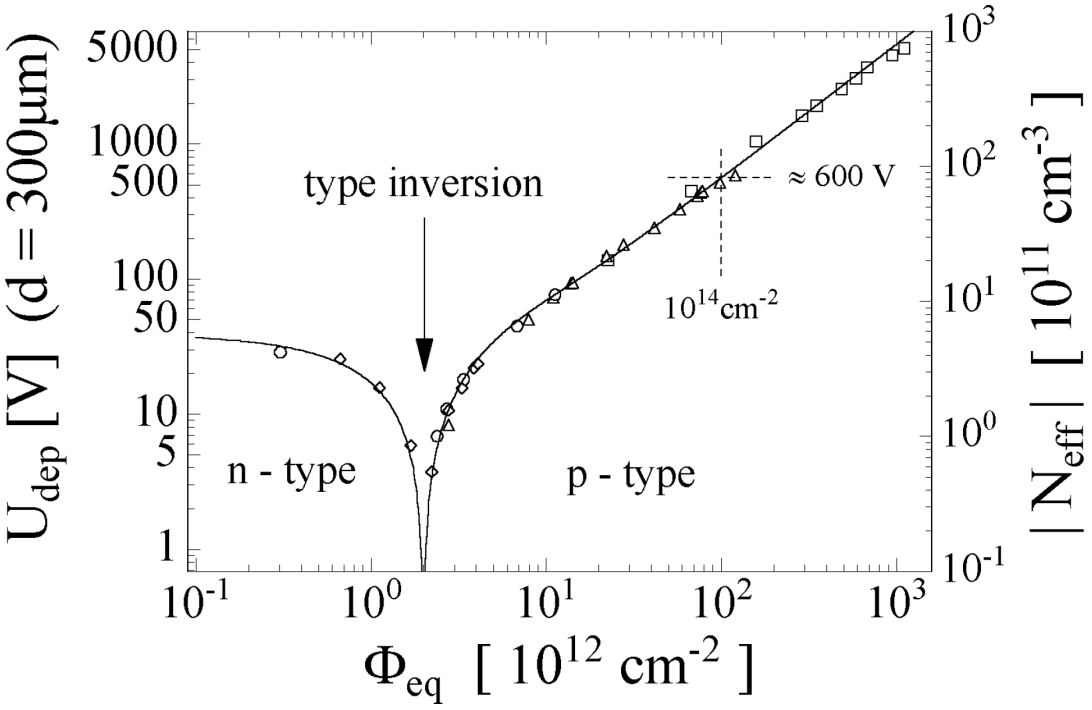

FIGURE 4.15: The depletion voltage and overall effective doping concentration as a function of fluence for an n-type bulk detector with a thickness of 300 μm [67].

leading to type inversion in the case of n-type bulk devices. The evolution of the depletion voltage and effective doping concentration with fluence, showing the point of type inversion, can be seen figure 4.15.

Irradiated devices undergo an irreversible termed *annealing*. At sufficient temperatures, defect states become mobile, migrating through the crystal until combine with other defects or surface charges, often creating new states in the process. This leads to changes in the macroscopic properties of the sensors over time, such as the full depletion voltage, seen in figure 4.16, and leakage current, through the damage constant α in equation (4.36) a seen in figure 4.17. Annealing is exponentially dependent on temperature, so that sensors must be stored cold in order to prevent any changes to detector properties over time.

Perhaps the most detrimental effect of radiation damage comes from signal loss. This loss arises from two sources

- Increase in the full depletion voltage at large fluences. This leads to a smaller depleted width for a given bias voltage, and thus less signal being generated over the active region of the device.
- Trapping of the signal by defect states with large capture cross sections and small trapping times.

Trapping becomes significant when trapping times become comparable to the collection time of the signal, typically around 10 ns. The number of generated charge

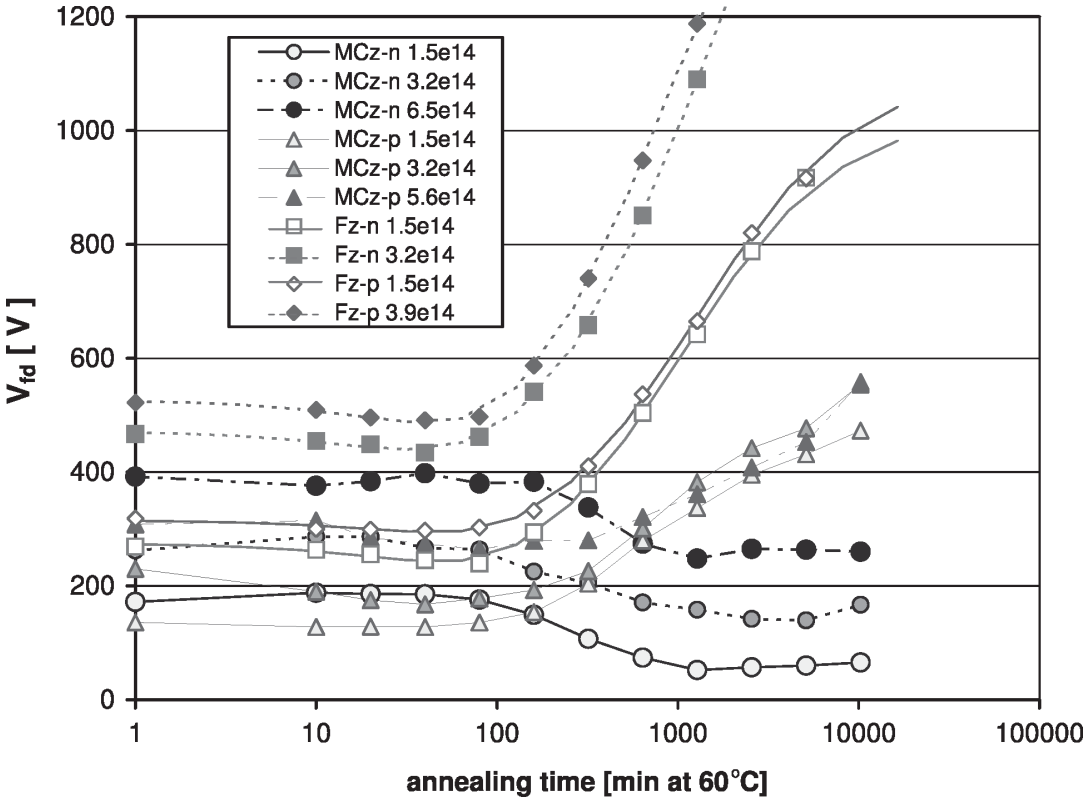

FIGURE 4.16: The annealing behavior of the full depletion voltage for a 300 μm thick pion irradiated sensor as a function of time. The annealing temperature was taken at 60° C [70].

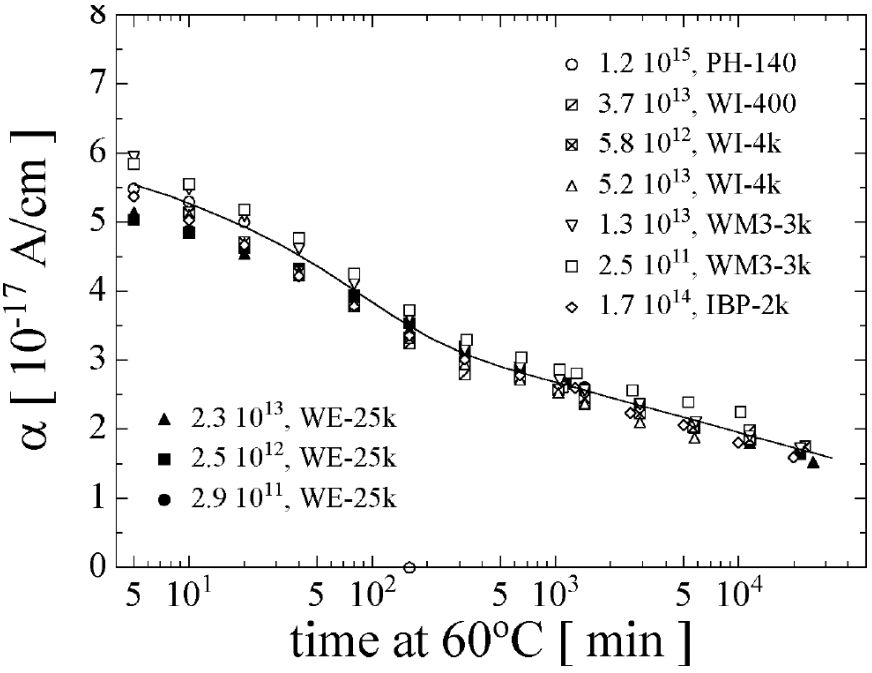

FIGURE 4.17: The damage constant α as a function of time taken at 60° C. Different data points are measurements on different sensors, showing a universal dependence on annealing [67].

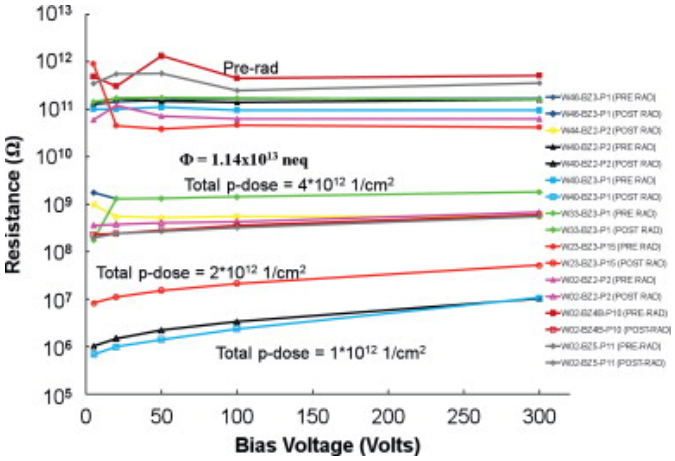

FIGURE 4.18: The interstrip resistance for proton irradiated silicon detectors showing the effect of higher p-dose on the strip isolation [71]

carriers will decrease over time according to

$$N(t) = N_0 e^{-\frac{t}{\tau_{n,p}}} \tag{4.37}$$

where N_0 is the initial number of created charge carriers, t the time. Switching from p-on-n to n-on-p sensors leads to a significant reduction in signal loss due to trapping, since n-on-p sensors collect electrons whereas p-on-n sensors collect holes. Electrons have a much larger mobility than holes, so traverse the detector in a smaller time than holes, and are thus less susceptible to trapping.

4.3.2 Surface damage

Ionizing radiation leads to surface damage via the creation of interface states in the Si-SiO_2 interface. This leads to a conductive layer at the surface that can short strips together, which leads to a loss in resolution of the device. Detectors comprised of a p-type substrate are particularly susceptible to degradation in position resolution caused by damage at the surface, due mainly from the mobile layer of inverted electrons at the Si-SiO_2 interface. To prevent such degradation, sensors are typically treated with positively doped ions at the surface, either in the form of a ionization spray known as *p-spray*, or through additional implants between readout strips known as *p-stops*. The idea is that the additional p-type states are able to combine with the electron layer to neutralize it. Larger concentration of the p-spray or p-stops leads to better isolation, especially after charged particle irradiation [71], as seen when looking at the *interstrip resistance* on proton irradiated silicon sensors in figure 4.18.

4.4 Various detector designs

Several different detector designs are available, each tailored to meet specific needs. We outline some of the most relevant types here, although this does not constitute an extensive or complete list of the different varieties.

4.4.1 Pad detectors

Silicon pad detectors are one of the simplest designs available. They have a very simple geometry, and are well approximated by 1D diode structures. This makes them of particular use as particle detectors where high granularity is not of great importance. Due to their simple geometry, they are also used in R&D applications, especially in the study of bulk characteristics of silicon detectors, where complications from surface geometry are minimal.

4.4.2 Strip detectors

Silicon strip detectors are by far the most common type of silicon detector used as tracking sensors. They are segmented at the surface into highly doped strip implants sitting on a bulk substrate, providing spatial information of traversing particles. The strip pitch can be very small, on the micron level, which gives them excellent spatial resolution. This makes them ideal for tracking purposes in high energy physics experiments such as ATLAS and CMS, where they extensively used in the inner regions.

4.4.3 Pixel detectors

Silicon pixel detectors are highly granulated detectors. Instead of being arranges in strips, the implants are arranged in small rectangles known as pixels. This provides much higher spatial resolution than strip detectors, which makes them ideal for the inner most layers of ATLAS and CMS, where the large particle fluxes require differentiation between primary and secondary vertices with high precision. They are more difficult to fabricate than standard strip devices, and the larger number of channels for a given area complicates readout. In high energy physics experiments, there is a need to keep the amount of material low to prevent secondary scattering, so readout becomes more of a challenge.

4.4.4 3D detectors

3D detectors represent one of the most promising candidates for radiation-hard detectors [73]. Unlike planar devices, such as pad, strip and pixel detectors, 3D detectors consist of alternating n and p type electrode columns etched into a bulk substrate. The columns are differentiated into junction and ohmic columns, with readout happening at the junction columns. All columns of opposite type from the junction columns are connected together to form an ohmic contact. Readout can be arranged in both pixel and strip formats. The basic design is shown in figure 4.19.

The advantage of 3D detectors comes from decoupling the charge collection length from the thickness. The length a signal must traverse becomes equal to the inter-column spacing instead of the full detector thickness. This makes them less prone to trapping effects. Since the distance between columns is typically much shorter than the device thickness, full depletion of the sensor happens at much lower voltages compared to planar devices. Furthermore, high electric fields around the junction columns leads to a strong multiplication effect [65]. This

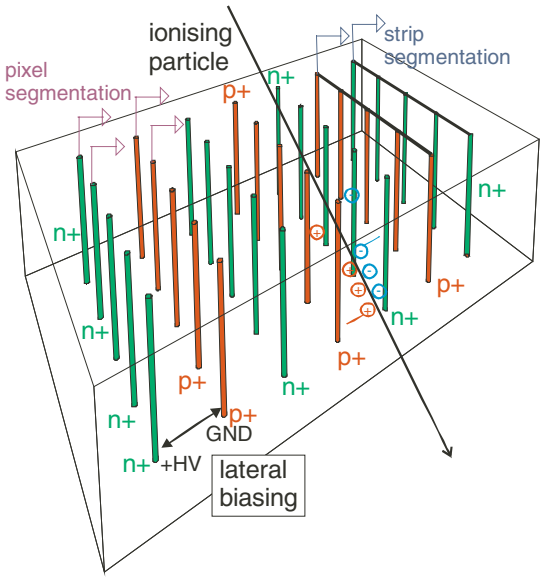

FIGURE 4.19: The basic layout of a 3D detector. Highly doped electrode columns are etched into a wafer substrate [72].

makes them particularly adept for high radiation environments and as radiation-hard detectors.

These detectors are not without their drawbacks. The processing and fabrication of 3D sensors is more complicated than planar devices, driving up production costs. Additionally, good spatial alignment of the electrode columns is difficult to achieve. The electrodes themselves constitute a dead area where very little charge can be collected and read out, reducing the efficiency in certain areas of the device. The reduced distance between the ohmic and junction contacts leads to a larger bulk capacitance, increasing the noise in such devices. Finally large electric fields, which can be beneficial in terms of increased signal, also lead to a larger instability during operation in the form of breakdown. Several of these concerns have been investigated and addressed, and 3D detectors still present themselves as viable candidates for high radiation environments, such as in the ATLAS insertable B-Layer (IBL) [74].

4.4.5 Charge multiplication detectors

In recent years there has been a keen interest in so called charge multiplication (CM) detectors [75–77]. These detectors come in various designs, from simple pad sensors and segmented strip detectors to 3D detectors. They rely on impact ionization to produce charge multiplication in the device. This is achieved by increasing the electric field in regions of the sensor, typically near the readout, through modifications in geometrical design or processing. There is also a radiation induced component of CM, as defect states also alter the electric field, and at high fluences and voltages, almost all sensors exhibit some sort of multiplication, regardless of design.

These sensors have the potential as viable candidates for high radiation environments, although many open questions remain. The exact source of the multiplication, more specifically the high fields, is still not fully understood. While there is a clear geometrical component and a radiation induced component to multiplication, differentiating which is the driving force for a particular application is not straightforward. The stability of such devices over large time periods and at high bias voltages, as would be relevant in actual operational conditions at the LHC, has only recently been investigated with worrisome results [78, 79]. The stability of such sensors, and their applicability as radiation hard sensors is discussed in more detail in chapter 9.

Chapter 5

The Large Hadron Collider and the ATLAS detector

ATLAS, one of four main experiments at the Large Hadron Collider (LHC) and shown in figure 5.1, is a general purpose detector located at the European Organization for Nuclear Research (CERN) in Geneva, Switzerland. The LHC and ATLAS will be described in what follows.

5.1 The Large Hadron Collider

The Large Hadron Collider is the world's largest particle accelerator. It designed to operate at a center-of-mass energy of up to $\sqrt{s} = 14$ TeV [81] with an instantaneous luminosity of $L = 10^{34}$ cm^{-2} s^{-1}. It is a proton-proton (pp) and heavy-ion collider built in the 26.7 km circumference tunnel which formerly housed the LEP machine. Collisions happen at four interaction points, which house four experiments: ATLAS, CMS, ALICE, and LHCb.

Both ATLAS (**A** **T**orodial **L**HC **A**pparatu**S**) [82] and CMS (**C**ompact **M**uon **S**olenoid) [83] are general purpose detectors optimized for new physics studies. These include the search for the Higgs boson as well searches for supersymmetry (SUSY). LHCb (**L**arge **H**adron **C**ollider **b**eauty) [84] focuses on the study of heavy flavor physics while ALICE (**A** **L**arge **I**on **C**ollider **E**xperiment) [85] focuses on quark-gluon plasma physics generated from heavy-ion collision. The entire CERN accelerator complex, including the LHC and its injector accelerators, is illustrated in figure 5.1.

Proton beams are accelerated in opposite directions along two evacuated beam pipes. Each beam consist of 2808 proton bunches, spaced 25 - 50 ns apart. Each bunch contains 10^{11} protons. While the LHC is designed to nominally run at 25 ns bunch spacing, the $\sqrt{s} = 7$ TeV and $\sqrt{s} = 8$ TeV runs both had a bunch spacing of 50 ns. Each bunch has a length of several cm within the beampipe.

Protons pass through several accelerator steps before being injected into the main ring. First protons are accelerated to 50 MeV by a linear accelerator (LINAC 2) and then passed to the Proton Synchrotron Booster (PSB) which further increases their energy to 1.5 GeV. The Proton Synchrotron (PS) takes the energy up further to 25 GeV. They are finally passed to the Super Proton Synchrotron (SPS) which injects the protons into the LHC ring with an energy of 450 GeV.

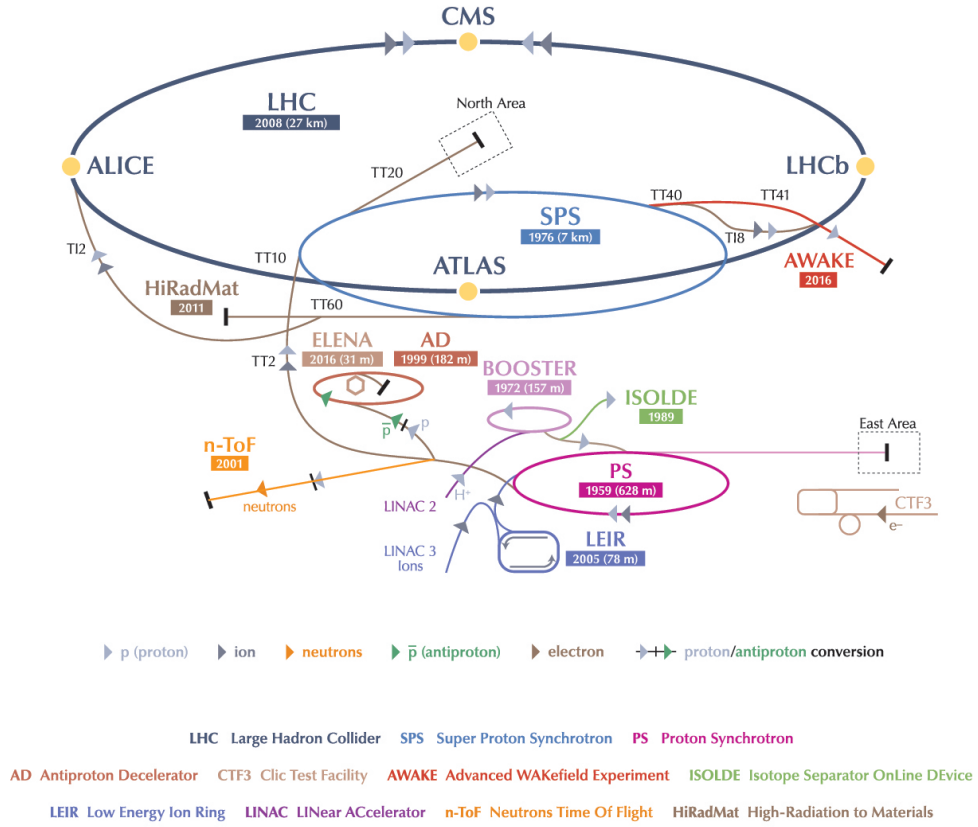

FIGURE 5.1: Illustration of CERN accelerator complex, with the LHC in blue [80]

Once protons are injected into the main ring of the LHC, it takes protons roughly 20 minutes to reach their nominal energy. Acceleration is performed by eight superconducting cavities which produce a high-frequency alternating electric field with a field gradient of 5 MV/m. The circular path of the beams is achieved by 1232 superconducting dipole magnets each capable of generating fields of 8.33 Tesla. They are cooled to 1.9 K by a superfluid helium. The beams do not have a constant size, but are constantly being re-focused by quadrupole magnets, and the final diameter at the interaction points is about 30 μm.

The instantaneous luminosity at the LHC is dependent soley on beam parameters and can be determined by

$$\mathcal{L} = \frac{N_b^2 n_b f_{rev} \gamma_r}{4\pi \epsilon_n \beta^*} F \tag{5.1}$$

where N_b corresponds to the number of particles per bunch, n_b is the number of bunches per beam, f_{rev} is the frequency for a complete revolution around the LHC, γ_r is the relativistic factor for the protons in the beam, ϵ_n is the emittance of the

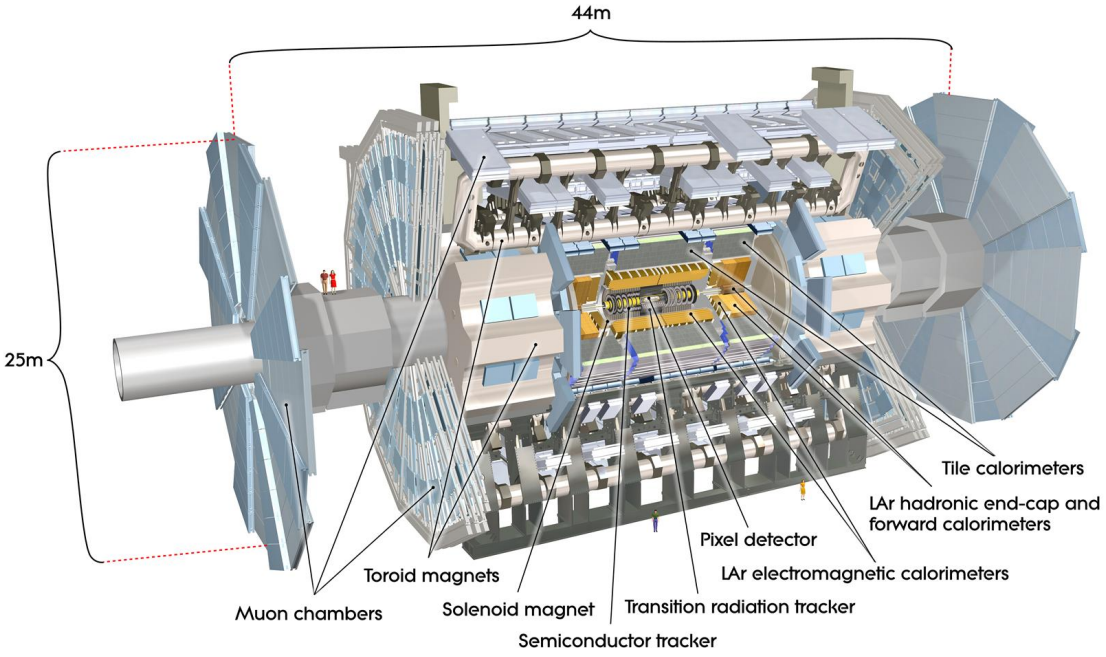

FIGURE 5.2: The ATLAS detector and its many subsystems. It is 25 m wide and 44 m in length with a weight of about 7000 tons [82].

beams which measures the departure of the protons from the nominal trajectory, β^* is the beta function at the interaction point and F is a factor measuring the reduction of luminosity due to the crossing angle at the interaction point. The large instantaneous luminosity leads to an average number of $\mu = 25$ interaction per bunch-crossing when running at a nominal energy of $\sqrt{s} = 14$ TeV.

The first collisions at the LHC took place in November of 2009 at a center-of-mass energy of $\sqrt{s} = 900$ GeV. After a shutdown in the winter, this was followed by collisions at $\sqrt{s} = 7$ TeV in March 2010 which lasted through 2011. In 2012 the center-of-mass energy was increased to $\sqrt{s} = 8$ TeV. The combined data taking period through 2012 is known as Run-1.

5.2 The ATLAS detector

The ATLAS detector, the largest detector at the LHC, covers nearly the entire solid angle around the collision point. It is one of two general detectors at the LHC, the other being the slightly smaller CMS detector. The primary goal of both experiments has been the discovery of the Higgs Boson, which has been used as a benchmark to investigate the performance of different sub-systems of ATLAS. The detector itself consists of many subsystems: The inner detector, the electromagnetic and hadronic calorimeters and the muon spectrometer. Each subsystem will be described in what follows. The entire ATLAS detector is shown in figure 5.2.

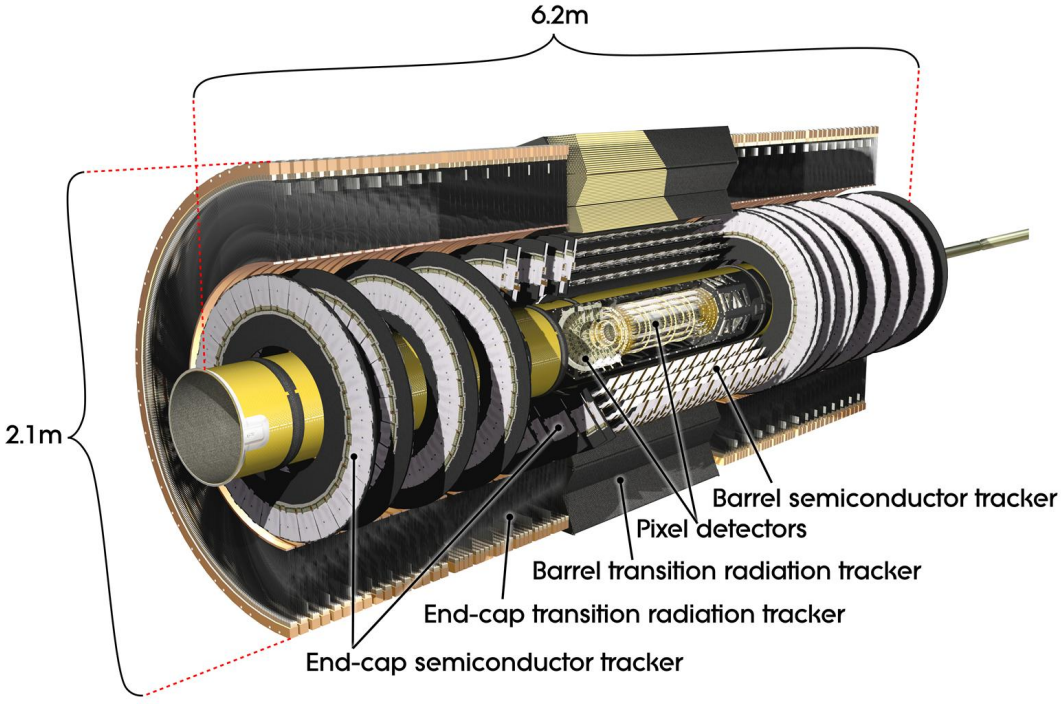

FIGURE 5.3: A cut-away view of the inner detector in ATLAS [82].

5.2.1 Coordinate system of ATLAS

The right-handed coordinate system is used in ATLAS. The origin is taken as the nominal interaction point and the z-axis is taken to be along the beam. The transverse x-y plane is defined so that positive x points toward the center of the LHC ring while positive y points upwards. More commonly the azimuthal angle ϕ is used. The polar angle θ between the z-axis and the x-y plane is used to define the pseudorapidity

$$\eta = -ln\left(\tan\left(\theta/2\right)\right). \tag{5.2}$$

Quantities such as the transverse energy E_T and transverse momentum p_T are defined as being in the transverse plane. Finally, the distance between two objects in η-ϕ space is defined as

$$\Delta R = \sqrt{\Delta\eta^2 + \Delta\phi^2} \tag{5.3}$$

where $\Delta\eta$ is the distance between the objects in η and $\Delta\phi$ the distance between the objects in ϕ.

5.2.2 The inner detector

The inner detector (ID) performs reconstruction of charged particle tracks, momentum and vertex measurements, and electron identification. It consists of a combination of silicon pixel (pixel) and strips detectors (SCT), which cover the inner most tracking volume up to $|\eta| < 2.5$, surrounded by straw-tube tracking detectors (TRT) which can generate and detect transition radiation. The entire

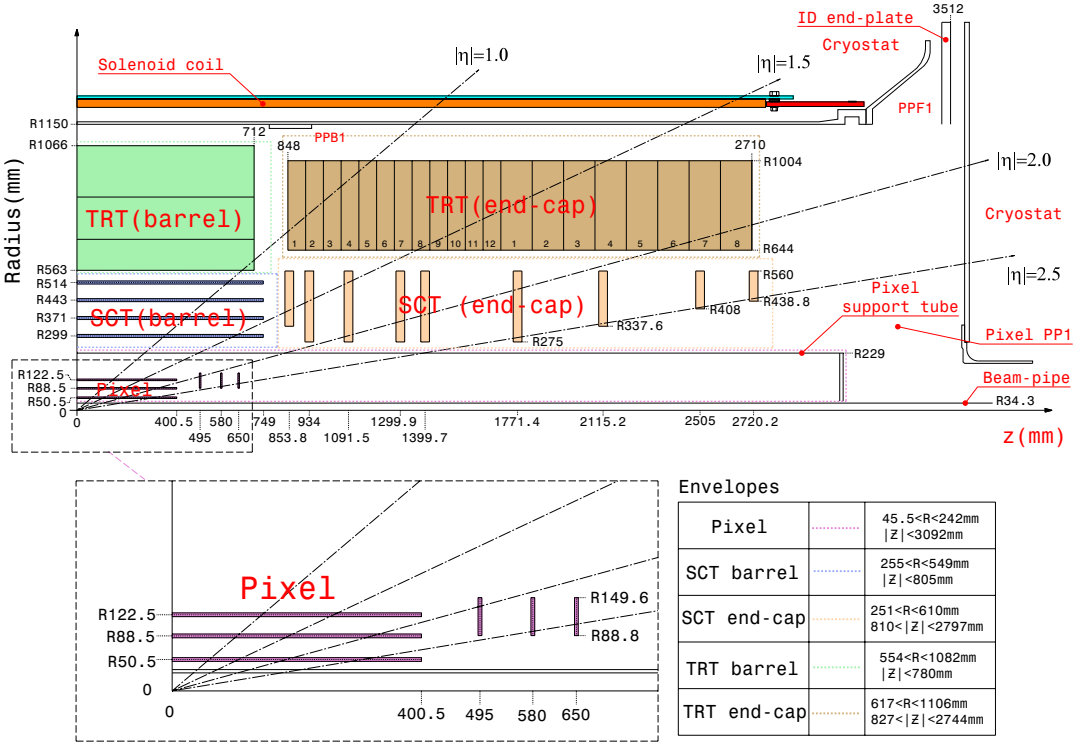

FIGURE 5.4: A schematic of a quarter-section of the ATLAS inner detector showing the arrangement of pixel layers [82].

inner detector is immersed in a 2 T magnetic field generated by a solenoid extending over a length of 5.3 m and having a diameter of 2.5 m. The entire inner detector is shown in figure 5.3.

At the heart of ATLAS closest to the interaction point one finds the silicon pixel detectors. Each pixel sensor consists of a n+ implants (AC coupled to the readout electronics) on an oxygenated n-type wafer, with a total thickness of 250 μm. The driving forces in the design of these sensors are stringent requirements on radiation hardness, resolution and occupancy. For this reason, such sensors require the latest and most cutting edge detector technology.

They are arranged so that each charged particle originating from the interaction point crosses at least three pixel layers. A total number 1744 pixel modules, each containing 47232 pixels, are arranged in three barrel layers and two endcap layers, with each endcap separated into three disk layers. The arrangement of the pixel layers within the inner detector is shown in figure 5.4. In total, there are 80.4 million pixels with a nominal pixel size of 50×400 μm^2.

Each pixel module contains 16 front-end electronic chips, each having 2880 channels which are bump bonded to the pixels. The modules are mounted on staves, with each stave containing 13 modules. Sectors are the endcap equivalent to barrel staves. 48 endcap sectors comprise the endcap layers. The resolution of each module is about 12 μm at normal incidence.

The SCT surrounds the pixel layer, with 4088 modules arranged in four barrel layers and nine endcap disks. This allows for at least four spatial points per track. In the barrel layers, each module consist of of two silicon strip detectors (SSDs)

with a length of 6.4 cm and thickness of 285 μm, each having 768 active strips with each strip having a *pitch* (distance between center of adjacent strips) of 80 μm. The endcap layers consists of three different types of wedge shaped sensors, with lengths ranging from 5.4 to 6.6 cm and strip pitches ranging from 57 to 83 μm. It total, there are 6.3 million readout channels covering a surface area of 63 m^2. The resolution of the SCT layer is 17 μm in transverse direction and 580 μm in longitudinal direction.

The final component of the inner detector is the transition radiation tracker, or TRT. It provides about 36 points in R-ϕ space per track up to $|\eta| = 2.0$. The elements of the TRT are Polyamide drift (straw) tubes of 4 mm diameter, with each tube having an accuracy of 130 μm. The straws run parallel to the beam in the barrel region and have a length of 144 cm. The endcap region contains straws which are arranged radially in wheels and are 37 cm long. In total, the TRT contains about 351,000 readout channels.

5.2.3 The calorimeters

Surrounding the inner detector and the solenoid magnets are the calorimeters. These are broken up into the electromagnetic calorimeter and the hadronic calorimeter. Their main purpose is to measure the energy deposited by electrons, photons and jets. They extend to very forward regions up to $|\eta| < 4.9$. The calorimeters are required to not only provide an accurate measure of energy depositions, but must also provide accurate spatial resolution in order to accurately reconstruct photons that don't leave tracks in the inner detector as well as provide an accurate description of the missing transverse energy from weakly interacting particles. This requires fine segmentation in both azimuthal and longitudinal directions. A cut-away view of the entire calorimeter system within ATLAS is shown in figure 5.5

The electromagnetic calorimeter is a liquid argon (LAr) sampling calorimeter which is intersected by lead absorber plates. It consists of a very finely segmented central barrel layer which covers regions up to $|\eta| < 1.4$, and an endcap layer covering the forward region up to $|\eta| < 3.2$. The barrel layer covers the entire azimuthal angle and has inner and outer radii of $r = 2.8$ m and 4 m, respectively. The endcap layer meanwhile has a radius of $r = 0.33$ m to 2.1 m with respect to the beam pipe.

The central barrel layer is broken into two half-barrels centered around the z-axis. These are further broken into three layers each with a different granularity; the first layer has a granularity of $\Delta\eta \times \Delta\phi = 0.0032 \times 0.098$, the second layer a granularity of $\Delta\eta \times \Delta\phi = 0.025 \times 0.0245$, and the third layer a granularity of $\Delta\eta \times \Delta\phi = 0.05 \times 0.0245$. The entire thickness corresponds to about 22-24 radiation lengths, which provides sufficient shower containment. A sketch of a barrel module showing the three layers is shown in figure 5.6.

The endcap layer is broken into two half wheels, one on each side of the barrel. It covers the region between $1.375 < |\eta| < 3.2$. A LAr presampler is implemented in front of the endcap and covering the range of $1.5 < |\eta| < 1.8$ in order to improve energy measurements for this region.

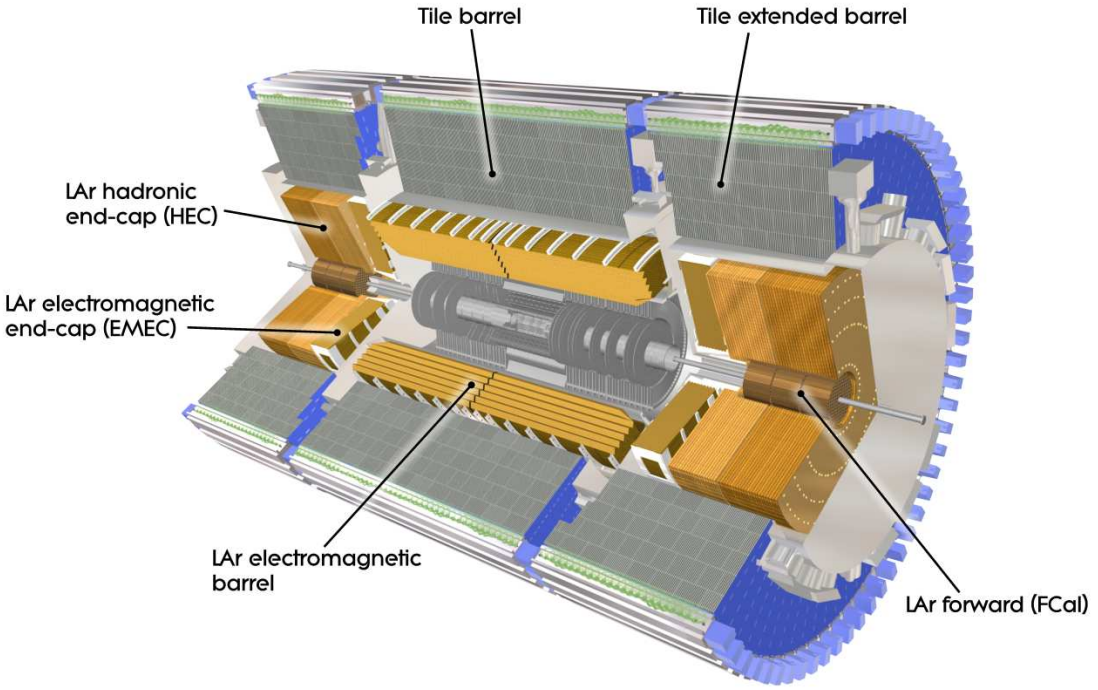

FIGURE 5.5: A cut-away of the calorimeter system within the ATLAS detector [82].

The hadronic calorimeter is able to measure the energy of charged and neutral hadrons. It is broken into three regions: a tile calorimeter, a LAr endcap hadronic calorimeter, and a LAr forward calorimeter.

The tile calorimeter [86] is a sampling calorimeter made up of steel as an absorber and scintillator as an active medium. It is located behind the LAr electromagnetic calorimeter in the region $|\eta| < 1.7$. It is further broken into a barrel which covers the region $|\eta| < 1.0$ and two extended barrels covering the range $0.8 < |\eta| < 1.7$. The barrel and extended barrels have three layers, with the first two having a granularity of $\Delta\eta \times \Delta\phi = 0.1 \times 0.1$ and the third having a granularity of $\Delta\eta \times \Delta\phi = 0.2 \times 0.1$.

The hadronic endcap calorimeter uses LAr as an active medium and copper as an absorber. It consists of two wheels in each endcap and shares the cryostat of the electromagnetic endcap calorimeter and covers the region $1.5 < |\eta| < 3.2$. It overlaps with both the tile calorimeter and forward calorimeter to ensure sufficient coverage of the transition area between different calorimeter subsystems. It has a granularity of $\Delta\eta \times \Delta\phi = 0.1 \times 0.1$. in the central region of $|\eta| < 2.5$ and a coarser granularity of $\Delta\eta \times \Delta\phi = 0.2 \times 0.2$ for larger regions of $|\eta|$.

The LAr forward calorimeter covers extreme forward regions near the beampipe between $3.1 < |\eta| < 4.9$. It is broken into three layers, the first of which uses copper as an active medium, while the other two are based on tungsten as an active medium. It has a granularity of $\Delta\eta \times \Delta\phi = 0.2 \times 0.2$.

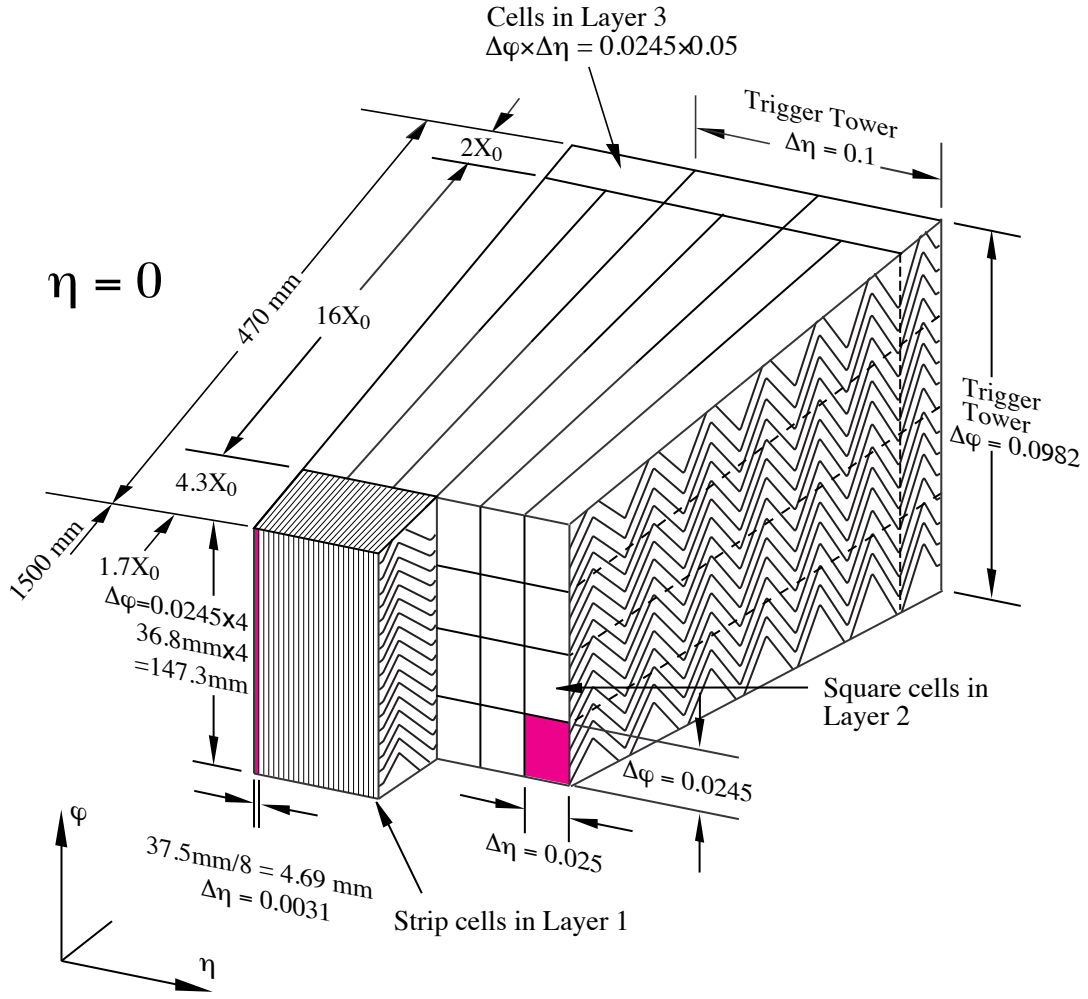

FIGURE 5.6: A sketch of a barrel module of the electromagnetic calorimeter. The segmentation and granularity of the three layers is clearly visible [82].

5.2.4 The muon spectrometer

The muon spectrometer (MS) is dedicated to measuring the momentum and charge of muons. It surrounds the calorimeter system and covers a range of $|\eta| < 2.7$. It is also able to trigger on particles in the region $|\eta| < 2.4$. It is the outmost layer of ATLAS and determines the total size of the detector. The entire system within ATLAS can be seen in figure 5.7.

Superconducting air-core toroid magnets are used for magnetic deflection of charged muons in order to accurately measure their momentum. A large barrel toroid provides the magnetic field in the range of $|\eta| < 1.4$ while two smaller endcap magnets are used for the region $1.6 < |\eta| < 2.7$. In the region $1.4 < |\eta| < 1.6$, referred to as the transition region, a combination of barrel and endcap fields provide magnetic deflection. This configuration provides fields which are mostly perpendicular to muon trajectories while minimizing loss of resolution due to multiple scattering. The barrel toroid provides bending power ranging from 1.5 to 5.5 Tm while the endcap region varies from 1 to 7.5 Tm. The bending power is reduced in the transition region.

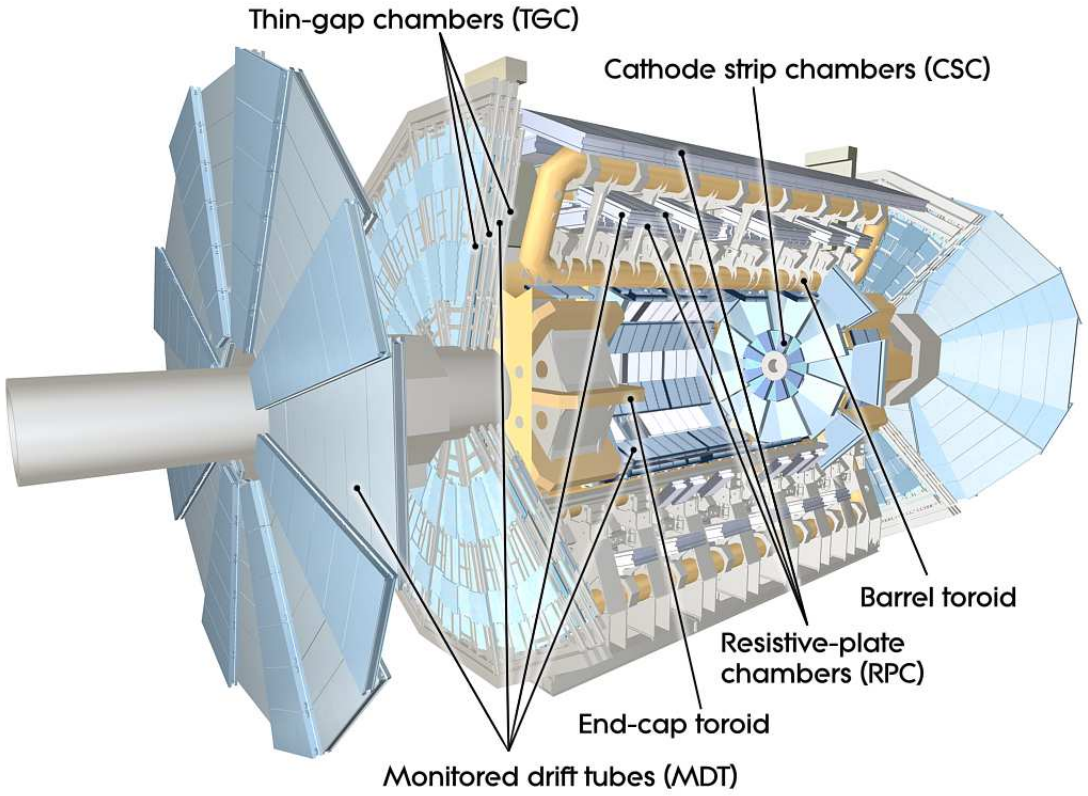

FIGURE 5.7: An illustration of the muon spectrometer as seen in ATLAS [82].

Monitored Drift Tubes (MDTs) provide precise measurement of track coordinates over most of the η range. The tubes are made up of aluminum filled with a Ar/CO_2 gas mixture at a pressure of 3 bar. Tungsten-rhenium wires, held at a voltage of 3080 V, collect electrons arising from the ionization of the gas. A total number of 1150 tubes are arranged in three cylindrical layers in the barrel region, 5 m to 10 m from the beam pipe, and in the endcap they are arranged into four wheels at $|z| = 7.4$ m. The spatial resolution of the tubes is about 80 μm.

Cathode Strip Chambers (CSCs) are used in the forward region between $2.0 < |\eta| < 2.7$. They are multi-wire proportional chambers with cathodes split into strips. There are a total 32 CSCs found in the inner most layer of the MS, where the large particle flux is greater than the limitation of the MDTs, and have a spatial resolution of about 60 μm.

Fast trigger information in the barrel is provided by Resistive Plate Chambers (RPCs), which cover the range$|\eta| < 2.4$. They consist of two parallel electrode plates spaced 2 mm apart. The gap between the plates is filled by a gas mixture, which is ionized by traversing particles. Trigger information for the endcaps is provided by Thin Gap Chambers (TGCs), which are arranged in four layers and cover the region $1.05 < |\eta| < 2.4$. They are multi-wire proportional chambers with good timing resolution suitable to high event rates. Both the RPCs and TGCs also provide complementary tracking information to the MDTs.

5.2.5 The trigger system

Due to the high collision rate of 40 MHz, continuous readout of the detector is not possible. The event rate is therefore reduced by a three tier trigger system that selects events of the most interest to physics analyses [82]. The first level (L1) is a hardware trigger that uses limited detector information to reduce the rate to 75 kHz. The second trigger (L2) is a software trigger that makes use of additional detector information to reduce the rate to 3.5 kHz. Finally the last trigger is an offline event filter (EF) that further reduces the rate to just 200 Hz, with each event being approximately 1.3 Mb in size.

The L1 trigger looks for high momentum leptons, photons, jets and missing transverse energy. Electrons, photons and jets are identified from calorimeter deposits using a reduced-granularity. Muons are identified using information from the barrel and endcaps of the muon spectrometer. The L1 trigger also identifies regions of interest (RoI) in η and ϕ to be further studied by higher level triggers. It is able to make a decision in less than 2.5 μs.

The L2 trigger is seeded by the RoI information from the L1 trigger. It makes use of the entire detector data within the RoI's, with full granularity and precision. The decision time is about 40 ms, averaged over all events. The final stage of the trigger system comes from the EF, which uses offline analysis procedures and takes about four seconds.

5.2.6 Luminosity measurements in ATLAS

For many analyses, the luminosity represents one of the largest sources of systematic uncertainty. Therefore a key component of the physics program in ATLAS is the measurement of the delivered luminosity. ATLAS measures the delivered luminosity with two detector subsystems dedicated for such measurements.

The first of these detectors, LUCID (**L**uminosity measurement **U**sing a **C**herenkov **I**ntegrating **D**etector) [87], is made up of two components located 17 m from the collision point on either side of ATLAS, as seen in figure 5.8. It measures the number of inelastic pp collisions using 20 Cherenkov tubes. It is able to measure the number of charged particles in the forward regions which is able to provide a measure of the relative luminosity as well as provide online monitoring of the instantaneous luminosity and beam conditions. The luminosity is measured using event counting and hit counting algorithms.

The second of these detectors, ALFA (**A**bsolute **L**uminosity **F**or **A**TLAS) [88] is a set of tracking detectors made up of scintillating fibers. It measures elastic scattering amplitude at very small scattering angles. They are located 240 m from the collision point in the Roman Pot of ATLAS. The Roman Pot is a vessel that allows a detector in a secondary vacuum to come near to the beam inside of the beam pipe but separated from the primary vacuum. Special runs with specific beam conditions are needed for ALFA measurements due to the very small scattering angles which are smaller than the beam divergence. An ALFA detector is shown in figure 5.9.

Measurements of the luminosity are performed in two steps. Simplified LHC runs using machine parameters are used to calibrate the absolute luminosity. These runs use *van der Meer* scans with the ALFA detectors to determine the vertical

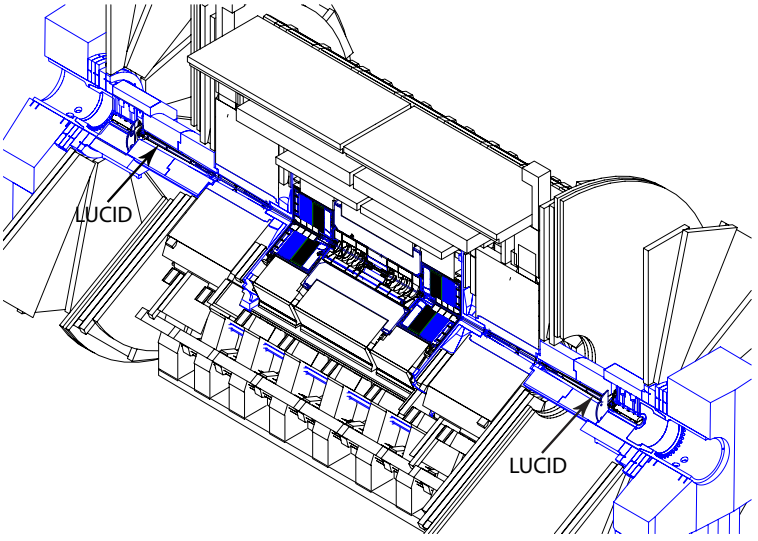

FIGURE 5.8: Position of the LUCID detector as seen in ATLAS [87].

and horizontal beam profiles. These are combined with relative luminosity measurements during nominal LHC conditions.

The total luminosity delivered by the LHC and recorded by ATLAS as a function of time and the recorded luminosity as a function of the mean number of interaction per bunch crossing between 2011 and 2012 can be seen in figure 5.10.

5.3 Object reconstruction and particle identification

The basis for all physics analyses within the ATLAS is the identification and reconstruction of physics objects originating from raw detector signals. The entire process of event reconstruction relies on a series of dedicated algorithms that reconstruct tracks from single hits in the tracking detector, or clusters of calorimeter deposits as opposed to signals from individual cells. The following describes the reconstruction of electrons, muons, jets and missing transverse momentum from tracks and calorimeter clusters.

5.3.1 Track and vertex reconstruction

In order to properly identify particles, the reconstruction of tracks and vertices stemming from primary hard interactions is required. Overlapping secondary proton-proton collisions on top of the primary interaction, known as *pileup*, makes reconstruction of the primary vertices more difficult. Events with low pileup are easy to reconstruct, and Monte Carlo simulations agree well with data [90]. When the number of interactions per bunch crossing increases, so does the number of pileup events, and a balance between tighter selection requirements, to ensure signal purity and reduce the number of fake tracks and vertices, and the loss of reconstruction efficiency must be found [91].

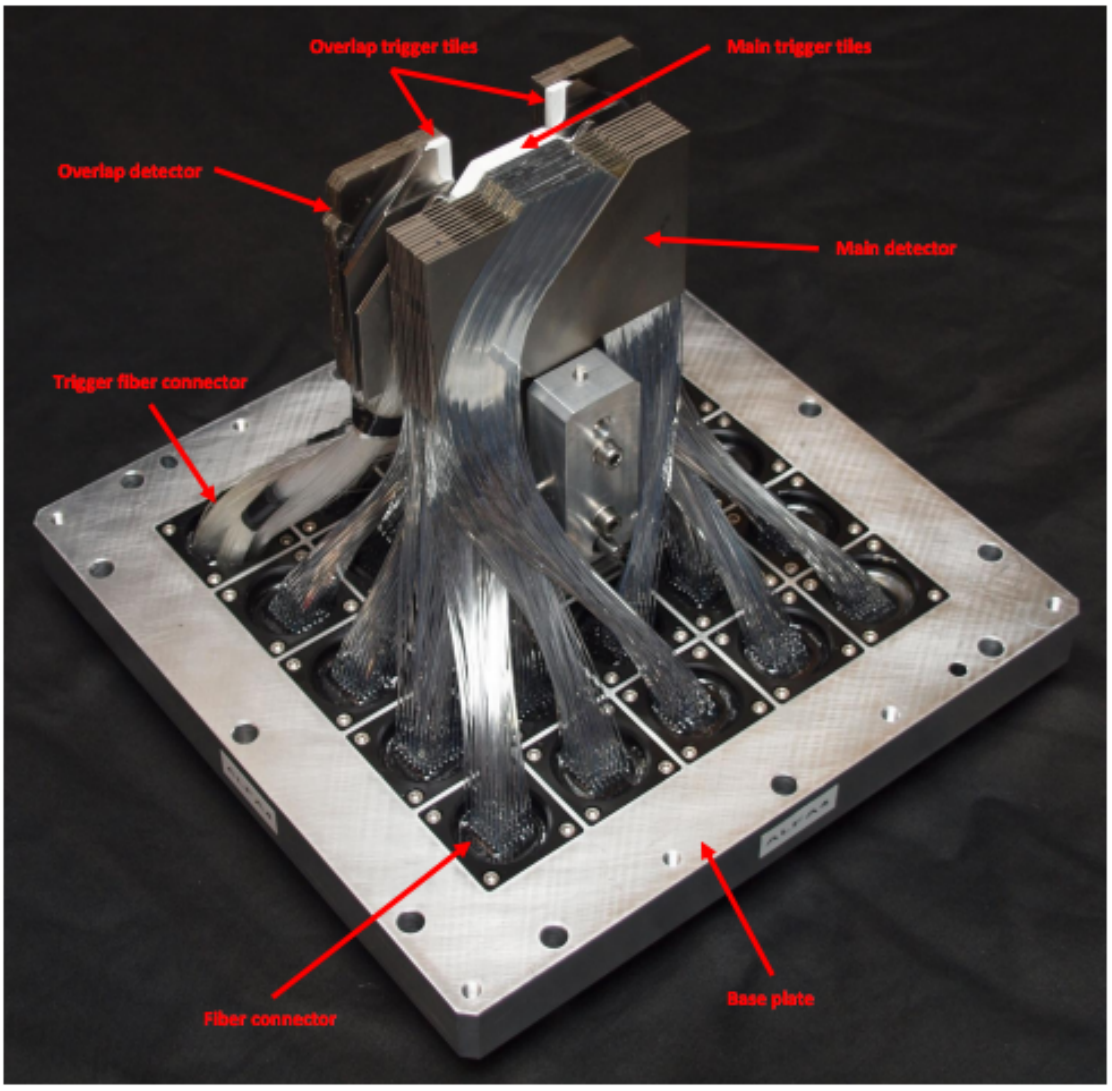

FIGURE 5.9: An ALFA detector which fits inside the Roman Pot [88].

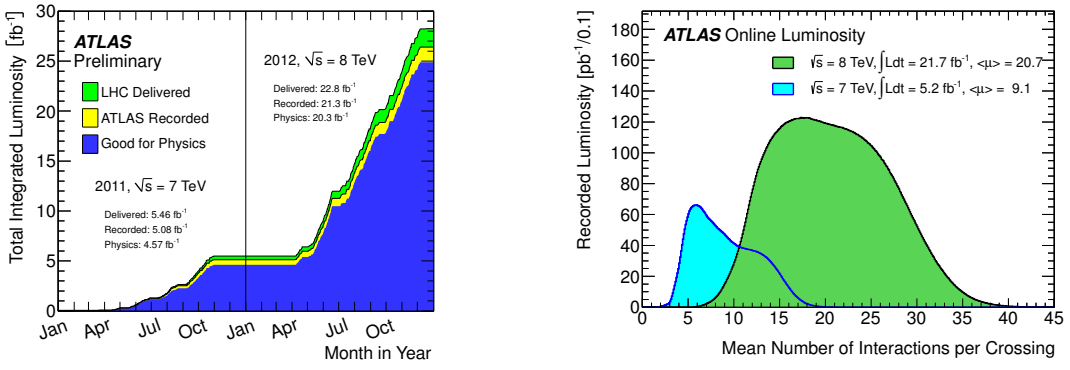

(a) (b)

FIGURE 5.10: The luminosity (a) as a function of time delivered by the LHC and recorded by ATLAS and (b) the recorded luminosity as a function of the mean number of interactions per bunch crossing for the 2011 and 2012 data taking runs [89].

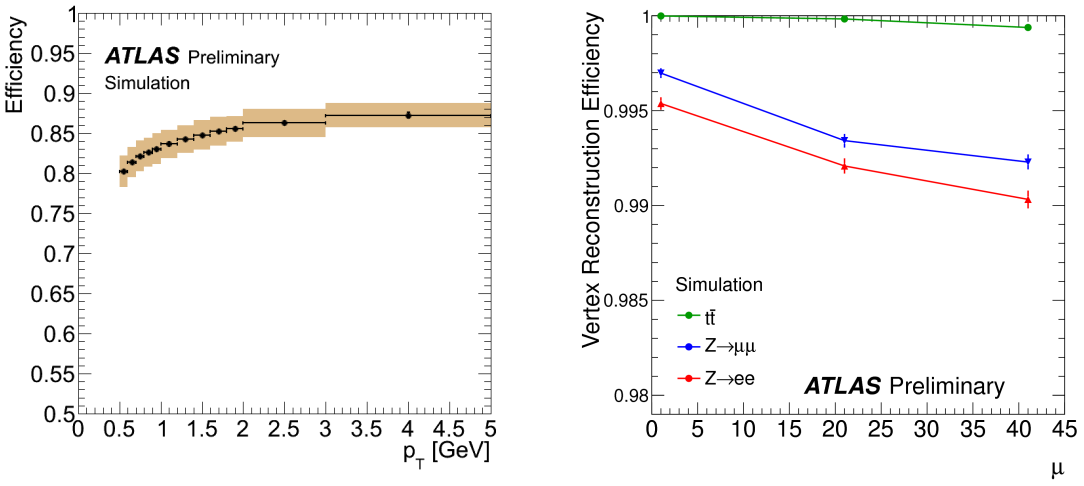

(a) (b)

FIGURE 5.11: (a) Tracking reconstruction efficiency as a function of the transverse momentum [92] and (b) the vertex reconstruction efficiency as a function number of interactions per event for different processes [91].

The reconstruction of tracks is based on three main algorithms. An *inside-out* algorithm reconstructs tracks starting from three adjoining seed hits from the tracking detectors. Additional hits that are compatible with the initial track are then added, and this is extended to the TRT. A p_T threshold of 400 MeV is required for each track. This is the primary algorithm used in track reconstruction. A *back-tracking* algorithm reconstructs tracks by starting with track fragments in the TRT. The tracks are extended by adding silicon hits as one moves closer to the interaction point. These tracks mostly arise from the decay products of primary particles. TRT tracks that have no segments in the pixel or SCT detector are known as *TRT-standalone*. A simulation of the track reconstruction efficiency, defined as a ratio between the number of tracks matched to charged particles and the number of generated charged particles, is shown in figure 5.11(a) as a function of the transverse momentum for $\sqrt{s} = 8$ TeV.

Vertices are reconstructed by using tracks as an input to an iterative χ^2 algorithm [93]. Vertex candidates are defined as the global maximum of the z-coordinate of the tracks extrapolated to the beamline. Initially, one vertex is defined from all tracks. Tracks are assigned a probability that they stem from the vertex candidate by the result of the χ^2 procedure, with outlying tracks down-weighted to their overall contribution to the vertex χ^2. Tracks that are incompatible with the vertex by more than about seven standard deviations are used to seed a new vertex. This procedure is repeated until no more tracks are left or no more vertices can be reconstructed. The vertex containing the largest sum of transverse momentum squared, $\sum p_T^2$, and having at least three or more tracks is taken as the primary vertex. Any vertex with two or less tracks is discarded. The simulated vertex reconstruction efficiency vs. the mean number of pp collisions per bunch crossing is shown in figure 5.11(b).

5.3.2 Electrons

Electrons can be identified with very high purity and reconstructed with high efficiency. They are reconstructed using energy clusters from the calorimeter cells, which are then matched to tracks from the inner detector. A sliding window algorithm scans the is used to look for a maximum of energy within a rectangular region of $\Delta\eta \times \Delta\phi = 0.075 \times 0.125$ containing an energy of at least 1.5 GeV with very loose selection criterion [94]. Tracks within $|\eta| < 2.5$ are then matched to the energy clusters by extrapolating the tracks to the center of the electromagnetic calorimeters. An electron candidate is reconstructed if the $\Delta\eta < 0.05$ and the $\Delta\phi < 0.1$ between the track and cluster.

The efficiency to detect electrons is broken into three parts: trigger, identification and reconstruction efficiencies. The total efficiency, ϵ_{total}, for each electron is determined by

$$\epsilon_{total} = \epsilon_{trigger} \times \epsilon_{identification} \times \epsilon_{reconstruction} \times \epsilon_{additional}. \tag{5.4}$$

For the central region ($|\eta|$ <2.47), cut based operating points for electrons are defined: `loose`, `medium`, `tight`, and `multilepton`. The `loose`, `medium`, and `tight` working points are arranged in order of increasing background rejection, where more cut variables are added to each, and already used variables are partially tightened. Thus, `tight` electrons are a subset of `medium` electrons, which are in turn a subset of `loose`. The `multilepton` working point is similar to `loose` but is optimized for the $H \to ZZ^* \to 4\ell$ analysis. The `loose`, `medium`, `tight` working points have also been reoptimized using the *PlusPlus*, or ++, menu, and are labeled `loose++`, `medium++`, `tight++`. A *tag-and-probe* technique is used on $Z \to ee$ events to determine the efficiencies. The electron identification efficiencies as a function of the transverse energy are shown in figure 5.12(a) and as a function of the number of reconstructed vertices in figure 5.12(b).

Trigger efficiencies are determined for electrons passing a certain identification scheme. Thus, there are dedicated sets of triggers for each working point. The W+c analysis presented later uses single electron triggers, denoted *EF_e24vhi_medium1*, *EF_e60_medium1*, where the *EF* stands for the event filter trigger, the number refers to the transverse momentum threshold required by the trigger and *medium* stands for electrons identified as `medium`.

Additional efficiencies are also taken into account, such as isolation efficiencies. Isolation requirements are applied to electrons in order to distinguish them from hadronic backgrounds. The calorimeter isolation energy in the transverse plane E_T^{iso} is computed by summing up the energy of all calorimeter cells within a cone of size $\Delta R = \sqrt{\Delta\eta^2 + \Delta\phi^2}$ around a given electron candidate [94]. A correction on E_T^{iso} is applied that subtracts the energy of the electron itself as well as contributions from the underlying event and pileup [96, 97]. A track isolation p_T^{iso} is also defined by summing the p_T of tracks inside a cone of size ΔR around the electron candidate. Tracks stemming from the electron are not considered in p_T^{iso}. Furthermore, tracks within the sum must have at least four hits from either the SCT or pixel detector and must be associated with the vertex with the highest number of tracks.

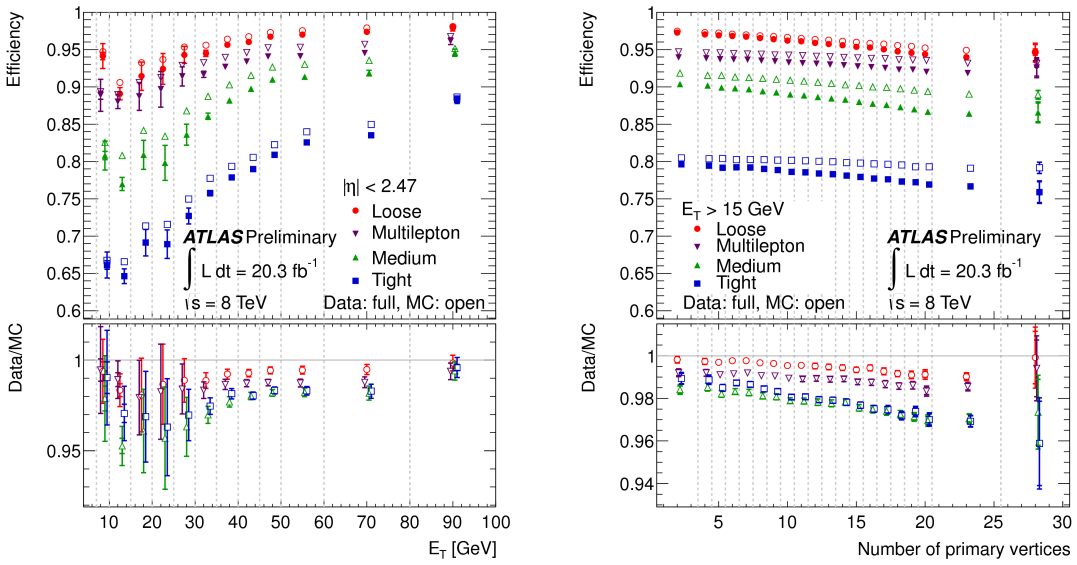

(a) (b)

FIGURE 5.12: Electron identification efficiency for the working points `loose`, `medium`, `tight`, and `multilepton` as a function of (a) electron E_T and (b) the number of reconstructed primary vertices. The efficiency in data is determined from the data-to-MC ratios and the MC prediction for electrons coming from $Z \to ee$ decays [95].

5.3.3 Muons

Muons deposit very little energy as they pass through the electromagnetic calorimeters, distinguishing them from electrons and jets. In ATLAS, they are identified from the muon chamber, the inner detector and to a lesser extent, the calorimeter. They can be reconstructed from different identification algorithms and are known as *stand-alone* (SA), *combined* (CB), *segment-tagged* (ST), and *calorimeter-tagged* (CaloTag) muons [98, 99]

- SA muons are reconstructed from tracks in the muon spectrometer. Tracks are extrapolated to the collision point to determine impact parameters. Energy loss in the electromagnetic calorimeters is also taken into account.

- CB muons combine tracks from the muon spectrometer and tracks from the inner detector, taking into account the full covariant matrix between the two.

- ST muons are seeded with tracks from the inner detector matched to at least one track from the muon spectrometer, and can be used to reconstruct muons in the range $2.5 < |\eta| < 2.7$.

- CaloTag muons are identified as such if tracks in the inner detector can be matched to energy deposits in the calorimeter consistent with minimum

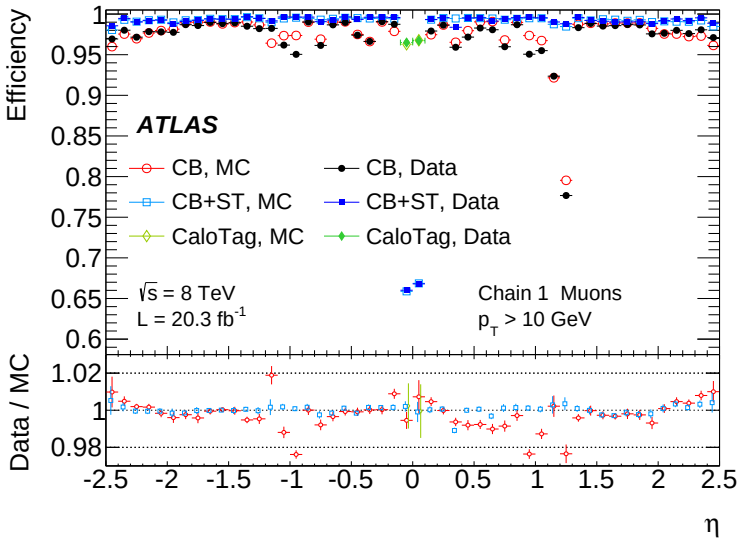

FIGURE 5.13: Reconstruction efficiency for different muon types vs. η for muons with $p_T > 10$ GeV measured with $Z \to \mu\mu$ events [99].

ionizing particles. These have the lowest purity of all muon types. CaloTag muons are optimized for $|\eta| < 0$ and $25 \lesssim p_T \lesssim 100$ GeV.

Combined muons have the highest purity. Acceptance losses in the muon spectrometer occur mainly in two regions: in the central region $\eta \approx 0$, where space is needed to provide support for the servicing of the inner detector and calorimeters, and in the region between the barrel and end-caps, $1.1 < |\eta| < 1.3$, where some regions of ϕ are only partially covered by the muon chambers.

Two independent software reconstruction packages, known as *Chains* [90], are used in the reconstruction of SA, CB, and ST muons. The first chain, *Chain* 1, performs a statistical combination of the SA muon track parameters and ID muons tracks, using the corresponding covariance matrices. The second chain, or *Chain* 2, takes hits from the MS and ID sub-detectors and performs a global refit of the muon tracks. There is a third chain, *Chain* 3, which combines the best features of the first two chains. The analysis of the $W + c$ cross section presented later makes use of these third chain muons. The reconstruction efficiency for Chain 1 muons as a function of η and measured in $Z \to \mu\mu$ events is shown in figure 5.13. Combining all muon types leads to an efficiency of 99% across most of the detector.

Besides the identification scheme for muons, mentioned above, they are also separated into different quality levels. These quality levels are defined by the level of falsely reconstructed muons, and follow the naming scheme of electron identification: `loose`, `medium`, and `tight`. For Run 1, only `loose` and `medium` are defined, while the `tight` working point is used in Run 2 analyses. The `medium` working point is further loosened to define the `medium+` working point, according to the combined performance group guidelines. More details about the different quality working points for muons can be found in [100].

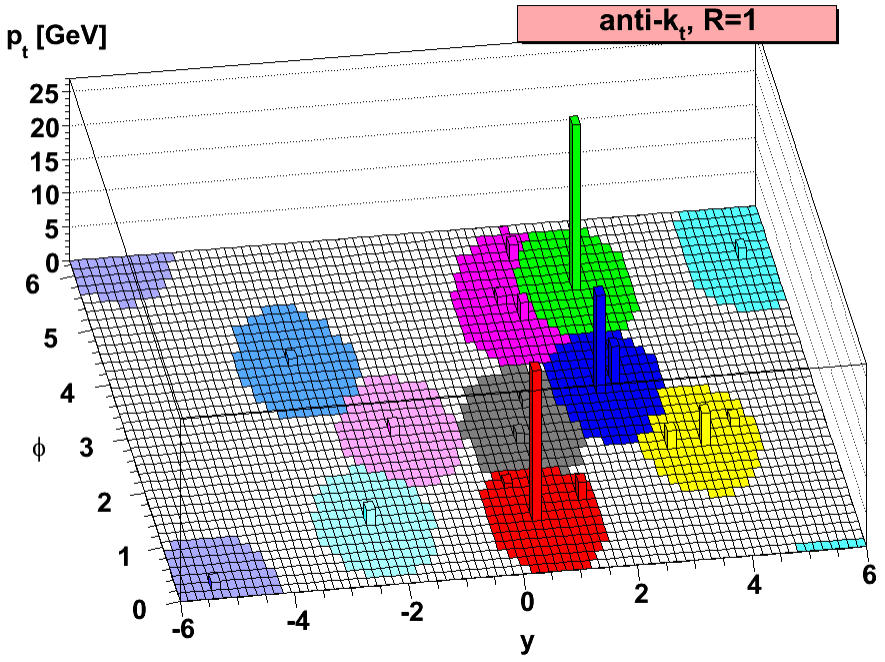

FIGURE 5.14: A simulated event using HERWIG and clustered using the anti-k_T algorithm with $R = 1$ [101].

5.3.4 Jets

Jets provide signatures for quarks and gluons, and are the dominant feature of pp collisions. The uncertainty of the jet energy is the largest source of experimental uncertainties in many physics analyses that contain jets in the final state. They are reconstructed from energy deposits in the calorimeters, and several algorithms have been developed to identify and reconstruct them.

The favored algorithm for identifying jets is the *anti-k_T* algorithm [101], which uses topological energy clusters as input. It begins by introducing the distance d_{ij} between objects i and j and d_{iB} between the object i and the beam B. the distance is defined as

$$d_{ij} = min(p_{T,i}^2, p_{T,j}^2)\frac{R_{ij}^2}{R^2} \tag{5.5}$$

where $R_{ij} = \sqrt{\Delta\eta_{ij}^2 + \Delta\phi_{ij}^2}$ and R is a fixed distance parameter. Clustering begins by determining the smallest distance between all objects. If d_{ij} is the smallest distance, then the objects i and j are combined, and if d_{iB} is the smallest distance, then it is labeled as a jet and removed from the list of objects. This procedure is repeated until the list of objects is exhausted.

If i is a hard particle and j a soft one, then the distance d_{ij} will be determined almost exclusively by the transverse momentum of i and R. Thus, soft particles will tend to cluster with hard particles before clustering with other soft particles. This also implies that the shape of the jets is not influenced much by soft particles, which makes this algorithm resilient in terms of soft-radiation, but flexible in terms of hard-radiation. A simulated event clustered using the anti-k_T algorithm with $R = 1$ is shown in figure 5.14.

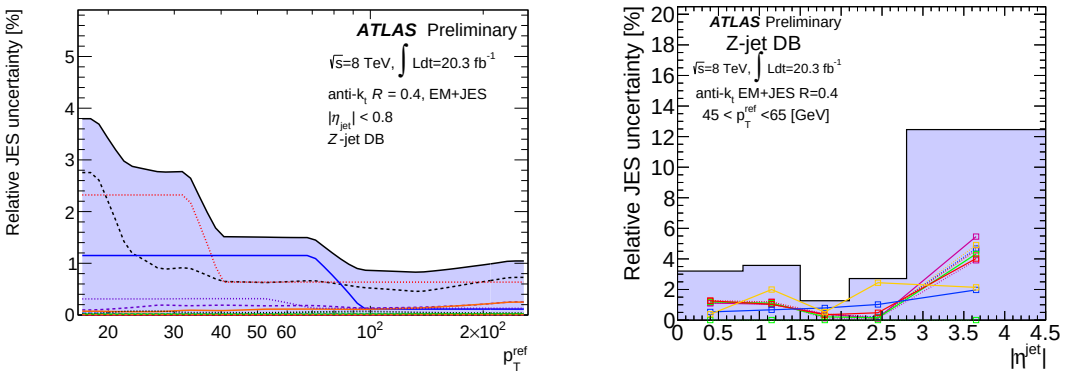

(a) (b)

FIGURE 5.15: The relative JES uncertainty for anti-k_T jets with $R = 0.4$ using $Z + jets$ events as a function of (a) jet p_T and (b) jet η [103].

Within ATLAS, jets are calibrated using a variety of schemes, each with varying levels of complexity and sensitivities to systematic effects [90]. Each scheme begins with calibration of the calorimeter performed with test-beam measurements using electrons in order to get a correct response from electromagnetic showers [102]. Since hadronic clusters have a lower energy density, his allows classification of clusters as being electromagnetic or hadronic in origin. Energy correction are then applied to hadronic clusters. The topology of energy clusters are also used in order to correct the energy loss due to nuclear energy losses, signal losses due to thresholds on noise and losses stemming from instrumentation gaps.

Systematic uncertainties stemming from the jet energy scale (JES) and the jet energy resolution (JER) are determined from in-situ measurement of the jet response asymmetry using $Z/\gamma + jets$ events [103]. Monte Carlo modeling effects, uncertainties on the material in ATLAS and effects from electronic noise are also considered. The JES uncertainty varies with jet p_T and η, being the largest in the forward regions of the detector where soft physics are assigned a conservative uncertainty. Smearing of jets is performed in simulation depending on jet p_T and η. The relative JES uncertainty for anti-k_T jets with $R = 0.4$ as a function of p_T is shown in figure 5.15(a) and as a function of η in figure 5.15(b) using $Z + jets$ events.

The *jet vertex fraction* (JVF) measures the probability that a given jet stems from the primary vertex [104]. It is useful in discriminating between jets coming from the hard interaction and jets coming from pileup. In this way, it is a very powerful tool in pileup suppression. For a given jet jet_i and a vertex v_j the JVF is defined as

$$JVF(jet_i, v_j) = \frac{\sum_k p_T(trk_k^{jet_i}, v_j)}{\sum_n \sum_\ell p_T(trk_\ell^{jet_i}, v_n)} \tag{5.6}$$

where trk^{jet_i} is a track associated with jet_i. The JVF ranges from 0 for soft-jets to 1 for hard jets. Calorimeter jets falling outside of the fiducial tracking region where no tracks have been associated are given a value $JVF = -1$. An illustration

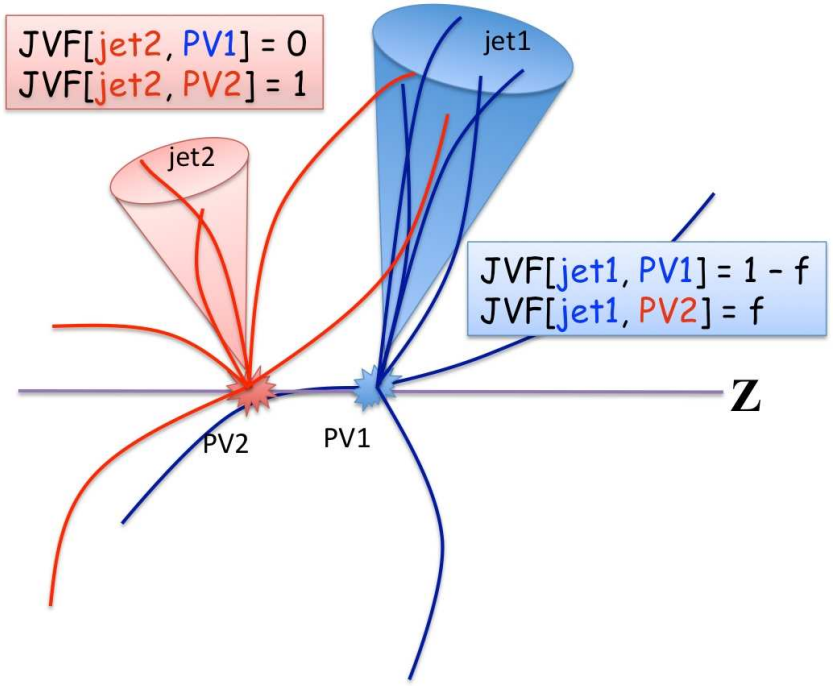

FIGURE 5.16: An illustration of the JVF principle [104].

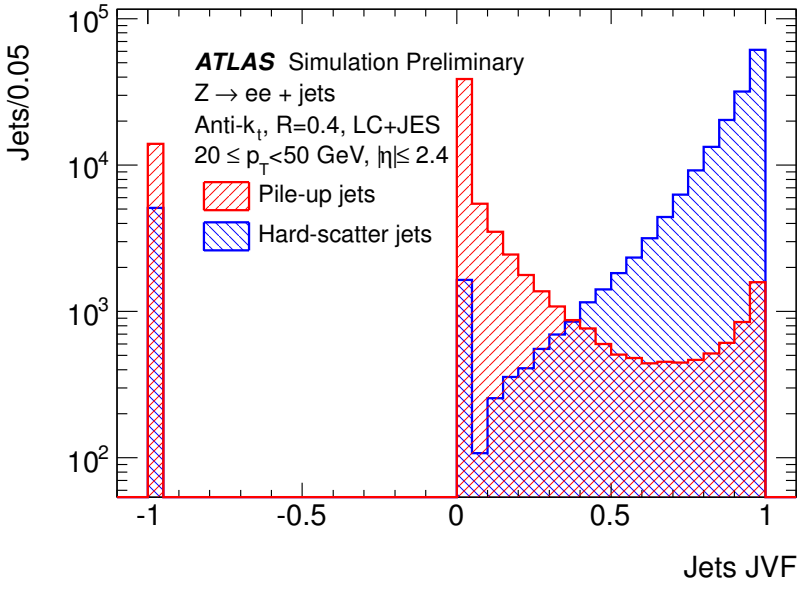

FIGURE 5.17: A simulation of $Z + jets$ showing the JVF distribution for hard-scatter (blue) and pileup (red) [104].

of the JVF procedure is shown in figure 5.16. The distribution of the JVF for hard scatter jets and pileup jets simulated on $Z + jets$ events can be seen in figure 5.17.

5.3.5 Missing Transverse Energy

Many particles leave the detector without being detected. These include neutrinos as well as other weakly interacting particles predicted by new physics models. They will manifest themselves as missing energy which can be inferred through momentum conservation in the transverse plane. Since the total momentum in the transverse plane must be 0, the missing transverse energy (MET), or E_T^{miss} is defined as

$$\mathbf{E}_T^{miss} = -\sum_{detected\ objects} \mathbf{p}_T^{objects}. \tag{5.7}$$

In ATLAS, all reconstructed objects are taken as inputs to the E_T^{miss} calculation. There are six terms that enter into the E_T^{miss} calculation corresponding to photons, electrons, muons, hadronically decaying taus, jets and soft terms. The soft terms account for all contributions not covered by the other terms. The E_T^{miss} is then determined by

$$\mathbf{E}_T^{miss} = \mathbf{E}_T^{miss,\gamma} + \mathbf{E}_T^{miss,e} + \mathbf{E}_T^{miss,\mu} + \mathbf{E}_T^{miss,\tau} + \mathbf{E}_T^{miss,jets} + \mathbf{E}_T^{miss,soft} \tag{5.8}$$

where each term is the negative sum of momentum components in the transverse plane of the corresponding fully calibrated physics objects. Furthermore, terms in $E_T^{miss,jets}$ only include jets with $p_T > 20$ GeV, while jets between $7 < p_T < 20$ are contained in $E_T^{miss,soft}$.

Pileup has a large effect on the determination of the MET and must be correctly taken into account. The effect of pileup on the average E_T^{miss} can be seen in figure 5.18. It is important to note that all the terms besides $E_T^{miss,soft}$ are already corrected for pileup. The correction on $E_T^{miss,soft}$ due to pileup is based on the *soft term vertex fraction* (STVF), which is similar to the JVF definition in equation (5.6) and is described in detail in [105].

5.4 The HL-LHC and the Phase-II upgrade to the ATLAS detector

5.4.1 The HL-LHC

The LHC is scheduled to undergo a luminosity upgrade sometime in the 2020s, dubbed the High-Luminosity LHC (HL-LHC) [106]. After about 2020, there will be minimal statistical gain in running the LHC unless the luminosity is significantly increased, as can be seen in the luminosity plan for the next few years in figure 5.19. The instantaneous luminosity will be increased by a factor of five to 5×10^{34} cm^{-2} s^{-1} and the integrated luminosity by a factor of ten. Several components of the LHC will need to be changed and improved due to operating in a harsher radiation environment, including the low-β triplet magnets, cryogenics and the collimation system.

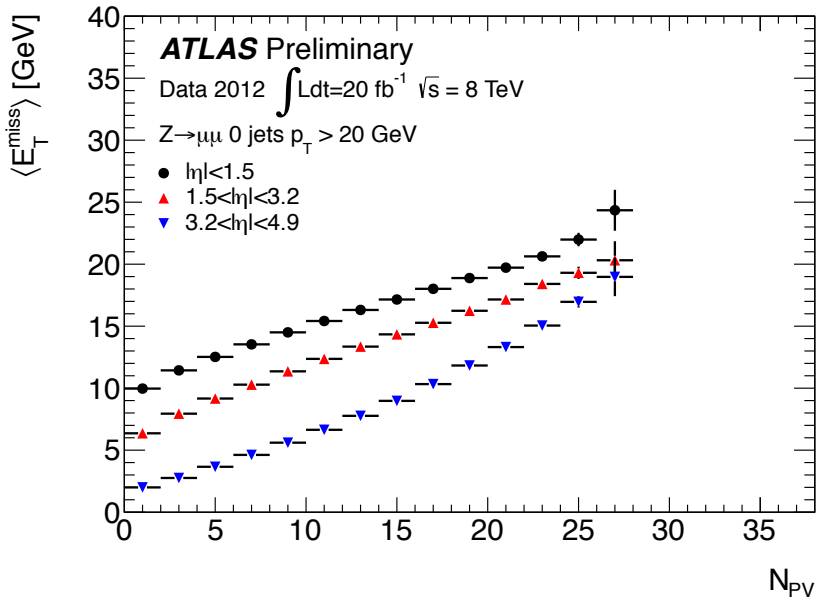

FIGURE 5.18: The effect of pileup on the average E_T^{miss} for $Z \to \mu\mu$ events reconstructed without jets $p_T > 20$ GeV.

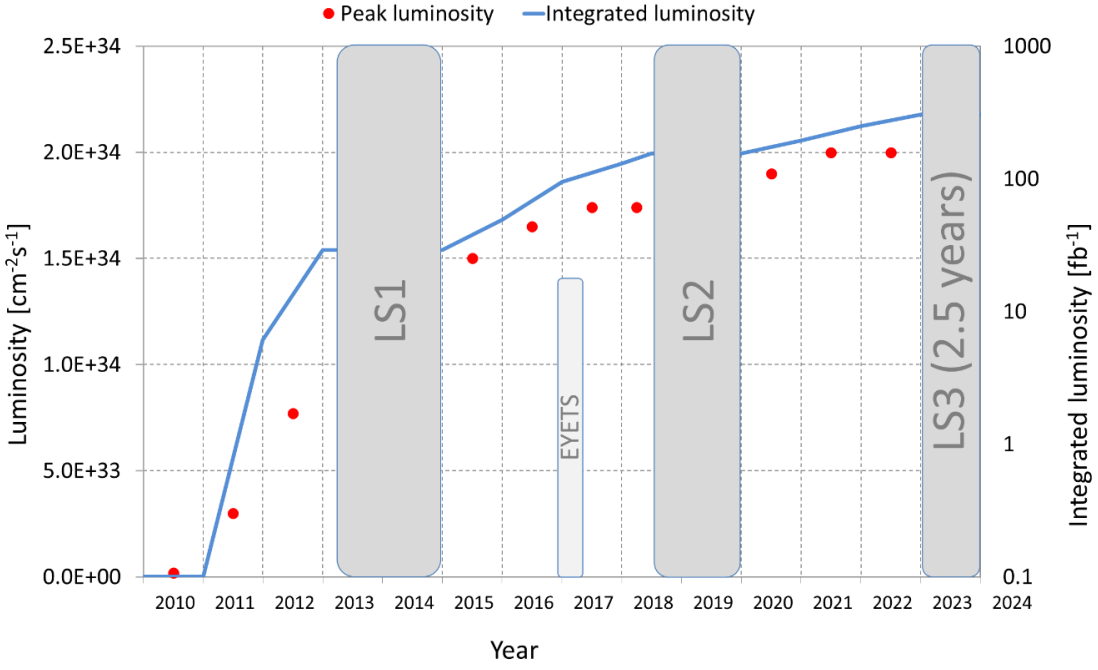

FIGURE 5.19: Luminosity plan for the LHC in the next few years. Both the peak luminosity (red) and integrated luminosity (blue) are shown. The shutdown periods, denoted LS1, LS2 and LS3 are shown in grey [106].

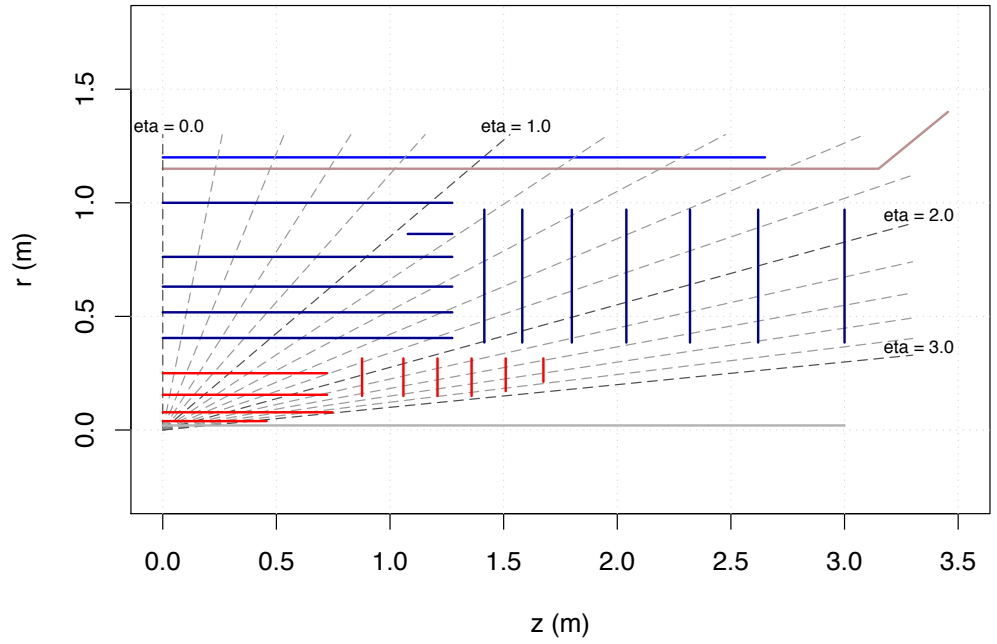

FIGURE 5.20: Layout of the new all-silicon tracker for the Phase-II upgrade of ATLAS showing the pixel layers (red) and strip layers (blue) [107].

5.4.2 The Phase-II upgrade to ATLAS

The ATLAS detector will also undergo significant changes in design to cope with the increased luminosity. This is termed the Phase-II upgrade [107, 108]. The current inner detector layout will no longer be suitable for Phase-II due to an increased radiation environment and higher luminosity. The TRT will be replaced with a new all-silicon tracker whose layout can be seen in figure 5.20. The calorimeters and the Muon system readout will also need to be upgraded to maintain performance given a larger number of collisions per bunch crossing. Changes in the trigger and computer software architecture will will be upgraded also to maintain and improve performance of event selection.

The radiation environment in the inner detector will be particularly harsh. The inner most pixel layers are expected to reach 1.4×10^{16} cm^{-2} n_{eq} while the strip layers will be exposed to 5.3×10^{14} n_{eq} in the barrel and 8.1×10^{14} n_{eq} in the endcaps. These high fluences require increased radiation-hardness of the silicon detectors, as the current detector designs are not able to withstand such fluences.

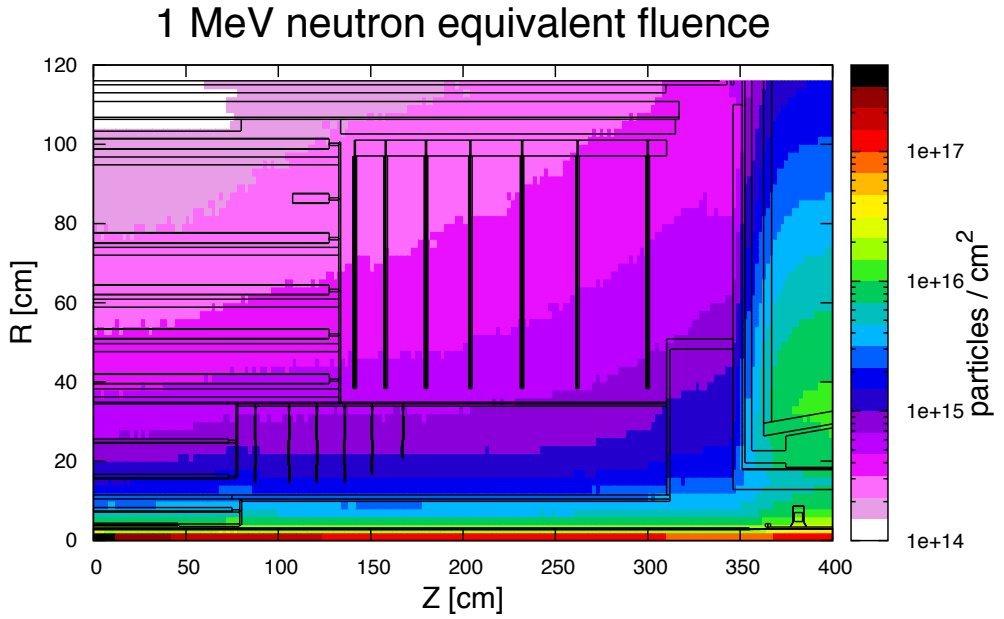

FIGURE 5.21: Expected radiation environment of the ATLAS inner detector for the Phase-II upgrade normalized to 3000 fb^{-1} [107].

Chapter 6

Measurement strategy for the W+c production cross-section

6.1 Motivation

The production cross-section of a W boson in association with a single charm quark at hadron colliders is sensitive to the strange quark content of the proton. As can be seen in figure 6.1, the strange quark PDF is not very well constrained. While measurements of the cross-section have been performed at the Tevetron and the LHC, only recently has there been the potential to use these measurements to constrain the PDF of the strange quark. The phase space covered by various experiments so far for the determination of the strange quark can be seen in figure 6.2.

The recent ATLAS [109] and CMS [110] measurements at $\sqrt{s} = 7$ TeV of this cross section have been able to reduce the uncertainties on the strange quark PDF, but the measurements still exhibit large statistical uncertainties. By using the full $\sqrt{s} = 8$ TeV data set, the hope is to have much smaller uncertainties, due to the fact that the peak luminosity and inclusive cross section should be roughly five times larger than at $\sqrt{s} = 7$ TeV. The systematic uncertainty on the background estimation, in particular the QCD and W+light-jets backgrounds, is also expected to be reduced due to the data driven methods used to normalize each.

Of paticular interest is the strange sea supression factor, defined as $r_s = (s + \bar{s})/2/\bar{d}$. Previous experiments, such as the NuTeV and CCFR neutrino scattering experiments, have indicated an asymmetry between the strange and anti-strange quark PDFs [111–114]. The error on the strange quark PDF and the asymmetry between the strange and anti-strange quark PDFs has further been constrained using the latest collider data, including measurements from ATLAS and CMS [115]. The latest results including CMS and ATLAS data are consistent with the PDFs being symmetric, as can be seen in figure 6.3. The analysis presented here also measures the ratio of $W^+ + \bar{c}$ to $W^- + c$ production.

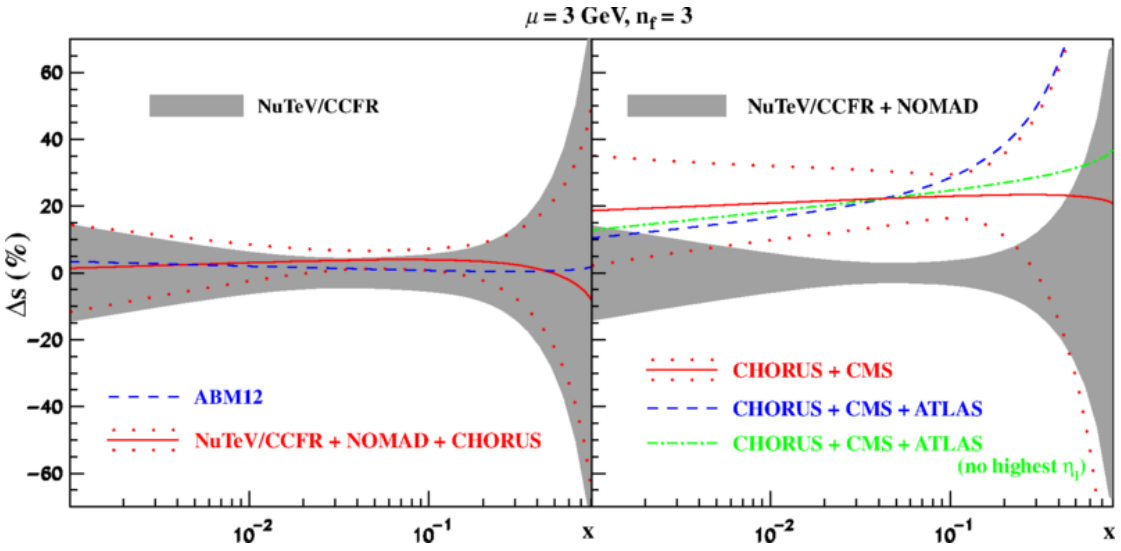

FIGURE 6.1: Relative strange quark PDF uncertainties including data from different experiments [115]. The left plot includes NuTeV/CCFR data in comparison with the one including also the NOMAD [116] and CHORUS [117] data. The right plot includes data from CMS and ATLAS

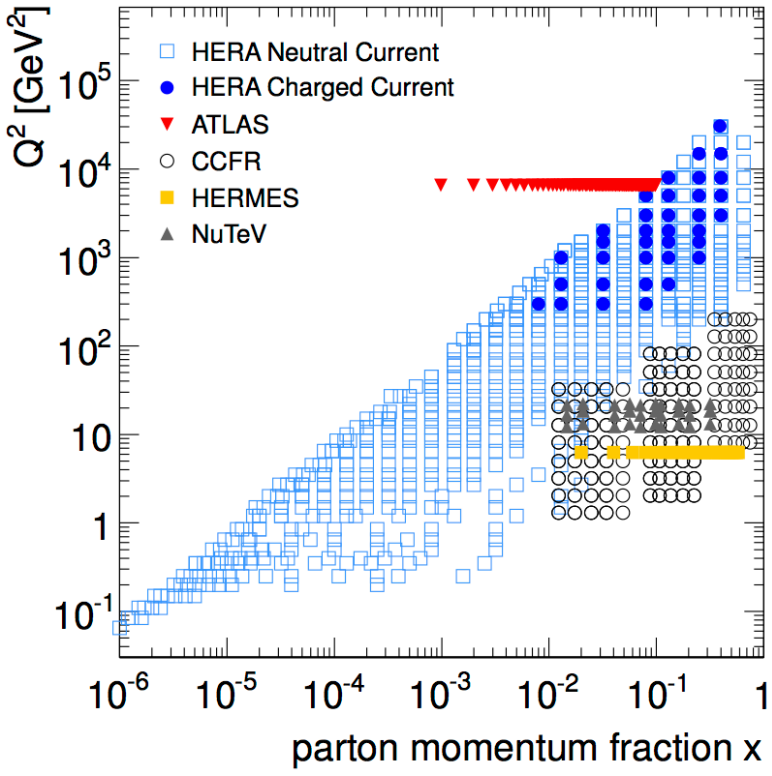

FIGURE 6.2: Kinematic phase space covered by different experiments for the determination of the strange quark PDF. ATLAS results are in red and taken at $Q^2 = m_W^2$ [118].

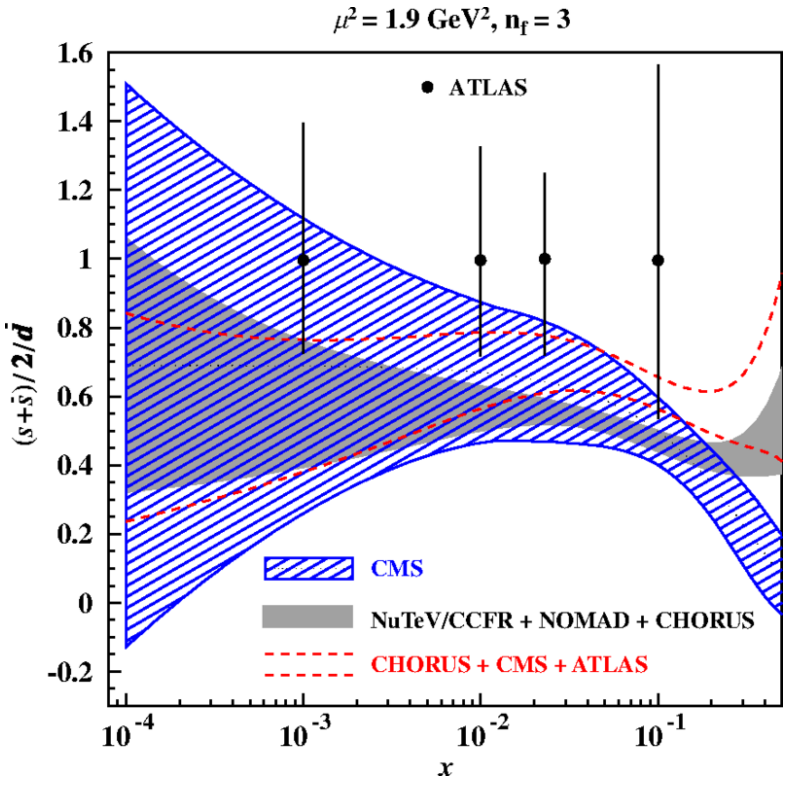

FIGURE 6.3: The strange sea suppression factor $r_s = (s + \bar{s})/2/\bar{d}$ as a function of the Bjorken x for determined from various experiments [115].

6.2 Data and simulation samples

6.2.1 Data sample

The measurement is carried out using the full 2012 ATLAS data set collected using single electron trigger, which are denoted as `EF_e24vhi_medium1` and `EF_e60_medium1`. The data is split into different periods, which followed the LHC configurations and the ATLAS trigger and detector conditions which changed with time. The full integrated luminosity for the sample is 20.3 fb^{-1}. The uncertainty on the integrated luminosity is $\pm 2.8\%$. It is derived following the methodology detailed in [119].

6.2.2 Simulation

Monte Carlo simulations are used for the background estimation of some of the background processes and to perform the calculation of the cross section from the measured signal yields. The backgrounds considered are QCD, W+light-jets, $W + b\bar{b}$, $W + c\bar{c}$, diboson, $t\bar{t}$, single top and Z+jets. The QCD and W+light-jets background processes are normalized using data driven methods, but the W+light-jets background shape is extracted using Monte Carlo while the QCD shape is extracted from the data, as described in section 6.5. Other backgrounds are estimated from simulation.

The $W + c$ signal process is simulated using `ALPGEN+PYTHIA`. It is broken into samples labeled W+c+NpX, where NpX represents the number of initial state partons, i.e. Np1 has one additional initial state parton, Np2 has two additional initial

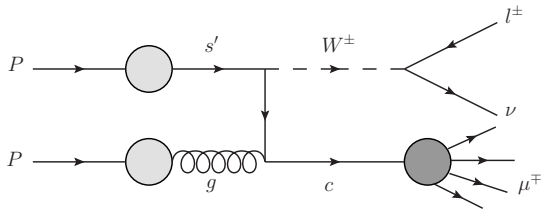

FIGURE 6.4: Diagram of strange-gluon fusion associated with the production of a W-boson and a single charm quark

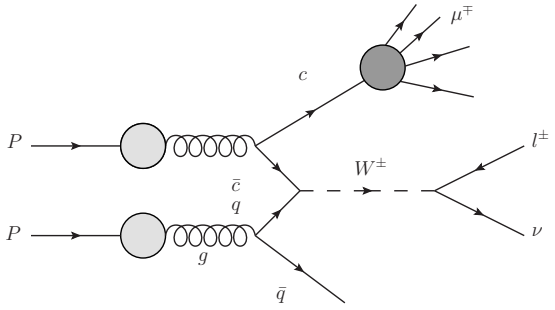

FIGURE 6.5: Diagram of gluon-gluon fusion associated with the production of a W-boson and a single charm quark

state partons, etc. W+light-jets, $W + b\bar{b}$, $W + c\bar{c}$ and $Z + jets$ are also estimated using `ALPGEN+PYTHIA`. *Diboson* and $t\bar{t}$ are estimated using `POWHEG+PYTHIA`. Single top is estimated using `AcerMC+PYTHIA` for all channels. The list of all background samples are listed in appendix A.

All Monte Carlo samples are reweighted to match the data beam spot, pileup, trigger and detector conditions. The samples are furthermore reweighted to match the data resolution and reconstruction efficiencies. K-factors are also applied to each sample.

6.3 General Strategy

$W + c$ production at hadron colliders is dominated by strange-gluon fusion, with a small contribution (∼10%) from down-gluon fusion suppressed by CKM couplings. The LO diagram for strange-gluon fusion is shown in figure 6.4. Events with additional jets at NLO can be produced through gluon-gluon fusion, as seen in figure 6.5. An important feature of the process is that the W boson and the charm quark always carry opposite charge sign. While the W boson is best selected through its leptonic decay, the charm quark can be selected either through selection of the fully reconstructed charmed hadron or through its semi-leptonic decay into a muon.

The present analysis uses the latter approach, that is selection via the semi-leptonic decay into a muon. The muon will carry the same charge sign as that of the charm quark, and thus have opposite charge to that of the W boson and the corresponding decay lepton, referred to as the signal lepton. Thus, $W + c$ events can be selected with high efficiency by requiring the signal lepton and muon to have opposite charge. Background processes are mostly symmetric between events

having opposite sign charge (OS) and having the same sign charge (SS) between the signal lepton and muon. Taking the difference of OS to SS events (OS-SS) will therefore select $W + c$ events with high purity while minimizing the background.

Some backgrounds, such as W+light-jets and QCD, will exhibit a small asymmetry between OS and SS events, and will contribute a small residual background in the OS-SS sample. The W+light-jets background will be mostly composed of $W + u/d$ that are produced via down/up-gluon fusion. The u/d quark charge is also correlated to the W boson charge, and thus a false reconstructed muon arising from the quark fragmentation products, will have opposite charge to the W-boson. Also, for some QCD background like $c\bar{c}$ and $b\bar{b}$ multijet production an asymmetry could be expected. The determination of the normalization and asymmetry of the dominant backgrounds is described in section 6.5.

To summarize, requiring the muon, from the semileptonic decay of a charm-jet, to have opposite charge sign to that of the signal lepton, arising form the leptonic W decay, selects W+c events with high efficiency. Subtracting the SS sample from the OS sample will cancel many backgrounds that are symmetric between OS and SS, and thus lead to a signal with high-purity. The strange quark distributions are enhanced by splitting the final events into different jet bins.

For events with a jet multiplicity greater than two, $t\bar{t}$ production becomes the dominant background. This makes extraction of the $W + c$ more difficult for higher jet multiplicities. The 1- and 2-jet yields are extrapolated to measure the production cross section of a W boson and a c-jet plus any number of jets.

The analysis is carried out for events with exactly one jet or exactly two jets. The sum of the 1 and 2 jet measurements is used to determine the 1-jet inclusive measurement. The analysis also measures the production of $W^+ + \bar{c}$ and $W^- + c$. This allows for the measurement of the ratio between the $W^+ + \bar{c}$ and $W^- + c$ cross section, which is important in constraining the ratio of the strange to anti-strange quark PDFs.

6.4 Event and Candidates Selection

The W boson is tagged by requiring events to have one isolated high-p_T lepton and a large missing transverse energy coming from neutrino production. Events are also required to have one or two jets, with one of the jets containing a muon.

All leptons and jets, as well as lepton isolation, are corrected according to the combined performance group recommendations. The E_T^{miss} and m_T^W are recomputed using the corrected properties of the objects. Scale factors, which correct object reconstruction and efficiency discrepancies between data and Monte Carlo, are also applied. The selection for $W \to e\nu$ selection is listed in table 6.1 .

6.4.1 Event selection

Data Quality Selection Data sample events need to pass detector quality requirements according to the Standard Model WZ good run list: data12_8TeV.periodAllYear_DetStatus-v61-pro14-02_DQDefects-00-01-00_PHYS_StandardGRL_All_Good.xml

Event Selection	
Detector conditions	GRL & LArError $\neq 2$
Trigger	EF_e24vhi_medium1, EF_e60_medium1
Primary vertex	$N_{tracks} \geq 3$
Signal electron selection	
Electron ID	Author 1 or 3
	tight++
Phase space	$\|\eta\| < 2.47$, exclude $1.37 < \|\eta\| < 1.52$
	$p_T > 25$ GeV
Isolation	etcone30/$p_T < 0.14$
	ptcone30/$p_T < 0.07$
Veto electron selection	
Electron ID	Author 1 or 3
	medium++
Phase space	$\|\eta\| < 2.47$, exclude $1.37 < \|\eta\| < 1.52$
	$p_T > 25$ GeV
Veto muon selection	
Muon ID	3^{rd} chain
	Medium+
	$\neq$StandAlone
Phase space	$\|\eta\| < 2.4$
	$p_T > 25$ GeV
MCP cuts	$N_{pixel}^{hits} + N_{pixel}^{dead-sensors} \geq 2$
	$N_{SCT}^{hits} + N_{SCT}^{dead-sensors} \geq 6$
	$N_{pixel}^{holes} + N_{SCT}^{holes} \geq 3$
	if $N_{TRT}^{hits} \geq 6$ then $N_{TRT}^{outliers}/(N_{TRT}^{hits}+N_{TRT}^{outliers}) < 0.9$
	if $0.1 < \|\eta\| < 1.9$ then $N_{TRT}^{hits} \geq 6$
Isolation	ptcone20/$p_T < 0.1$
$W \to e\nu$ event selection	
Lepton	exactly one signal electron
	no veto electrons or muons
Trigger matching	offline signal electron match to trigger muon is $\Delta R < 0.15$
Electron-jet overlap	remove jet if ΔR(jet, electron) < 0.5
E_T^{miss} cleaning	looser jet cleaning
	LAr hole SimpleVeto
Missing transverse energy	$E_T^{miss} > 25$ GeV
W transverse mass	$m_T(W) > 40$ GeV

TABLE 6.1: Summary of event selection cuts

Trigger Selection The analysis focuses on the $W \to e\nu$ (electron) channel. The eGamma stream is used for this channel. Events are required to pass the trigger, listed in table 6.1, with the lowest threshold. The trigger varies with different data periods corresponding to the increasing LHC luminosity.

Primary Vetex Multiple proton-proton interactions can lead to several vertices reconstructed in a given event. The vertex with the highest $\sum p_T^2$ is selected as the primary vertex corresponding to the hard interaction.

6.4.2 W$\to \ell\nu$ selection

Selection of a W boson candidate is done through its leptonic decay. The lepton selection, with additional E_T^{miss} and m_T^W cuts, are chosen to maximize the the statistics while minimizing background contributions. The selection for the electron channel is described below and detailed in table 6.1.

Signal Electrons Electrons are reconstructed using the calorimeter-seeded algorithm dedicated to reconstructing isolated high-p$_T$ electrons (author == 1 or 3). Following the eGamma combined performance group recommendations, a rescaling is done on the data while smearing of the electron cluster energy is done Monte Carlo. `Tight++` electrons are used and are required to have p_T >25 GeV and cluster $|\eta|$ <2.47 (excluding 1.37 <$|\eta|$ <1.52). Electrons are required to be isolated by requiring the relative energy deposited in the calorimeters in a cone of ΔR <0.3 around the electron to be less than 0.14, while the relative energy of all tracks in a cone of ΔR <0.3 around the electron must be less than 0.07. The energy is corrected for leakage and pileup effects. Lastly, the selected electron must match the trigger electron object within ΔR <0.15. Scale factors for the electron trigger, reconstruction and identification are applied to the simulation to account for differences in efficiency with respect to data. Additional scale factors are applied to correct for impact parameter and the isolation cut efficiency on Monte Carlo.

Veto Leptons Events are allowed to contain exactly one isolated lepton. Events with additional isolated electrons or muons are rejected. The veto criteria for electrons are looser than for signal electrons: `medium++` electrons are rejected, while the isolation requirement is also dropped.

Missing Transverse Energy and the W Boson Transverse Mass The E_T^{miss} of an event is computed using fully calibrated objects. Both the electron and muon channel use the E_T^{miss} built with with track-based soft terms (MET RefFinal TST), which is recommended by the JetEtMiss combined performance group [120]. The transverse mass m_T^W is determined from the electron and neutrino (missing energy) momenta in the transverse plane by

$$m_T^W = \sqrt{2p_T^e p_T^\nu (1 - cos(\phi^e - \phi^\nu))} \tag{6.1}$$

where p_T^e and ϕ^e is the transverse momentum and azimuthal angle of the electron and p_T^ν and ϕ^ν is the transverse momentum and azimuthal angle

Jet selection	
Jet ID	anti-k$_T$
	$\Delta R = 0.4$
	`Loose`
Phase space	$\|\eta\|$ <2.4
	p$_T$ >25 GeV
Jet vertex fraction	$\|JVF\|$ >0.5 for 50 GeV <p$_T$ <100 GeV

TABLE 6.2: Summary of jet cuts

of the neutrino. A 40 GeV cut is placed on m_T^W which optimizes the signal efficiency and background rejection.

6.4.3 Jet selection

Jet selection Jet reconstruction is done using the anti-k$_T$ algorithm with a distance parameter of $\Delta R = 0.4$. Jet energy is calibrated at the hadronic scale and is corrected for pileup effects. Jets are required to have p_T>25 GeV and $|\eta|$ <2.4. The jet vertex fraction (JVF) is required to be $|JVF|$ >0.5 for jets with p_T <50 GeV, which helps remove jets reconstructed from energy deposits coming from pileup events. Only events with one or two jets are considered. BadLooseMinus requirement are rejected. A summary of the jet selection can be found in table 6.2

Lepton-Jet Overlap and Isolation Jets, selected as described in table 6.2, that are found within ΔR <0.5 of a signal lepton are rejected. These jets are required to have p_T >25 GeV and a $|JVF|$ >0.5 for jets with p_T <50 GeV.

Charm-jet tagging The Soft Muon Tagger (SMT) tool is used to associate muons coming from semi-leptonic heavy flavor decays to jets. The tagger searches muons inside jets. Exactly one muon is required to be associated to a jet. Events with more than one muon are rejected. Events with more than 1 muon tagged jets are also rejected.

The SMT uses staco muons and fully calibrated jets as an input. muons are required to have a p_T >4 GeV, $|\eta|$ <2.5, $|d0|$ <3 mm, $|z0\ sin\theta|$ <3 mm, and pass the MCP cuts. SMT tagged jets must have an EM fraction <0.8 and contain more than 3 tracks. Cuts applied by the SMT are listed in table 6.3.

6.5 The Background Composition

The analyses takes the difference between OS and SS events. Many backgrounds are symmetric between OS and SS events, and only events with a significant asymmetry will contribute to the final sample. Processes such as W+$b\bar{b}$ and W+$c\bar{c}$ are completely symmetric between OS and SS events, and will largely cancel in the subtraction. Backgrounds such as $t\bar{t}$, *diboson*, and single top are estimated using

muon selection	
Muon ID	Staco
Phase space	$\|\eta\|$ <2.5
	p_T >4 GeV
MCP cuts	$N^{hits}_{pixel} + N^{dead-sensors}_{pixel} \geq 2$
	$N^{hits}_{SCT} + N^{dead-sensors}_{SCT} \geq 6$
	$N^{holes}_{pixel} + N^{holes}_{SCT} \geq 3$
	if $N^{hits}_{TRT} \geq 6$ then $N^{outliers}_{TRT}/(N^{hits}_{TRT} + N^{outliers}_{TRT}) < 0.9$
	if 0.1 <$\|\eta\|$ <1.9 then $N^{hits}_{TRT} \geq 6$
Impact parameter	$\|z0\ sin\theta\|$ <3 mm
	$\|d0\|$ <3 mm
SMT tagged jets	N_{tracks} >3 & EM fraction <0.8

TABLE 6.3: Summary of cuts applied by the SMT

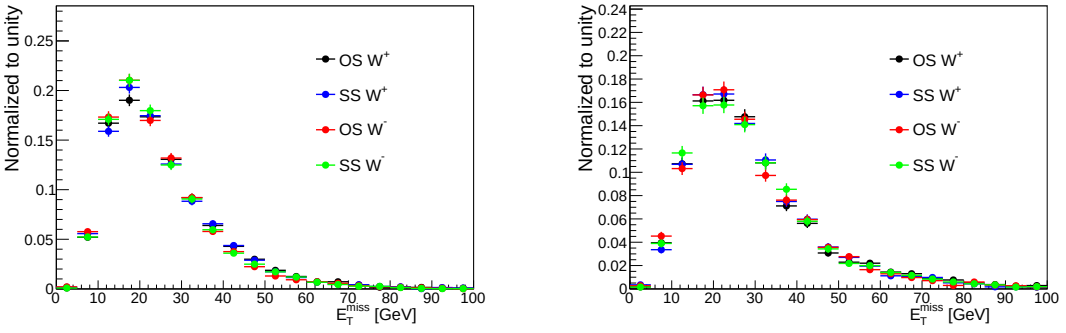

(a) (b)

FIGURE 6.6: The QCD template for the (a) 1-jet and (b) 2-jet bin

MC simulations. Additionally, W+light-jet and QCD events contribute significantly in the final OS-SS sample.

The estimation of $W + light - jets$ and QCD backgrounds are broken up into two components: the overall normalization of QCD and W+light-jets in the SS sample, and determination of the asymmetry for each, which is used to extrapolate the normalization in the SS sample to the OS-SS sample. The asymmetry is defined as

$$A = \frac{N^{OS} - N^{SS}}{N^{OS} + N^{SS}} \tag{6.2}$$

where N^{OS} and N^{SS} are the number of events in the OS and SS samples respectively.

6.5.1 QCD and W+light-jet normalization

A data driven method is used in order to determine the correct normalizations for the QCD and W+light-jets backgrounds. The normalization of the QCD and W+light-jets backgrounds are extracted from the SS sample, which is mostly signal

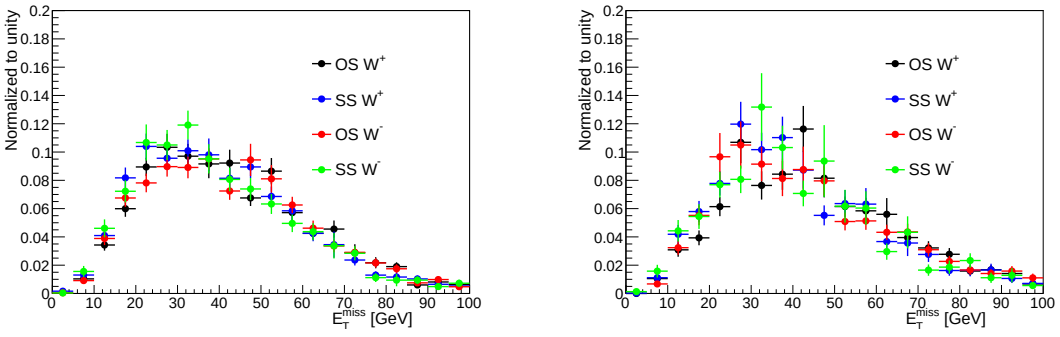

(a) (b)

FIGURE 6.7: The W+light-jets template for the (a) 1-jet and (b) 2-jet bin

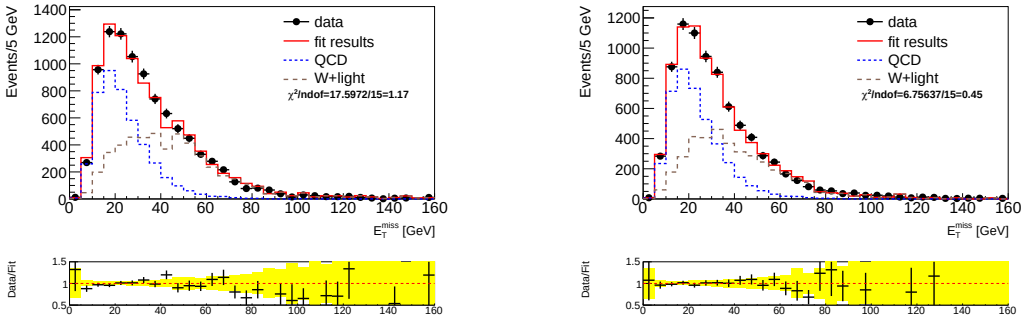

(a) 1-jet W^+ (b) 1-jet W^-

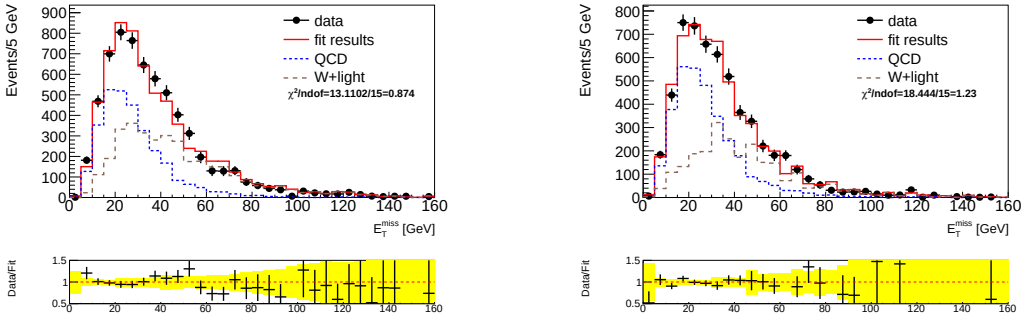

(c) 2-jet W^+ (d) 2-jet W^-

FIGURE 6.8: E_T^{miss} fits used to determine $R(+/-)$ in the SS sample

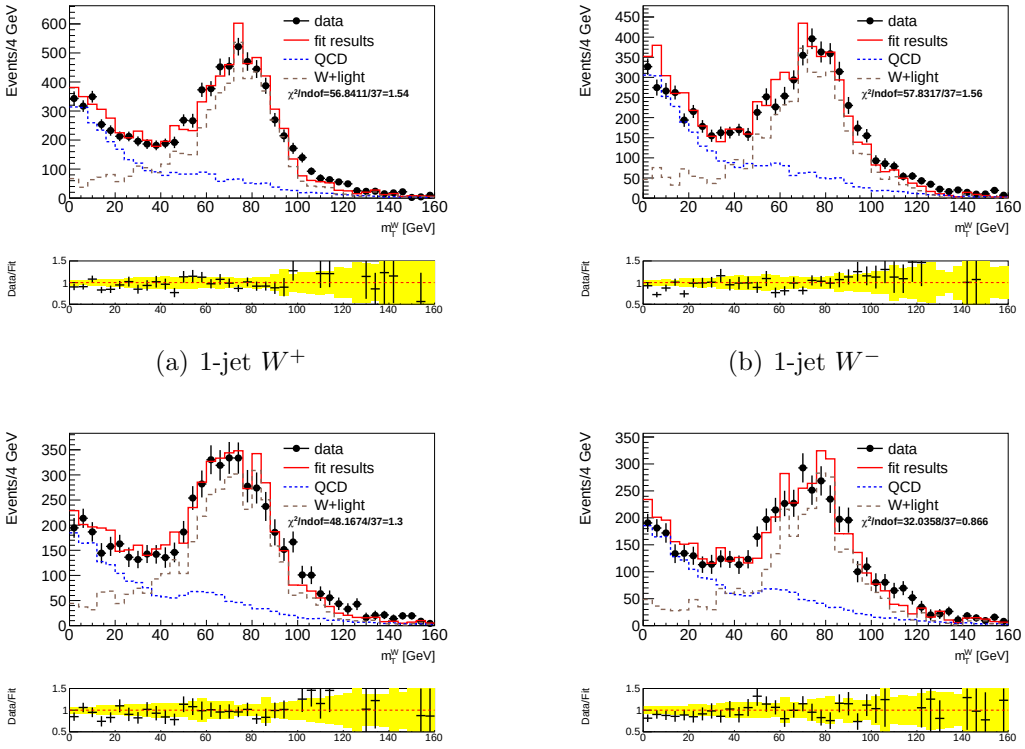

(a) 1-jet W^+ (b) 1-jet W^-

(c) 2-jet W^+ (d) 2-jet W^-

FIGURE 6.9: m_T^W fits used to determine $R(+/-)$ in the SS sample

free. E_T^{miss} is used as a discriminant variable and a binned maximum likelihood fit is then carried out to extract the fraction of QCD and $W + light - jet$ events from the data. One can alternatively perform the fits using m_T^W as a discriminant variable, but this leads to upwards of a 40% difference in the QCD normalization between fitting in E_T^{miss} and m_T^W. The normalization of the QCD and W+light-jets backgrounds are thus not extracted directly from the fits, but instead are used to measure the ratio of W^+ and W^- events, in which the difference between fitting in the two variables should largely cancel out. The ratio,

$$R = N^+/N^-, \tag{6.3}$$

can be used to constrain the QCD and W+light-jets yields in the SS sample by taking advantage of the fact that the W^+ sample will be larger than the W^- sample due to charge conservation in proton-proton collisions. Here $N^{+/-}$ are the number of events stemming from $W^{+/-}$. The procedure for obtaining the normalization for the QCD and W+light-jets backgrounds is outlined in what follows.

For the QCD, a template is constructed from the data control sample by inverting some electron ID cuts: Namely, the electrons are required to pass the `medium++` requirements but fail at least one of the `tight++` as well as have an anti-isolation cut of 3 GeV. The QCD sample is also required to contain a b-layer hit. As seen in figures 6.6(a) and 6.6(b), the QCD template has the same shape in the OS^+, OS^-, SS^+ and SS^- samples, thus the combined OS+SS template is used

in all fits to increase statistics. The W+light-jets template, seen in figures 6.7(a) and 6.7(b), is taken from MC simulation, as are all other non-QCD templates. The fits are performed after all non-QCD/W+light-jets (including W+c signal) are subtracted.

The sample constructed from data using the inverted electron isolation cuts mainly consists of QCD events. Real electrons can fail the identification cuts, causing a small contribution from W and Z bosons and top quark production. Electrons are in general well described by the detector simulation, and the residual non-QCD contributions is estimated and subtracted from the QCD template using Monte Carlo simulation. The residual non-QCD background's contribution to the QCD template are listed in table 6.4.

The same sign sample is broken up into samples consisting of W^+ and W^- candidates. The number of events in the W^+ and W^- can be written as

$$N^+_{data} = N^+_{QCD} + N^+_{W+light}$$
$$N^-_{data} = N^-_{QCD} + N^-_{W+light}$$

where N_{data} is the number of events measured in data minus all non-QCD and non-W+light-jets backgrounds, which are taken from Monte Carlo. N_{QCD} and $N_{W+light}$ are the number of events in QCD and W+light-jets respectively. The total number of events for W+light-jets and QCD in the SS sample can thus be written as

$$N^{SS}_{W+light} = \frac{R_{W+light} + 1}{R_{W+light} - R_{QCD}} \left(N^+_{data} - R_{QCD} N^-_{data}\right) \tag{6.4}$$

$$N^{SS}_{QCD} = N^{SS}_{data} - N^{SS}_{W+light} \tag{6.5}$$

where $N^{SS}_{data} = N^+_{data} + N^-_{data}$. Lastly, one can write the number of events for QCD and W+light-jets in the SS W^+ and W^- samples as

$$N^{SS+} = \frac{N^{SS} \times R}{R+1} \tag{6.6}$$

$$N^{SS-} = \frac{N^{SS}}{R+1} \tag{6.7}$$

The ratios R_{QCD} and $R_{W+light}$ are measured using the E_T^{miss} fits from data for the W^+ and W^- samples. The difference to the results using the m_T^W fits is then taken as a systematic uncertainty on the ratios. The results of the fits for the 1- and 2-jet bins are listed in tables 6.5 and 6.6 respectively.

The E_T^{miss} fits used to determine $R = N^+/N^-$ for QCD and W+light-jets in the SS sample are shown in figure 6.8 for both the 1- and 2-jet bins, while the corresponding fits in m_T^W are shown in figure 6.9. The resulting values of $R = N^+/N^-$ and the resulting yields in the SS sample for the QCD and W+light-jets backgrounds are listed in table 6.7 .

	1-jet	2-jet
$W + b\bar{b}$	0.03%	0.9%
$W + c\bar{c}$	0.04%	0.7%
$t\bar{t}$	0.3%	2.2%
single top	0.3%	0.8%
diboson	<0.1%	<0.1%
Z+jets	0.3%	0.4%
W+light-jets	1.8%	1.9%
W+c	5.1%	3.3%
Total	8.5%	10.3%

TABLE 6.4: Fractional contribution of different processes to the QCD template

1-jet	QCD	W+light-jets
N^{SS+} fit	4479 ± 36	5052 ± 97
N^{SS-} fit	4053 ± 33	3867 ± 93
SUM	8532 ± 48	8918 ± 135
N^{SS} fit	8559 ± 69	8898 ± 134

TABLE 6.5: Yields in the 1-jet bin of the QCD and W+light-jet backgrounds in the control region for the SS sample. The W^+ and W^- fits are performed separately and compared to the combined sample result. All numbers are rounded to the nearest integer

2-jet	QCD	W+light-jets
N^{SS+} fit	3011 ± 30	3396 ± 75
N^{SS-} fit	3217 ± 33	2421 ± 67
SUM	6228 ± 45	5818 ± 101
N^{SS} fit	6142 ± 62	5909 ± 102

TABLE 6.6: Yields in the 2-jet bin of the QCD and W+light-jet backgrounds in the control region for the SS sample. The W^+ and W^- fits are performed separately and compared to the combined sample result. All numbers are rounded to the nearest integer

	1-jet	2-jet
R_{QCD}	1.10 ± 0.07	0.94 ± 0.06
$R_{W+light}$	1.31 ± 0.05	1.40 ± 0.04
N^{SS}_{QCD}	1673 ± 2527	2916 ± 907
$N^{SS}_{W+light}$	8676 ± 2560	4900 ± 925

TABLE 6.7: Measured values of $R(+/-)$ and the resulting SS yields evaluated according to equations (6.4) and (6.5)

.

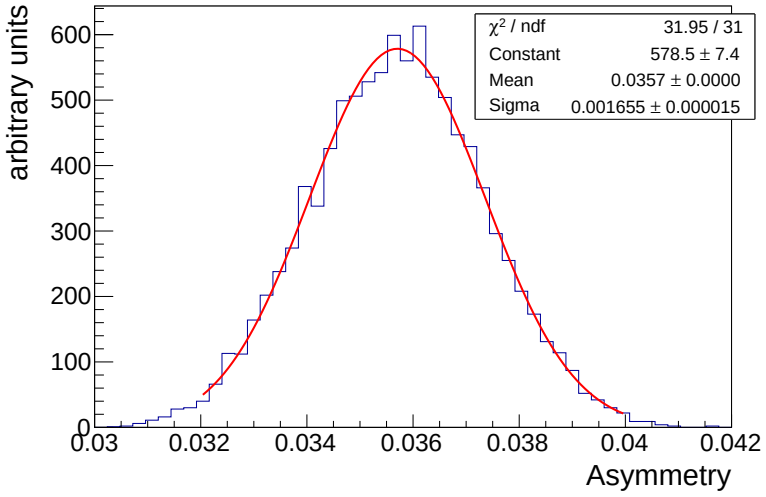

(a)

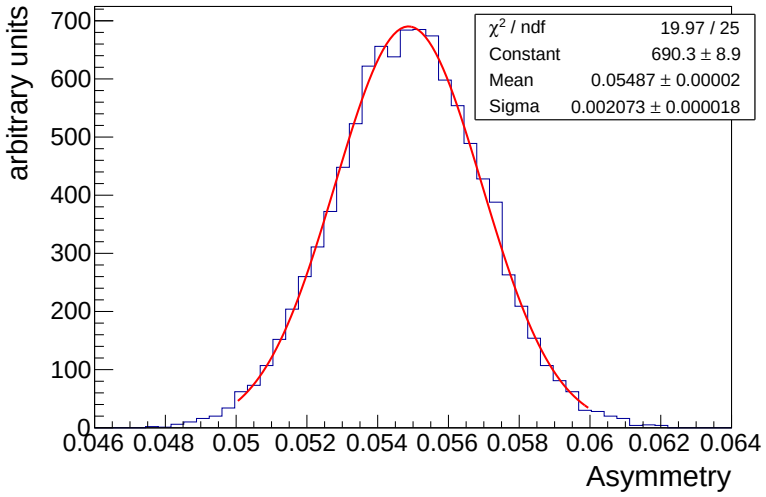

(b)

FIGURE 6.10: Fit to calculate the asymmetry for QCD in the 1- and 2-jet bins

6.5.2 Estimation of the QCD asymmetry

The asymmetry is important in extrapolating the normalization from the SS sample to the OS sample. Fits are performed in the SS and OS samples, and asymmetry is calculated using equation (6.2).

The fits do not take into account the statistical uncertainty of the templates. To account for this the templates are varied randomly bin by bin within their statistical uncertainties and the asymmetry for QCD is recomputed. This is carried for 10000 toy experiments. The asymmetry and its uncertainty are determined from a Gaussian fit to the resulting asymmetry distributions, as seen in figure 6.10(b).

The nominal result is taken from the fit range of 10 - 90 GeV. Additional variations are performed as to not underestimate the systematic uncertainty on the asymmetry. One variation is that of different fit ranges. Another variation is performed where each non-QCD Monte Carlo template is varied up and down

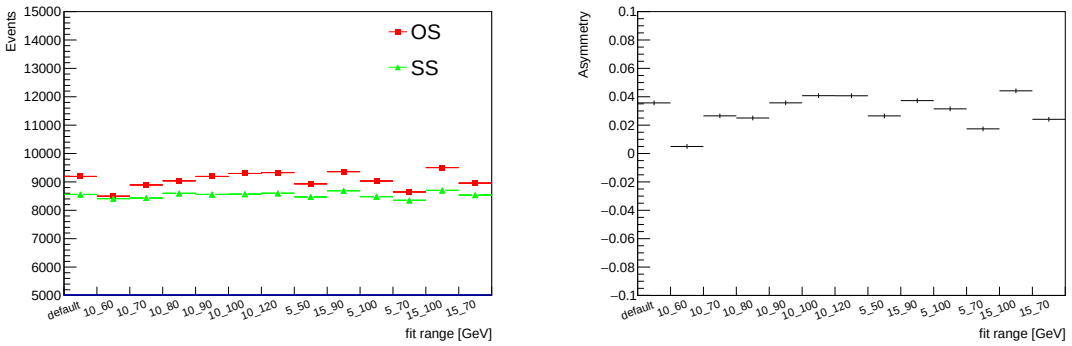

(a) (b)

FIGURE 6.11: The 1-jet QCD E_T^{miss} (a) yields and (b) the resulting asymmetry calculated using the OS and SS samples for different fit ranges.

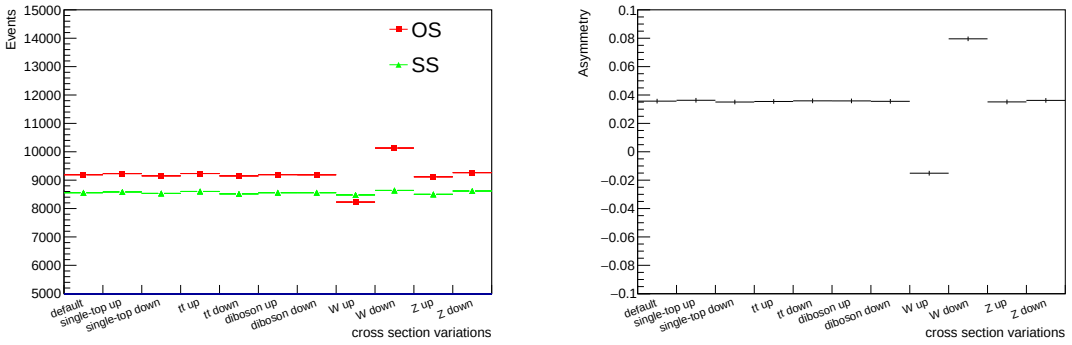

(a) (b)

FIGURE 6.12: The 1-jet QCD E_T^{miss} (a) yields and (b) the resulting asymmetry calculated using the OS and SS samples by varying the background cross sections up and down by 15%.

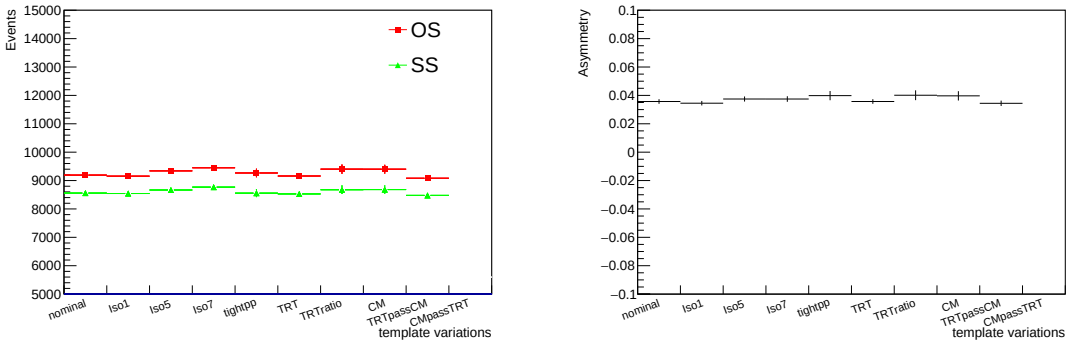

(a) (b)

FIGURE 6.13: The 1-jet QCD E_T^{miss} (a) yields and (b) the resulting asymmetry calculated using the OS and SS samples for different QCD template definitions.

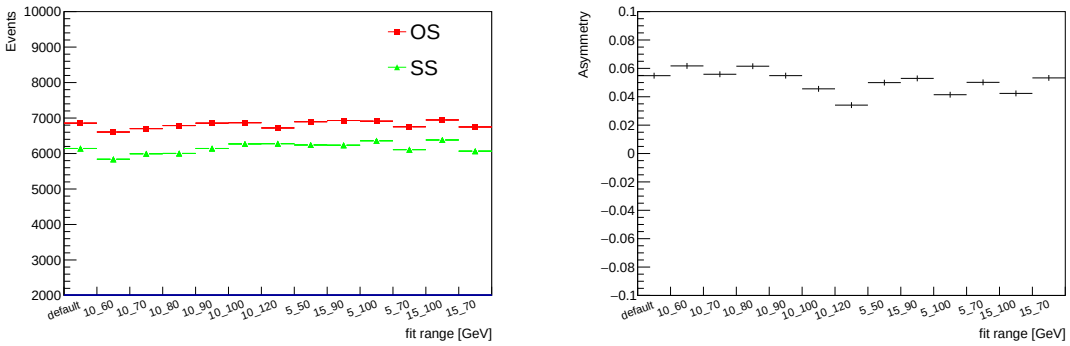

(a) (b)

FIGURE 6.14: The 2-jet QCD E_T^{miss} (a) yields and (b) the resulting asymmetry calculated using the OS and SS samples for different fit ranges.

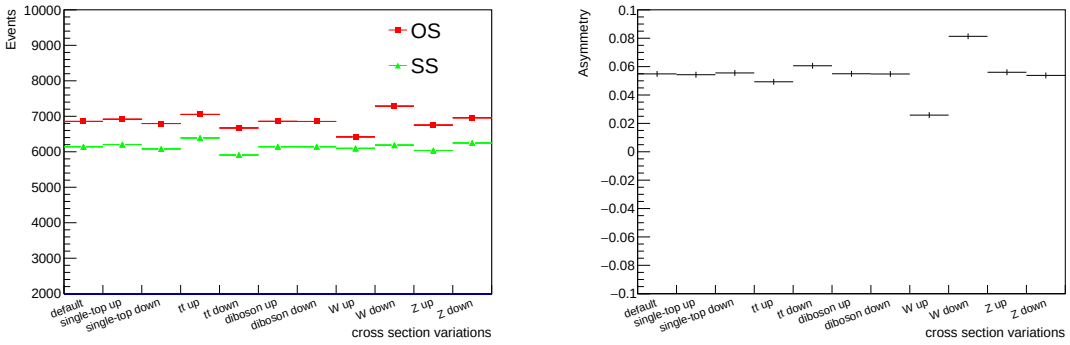

(a) (b)

FIGURE 6.15: The 2-jet QCD E_T^{miss} (a) yields and (b) the resulting asymmetry calculated using the OS and SS samples by varying the background cross sections up and down by 15%.

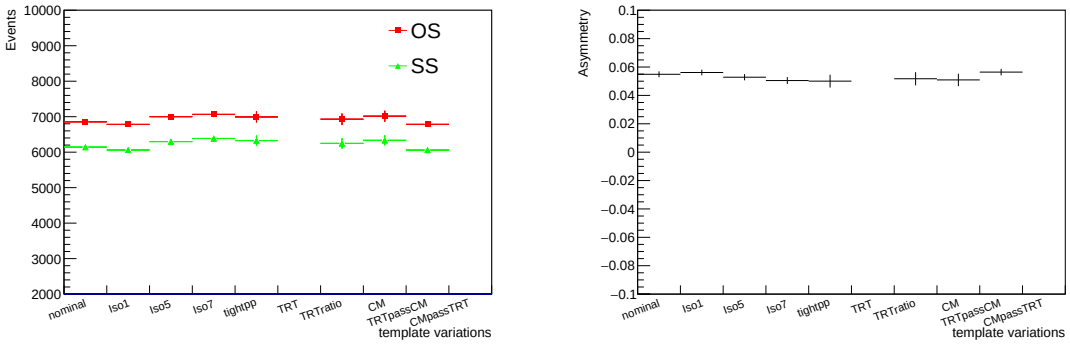

(a) (b)

FIGURE 6.16: The 2-jet QCD E_T^{miss} (a) yields and (b) the resulting asymmetry calculated using the OS and SS samples for different QCD template definitions.

	Identification	Isolation Cut
Default	failed ConverstionMatch or TrackTRThits	3 GeV
Iso1	failed ConverstionMatch or TrackTRThits	1 GeV
Iso5	failed ConverstionMatch or TrackTRThits	5 GeV
Iso7	failed ConverstionMatch or TrackTRThits	7 GeV
Tight++	pass ConverstionMatch and TrackTRThits	3 GeV
TRT	failed TrackTRThits	3 GeV
CM	failed ConverstionMatch	3 GeV
TRTpassCM	pass ConverstionMatch and failed TrackTRThits	3 GeV
CMpassTRT	failed ConverstionMatch and passed TrackTRThits	3 GeV

TABLE 6.8: Different template definitions used for the template variation of the QCD background

	1-jet	2-jet
A_{QCD}	0.036 ± 0.060	0.055 ± 0.035

TABLE 6.9: The QCD asymmetry in the 1- and 2-jet bins

by 15%, leading to a different QCD and data template shapes. This takes into account inaccurate cross sections of the backgrounds. Additionally, the extraction of the QCD template is considered as another systematic uncertainty: inverting some of the electron identification and isolation cuts might lead to a bias in the E_T^{miss} shape. Due to neutrinos produced in semileptonic decays of heavy flavor particles, non-isolated electrons from these decays will on average have a larger E_T^{miss} compared to the sample of conversion and fake electrons in our template. The different template definitions used in the variation are listed in table 6.8. The yields in the 1-jet bin of the different variations are shown in figures 6.11(a), 6.12(a) and 6.13(a) and the corresponding asymmetries in figures 6.11(b), 6.12(b) and 6.13(b). The yields in the 2-jet bin of the different variations are shown in figures figures 6.11(a), 6.12(a) and 6.13(a) and the corresponding asymmetries in figures 6.11(b), 6.12(b) and 6.13(b)

The final asymmetry is taken as the nominal value and the uncertainty is taken to cover the largest difference for each variation and then added in quadrature to get the final uncertainty. The uncertainty extracted from the QCD template variation excludes the result of the CMpassTRT variation in the 1-jet bin due to a poor fit result. The final results for the QCD asymmetry are listed in table 6.9.

6.5.3 Estimation of the W+light-jets asymmetry

W+light events can pass the selection by mis-tagging a light-jet as a c-jet. The muons reconstructed inside a light-jet are either fake or decay in flight muons which can mimic a muon decay signature. Tracks are taken as candidates to be reconstructed as muons. Therefore sample containing tracks inside jets, instead of muons inside jets, with a $\Delta R < 0.5$, is taken as the *pre-tagged* sample which is dominated by W+light-jet events.

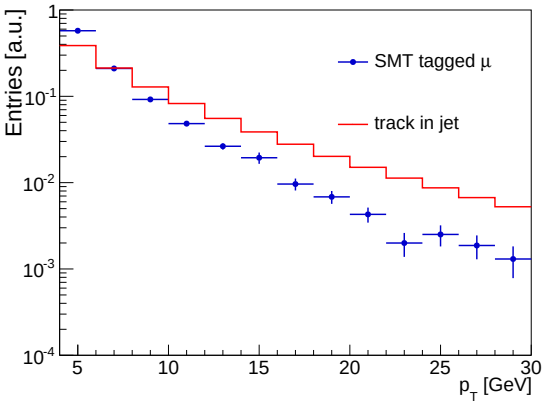

(a)

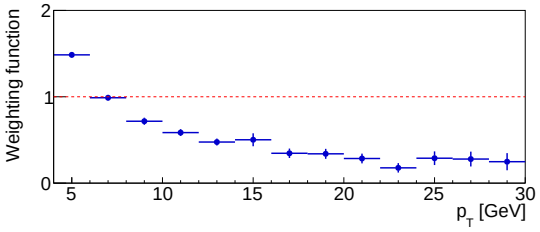

(b)

FIGURE 6.17: 1-jet spectrum of (a.) p_T^{μ} and p_T^{track} normalized to unity and (b.) the scaling function applied to the p_T^{track} distribution

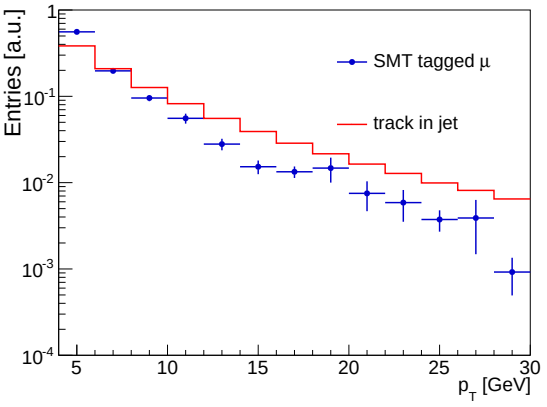

(a)

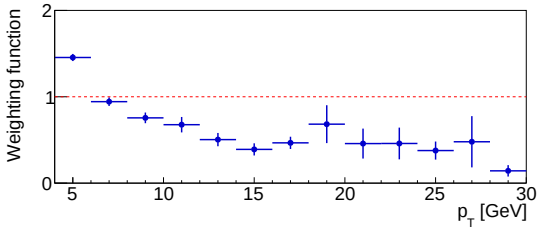

(b)

FIGURE 6.18: 2-jet spectrum of (a.) p_T^{μ} and p_T^{track} normalized to unity and (b.) the scaling function applied to the p_T^{track} distribution

The p_T spectrum for tracks should be harder than that of tagged muons due to high p_T kaons and pions decaying into muons outside the muon chamber, while the low p_T kaons and pions will generally decay to a muon before the muon chamber. This also leads to different asymmetries between tracks and muons in different p_T regions. To account for this the track p_T is reweighted to the muon p_T and the track asymmetry recalculated. The measurement of the W+light-jets asymmetry is described in detail in what follows.

The re-weighting function of track p_T to muon p_T is extracted using the Monte Carlo prediction. The weights for each p_T bin are calculated from the OS+SS sample and are then applied to the OS and SS samples separately. The asymmetry for tracks is then recomputed.

The W+light-jet asymmetry can be estimated from data using the assumption that any track inside a jet that passes the same kinematic, impact parameter and inner detector cuts has an equal probability to fake a muon. A correction factor to the asymmetry between muons and tracks using Monte Carlo is applied to correct for residual differences between tracks and reconstructed muons. The asymmetries for tracks measured in the data pre-tag sample is corrected using Monte Carlo to get the final W+light-jet asymmetry using the following:

	1-jet	2-jet
muon asymmetry (MC)	0.1065 ± 0.0114	0.0734 ± 0.0131
track asymmetry before reweighting (MC)	0.1164 ± 0.0004	0.0658 ± 0.0004
track asymmetry after reweighting (MC)	0.0861 ± 0.0003	0.0477 ± 0.0004
correction factor (MC)	1.24 ± 0.13	1.54 ± 0.27
measured track asymmetry before reweighting	0.0967 ± 0.0007	0.0500 ± 0.0007
measured track asymmetry after reweighting	0.0719 ± 0.0007	0.0337 ± 0.0007
corrected data asymmetry	0.0892 ± 0.0094	0.0516 ± 0.0091

TABLE 6.10: Values of the asymmetries for muons, tracks before and after p_T re-weighting, the correction factor and the measured asymmetry

	1-jet	2-jet
Data statistics	0.37%	0.94%
Monte Carlo p_T re-weighting	10.48%	17.53%
W+c background	0.12%	0.30%
QCD background	0.08%	0.26%
Other backgrounds	0.09%	0.34%
Total	10.54%	17.64%

TABLE 6.11: Breakdown of contributions to the W+light-jet asymmetry

$$A^{corrected}_{W+light} = \frac{A^{MC}_{W+light(muons)}}{A^{MC}_{W+light(tracks)}} \times A^{data}_{W+light(tracks)} \tag{6.8}$$

where $A^{data}_{W+light(tracks)}$ is calculated from the data sample minus the Monte Carlo prediction for all non-W+light-jet processes. The p_T spectrum for tracks and muons together with the re-weighting function are shown in figures 6.17(a) and 6.17(b) for the 1-jet bin and in figures 6.18(a) and 6.18(b) for the 2-jet bin.

The uncertainty on the asymmetry is split into two parts: the uncertainty on the data pre-tag sample asymmetry due to background determination and the uncertainty on the correction factor due to Monte Carlo statistics. These uncertainties are determined as follows:

- The **uncertainty on the background determination** is split into the uncertainty from the QCD background determination and the contribution from all other backgrounds including the W+c signal. The QCD background and uncertainty in the pre-tag sample is computed in the same way as described in the previous sections.

- The **uncertainty on the correction factor** coming stemming largely from Monte Carlo statistics in the W+light-jets sample with an SMT muon.

The track and muon asymmetries before and after re-weighting as well as the correction factor are listed in table 6.10. A breakdown of the uncertainty on the asymmetry is listed in table 6.11. The uncertainty is listed as the fractional error to the overall asymmetry.

	OS	SS	OS-SS
QCD	1798 ± 2724	1673 ± 2527	125 ± 287
W+light	10376 ± 3069	8676 ± 2560	1700 ± 540

TABLE 6.12: Yields of the QCD and W+light-jet backgrounds in the signal region for the 1-jet bin

	OS	SS	OS-SS
QCD	3255 ± 1038	2916 ± 907	339 ± 252
W+light	5433 ± 1031	4900 ± 925	533 ± 142

TABLE 6.13: Yields of the QCD and W+light-jet backgrounds in the signal region for the 2-jet bin

6.5.4 QCD and W+light-jet yields in the OS-SS sample

The number of QCD and W+light-jet events in the OS and OS-SS samples can be computed from the SS sample and the asymmetry by

$$N^{OS} = \frac{(1+A) \times N^{SS}}{1-A} \tag{6.9}$$

$$N^{OS-SS} = \frac{2 \times A \times N^{SS}}{1-A} \tag{6.10}$$

The final yields in the signal region for the QCD and W+light-jet backgrounds in the 1- and 2-jet bins are listed in tables 6.12 and 6.13 respectively.

6.5.5 Other backgrounds

All other backgrounds are taken from their Monte Carlo prediction and represent a relatively small contribution to the total background yield in the OS-SS sample. The largest background besides QCD and W+light-jets is $t\bar{t}$, whose contribution in the 1-jet bin in minimal and in the 2-jet, while it quickly dominates at high jet multiplicities.

Chapter 7

Results of the $W + c$ production cross-section

7.1 Extraction of the $W + c$harm final yields

The final yield of background events are listed in table 7.1 and 7.2 for the 1- and 2-jet bins respectively and on table 7.3 for the combined 1+2-jet bin. The QCD and

1-jet	N^{OS}	N^{SS}	N^{OS-SS}
$W + b\bar{b}$	946 ± 29	1014 ± 30	-67 ± 42
$W + c\bar{c}$	863 ± 27	836 ± 27	27 ± 38
$t\bar{t}$	651 ± 11	583 ± 10	68 ± 15
single top	1171 ± 31	743 ± 25	428 ± 40
diboson	73 ± 1	24 ± 1	50 ± 2
Z+jets	246 ± 18	185 ± 14	62 ± 23
W+light-jets (measured)	10376 ± 3069	8676 ± 2560	1700 ± 540
QCD (measured)	1798 ± 2724	1673 ± 2527	125 ± 287
Total	16317 ± 1608	13711 ± 1352	2392 ± 578

TABLE 7.1: List of background yields in the OS, SS, and OS-SS sample in the 1-jet bin

2-jet	N^{OS}	N^{SS}	N^{OS-SS}
$W + b\bar{b}$	1353 ± 33	1391 ± 34	-38 ± 48
$W + c\bar{c}$	1266 ± 32	1217 ± 31	48 ± 45
$t\bar{t}$	3925 ± 26	3351 ± 24	573 ± 36
single top	1803 ± 38	1260 ± 32	543 ± 50
diboson	39 ± 1	17 ± 1	22 ± 1
Z+jets	349 ± 19	284 ± 16	66 ± 25
W+light-jets (measured)	5433 ± 1031	4900 ± 925	533 ± 142
QCD (measured)	3255 ± 1038	2916 ± 907	339 ± 252
Total	17423 ± 945	15335 ± 853	2086 ± 286

TABLE 7.2: List of background yields in the OS, SS, and OS-SS sample as well as the asymmetry in the 2-jet bin

(1+2)-jet	N^{OS}	N^{SS}	N^{OS-SS}
$W + b\bar{b}$	2299 ± 44	2405 ± 45	-105 ± 64
$W + c\bar{c}$	2129 ± 42	2053 ± 41	75 ± 59
$t\bar{t}$	4576 ± 28	3934 ± 26	641 ± 39
single top	2974 ± 49	2003 ± 41	971 ± 64
diboson	112 ± 1	41 ± 1	72 ± 2
Z+jets	595 ± 26	469 ± 21	128 ± 34
W+light-jets (measured)	15809 ± 2915	13576 ± 2722	2233 ± 558
QCD (measured)	5053 ± 2915	4589 ± 2685	464 ± 382
Total	33740 ± 1865	29046 ± 1599	4478 ± 645

TABLE 7.3: List of background yields in the OS, SS, and OS-SS sample as well as the asymmetry in the (1+2)-jet bin

1-jet	N^{OS}	N^{SS}	N^{OS-SS}
data	38570±196	14592±121	23978±231
estimated background	16317±1608	13711±1352	2392±578
W+c (measured)	22748±196(stat)±1608(syst)	881±121(stat)±1352(syst)	21586±231(stat)±578(syst)
fractional error	0.86%(stat) + 7.07%(syst)	13.71%(stat) + 153.45%(syst)	1.07%(stat) + 2.66%(syst)

TABLE 7.4: Final measured $W + c$ yields in the 1-jet bin

2-jet	N^{OS}	N^{SS}	N^{OS-SS}
data	25652±160	15732±125	9920±203
estimated background	17152±945	15335±853	2086±286
W+c (measured)	8229±160(stat)±945(syst)	397±125(stat)±853(syst)	7834±203(stat)±286(syst)
fractional error	2.05%(stat) + 11.12%(syst)	31.49%(stat) + 214.86%(syst)	2.59%(stat) + 3.65%(syst)

TABLE 7.5: Final measured $W + c$ yields in the 2-jet bin

(1+2)-jet	N^{OS}	N^{SS}	N^{OS-SS}
data	64222±253	30324±174	33898±308
estimated background	33740±1865	29046±1599	4479±645
W+c (measured)	30482±253(stat)±1865(syst)	1278±174(stat)±1599(syst)	29419±308(stat)±645(syst)
fractional uncertainty	0.83%(stat) + 6.11%(syst)	1.36%(stat) + 125.00%(syst)	1.05%(stat) + 2.19%(syst)

TABLE 7.6: Final measured $W + c$ yields in the (1+2)-jet bin

Source	1-jet	2-jet
QCD & W+light-jets normalization	2.35%	1.96%
QCD asymmetry	0.93%	2.60%
W+light-jets asymmetry	0.75%	1.14%
Monte Carlo statistics	0.35%	1.19%
Total	2.66%	3.65%

TABLE 7.7: Breakdown the systematic uncertainty to the 1- and 2-jet yields. The dominant contributions come from the normalization of QCD and W+light-jets and the QCD asymmetry

W+light-jets backgrounds are extracted from the data as described in section 6.5. Other backgrounds are estimated from their Monte Carlo prediction. The total data and background contributions and the final measured and expected $W + c$ yields are listed in tables 7.4 to 7.6 for the 1-jet, 2-jet and 1-jet inclusive bins respectively. The final uncertainties take into account the correlations between OS and SS samples and also the correlation between the QCD and W+light-jet backgrounds extracted from equations (6.4) and (6.5). The statistical uncertainties from the various backgrounds are included in the final systematic uncertainty.

A breakdown of the systematic uncertainties on the 1- and 2-jet yields is listed in table 7.7. The dominant contributions come from the QCD and W+light-jets normalization and the QCD asymmetry determination. These are followed by the W+light-jets asymmetry determination and Monte Carlo statistics.

Several kinematic distributions are checked to compare the agreement between data and expectation in the OS-SS sample. These distributions are constructed with all non-QCD/W+light-jet set to their Monte Carlo predictions, while the QCD and W+light-jets backgrounds are estimated using the data-driven method mentioned in section 6.5. The $W + c$ signal in each figure is scaled by the ratio of the measured signal yield to the Monte Carlo prediction. Different electron kinematics variables are shown in figures 7.1(a) to 7.3(b). Charm-jet kinematics are shown in figures 7.4(a) to 7.6(b) and the associated muon kinematics can be seen on figures 7.7(a) to 7.9(b). The ΔR between SMT-tagged muons and jets is shown in figures 7.10(a) and 7.10(b) and the ratio SMT-tagged muon p_T to the charm-jet p_T is shown in figures 7.11(a) and 7.11(b). The corresponding OS and SS distributions can be found in appendix B

7.2 Yields for the W^+ and W^- production

The extraction of yields split between W^+ and W^- production mirrors the procedure used for the total cross-section measurement. The measured ratio of the signal in the OS-SS sample is given by

$$R^{OS-SS} = \frac{N^{OS-SS}_{data^+} - N^{OS-SS}_{bkg^+}}{N^{OS-SS}_{data^-} - N^{OS-SS}_{bkg^-}} \tag{7.1}$$

The normalization in the SS sample for the QCD and W+light-jets backgrounds is determined from equations (6.4) and (6.5), while all other backgrounds are estimated using their Monte Carlo prediction. Yields for the QCD and $W + light - jet$ backgrounds in the OS-SS sample are determined from the normalization in the SS sample and the asymmetries, calculated separately for W^+ and W^-, as detailed in section 6.5. The number of events in the W^+ and W^- samples for QCD and W+light-jets can be found in tables tables 7.8 and 7.9 for the 1- and 2-jet bins respectively.

While the analysis can be performed separately for the W^+ and W^- samples, a different approach is used which reduces the uncertainties and simplifies the correlation between the two samples. The ratio is $R(W^+/W^-)$ is computed separately for each background and combined with the total yields to get the yields in the W^+ and W^- samples.

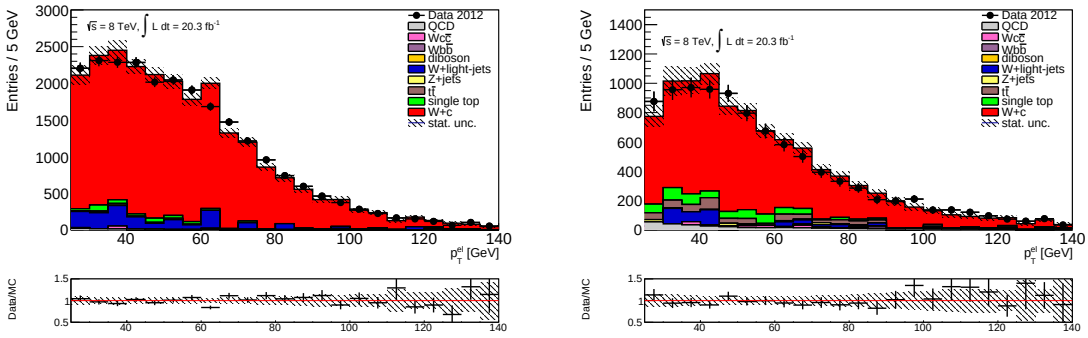

(a) (b)

FIGURE 7.1: Electron p_T for the 1-jet (left) and 2-jet (right) bins in the OS-SS sample.

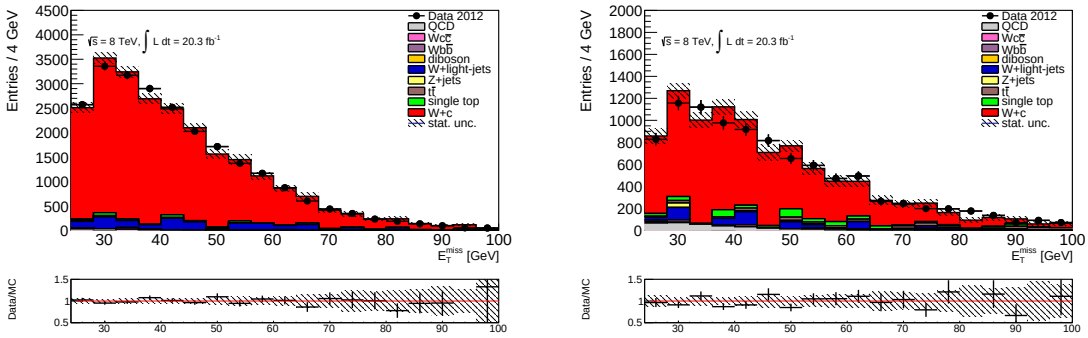

(a) (b)

FIGURE 7.2: The reconstructed E_T^{miss} for the 1-jet (left) and 2-jet (right) bins in the OS-SS sample.

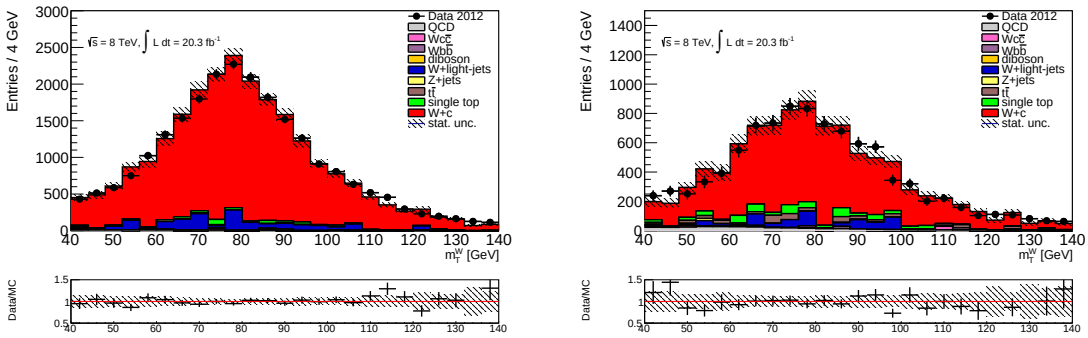

(a) (b)

FIGURE 7.3: The reconstructed W boson transverse mass for the 1-jet (left) and 2-jet (right) bins in the OS-SS sample.

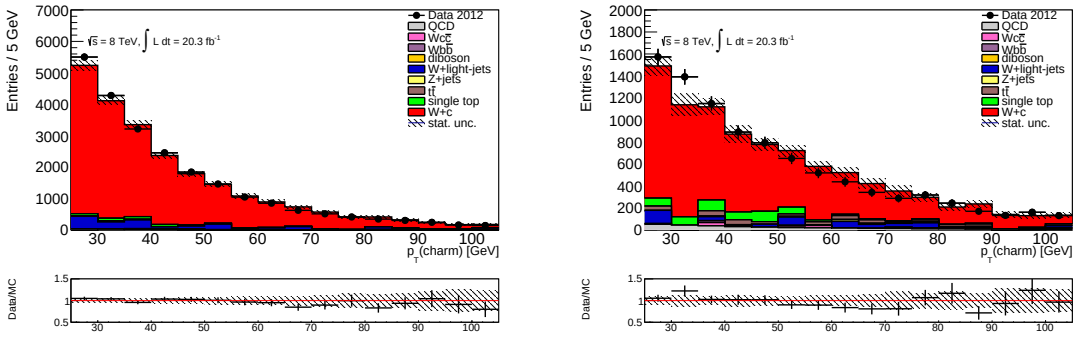

(a) (b)

FIGURE 7.4: Charm-jet $p_T$for the 1-jet (left) and 2-jet (right) bins in the OS-SS sample.

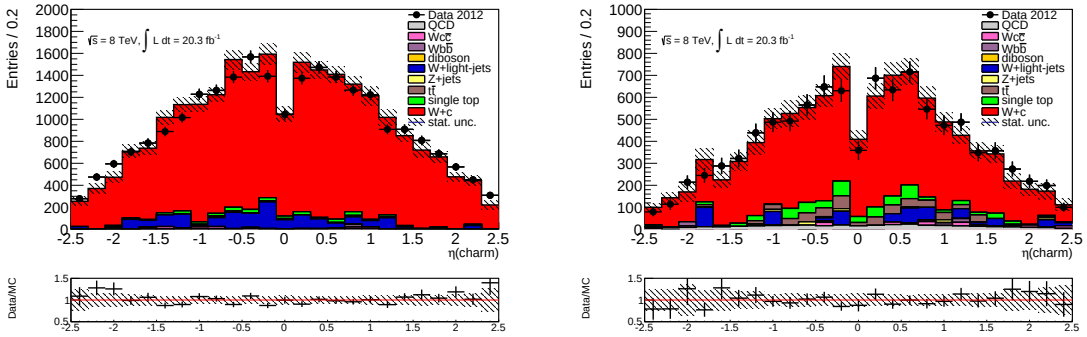

(a) (b)

FIGURE 7.5: Charm-jet η for the 1-jet (left) and 2-jet (right) bins in the OS-SS sample.

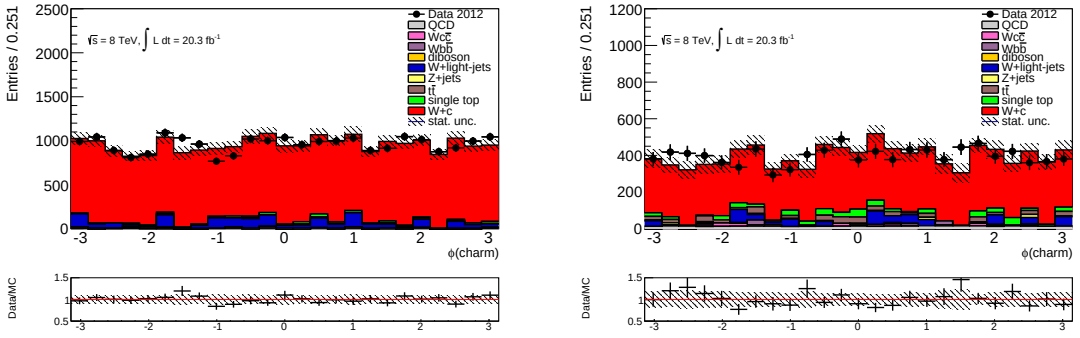

(a) (b)

FIGURE 7.6: Charm-jet ϕ for the 1-jet (left) and 2-jet (right) bins in the OS-SS sample.

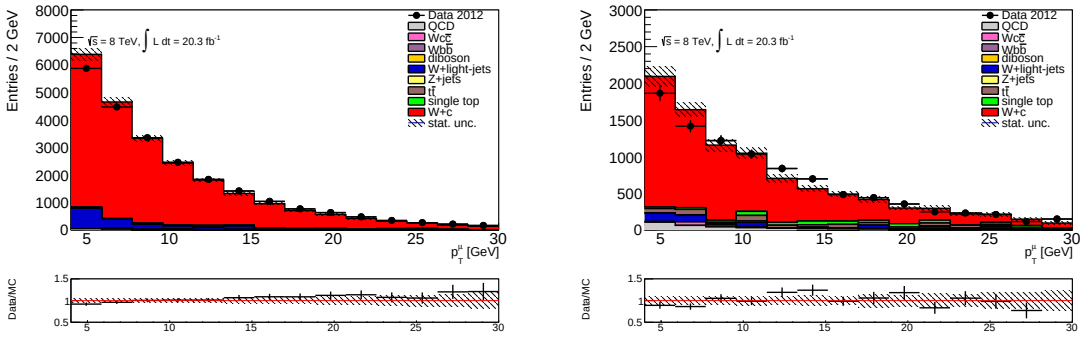

(a) (b)

FIGURE 7.7: Muon p_T for the 1-jet (left) and 2-jet (right) bins in the OS-SS sample.

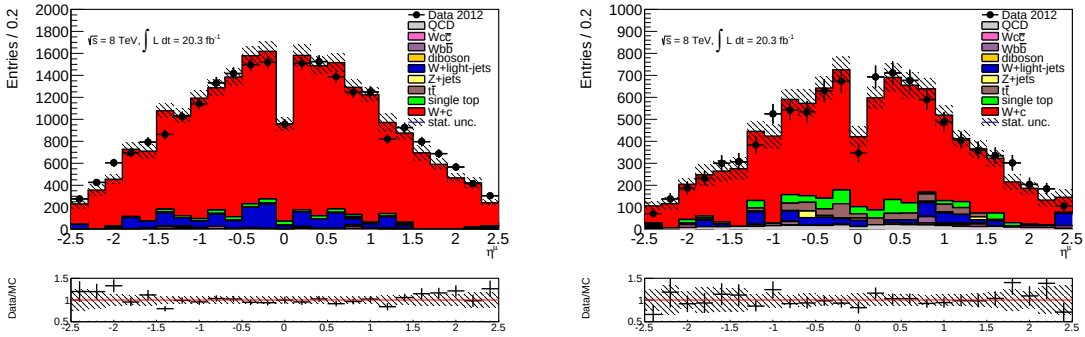

(a) (b)

FIGURE 7.8: Muon η for the 1-jet (left) and 2-jet (right) bins in the OS-SS sample.

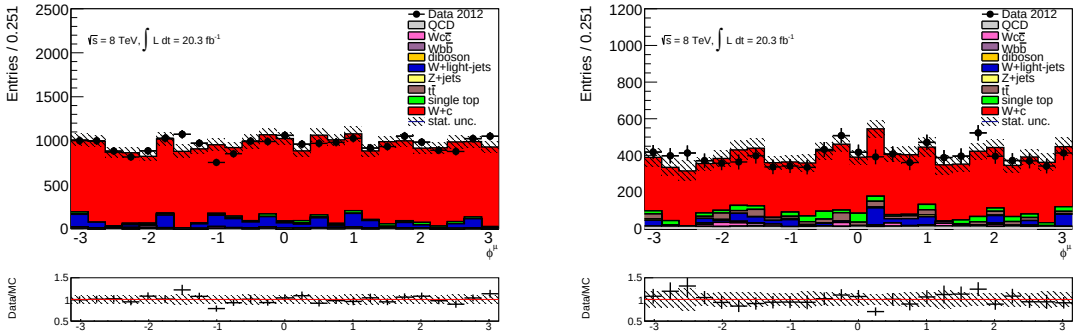

(a) (b)

FIGURE 7.9: Muon ϕ for the 1-jet (left) and 2-jet (right) bins in the OS-SS sample.

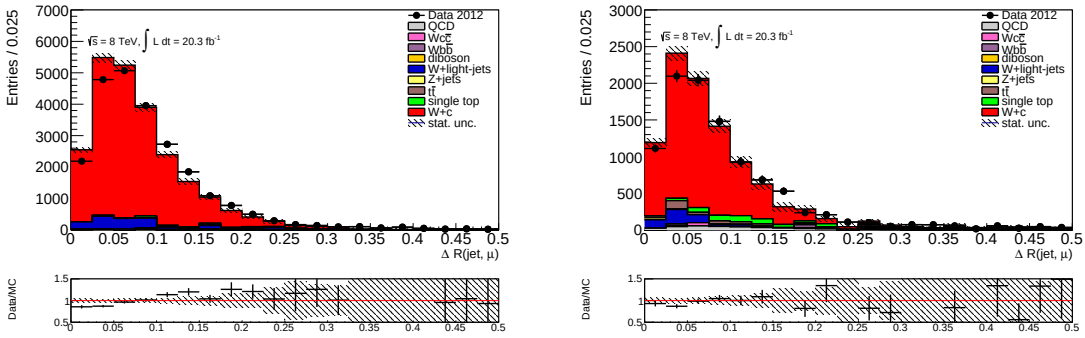

(a) (b)

FIGURE 7.10: $\Delta R(jet, \mu)$ for the 1-jet (left) and 2-jet (right) bins in the OS-SS sample.

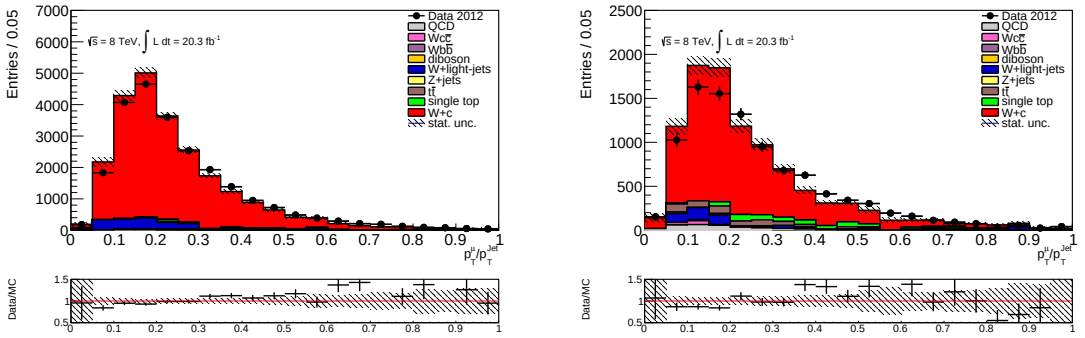

(a) (b)

FIGURE 7.11: $p_T^{\mu}/p_T^{charm-jet}$ for the 1-jet (left) and 2-jet (right) bins in the OS-SS sample.

The ratio for the two dominant backgrounds, W+light-jets and QCD, are determined as in section section 6.5. All other backgrounds are determined form their Monte Carlo predictions. The ratio for both W+light-jets and QCD are assumed to be independent of the charge of the SMT tagged muon, and thus the results taken from the E_T^{miss} fits in the SS samples are used. The values of the ratio and the resulting yields for the backgrounds in the W^+ and W^- samples is listed in tables 7.8 and 7.9 for the 1- and 2-jet bins respectively. The final W^+ and W^- yields and the ratio for the signal is listed in sections 7.2 and 7.2 and **??** for the 1-, 2- and 1+2-jet bins, respectively.

7.3 Determination of the W+c cross-section

The cross-section is measured based on the event yields in the OS-SS sample obtained in section 7.1. The production cross-section of a W boson associated with a muon inside of a jet from a charm quark is given by

$$\sigma^{fid,OS-SS}_{W+c(c\to\mu)} \times BR(W \to \ell\nu) = \frac{N^{OS-SS}_{data} - N^{OS-SS}_{bkg}}{U \cdot \int \mathcal{L}\, dt} \tag{7.2}$$

1-jet	$R(W^+/W^-)$	N_+^{OS-SS}	N_-^{OS-SS}
$W + b\bar{b}$	1.79 ± 0.08	-43 ± 27	-24 ± 15
$W + c\bar{c}$	1.70 ± 0.08	17 ± 24	10 ± 14
$t\bar{t}$	0.98 ± 0.02	34 ± 7	34 ± 8
single top	1.79 ± 0.08	274 ± 26	154 ± 15
diboson	0.89 ± 0.03	24 ± 1	26 ± 1
Z+jets	1.03 ± 0.11	31 ± 12	31 ± 11
W+light-jets (measured)	1.31 ± 0.05	964 ± 307	736 ±234
QCD (measured)	1.10 ± 0.07	65 ± 150	60 ± 137

TABLE 7.8: List of background yields in the OS-SS sample for W^+ and W^- in the 1-jet bin

2-jet	$R(W^+/W^-)$	N_+^{OS-SS}	N_-^{OS-SS}
$W + b\bar{b}$	1.78 ± 0.06	-24 ± 31	-14 ± 17
$W + c\bar{c}$	1.61 ± 0.06	30 ± 28	18 ± 17
$t\bar{t}$	0.99 ± 0.01	285 ± 18	288 ± 18
single top	1.90 ± 0.07	356 ± 33	187 ± 18
diboson	0.93 ± 0.04	11 ± 1	11 ± 1
Z+jets	1.01 ± 0.08	33 ± 13	33 ± 12
W+light-jets (measured)	1.40 ± 0.04	311 ± 83	222 ± 59
QCD (measured)	0.94 ± 0.06	164 ± 122	175 ± 130

TABLE 7.9: List of background yields in the OS-SS sample for W^+ and W^- in the 2-jet bin

(1+2)-jet	$R(W^+/W^-)$	N_+^{OS-SS}	N_-^{OS-SS}
$W + b\bar{b}$	1.79 ± 0.05	-67 ± 41	-38 ± 23
$W + c\bar{c}$	1.64 ± 0.05	47 ± 37	28 ± 22
$t\bar{t}$	0.99 ± 0.01	318 ± 19	323 ± 20
single top	1.85 ± 0.05	630 ± 42	341 ± 23
diboson	0.90 ± 0.02	34 ± 1	38 ± 1
Z+jets	1.02 ± 0.06	65 ± 17	63 ± 17
W+light-jets (measured)	1.34 ± 0.03	1275 ± 317	958 ± 241
QCD (measured)	1.03 ± 0.01	230 ± 194	234 ± 189

TABLE 7.10: List of background yields in the OS-SS sample for W^+ and W^- in the (1+2)-jet bin

1-jet	N^+	N^-	$R(W^+/W^-)$
data	11635±108	12343±111	–
estimated background	1223±341	900±270	–
W+c (measured)	10269±108(stat)±341(syst)	11316±78(stat)±270(syst)	0.91±0.02(stat)±0.04(syst)

TABLE 7.11: Measured $W^+ + \bar{c}$ and $W^- + c$ yields and their ratio in the 1-jet bin

2-jet	N^+	N^-	$R(W^+/W^-)$
data	4631±68	5289±72	–
estimated background	1165±157	921±147	–
W+c (measured)	3466±68(stat)±157(syst)	4368±72(stat)±147(syst)	0.79±0.03(stat)±0.04(syst)

TABLE 7.12: Measured $W^+ + \bar{c}$ and $W^- + c$ yields and their ratio in the 2-jet bin

(1+2)-jet	N^+	N^-	$R(W^+/W^-)$
data	16266±128	17632±133	–
estimated background	2531±379	1948±310	–
W+c (measured)	13735±128(stat)±379(syst)	15684±133(stat)±310(syst)	0.88±0.01(stat)±0.03(syst)

TABLE 7.13: Measured $W^+ + \bar{c}$ and $W^- + c$ yields and their ratio in the (1+2)-jet bin

Lepton from $W \to \ell\nu$	
p_T^ℓ	>20 GeV
$\lvert\eta^\ell\rvert$	<2.5
Neutrino from $W \to \ell\nu$	
p_T^ν	>25 GeV
W boson	
m_T^W	>40 GeV
Jets	
p_T^{jet}	>25 GeV
$\lvert\eta^{jet}\rvert$	<2.5
Exactly 1 c-jet identified using a c-hadron with:	
$p_T^{c-hadron}$	>5 GeV
ΔR(c-hadron-jet)	<0.3
W and c-hadron charges	OS-SS
Muon inside c-jet	
p_T^μ	>4 GeV
$\lvert\eta^\mu\rvert$	<2.5 GeV
$\Delta R(\mu$-jet)	<0.5 GeV

TABLE 7.14: Fiducial phase space for the $\sigma^{fid,OS-SS}_{W+c(c\to\mu)} \times BR(W \to \ell\nu)$ measurement. One of the jets is required to be matched within ΔR <0.3 with a c-hadron with $p_T > 5$ GeV. Only weakly decaying c-hadrons with p_T >5 GeV are used; c-hadrons originating from b-hadron decays are not considered. For the $\sigma^{fid,OS-SS}_{W+c} \times BR(W \to \ell\nu)$ measurement the same fiducial space is used for the jets, for the leptons originated from the W boson decay and for the W boson except the muon inside c-jets requirement is dropped.

where N_{data}^{OS-SS} and N_{bkg}^{OS-SS} are the yield measured in data and the estimated number of background events respectively, $\int \mathcal{L}\, dt$ is the integrated luminosity and U is the acceptance factor. One can determine the production cross-section of a W boson associated with a charm quark, where the charm quark does not necessarily decay semileptonically into a muon, through

$$\sigma_{W+c}^{fid,OS-SS} \times BR(W \to \ell\nu) = \frac{\sigma_{W+c(c\to\mu)}^{fid,OS-SS} \times BR(W \to \ell\nu)}{B} \tag{7.3}$$

where B is a correction factor that takes one from events where the c-quark decays semileptonically into a muon to events without requiring a muon inside of the jet.

The acceptance factor U is determined from the Monte Carlo `ALPGEN+PYTHIA` fully simulated signal sample using

$$U = \frac{N_{MC,reco}^{W+c,OS-SS}(\text{analysis cuts})}{N_{MC,truth}^{W+c,OS-SS}(\text{fiducial cuts})} \tag{7.4}$$

where $N_{MC,reco}^{W+c,OS-SS}$(analysis cuts) is the W+c Monte Carlo expected OS-SS yield extracted in 7.1 and $N_{MC,truth}^{W+c,OS-SS}$(fiducial cuts) is the number of OS-SS events in the Monte Carlo signal sample with truth objects satisfying the kinematic cuts of the fiducial phase space defined in table 7.14. The correction factor B is defined as

$$B = \frac{N_{MC,reco}^{W+c,OS-SS}(\text{fiducial cuts})}{N_{MC,truth}^{W+c,OS-SS}(\text{fiducial cuts without the muon requirement})}. \tag{7.5}$$

The fiducial region is chosen to be as close as possible to the kinematic cuts applied at reconstruction level.

Dressed electrons [1] are used to define the fiducial cross-section. Truth jets used the same anti-k$_T$ algorithm with a $\Delta R < 0.4$ as jets on reconstruction level. The electron and neutrino from the W-boson are not used as input objects for truth jets.

On truth level, c-jets are defined to be jets containing at least one c-hadron with $\Delta R < 0.3$ to a truth jet. Only weakly decaying c-hadrons with a $p_T > 5$ GeV are considered, while c-hadrons arising from b-decays are not considered. Each event is required to have at least one c-jet. For the 1-jet bin, no additional jets are allowed, while for the 2-jet bin at least one other jet is required. Jets are required to contain a muon with $\Delta R < 0.5$ to the c-jet. Decay in-flight muons are not considered. Muons are required to have $p_T > 4$ GeV and $|\eta| < 2.5$, but are not explicitly required to have come from a c-hadron.

`Alpgen+Pythia` is used to determine the factors U and B. The fragmentation and decay of c-hadrons are not well modeled, and are reweighted before calculating the U and B factors. The fragmentation is described by two quantities:

[1] Dressed electrons are taken as born level electrons with additional energy contributions stemming from radiated photons. The energy of the photons are added is the $\Delta R < 0.2$ between the candidate electron and a photon.

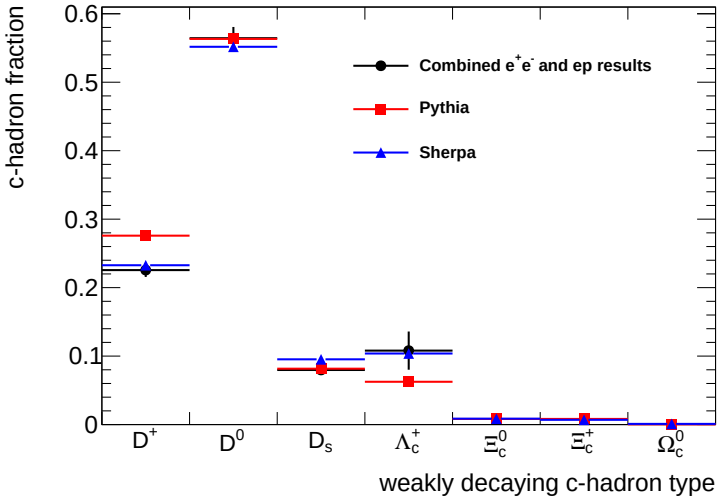

FIGURE 7.12: Relative fraction of weakly decaying c-hadron types.

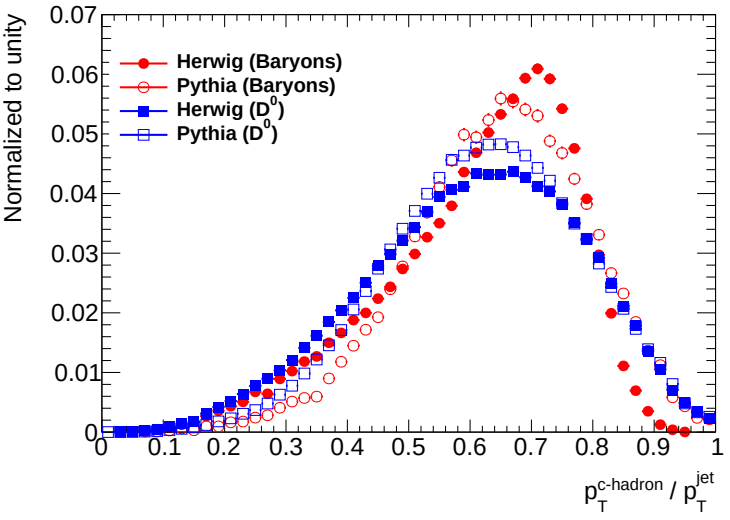

FIGURE 7.13: $p_T^{c-hadron}/p_T^{jet}$ distribution for the D^0 and the charmed Baryons considered.

- The relative fraction of weakly decaying c-hadrons. Only the most relevant weakly decaying c-hadrons are considered: D^+, D^0, D_s, Λ_C^0, Ξ_C^0, Ξ_C^+ and Ω_C^0.
- The fractional energy carried by the c-hadron, which is modeled by the fraction of c-hadron p_T with respect to the c-jet p_T.

The fractions of weakly decaying c-hadrons are reweighted to the latest e^+e^- and ep results [121]. The fractions of weakly decaying c-hadrons for `Pythia`, `Sherpa` and the e^+e^- and ep results is shown in figure 7.12.

`HERWIG` is found to provide a better description of the $p_T^{c-hadron}/p_T^{c-jet}$ shape than Pythia, therefore the shape in `Pythia` is reweighted to `Herwig++` separately for the different c-hadron types. The $p_T^{c-hadron}/p_T^{c-jet}$ shapes for different c-hadrons is shown in figure 7.13.

The decay of c-hadrons inside jets is modeled by two quantities:

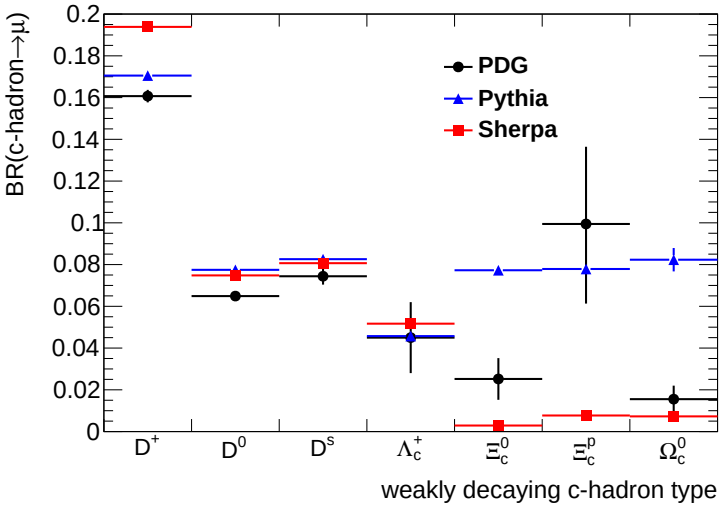

FIGURE 7.14: Branching ratio of weakly decaying c-hadron into soft-muons.

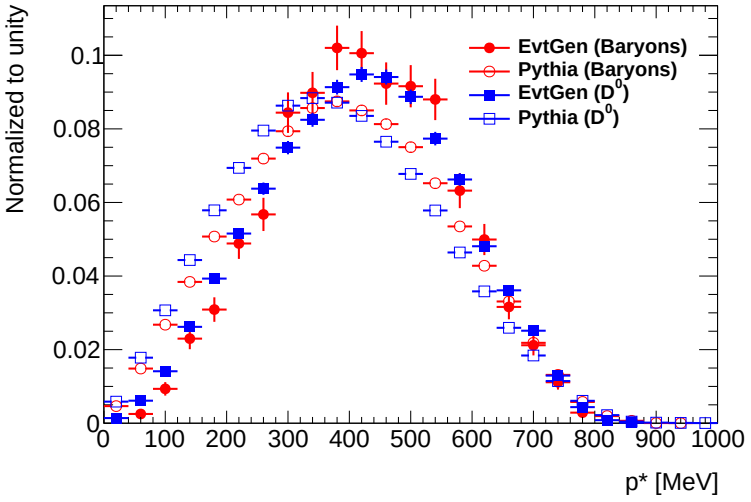

FIGURE 7.15: $p*$ distribution for the D^0 and the charmed Baryons considered.

- The branching ratio of different c-hadrons into soft-muons
- The momentum of the soft-muon in the rest frame of the c-hadron ($p*$), which provides a way to describe the muon kinematics independent of the c-hadron kinematics.

The branching ratio calculated from Pythia is reweighted to values determined from the PDG. The branching ratio into electrons for D^+ and D^0 is used instead of the branching ratio into muons because it is measured to a higher precision. For the Λ_C^0 the branching ratio into electrons is used because the measurement for muons is not available. This is justified assuming the leptons couple universally to W bosons. The branching ratio into muons, including $\tau \to \mu$ decays, is used for the D_s. No measurement is available for the Ξ_c^0, Ξ_c^+ and Ω_c^0, so the lifetime of those c-hadrons with the measurement of the Λ_C^0 is used to determine the branching ratios by,

$$BR(\Xi_c^0, \Xi_c^+, \Omega_c^0) = \frac{\tau_{\Xi_c^0, \Xi_c^+, \Omega_c^0}}{\tau_{\Lambda_C^0}} \times BR(\Lambda_C^0) \tag{7.6}$$

where τ represents the respective lifetime of the c-hadrons. The branching ratios from Pythia, Sherpa and those calculated form the PDG are shown in figure 7.14. The systematic uncertainties are estimated by re-weighting the correction factors to the up and down uncertainties of the PDG. The final uncertainty is obtained by doing this separately for each c-hadron type and adding the results in quadrature.

The $p*$ distribution from `PYTHIA` is reweighted to the distribution from `EvtGen`, which provides a better description of c-hadron decays. The $p*$ distribution for `PYTHIA` and `EvtGen` are shown in figure 7.15. The systematic uncertainty is determined by taking the difference between the correction factor before and after re-weighting.

The modelling of the number of reconstructed jets is also taken into account. The ratio of 1- to 2-jet yields in `PYTHIA` is reweighted to the measured ratio in data, the correction factors recomputed, and the difference taken as a systematic.

Residual non-perturbative effects not accounted for in the re-weighting presented above are also taken into account by comparing different generators, in this case `PYTHIA` and `SHERPA`. The c-fragmentation and decay are reweighted for `SHERPA` in the same way as is done for `PYTHIA`, and the difference between the two is taken as a systematic. This uncertainty takes into account differences in modelling of the parton shower and fragmentation of non-c-jets. Differences in fragmentation should mostly cancel in the OS-SS subtraction, so most of the difference comes from the parton shower. It should be noted that additional differences between `PYTHIA` and `SHERPA` arise due to a lower number of generated samples for `SHERPA`, which lead to a larger statistical uncertainty in these samples compared to those generated with `PYTHIA`.

Different PDF sets have a significant impact on the total normalization of the $W + c$ signal. Using different PDF sets changes the correction factors and thus the measured cross section by altering the kinematic shapes and by virtue the reconstruction and acceptance efficiencies. The uncertainties arising from such shape differences are estimated by comparing the correction factors after re-weighting to different PDF sets. The `PYTHIA` sample used to determine the nominal correction factors was produced with CTEQ6LL [122], and a comparison is made to MSTW2008nlo68cl, CT10nlo, NNPDF30_nlo and HERAPDF15NLO. Re-weighting to CT10nlo shows the largest difference to the nominal and the difference is taken as a systematic.

The final correction factors after full re-weighting are presented in table 7.15. The uncertainties shown are statistical only. The full systematic uncertainties due to modelling effect are presented in table 7.16, where the dominant source comes from modelling of the fragmentation of c-hadrons to jets.

jet multiplicity	U	B	$U \times B$
1-jet	0.3460 ± 0.0029	0.0515 ± 0.0002	0.0178 ± 0.0002
2-jet	0.4462 ± 0.0063	0.0550 ± 0.0004	0.0246 ± 0.0004
1-jet inclusive	0.3845 ± 0.0026	0.0529 ± 0.0002	0.0203 ± 0.0002

TABLE 7.15: Correction factors U, B and their product $U \times B$ for $W \to e\nu$. The uncertainties are statistical only

	1-jet		2-jet		1-jet incl.	
Source	U	$U \times B$	U	$U \times B$	U	$U \times B$
D^0 fraction	0.08%	0.18%	0.09%	0.15%	0.09%	0.17%
D^+ fraction	0.12%	0.64%	0.09%	0.25%	0.15%	0.49%
D_s fraction	0.02%	0.09%	0.02%	0.11%	0.02%	0.47%
Baryon fraction	0.01%	0.54%	0.11%	0.55%	0.07%	1.41%
Fragmentation function	1.95%	2.22%	2.51%	2.07%	2.60%	1.55%
Residual	0.44%	1.25%	0.83%	1.90%	0.61%	1.05%
D^0 decay	0.05%	0.11%	0.06%	0.10%	0.06%	0.11%
D^+ decay	0.07%	0.28%	0.09%	0.25%	0.08%	0.27%
D_s decay	0.02%	0.09%	0.02%	0.10%	0.02%	0.09%
Baryon decay	0.09%	2.40%	0.41%	2.03%	0.25%	2.23%
p^*	0.09%	0.27%	0.05%	0.39%	0.07%	0.34%
PDF	0.64%	0.94%	0.69%	0.95%	0.68%	0.94%
nJets modelling	1.69%	1.48%	0.72%	0.53%	0.73%	0.57%
Total	2.71%	4.01%	2.86%	3.71%	2.74%	3.95%

TABLE 7.16: Relative systematic uncertainties on the correction factors due to Monte Carlo modelling effects

	U^+B^+/U^-B^-
1-jet	0.9811 ± 0.0127
2-jet	1.0222 ± 0.0256
1-jet inclusive	0.9855 ± 0.0109

TABLE 7.17: Correction factor for the ratio measurement. Uncertainties are statistical only.

7.3.1 Determination of $\sigma^{fid,OS-SS}_{W^+ + \bar{c}}$, $\sigma^{fid,OS-SS}_{W^- + \bar{c}}$ and their ratio

The ratio $\sigma^{fid,OS-SS}_{W^+ + \bar{c}} / \sigma^{fid,OS-SS}_{W^- + \bar{c}}$ is measured according to

$$R^{+/-}_{fid} = \frac{R^{+/-}_{yields}}{U^+B^+/U^-B^-} \tag{7.7}$$

where $R^{+/-}_{yields}$ is the ratio of the measured $W^+ + \bar{c}$ and $W^- + c$ yields presented in section 7.2. Limited number of events lead to large statistical uncertainties on the U^+B^+/U^-B^- factors. For this reason, a sample of $W + c$, with a large number of generated events, filtered to contain only events where the charm decays

Source	1-jet	2-jet	1-jet inclusive
D^0 fraction	0.04%	0.02%	0.01%
D^+ fraction	0.03%	0.01%	0.01%
D_s fraction	0.01%	<0.01%	<0.01%
Baryon fraction	0.02%	0.04%	0.01%
Fragmentation function	0.04%	0.27%	0.22%
Residual	0.33%	0.92%	0.33%
D^0 decay	0.02%	0.01%	0.01%
D^+ decay	0.02%	0.01%	0.01%
D_s decay	0.01%	<0.01%	<0.01%
Baryon decay	0.12%	0.12%	<0.01%
p^*	0.04%	0.18%	0.19%
PDF	0.10%	0.30%	0.06%
nJets modelling	<0.01%	0.02%	0.01%
Total	0.47%	1.00%	0.49%

TABLE 7.18: Relative systematic uncertainties on U^+B^+/U^-B^- due to Monte Carlo modelling effects

semileptonically into a soft-muon is used to determine U^+/U^-. Details of this sample can be found in table A.2. The correction factor for the ratio is listed in table 7.17 and the uncertainty due to MC modelling effects in table 7.18.

7.3.2 Systematic uncertainties due to Reconstruction Effects

The combined performance groups' recommendations are used to correct all reconstructed objects to match the efficiencies and resolution measured in data. Each correction is varied within its uncertainty and the correction factors recomputed. The difference with the nominal value is taken as the systematic uncertainty. The uncertainties are then added in quadrature. In cases where the up and down variations disagree the largest one is chosen and the uncertainty symmetrized. The reconstruction uncertainty values are listed in table 7.19.

The JES is the dominant source of uncertainty in both the 1- and 2-jet bins. The JES uncertainty is composed of 18 different components which are added in quadrature to get the total JES uncertainty. The breakdown of the JES is also listed in table 7.19.

The reconstruction uncertainties for the ratio measurement are listed in table 7.20. Many components cancel in the ratio, such as the JES and JER, which do not depend on the charge of the W-boson. Due to large statistical fluctuations in the JES, JER, and MET, the uncertainties are extracted from the sample before requiring a SMT muon, where charge-dependent effects on these uncertainties are negligible.

Source	1-jet	2-jet	1-jet incl.
Electron efficiency	0.86%	0.87%	0.86%
Electron energy scale	0.19%	0.38%	0.24%
Electron resolution	0.06%	0.04%	0.05%
Soft-muon efficiency	1.17%	1.07%	1.14%
Muon energy scale	0.43%	0.63%	0.13%
Muon energy resolution	0.29%	0.32%	0.30%
SMT efficiency	0.50%	0.50%	0.50%
JER	0.56%	0.68%	0.79%
JES	2.18%	6.21%	3.16%
MET soft resolution	0.33%	0.27%	0.31%
MET soft scale	0.30%	0.34%	0.31%
Total	2.82%	6.48%	3.64%
JES breakdown			
EffectiveNP1	1.13%	3.15%	1.71%
EffectiveNP2	0.33%	0.67%	0.47%
EffectiveNP3	0.10%	0.12%	0.14%
EffectiveNP4	0.04%	0.12%	0.07%
EffectiveNP5	0.04%	0.09%	0.04%
EffectiveNP6restTerm	0.14%	0.20%	0.16%
EtaIntercalibrationModelling	0.21%	0.58%	0.31%
EtaIntercalibrationTotalStat	0.30%	0.63%	0.44%
SingleParticleHighPt	<0.01%	<0.01%	<0.01%
RelativeNonClosureMC12a	<0.01%	<0.01%	<0.01%
PileupOffsetMuTerm	0.10%	0.03%	0.07%
PileupOffsetNPVTerm	0.12%	0.44%	0.03%
PileupOffsetPtTerm	<0.01%	<0.01%	<0.01%
PileupOffsetRhoTopology	0.76%	2.29%	1.18%
FalvorComp	0.78%	2.38%	1.14%
FlavorResponse	1.25%	3.45%	1.55%
BJES	0.66%	2.08%	0.99%
PunchThrough	<0.01%	<0.01%	<0.01%
Total	2.18%	6.21%	3.16%

TABLE 7.19: Systematic uncertainties due to reconstruction effects for the $W^+ + W^-$ inclusive measurement

Source	1-jet	2-jet	1-jet incl.
Electron efficiency	0.02%	0.03%	0.02%
Electron energy scale	0.35%	0.31%	0.27%
Electron resolution	0.29%	0.37%	0.21%
Soft-muon efficiency	0.02%	0.03%	0.01%
Muon energy scale	0.01%	0.01%	<0.01%
Muon energy resolution	<0.01%	<0.01%	<0.01%
SMT efficiency	0.01%	<0.01%	<0.01%
JER	0.09%	0.17%	0.07%
JES	0.19%	0.91%	0.17%
MET soft resolution	0.26%	0.28%	0.28%
MET soft scale	0.25%	0.36%	0.76%
Total	0.62%	1.14%	0.90%
JES breakdown			
EffectiveNP1	0.13%	0.17%	0.06%
EffectiveNP2	0.03%	0.10%	0.03%
EffectiveNP3	0.01%	0.02%	<0.01%
EffectiveNP4	0.01%	0.02%	0.01%
EffectiveNP5	0.01%	0.02%	0.02%
EffectiveNP6restTerm	0.02%	0.02%	0.01%
EtaIntercalibrationModelling	0.01%	0.57%	0.03%
EtaIntercalibrationTotalStat	0.01%	0.28%	0.05%
SingleParticleHighPt	<0.01%	<0.01%	<0.01%
RelativeNonClosureMC12a	<0.01%	<0.01%	<0.01%
PileupOffsetMuTerm	0.02%	0.08%	0.05%
PileupOffsetNPVTerm	0.06%	0.25%	0.05%
PileupOffsetPtTerm	<0.01%	<0.01%	<0.01%
PileupOffsetRhoTopology	0.01%	0.12%	0.04%
FalvorComp	0.12%	0.21%	0.03%
FlavorResponse	0.01%	0.43%	0.09%
BJES	0.01%	0.25%	0.06%
PunchThrough	<0.01%	<0.01%	<0.01%
Total	0.19%	0.91%	0.17%

TABLE 7.20: Systematic uncertainties due to reconstruction effects for the W^+/W^- ratio measurement

$\sigma^{fid,OS-SS}_{Wc(c\to\mu)}\times\mathrm{BR}(W\to\ell\nu)$	
1-jet	3.07 ± 0.03(stat) ± 0.17(syst) [pb]
2-jet	0.86 ± 0.02(stat) ± 0.07(syst) [pb]
1-jet inclusive	4.11 ± 0.04(stat) ± 0.22(syst) [pb]
$\sigma^{fid,OS-SS}_{Wc}\times\mathrm{BR}(W\to\ell\nu)$	
1-jet	59.68 ± 0.64(stat) ± 3.79(syst) [pb]
2-jet	15.74 ± 0.41(stat) ± 1.40(syst) [pb]
1-jet inclusive	77.72 ± 0.74(stat) ± 4.68(syst) [pb]
$\sigma^{fid,OS-SS}_{W^+\bar{c}}/\sigma^{fid,OS-SS}_{W^-c}$	
1-jet	0.92 ± 0.02(stat)± 0.04(syst)
2-jet	0.78 ± 0.03(stat) ± 0.05(syst)
1-jet inclusive	0.89 ± 0.01(stat) ± 0.03(syst)

TABLE 7.21: Measured $W + c$ cross-section and their ratios for the 1-, 2- and 1-jet inclusive bins.

$\sigma^{fid,OS-SS}_{Wc}\times\mathrm{BR}(W\to\ell\nu)$			
source	1-jet	2-jet	1-jet incl.
data statistics	1.07%	2.59%	0.96%
Background yield	2.66%	3.65%	2.01%
Detector systematics	2.82%	6.48%	3.64%
MC statistics	0.84%	1.41%	0.68%
MC modelling	2.71%	2.86%	2.74%
Total systematics	4.80%	8.09%	4.44%
Luminosity	2.8%	2.8%	2.8%

TABLE 7.22: Breakdown of the uncertainty on the $\sigma^{fid,OS-SS}_{Wc(c\to\mu)}\times\mathrm{BR}(W\to\ell\nu)$ measurement.

7.4 Cross-section results

The measured fiducial W+c cross sections and their ratios are summarized in table 7.21. The measurements are performed independently for the 1-, 2- and 1-jet inclusive samples. The systematic errors include uncertainty on the background yields, correction factors, reconstruction effects and the luminosity. The breakdown of the uncertainty for $\sigma^{fid,OS-SS}_{Wc}\times\mathrm{BR}(W\to\ell\nu)$ is listed in table 7.23, where the largest source of systematic error arises from Monte Carlo modelling effects. A breakdown of the uncertainty for $\sigma^{fid,OS-SS}_{Wc}\times\mathrm{BR}(W\to\ell\nu)$ in table 7.24, where the dominant source of uncertainty comes from background estimation which does not cancel in the ratio measurement. The 1-jet inclusive measurement uses the (1+2)-jet yields and ratio and multiplying it by the ratio of 1-jet inclusive results to (1+2)-jet results using Monte Carlo.

$\sigma_{Wc}^{fid,OS-SS} \times \mathrm{BR}(W \to \ell\nu)$			
source	1-jet	2-jet	1-jet incl.
data statistics	1.07%	2.59%	0.96%
Background yield	2.66%	3.65%	2.01%
Detector systematics	2.82%	6.48%	3.64%
MC statistics	1.12%	1.63%	0.99%
MC modelling	4.01%	3.71%	3.95%
Total systematics	5.69%	8.47%	5.32%
Luminosity	2.8%	2.8%	2.8%

TABLE 7.23: Breakdown of the uncertainty on the $\sigma_{Wc}^{fid,OS-SS} \times \mathrm{BR}(W \to \ell\nu)$ measurement.

$\sigma_{W^+\bar{c}}^{fid,OS-SS} / \sigma_{W^-c}^{fid,OS-SS}$			
source	1-jet	2-jet	1-jet incl.
data statistics	1.44%	2.13%	1.26%
Background yield	4.40%	5.06%	3.40%
Detector systematics	0.62%	1.14%	0.90%
MC statistics	1.29%	2.50%	1.11%
MC modelling	0.47%	1.00%	0.49%
Total systematics	4.65%	5.85%	3.73%

TABLE 7.24: Breakdown of the uncertainty on the $\sigma_{W^+\bar{c}}^{fid,OS-SS} / \sigma_{W^-c}^{fid,OS-SS}$ measurement.

7.5 Comparison to theoretical predictions

The measurements are compared to their `ALPGEN+PYTHIA` LO prediction produced with the CTEQ6LL PDF set [122]. A k-factor of $k = 1.092$ is applied between the LO and NLO prediction, calculated from the W inclusive sample. The results are summarized in table 7.25 for the 1-jet measurement, in table 7.26 for the 2-jet measurement and in table 7.27 for the 1-jet inclusive measurement. A comparison to the LO prediction for the $\sigma_{Wc}^{fid,OS-SS} \times \mathrm{BR}(W \to \ell\nu)$ cross section is shown in figure 7.16 and for the ratio $\sigma_{W^+\bar{c}}^{fid,OS-SS} / \sigma_{W^-c}^{fid,OS-SS}$ in figure 7.17 for the 1-jet inclusive measurement.

The agreement between the prediction and the measurement is the best for the 1-jet inclusive bin, with all measured values being within one standard deviation to the prediction. This is to be expected, as it is known that theoretical predictions are most precise for the inclusive measurements. In the 1-jet bin, there is agreement within one and a half standard deviations for $W+c(c \to \mu)$ and $W+c$, while the ratio between $\sigma_{W^+\bar{c}}^{fid,OS-SS} / \sigma_{W^-c}^{fid,OS-SS}$ agrees well below one standard deviation. The 2-jet measurement shows agreement of the cross-sections within one standard deviation, but the ratio is off by more than two standard deviations. This is an unexpected result, as the dominant contribution to $W+c$ production at this jet multiplicity should come from gluon-gluon fusion, which should be largely symmetric between W^+ and W^- events, and should be investigated further.

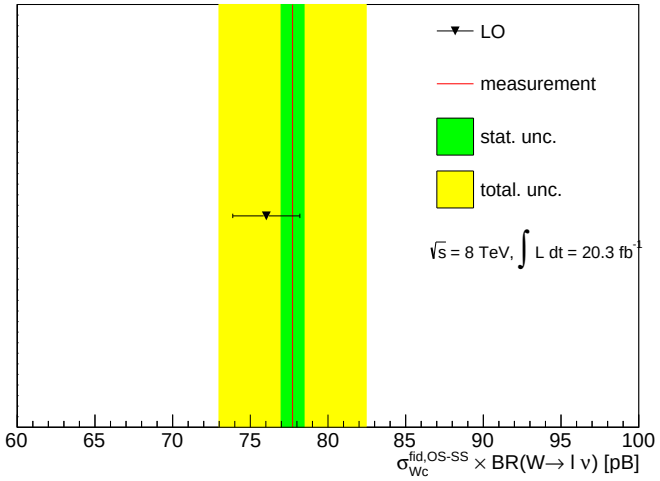

FIGURE 7.16: Measurement of the $\sigma_{Wc}^{fid,OS-SS} \times \mathrm{BR}(W \to \ell\nu)$ cross section in the 1-jet inclusive sample compared to the LO `ALPGEN+PYTHIA` prediction.

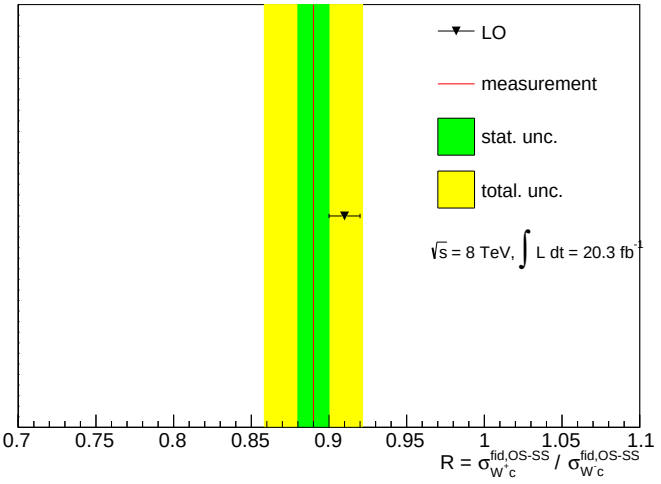

FIGURE 7.17: Measurement of the $\sigma_{W^+\bar{c}}^{fid,OS-SS}/\sigma_{W^-c}^{fid,OS-SS}$ cross section ratio in the 1-jet inclusive sample compared to the LO `ALPGEN+PYTHIA` prediction.

The measurements would greatly benefit from comparison to the NLO predictions such as with `McAtNLO`, and by comparing the effect of different PDF sets, as the main goal of such a measurement is to constrain the strange quark PDF. This could further shed light on the large asymmetry between $W^+\bar{c}$ and W^-c production observed in the 2-jet bin.

$\sigma^{fid,OS-SS}_{Wc(c\to\mu)}\times \mathrm{BR}(W\to\ell\nu)$	
1-jet measurement	3.07 ± 0.03(stat) ± 0.17(syst) [pb]
`ALPGEN+PYTHIA` prediction	2.85 ± 0.08 [pb]
$\sigma^{fid,OS-SS}_{Wc}\times \mathrm{BR}(W\to\ell\nu)$	
1-jet measurement	59.68 ± 0.64(stat) ± 3.79(syst) [pb]
`ALPGEN+PYTHIA` prediction	55.33 ± 1.58 [pb]
$\sigma^{fid,OS-SS}_{W^+\bar{c}}/\sigma^{fid,OS-SS}_{W^-c}$	
1-jet measurement	0.92±0.02(stat)±0.04(syst)
`ALPGEN+PYTHIA` prediction	0.91 ± 0.01

TABLE 7.25: Measured and predicted 1-jet $W+c$ cross-section and their ratios.

$\sigma^{fid,OS-SS}_{Wc(c\to\mu)}\times \mathrm{BR}(W\to\ell\nu)$	
2-jet measurement	0.86 ± 0.02(stat) ± 0.07(syst) [pb]
`ALPGEN+PYTHIA` prediction	0.90 ± 0.03 [pb]
$\sigma^{fid,OS-SS}_{Wc}\times \mathrm{BR}(W\to\ell\nu)$	
2-jet measurement	15.74 ± 0.41(stat) ± 1.40(syst) [pb]
`ALPGEN+PYTHIA` prediction	16.30 ± 0.49 [pb]
$\sigma^{fid,OS-SS}_{W^+\bar{c}}/\sigma^{fid,OS-SS}_{W^-c}$	
2-jet measurement	0.78 ± 0.03(stat) ± 0.05(syst)
`ALPGEN+PYTHIA` prediction	0.92 ± 0.01

TABLE 7.26: Measured and predicted 2-jet $W+c$ cross-section and their ratios.

$\sigma^{fid,OS-SS}_{Wc(c\to\mu)}\times \mathrm{BR}(W\to\ell\nu)$	
1-jet inclusive measurement	4.11 ± 0.04(stat) ± 0.22(syst) [pb]
`ALPGEN+PYTHIA` prediction	4.02 ± 0.11 [pb]
$\sigma^{fid,OS-SS}_{Wc}\times \mathrm{BR}(W\to\ell\nu)$	
1-jet inclusive measurement	77.72 ± 0.74(stat) ± 4.68(syst) [pb]
`ALPGEN+PYTHIA` prediction	76.03 ± 2.16 [pb]
$\sigma^{fid,OS-SS}_{W^+\bar{c}}/\sigma^{fid,OS-SS}_{W^-c}$	
1-jet inclusive measurement	0.89 ± 0.01(stat) ± 0.03(syst)
`ALPGEN+PYTHIA` prediction	0.91 ± 0.01

TABLE 7.27: Measured and predicted 1-jet inclusive $W+c$ cross-section and their ratios.

Chapter 8

Detectors under study and measurement set-up

8.1 Devices under study

The detectors used in this thesis are all n-in-p FZ silicon strip detectors (SSD). Detectors came from three manufacturers, MICRON Semiconductor Co. Ltd. in Sussex, UK, Hamamatsu Photonics K.K. (HPK) in Hamamatsu, Japan and the Fondazione Bruno Kessler (FBK) in Trento, Italy.

8.1.1 MICRON detectors

The MICRON detectors used in this thesis are specially designed charge multiplication (CM) detectors produced within the framework the CERN RD50 group [66]. The detectors are 1×1 cm^2 n-in-p FZ planar SSDs. These devices have a thickness ranging from 150 to 675 μm, varying strip widths and pitches, as well as some sensors having either floating or biased intermediate strips between readout strips. Strip isolation is achieved through p-spray with a concentration of 2×10^{12} ions/cm^2.

A total of five different types of wafers were produced; a standard wafer (std.), a wafer where the energy of the implants during processing was doubled (2E imp.), a wafer where the diffusion time for the implants was doubled during processing (extr. diff.), a thin wafer having a thickness 150 μm instead of the standard 300 μm (thin) and a wafer with a thickness of 675 μm (thick). The resistivity for the different wafer types as given by the manufacturer is shown in table 8.1. The effect of including an intermediate implant strip between the readout strips is also investigated, where the intermediate strip can either be biased (i) or left floating (f). This study will focus on the std, 2E imp, and extra diff. wafers. All sensors

Wafer type	Thickness (μm)	Resistivity ($k\Omega$cm)
Standard (std.)	305	13
Double diffusion time (extr. diff.)	305	13
Double implant energy (2E imp.)	300	10-13

TABLE 8.1: Thickness and resistivity of the three MICRON wafers investigated.

Production run	Thickness (μm)	Resistivity (kΩcm)
ATLAS07	320	>2
ATLAS12a	310	4-8

TABLE 8.2: The thickness and resistivity of the HPK sensors investigated

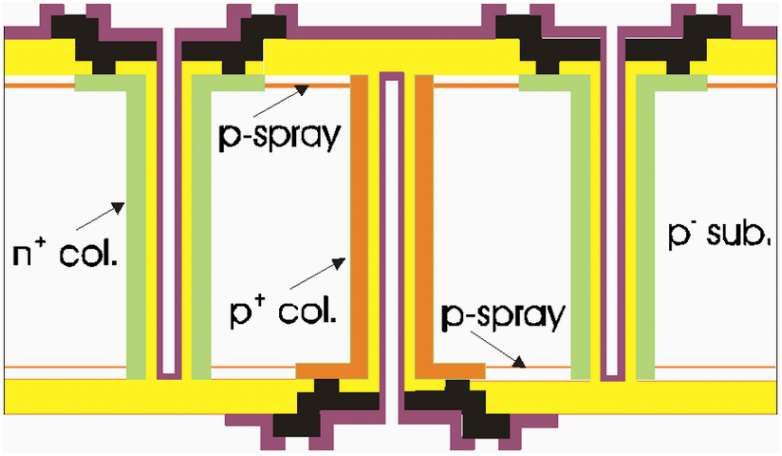

FIGURE 8.1: Cross-section schematic of a 3D-DDTC detector with passing through columns.

in the study will be compared to a standard sensor with a strip width of 25 μm and pitch of 80 μm (std., p80, w25) at the corresponding radiation fluence.

The aim of such devices is to increase the electric field near the readout strips, in particular near the strip edges, where the focusing of the electric field is the strongest [123]. The strength of the electric field in such regions is heavily dependent on the strip width/pitch (w/p) ratio, with lower w/p leading to higher fields near the strip edges.

8.1.2 HPK detectors

The detectors by HPK are 1 $\times$ 1 cm^2 n-in-p FZ SSDs. The sensors in this study were part of the ATLAS07 [124] and ATLAS12A [125] production runs. The thickness of the sensors are 320 $\pm$ 15 μm for ATLAS07 and 310 $\pm$ 25 μm for ATLAS12A. The ATLAS07 sensors have a strip pitch of 74.5 μm while the ATLAS12a sensors have a pitch ranging from 63.6 - 105 μm. For the ATLAS07 sensors strip isolation was achieved through use of either p-stop implants placed between read-out strips with a concentration around 1 $\times$ 10^{13} ions/cm^2 or with p-spray with a concentration of 2 $\times$ 10^{12} ions/cm^2. ATLAS12a sensors achieved strip isolation through p-stop implants with a concentration of 4 $\times$ 10^{12} ions/cm^2. The resistivity of the wafers from the two production runs is listed in table 8.2.

8.1.3 FBK detectors

The FBK detectors are 1 $\times$ 1 cm^2 n-in-p FZ double-sided 3D (3D-DDTC) SSDs. The geometrical configuration of such sensors can be seen in figure 8.1. They consist of 102 strips of 8 mm length with each strip containing 102 junction columns

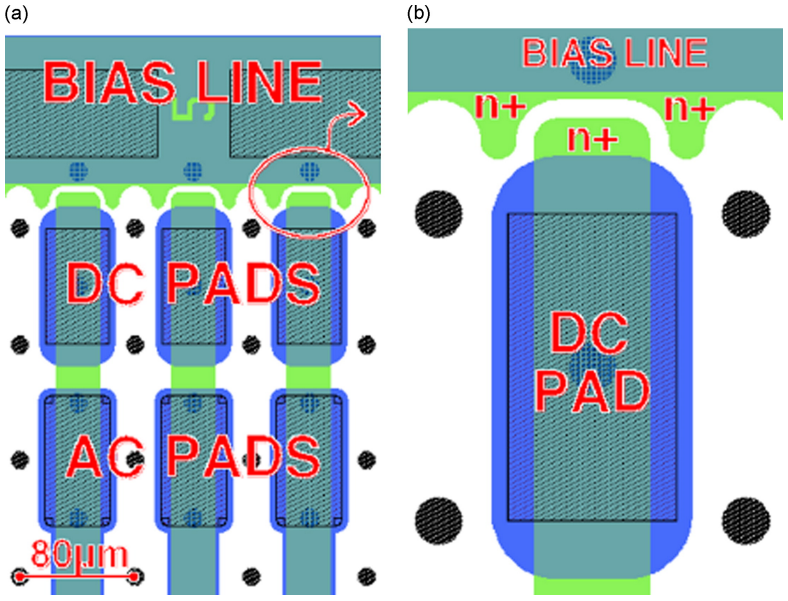

FIGURE 8.2: Geometrical configuration of the considered 3D strip sensors with 80 μm pitch between columns of the same doping type (a). The enhanced punch-through structure layout is also highlighted (b).

(n^+), each surrounded by four ohmic columns (p^+). Sensors have a thickness of 230 $\pm$ 20 μm and a resistivity in the range between 10 and 30 kΩ cm. Devices used in this study come from the ATLAS IBL production batch named ATLAS10 [126]. The main layout properties are shown in figure 8.2(a). Both AC and DC pads are available. The strips employ punch-through biasing. The final layout of the ATLAS10 design can be seen in figure 8.2(b). The distance between the n^+ strip implant and the bias line was reduced from 20 μm of the previous 3D generation to 5 μm and the bias line geometry was altered to assure a better coupling to the strips. Strip isolation was obtain by means of p-spray implantations on both wafer sides.

8.2 Measurement set-up

This section describes different measurement types used to characterize and test sensors investigated in this thesis. Measurements include current-voltage (IV), capacitance-voltage (CV), punch-through measurements and charge collection (CC) with either beta source or a laser source. Other tests performed, but not shown in this thesis, include interstrip resistance and capacitance measurements.

8.2.1 Capacitance-Voltage and Current-Voltage measurements

The leakage current is measured using a Keithly 237 power supply which provides the HV and is typically applied to the detector backplane while the bias rail is grounded. For pre-irradiated sensors the measurements are performed in a probe station at room temperature. For irradiated sensors the measurements are carried

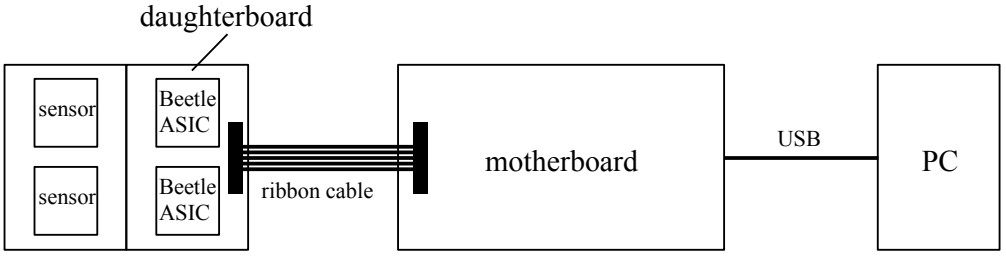

FIGURE 8.3: Schematic of the ALIBAVA read-out system.

out in a freezer while already bonded to boards for charge collection measurements, as described in section 8.2.2.

The capacitance as a function of the detector bias voltage is measured using a HP 4284A Precision LCR Meter. For pre-irradiated detectors, the capacitance is measured at room temperature with a frequency of 10 kHz, which is less than the high-frequency cut-off introduced by the strip geometry of the sensor. The capacitance in irradiated detectors must be corrected due to the non-trivial frequency response of radiation induced defect states to the AC signal used to in the measurement. The general rule is to correct the capacitance measured at 10 kHz and at room temperature to any other temperature [127].

8.2.2 Charge collection measurements

Charge collection measurements are used for determining the efficiency of a given sensor and also its general robustness. The signal-to-noise ratio (SNR) is an important quantity to assess the radiation-hardness of silicon detectors. The signal itself also constitutes an important part of sensor R&D, as it is generally free of external influences that affect the noise, such as temperature, the readout electronics and surface geometry of a given sensor. Limiting thegDegradation of the signal with increasing radiation fluence is an important driver of detector design and optimization.

8.2.2.1 The ALIBAVA read-out system

All charge collection measurements are carried out using the ALIBAVA read-out system [128]. ALIBAVA is an analogue read-out system that was developed within the framework of the RD50 collaboration for testing the collected charge in silicon detectors. It was designed to be of a similar read-out as the LHC electronics, and is compact and portable. Developed by the institutes in Liverpool, Barcelona and Valencia, ALIBAVA stands for *A*nalogue *Li*verpool *Ba*rcelona *Va*lencia read-out system.

The system consists of two parts, a hardware part and a software part. The hardware part is further divided into two subsystems: a *daughterboard* which performs amplification and shaping of the detector signal and a *motherboard* which processes the analogue data and sends it to a PC for analysis via a USB cable. The software part controls the entire system and processes the data coming from the motherboard. The processed data is saved in a file format so that it can be read

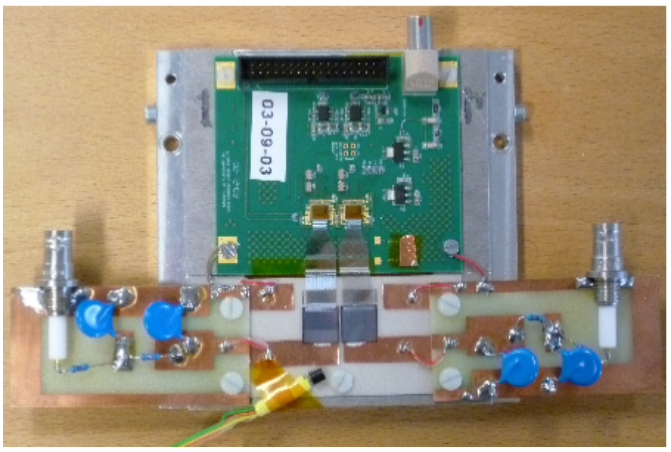

FIGURE 8.4: A detector board with two mini SSDs bonded to Beetle chips on the daughter board. A thermistor can be seen attached the detector board.

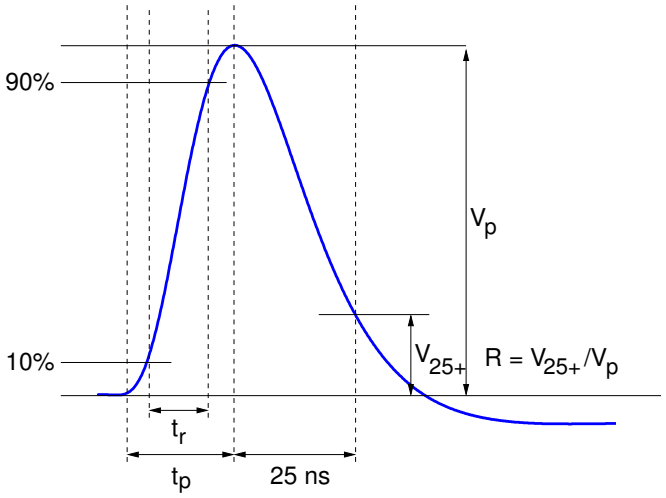

FIGURE 8.5: Signal shape of the Beetle chip output [129].

and analyzed using custom software based on the ROOT framework. A schematic of the ALIBAVA system is shown in figure 8.3.

The *daughterboard* takes the signal from the silicon detectors and performs amplification and shaping of the signal with on-board Beetle chips, whose characteristics and internal architecture can be found in [129]. The output pulse shape of the Beetle chip can be seen in figure 8.5. Each board contains two Beetle chips having 128 channels each. This allows for placement of two detectors at a time. A fan-in chip is used to bond the read-out strips of the detectors to the Beetle chip channels. The fan-in chips have pads with 80 μm pitch with ten rows for multiple wire bonding. This allows for testing multiple detectors for a given Beetle chip. Detectors are placed on a detector board, which is then bonded to the daughterboard.

The detector board is composed of aluminum nitride, which has a high thermal conductivity. Detectors are placed onto the boards using a layer of double sided tape, as opposed to glue or epoxy, in order to ensure the quick and safe removal of detectors after completion of the measurement. The tape covers the backside

detector surface only partially to allow for backside electrical contact for biasing. The backside contact is achieved with copper tape, which is then connected to the HV power supply. There is an additional low pass filter connected to each board to reduce external noise and avoid large voltage spikes. A picture of a detector board bonded to a daughterboard is shown in figure 8.4.

The temperature can be read-out from internal sensors on the Beetle chips, or by a thermistor placed as close as possible to the detectors. The source of the temperature measurement, from the chip or thermistor, is controlled by the ALIBAVA software. There is also the option to supply the HV to the detector directly from the daughterboard.

The *motherboard* processes signals from the daughterboard and puts them into a binary format for the PC to read. It is controlled by an FPGA (field programmable gate array). The analogue data from the daughterboard is converted into digital counts via the ALIBAVA ADC (analogue to digital converter). The motherboard also handles the inputs of external triggers. Once a trigger signal is received, the motherboard initiates read-out of the Beetle chips, which are sampled every 25 ns. An onboard TDC (time to digital converter) measures the phase shift of the trigger with respect to a 10 MHz clock. Thus the analogue signal from the Beetle can be reconstructed in a 100 ns time window.

During laser source measurements, the motherboard also facilitates the use of a fixed time trigger. The trigger coincides with the creation of a laser pulse, whose delay with respect to the trigger can be adjusted in 1 ns increments. The delay can be varied to find the maximum of the Beetle signal pulse.

8.2.2.2 Calibration of detector boards

Detector boards need to be calibrated in order to convert the signal from ADC into charge. Signal measured in charge, $CC(ke^-)$ is determined by

$$CC(ke^-) = S(ADC)G(T) \tag{8.1}$$

where $S(ADC)$ is the signal measured by the beetle chip in ACD and $G(T)$ is the gain of the chip as a function of temperature T. The gain $G(T)$ as a function of temperature is given by

$$G(T) = \frac{Q_{cal}}{A + BT} \frac{f(C_{det})}{f(C_{cal})} \tag{8.2}$$

where Q_{cal} is the signal expected at full depletion of a calibration detector of a known thickness, A and B are constants to be fitted for, T the temperature in $^\circ$ C, C_{det} the capacitive load of the detector being measured, C_{cal} the capacitive load of the calibration detector and $f(C)$ a function of the capacitive load, derived in [130] and given by

$$f(C) = 0.999 + 0.018C \tag{8.3}$$

where C is taken in units of pF. The constants A and B are determined by fitting the signal $S(ADC)$ to a linear function $A+BT$, which can be seen in figure 8.6 for a particular board with an ATLAS07 sensor used for calibration. Typically, the uncertainty on the calibration detector thickness dominates the total uncertainty on the gain.

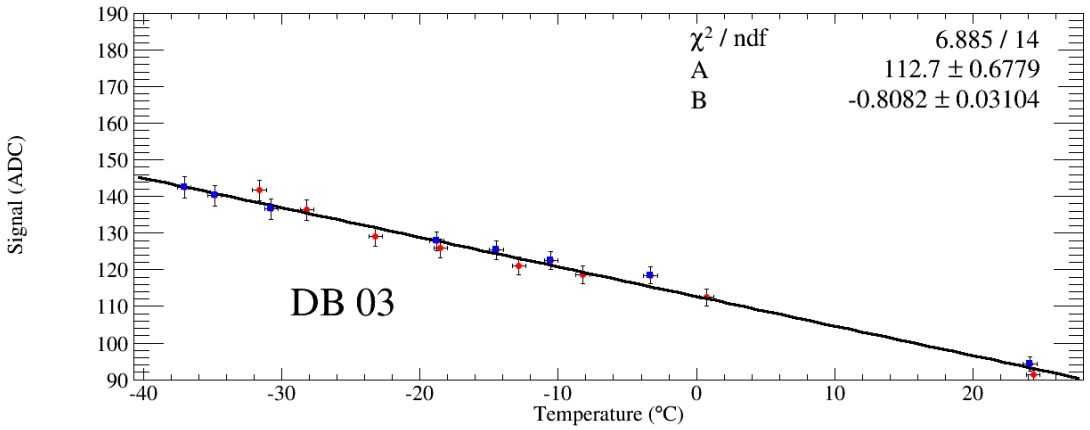

FIGURE 8.6: Measured signal in ADC as a function of temperature for an ATLAS07 sensor used to calibrate detector boards. The red points indicate temperatures taken with an external thermistor, as seen in figure 8.4, while the blue points represent temperatures taken with the internal temperature sensor of the ALIBAVA beetle chips.

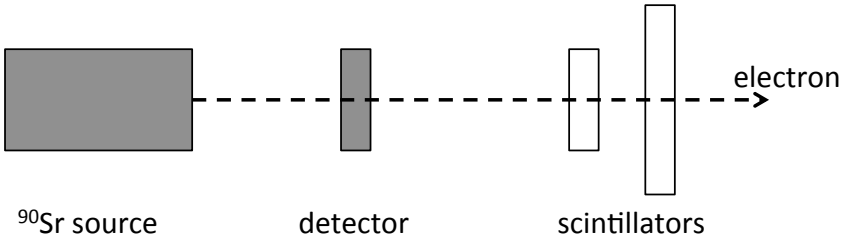

FIGURE 8.7: A schematic diagram of the beta source set-up

8.2.2.3 Beta source measurements

For beta source measurements signals are generated using MIPs from a ^{90}Sr source. Two scintillators read out in coincidence are located behind the sensor and are used to trigger. A schematic of the set-up is shown in figure 8.7. The entire set-up is housed in a freezer that can be cooled down to -20° C. Temperatures as low as -60° C can be attained using an external liquid nitrogen system. During measurements, the temperature was kept at approximately -20° C for fluences of 1×10^{15} n_{eq}, while sensors $\geq 5\times10^{15}$ n_{eq} were tested at about -40° C. Nitrogen gas was used to bring the relative humidity in the freezer below 5%.

Each measurement begins with a pedestal run. The pedestal run is a measurement of the signal in the absence of traversing particles, and is performed with a random trigger. The mean signal for each channel is calculated and subtracted from the data. The noise for each measurement is calculated as the RMS deviation of the signal in the pedestal run. The noise should follow a Gaussian distribution, but this is not always the case, as typically there are a few "hot" channels that exhibit large noise deviations which lead to non-Gaussian tails. These can arise from damage to the strips on the sensor, faulty wire bonds or damage to channels of the Beetle chips. Only a small fraction, typically <10%, of channels exhibit high noise and these are disregarded from the measurement. The effect on the final measured signal is negligible. Ideally, the beta source should be removed or

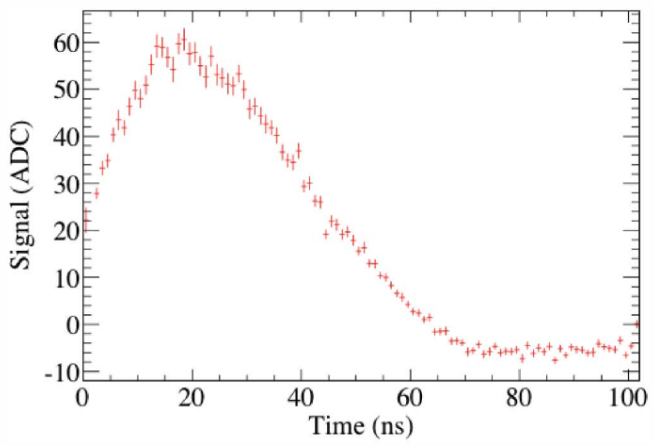

FIGURE 8.8: Signal in ADC as a function of the time measured by the ALIBAVA TDC.

covered during pedestal runs, but this is not practical most cases. The beta source is therefore left in place, and the increase in noise was found to be in the order of 1%.

A common shift in the signal to all channels can be introduced through external noise contributions which tend to broaden the signal distributions. Since it is common to all channels, it can be corrected for. After subtracting out the pedestal measurement from the data, the common mode is calculated as the mean signal over all channels event by event. Furthermore, channels with excessive signals are disregarded from the common mode calculation, which ensures that signals from electrons traversing the detector do not contribute.

The time between a trigger signal and a 10 MHz clock is measured by the ALIBAVA TDC. The spectrum for such a signal arising from a beta source can be seen in figure 8.8. For each event, the channel having the highest signal-to-noise ratio (SNR) is taken and the average for each 1 ns bin is calculated. Only events within a 10 ns time window around the peak of the distribution are considered. A fit to the peak is performed to determine the maximum and the range of the window. A SNR cut is applied, and events below the cut are disregarded.

The signal is reconstructed from a charge cluster in order to account for charge sharing between strips. After passing the signal SNR cut, the SNR of the adjacent strips is calculated. If the SNR of the neighboring strips is larger than the neighbor SNR cut (usually smaller than the signal SNR cut), then the neighbor signal is added to the seed signal to get the cluster signal. This is repeated as long as the strips pass the SNR cut. The final cluster signal is fitted with a convolution of a Landau and Gaussian function. The final signal for each event is taken as the most probable value (MPV) of the Landau function extracted from the fit.

8.2.2.4 Laser source measurements

The laser source measurements make use of an infrared pulsed laser (λ = 974 nm), with pulses shorter than 1 ns. The laser pulses are fed through an optical microscope (Leica Polyvar SC) by means of a 1 m long optical fiber, and are focused on the sensor front surface. The trigger for the laser is provided by the

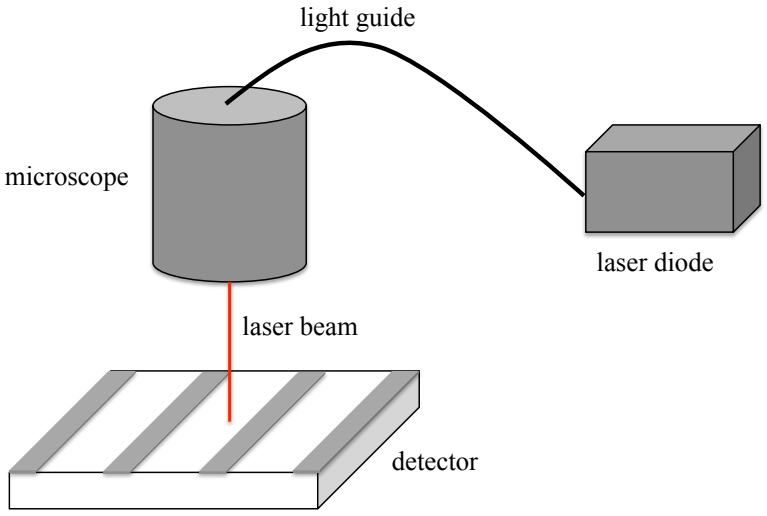

FIGURE 8.9: A schematic diagram of the laser source set-up

ALIBAVA system. The laser profile has a Gaussian spatial distribution with a diameter of about 4 μm. Sensors are mounted on a cooling structure that can be moved in both x and y directions, with 1 μm precision, by motorized stages remotely controlled via software. This allows to perform laser scans on large areas in order to investigate the spatial uniformity of the sensors response. Detectors are mounted on similar boards to that of the beta source measurements. Before each measurement, the sensor position and laser focus must be adjusted. The detector orientation is adjusted so that the focus of the laser is equal over the entire surface.

The absorption length of $\lambda = 974$ nm light is about 100 μm in silicon at a temperature of -30° C, which means that the signal is primarily generated near the sensor surface. This leads to a strong dependence of the measurement on surface effects. Due to the small absorption length, absolute signal charge from the sensor cannot be determined, but only relative changes can be investigated.

The pedestal and common mode calculation is performed in the same way as in the beta source measurements. For the signal measurement, 500 laser pulses are generated for each point. The resulting spectrum follows a gaussian distribution, and a fit is performed to get the mean of the distribution, which is taken as the signal for that point. The delay between the trigger and laser pulse is adjusted as to ensure that the signal from the Beetle chip is always sampled around the maximum. The Beetle chip signal as a function of the laser delay is shown in figure 8.10.

8.2.3 Long-term HV measurements

During long-term measurements, sensors are tested over long periods (several days to weeks) under two scenarios:

- A constant high voltage ranging from several hundred V to a few kV
- Tests where the HV is turned off between measurements but the ^{90}Sr source is left placed in front of the sensor. After a drop of signal was observed, a few

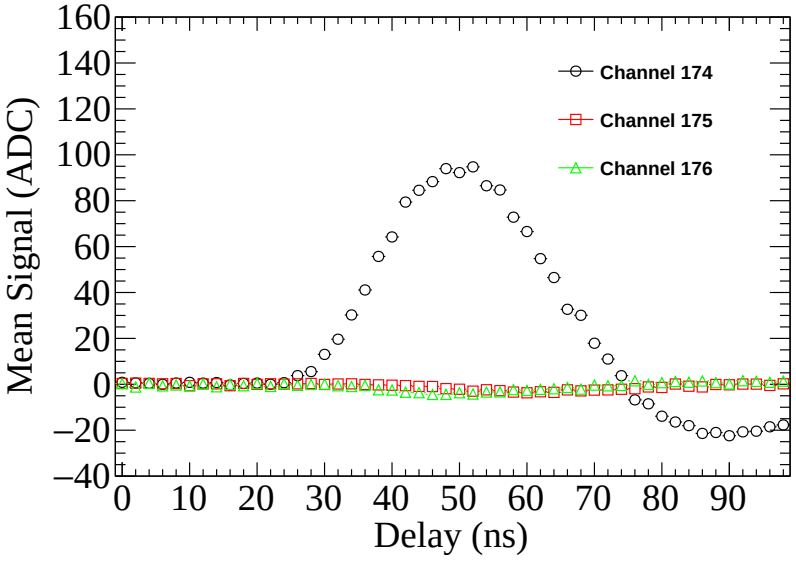

FIGURE 8.10: Signal measured in ADC as a function of the laser delay for a seed strip and its two nearest neighbors.

methods for recovering the lost charge were tested. This included removing the HV for a period spanning a few hours to several months, forward biasing the sensor for a period of time and shining UV light over the sensor (no HV) for a period of time, in an attempt to relax any residual surface charges.

8.3 Irradiation facilities

Devices were irradiated with either reactor neutrons at the Jozef Stefan Institute in Ljubljana from the TRIGA Mark II research reactor [131] or with 25 MeV protons from the Proton-Compact Cyclotron in Karlsruhe [132]. A relative error of 10% is assumed for each fluence. Sensors were kept unbiased during irradiations. After irradiation, sensors were transferred to a freezer to prevent annealing. Sensors are shipped from the irradiation institutes with frozen gel packs and insulated packaging. Some uncontrolled annealing occurs at room temperature during preparation times for measurements, which include mounting and bonding to detector boards and placement in the freezer before cooling. This source of uncontrolled annealing is negligible and covered by the errors of the measurement.

Chapter 9

Results of detector measurements

9.1 Characterization of 3D-DDTC strip sensors with passing-through columns

Sensors in this section were produced by FBK as part of the ATLAS10 production run as outlined in the previous chapter. Devices were chosen from on-wafer IV measurements, looking for those showing higher breakdown voltages, in order to assure the best performance both before and after irradiation. Devices were initially tested and then diced at FBK and sent to the University of Freiburg for charge collection measurements. Pre-irradiated tests at Freiburg were followed up by tests performed after proton irradiation. TCAD and PSPICE simulations were carried out at FBK and compared to the measurements performed in Freiburg.

9.1.1 Electrical characterization

The current-voltage (IV) measurements were performed by grounding the bias line and sweeping the bias voltage from the back side p^+ contact. The IV curves for all shipped sensors are shown in figure 9.1.

All currents saturate before 10 V of bias, which suggests a small depletion voltage, as expected in 3D detectors. Breakdown is observed at about 40 V, although one sensor exhibited high current before this. The current slope is rather steep after 20 V but is still within the expected behavior identified on 3D diodes with 80 μm pitch, and confirmed by numerical simulations [133]. Current measurements were also performed on single strips showing a current value of about 200 pA, corresponding to roughly 2 pA/column, which is in good agreement with what was found on other sensors from the same batch [134] and slightly larger than found in previous 3D-DDTC technologies [135].

The effective bias voltage of the single strip was also measured to confirm the proper operation of the modified punch-though biasing structure. Results are shown in figure 9.2 and show good agreement with numerical simulations. The measurements were performed by reverse biasing the entire strip detector and by monitoring the voltage of a single strip from the DC pad. The current was held to 0 while monitoring the floating potential of the strip. These results indicated an effective bias voltage of about 27 V for an applied potential of 40 V. This is rather

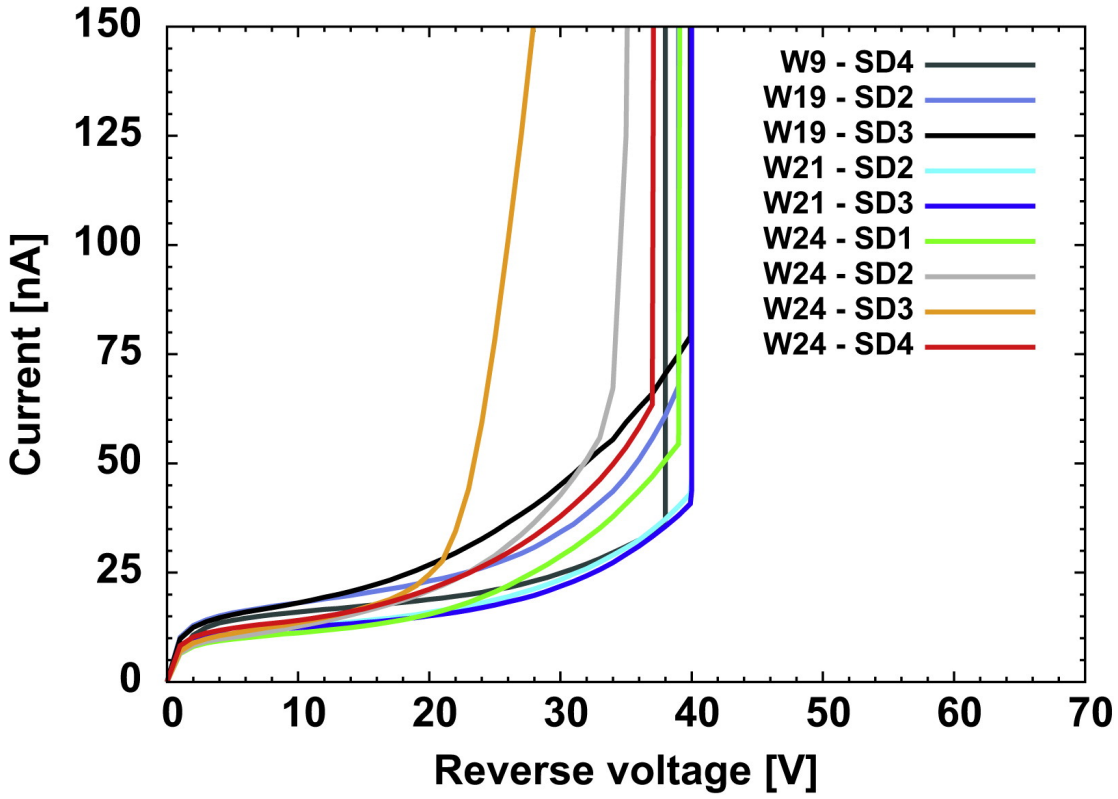

FIGURE 9.1: I–V measurements of different 3D sensors.

low, but is more than enough to fully deplete the device. The correct operation of the punch-though mechanism in these devices has also been confirmed after irradiation.

Capacitance measurements were also performed. The strip-to-backplane capacitance was found to be about 9 pF at full depletion. The full depletion voltage extracted from CV curves was found to be $\sim$ 6 V in good agreement with TCAD simulations [133]. The interstrip capacitance was found to be about 0.9 pF at full depletion. The integrated AC capacitor was also measured and was found to have a capacitance of about 8.1 pF. As will be shown later, this low value has a strong effect on the signal measured with AC coupled devices. Such a low value is attributed to the rather thick passivation layers present on the surface of the device, used as etch stop for the DRIE (Deep Reactive-Ion Etching) during fabrication. The most relevant electrical parameters are listed in table 9.1.

The current after proton irradiation can be seen in figure 9.3 for a select set of sensors at different fluences. Different measurements were carried out at different temperatures, ranging from -15° C to -41 ° C, so currents were normalized to -20° C for easy comparison. As expected, there is proper scaling of the current with fluence. The breakdown voltage also increased after irradiation, although not always high enough for full charge collection efficiency, as will be seen in the following subsection.

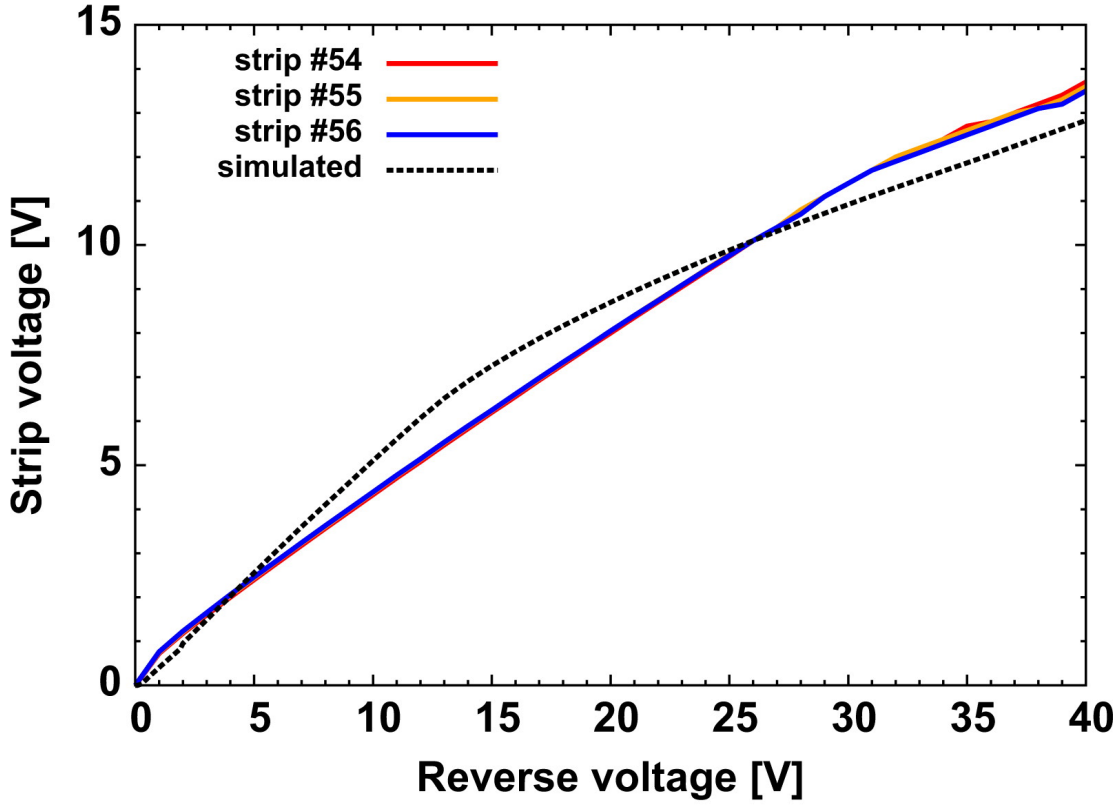

FIGURE 9.2: Measured (solid lines) voltages on a single strip compared with the simulated strip voltage (dashed line).

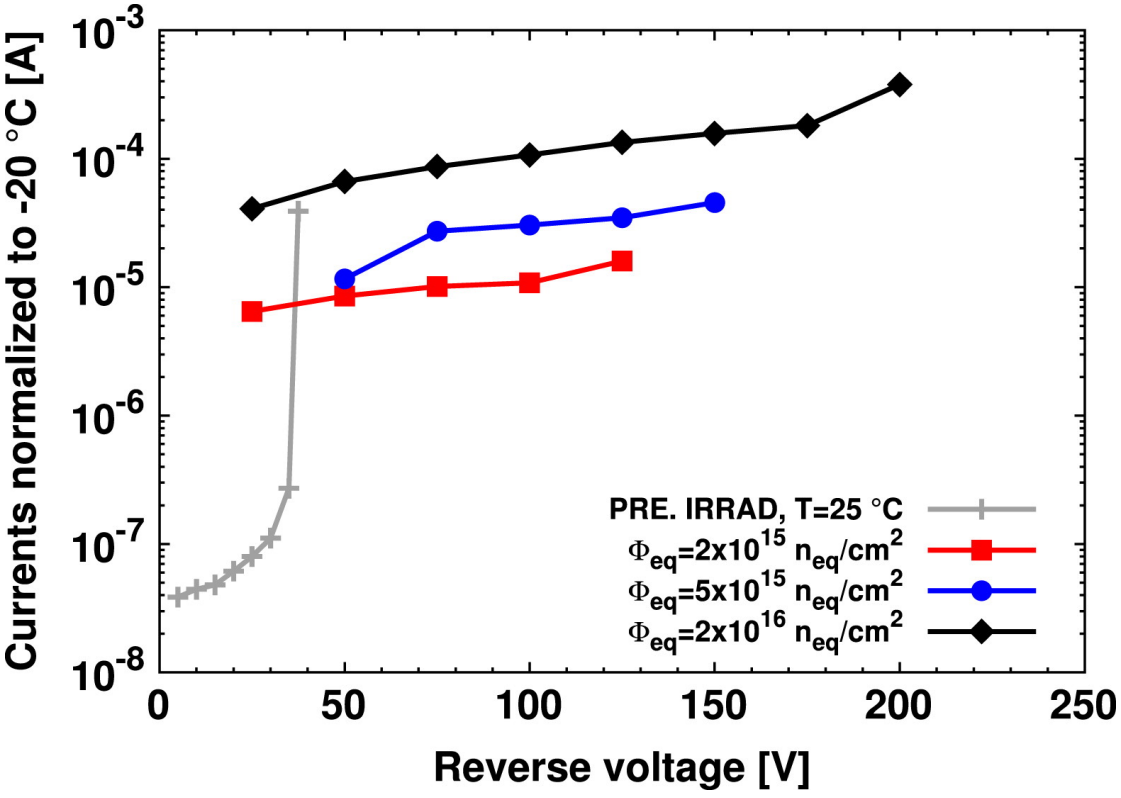

FIGURE 9.3: IV measured on 3D detectors at three different fluences, normalized to -20° C, and on a non-irradiated one taken at room temperature.

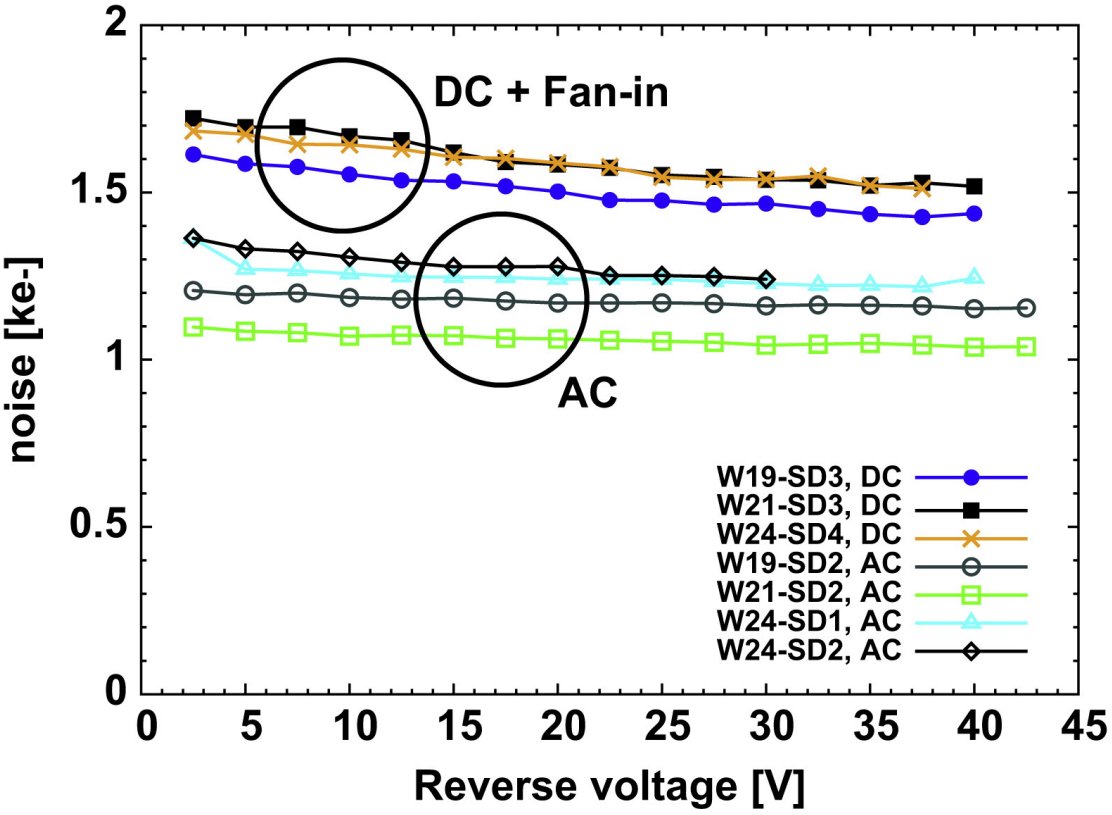

FIGURE 9.4: Noise as a function of the bias voltage. Noisy sensors are not shown and have values around 5–6 ke$^-$.

Parameter	Unit	Value
Full depletion voltage	V	∼6
Breakdown voltage	V	∼40
Strip current at full depletion	pA	200
Strip to back capacitance at full depletion	pF	9.0
Interstrip capacitance at full depletion	pF	0.9
Coupling capacitance	pF	8.1

TABLE 9.1: Summary of the main electrical parameters of the considered 3D strip detectors.

9.1.2 Beta source measurements

Due to the low value of the coupling capacitor, devices were assembled with two different configurations: a group of five devices were connected to the readout electronics using the DC coupled pads and an external RC fan-in (R = 1 MΩ, C = 275 pF), while a group of four sensors were bonded to the electronics directly from their AC pads.

The noise of the system was measured as a function of the bias voltage and was found to be between 1-2 ke$^-$ for most of the devices. As is seen in figure 9.4, only two devices showed rather large noise (in the order of 5-6 ke$^-$ for W9-SD4 and W24-SD3), because of low breakdown effects, but this did not affect their operation as explained later. While the noise decreases slightly with respect to

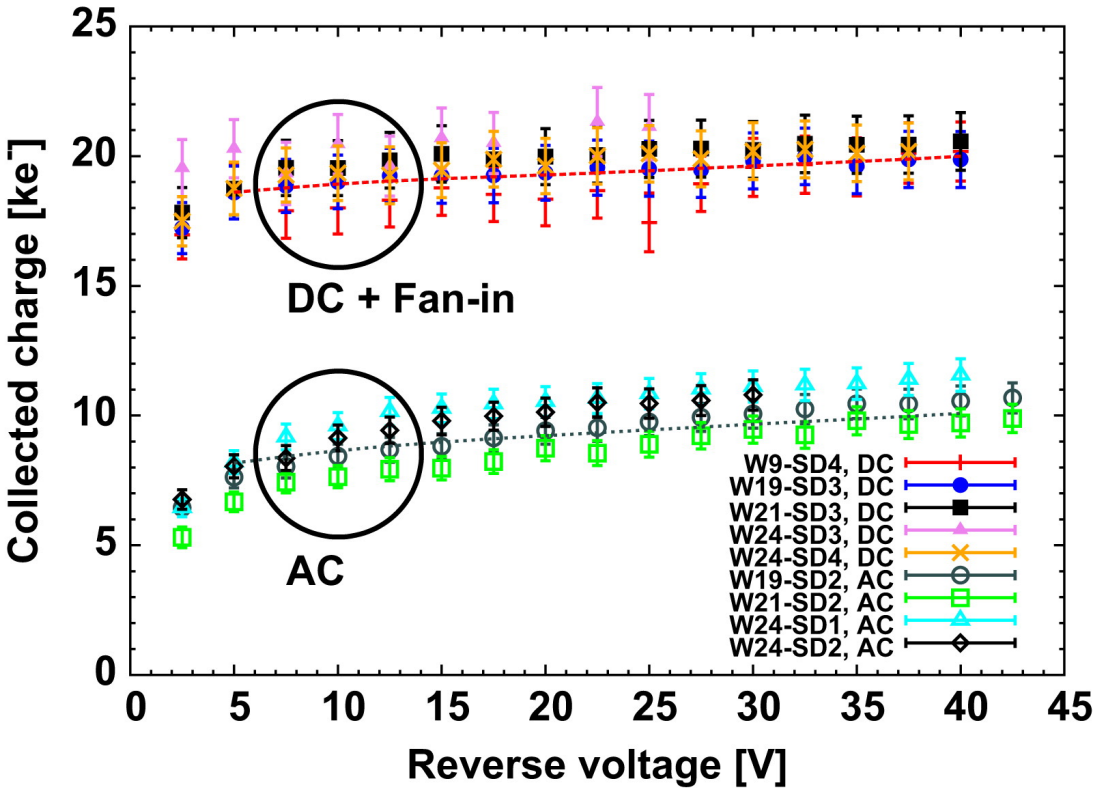

FIGURE 9.5: Measured collected charge as a function of the bias voltage using the beta source setup. Dashed lines represent PSPICE simulation results as described in the text.

the bias voltage, it is almost flat, confirming that full depletion is achieved at low biases.

Sensors using DC pads in conjunction with the external RC fan-ins showed slightly larger noise than the AC coupled sensors. A partial explanation could be that when strips are biased by punch-through (i.e. in sensors using the AC pads), a contribution to the noise of the system is given by the punch-through current flowing toward the bias line, which is equal to the noise contribution of the leakage current and adds quadratically to it (with a current noise spectral density of $2qI_{strip}$) [136]. When DC pads are used in combination with an external fan-in, a parallel noise term is added by the external 1 MΩ resistor, contributing to the overall noise with a current noise spectral density of 4 kT/R. This results in a larger total noise for this configuration. However, at a shaping time of 25 ns, this difference in the parallel noise term is quite small (a few tens of electrons) so that it is not large enough to explain the difference in noise between the two configurations. A more significant decrease in the noise of the AC devices actually comes from the low value of the integrated coupling capacitance, which causes the noise (as well as the signal, as will be shown in the following) to redistribute over the parasitic capacitances.

For a 230 μm thick silicon sensor, the expected charge from an incoming MIP is equal to 18.4 ke$^-$. The pre-irradiated signal for different sensors is shown in figure 9.5. Two groups of curves can be seen. The DC coupled devices exhibit

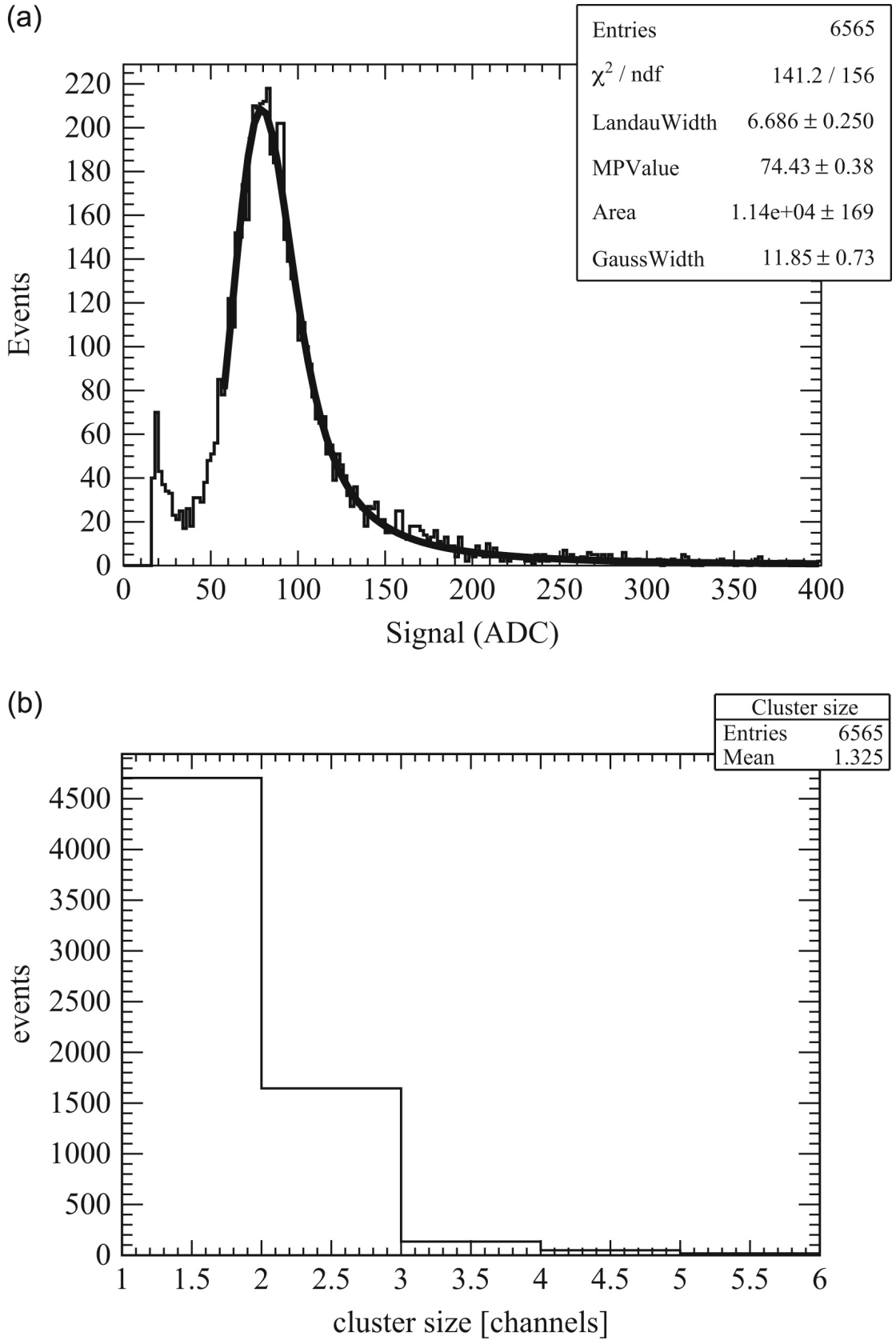

FIGURE 9.6: Fitted Landau distribution (a) and cluster size measurement (b) using the beta source set-up and tested at a bias voltage of 15 V.

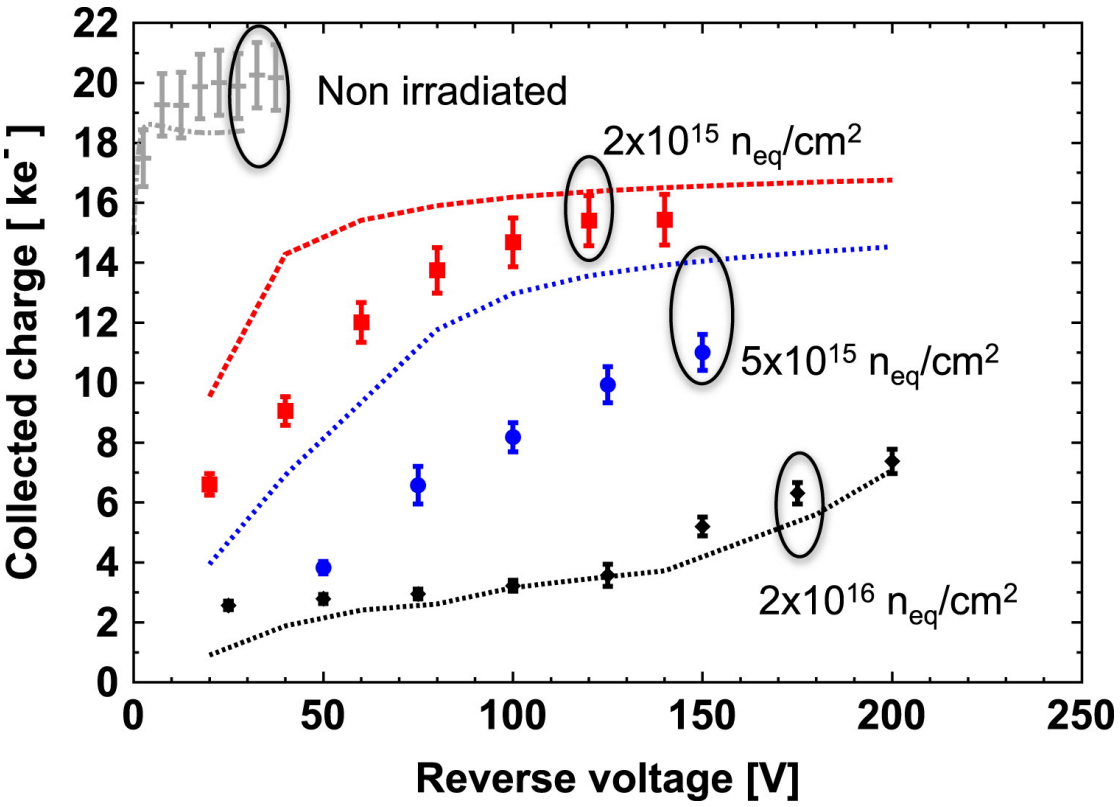

FIGURE 9.7: Measured and simulated collected charge on 3D detectors at three different fluences and on a non-irradiated one taken at room temperature.

charge saturation before 10 V of bias and a maximum charge collection slightly larger than expected ($\sim$ 20 ke$^-$). This can be attributed to uncertainties on the wafer thickness (20 μm) and to particles impinging the device with angles different from 90°, thus traveling larger distances in the bulk and generating more charge inside the devices. It is important to note that both sensors with high noise (W9-SD4 and W24-SD3) also exhibit full charge collection.

As expected, the AC sensors using the integrated coupling capacitor exhibit lower chare. The collected charge corresponds to roughly half of the charge collected by the other sensors. In order to confirm the effect of the small coupling capacitance on the sensor performance, PSPICE simulations were performed incorporating all the measured electrical parameters and also including the AC coupling and parasitic capacitors. The strip was modeled using a pulsed current generator with the strip capacitance in parallel. The charge collected from the DC coupled sensors was injected into the circuit and the readout was simulated using a simple integrator. Simulation results were found tp be in good agreement with the measured ones and are shown in figure 9.5. Since the coupling capacitance is comparable to the parasitic capacitances, the signal charge is not effectively coupled to the readout electronics and part of it is lost.

The Landau fit and cluster size distribution for at a bias voltage of 15 V can be seen in figure 9.6, and are fully compatible with those found in FE-I4 pixel detectors coming from the same batch [137]. Due to their unique structure, which provides a sort of self-shielding effect between adjacent cells, 3D detectors feature

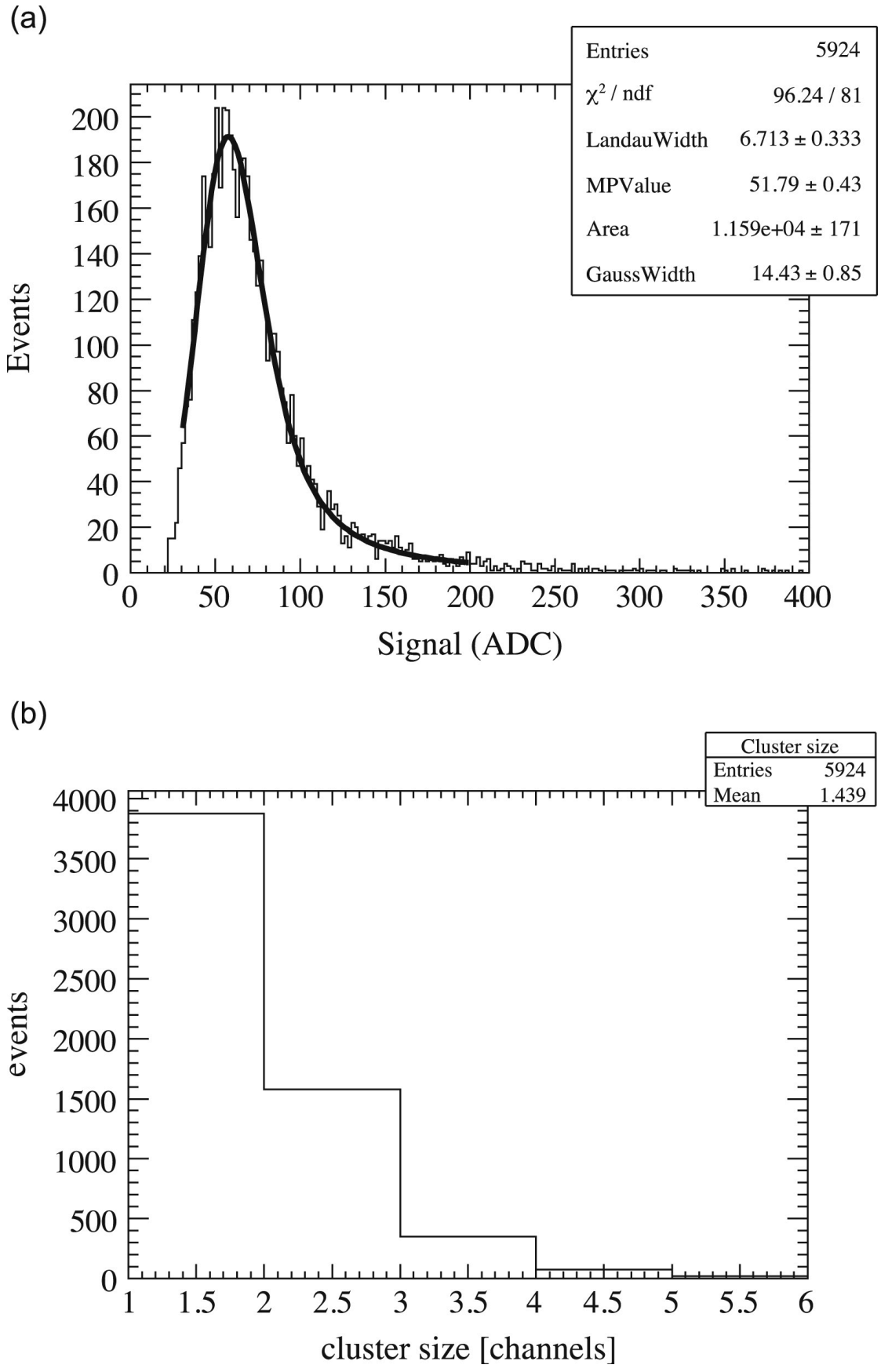

FIGURE 9.8: Measured and fitted Landau spectrum (top) and cluster size (bottom) on an irradiated 3D sensor after a proton fluence of 5×10^{15} n_{eq} tested at 150 V.

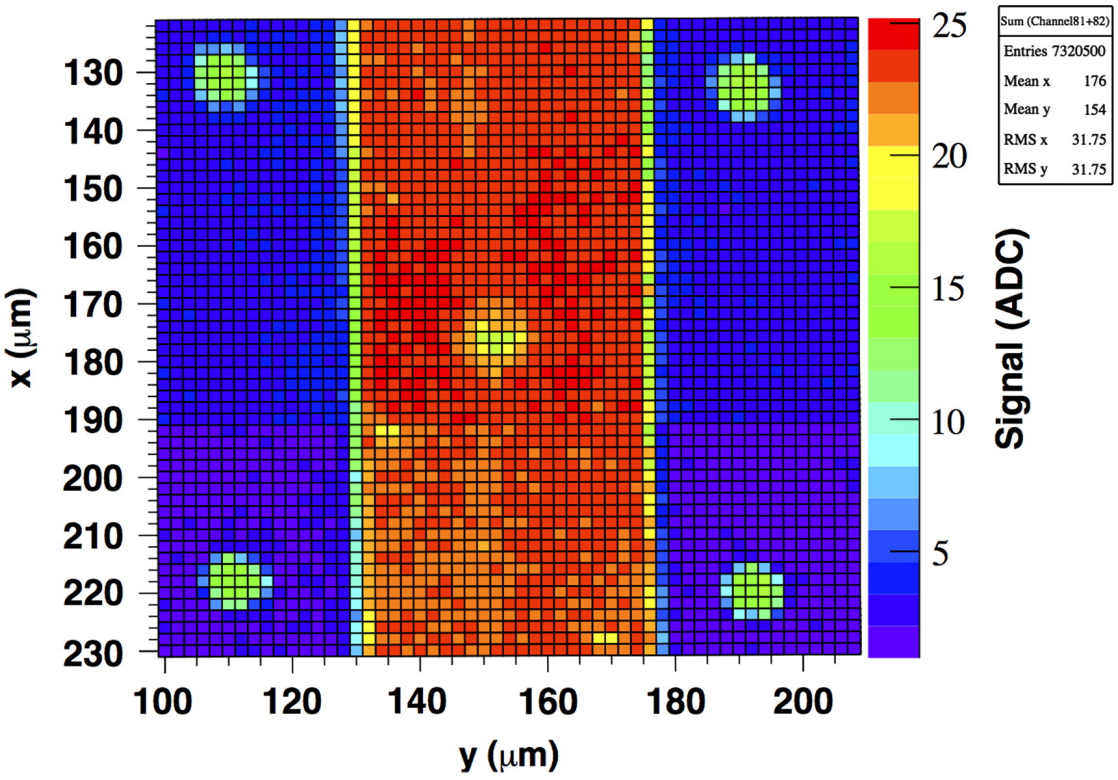

FIGURE 9.9: Laser scan performed on DC coupled strip sensor over an area of $\sim 100 \times 100\ \mu m^2$ at a bias voltage of 30 V.

lower charge sharing between adjacent electrodes with respect to planar devices.

The noise was not significantly affected by irradiation, so long as the sensors were properly cooled to reduce the leakage current. The values ranged from $\sim$ 1 ke^- to $\sim$ 3 ke^-, with most sensors being below 1.5 ke^-, which is close to the pre-irradiated values.

The collected charge for three irradiated sensors is shown in figure 9.7. The signal from a pre-irradiated sensor is added for comparison. A distinction of the signal from the noise can been seen already for very low voltages, and the increase with voltage agrees well with expectations. Only the 2×10^{15} n_{eq} sensor reached saturation before breakdown. The data was compared to TCAD simulations performed with Synopsys Sentarus, incorporating the "Perugia" trap model [138] modified to account for radiation damage, as described in [139]. Despite the signal overestimate, the agreement between the measurements and simulations is acceptable given the uncertainties in fluences and detector thickness.

Finally, the signal spectra shape and cluster size distribution is not significantly different from the pre-irradiated case, as can be seen in figure 9.8 for a given sensor at a bias of 150 V and fluence of 5×10^{15} n_{eq}. This confirms the low charge sharing properties of 3D devices.

9.1.3 Laser source measurements

Laser scan measurements at different bias voltages were also performed. The measurements for one DC coupled device at a bias of 30 V is shown in figure 9.9. The

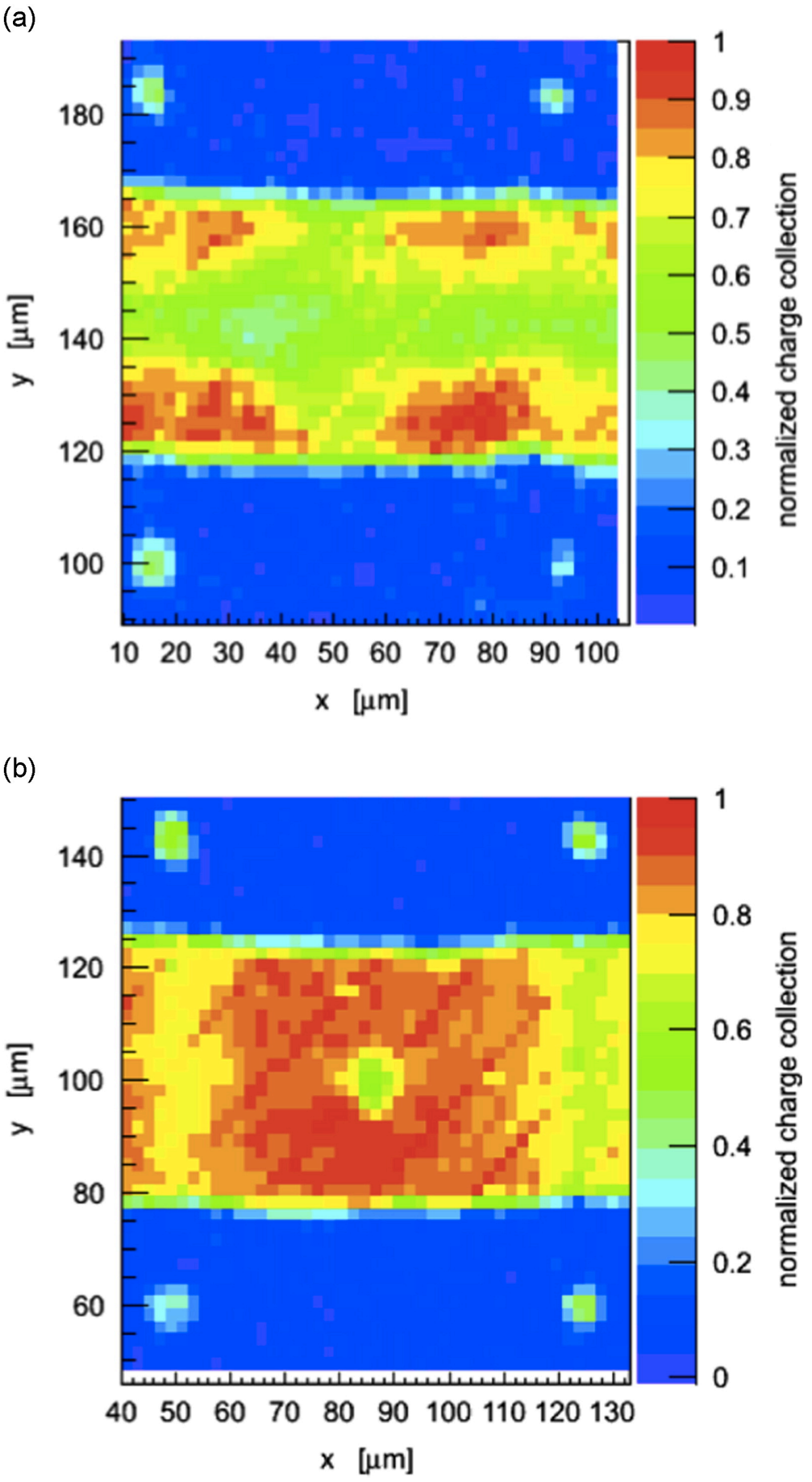

FIGURE 9.10: Laser scan performed on a sensor irradiated with protons to a fluence of $2{\times}10^{15}$ n_{eq} over an area of $\sim 100 \times 100$ μm^2 at a bias voltage of 50 V (top) and 120 V (bottom).

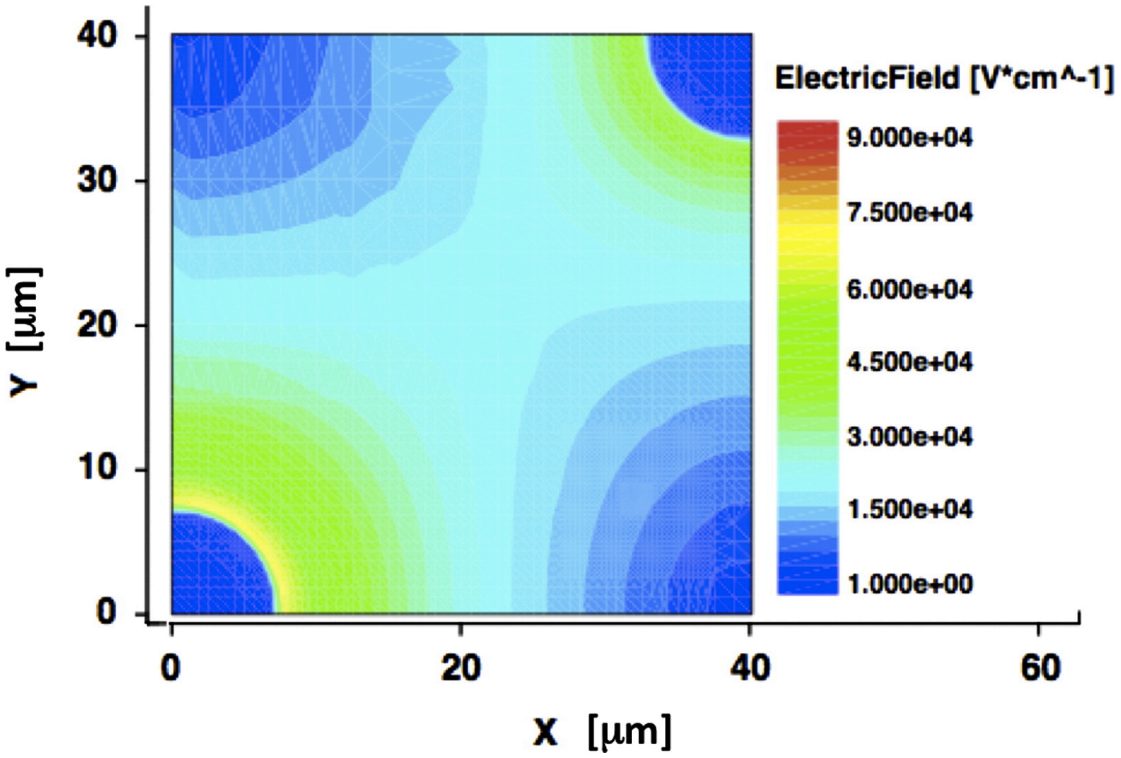

FIGURE 9.11: The electric field simulated on a sensor irradiated to 2×10^{15} n_{eq} at 120 V. The range of the simulation extends from the enter of a junction column (0 μm,0 μm) to the center of an ohmic column (40 μm, 40 μm).

scanned area corresponds to a region of $\sim 100 \times 100$ μm^2, four junction electrodes can be seen at the corners and one ohmic electrode (etched from the backside) is visible in the middle. Due to the reflectivity of the metal strips on the front surface, no charge is collected from these regions. The electrode columns also appear as inefficient regions because they are empty, which was observed also on previous generations of 3D-DDTC strip sensors [135]. The central region of the scan appears to be very uniform, confirming that the device is operating in full depletion and is fully efficient. The metal readout strips are slightly misaligned with respect to the electrodes, which is caused by the wafer bowing during the fabrication process [140]. As the metallization is one of the last steps, the lithography of this layer is particularly critical and a misalignment can occur already for wafer curvatures in the order of 10-20 μm. This effect was seen from optical inspection of the wafers and is here confirmed by the laser scan.

Measurements were also performed on irradiated sensors, one for each fluence. Comparisons are made to TCAD simulations described earlier. The results for a sensor irradiated to a fluence of 2×10^{15} n_{eq} is shown in figure 9.10 at two different bias voltages. For a bias of 50 V (top) the signal is maximal around the junction columns, while at 120 V (bottom) the maximum is in a wider region between the junction and ohmic columns. This is in good agreement with simulation, shown in figure 9.11, with a lateral spread of the depletion region and electric field. A low signal region can be seen in the measurement at 120 V between the junction columns of adjacent strips, due to two simultaneous effects: (a) the lower electric field in regions between electrodes of the same doping type, a well known property

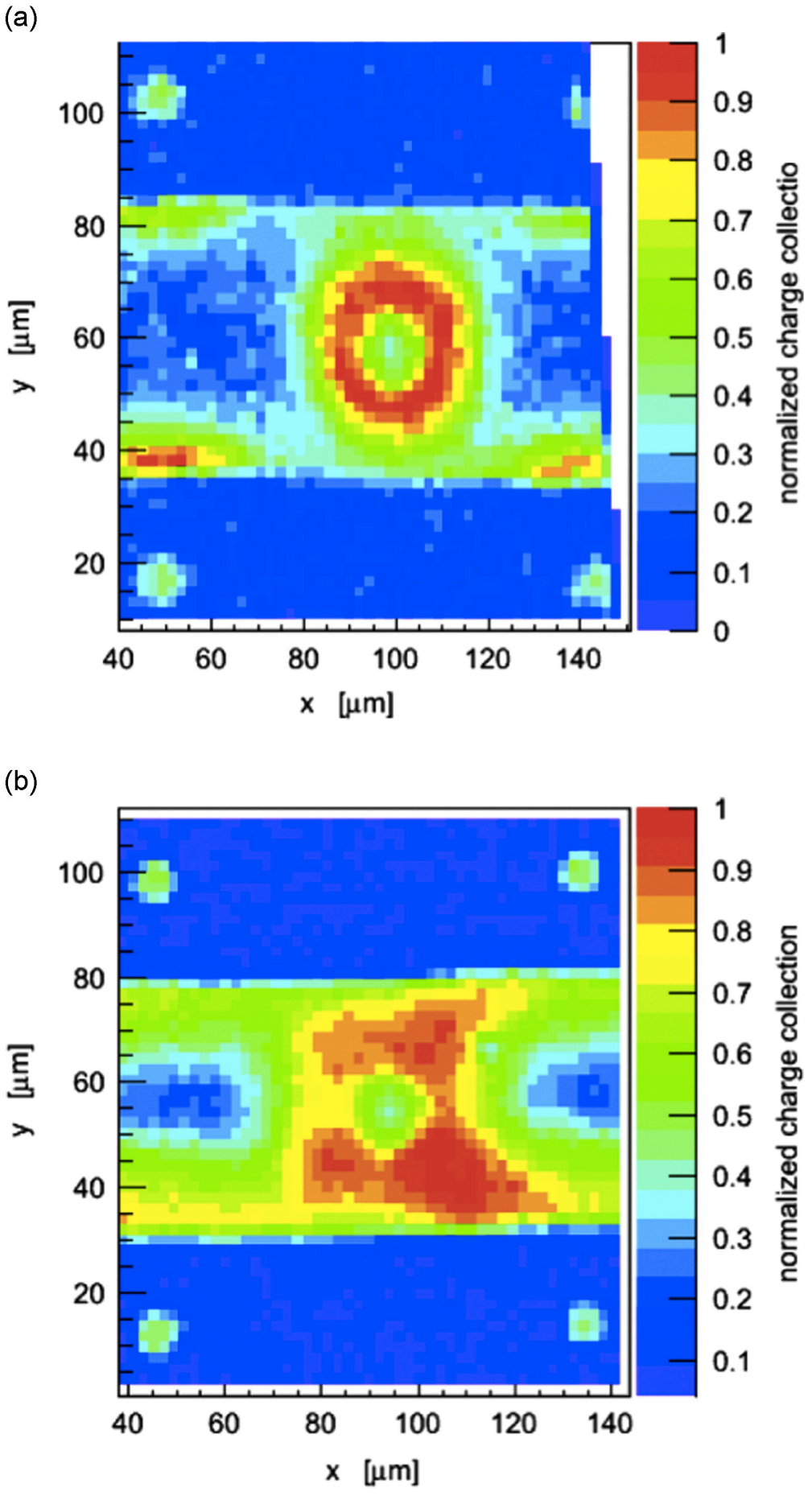

FIGURE 9.12: Laser scan performed on a sensor irradiated with protons to a fluence of 2×10^{16} n_{eq} over an area of $\sim 100 \times 100$ μm^2 at a bias voltage of 50 V (top) and 150 V (bottom).

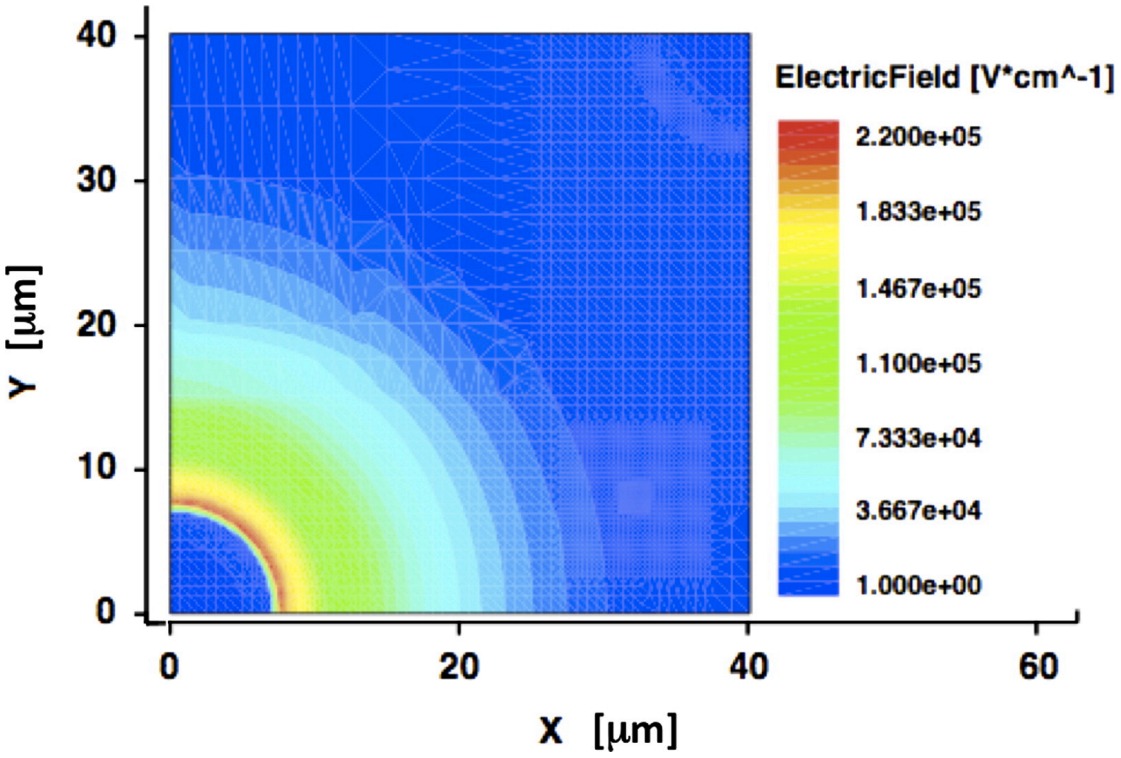

FIGURE 9.13: The electric field simulated on a sensor irradiated to 2×10^{16} n_{eq} at 150 V. The range of the simulation extends from the enter of a junction column (0 μm,0 μm) to the center of an ohmic column (40 μm, 40 μm).

of 3D detectors which makes those regions more prone to trapping; (b) the "non-collecting" strip will induce a fast signal on the "collecting" strip, so that a partial compensation of the fast part of the two signals happens since they are summed.

Results at 2×10^{16} n_{eq} can be seen in figure 9.12. The measurement taken at 50 V (top) shows a peculiar feature; a maximum around both the junction and ohmic columns which is indicative of a double-junction effect, also observed in CNM sensors [141]. At a larger voltage of 150 V, the high signal region extends between the junction and ohmic columns, albeit with a lower efficiency region in-between, for the same reasons as described above. These effects are enhanced due to the fact that the sensor is running below full depletion. This is confirmed by simulation, seen in figure 9.13, which fails to describe the double-junction effect.

9.1.4 Discussion

3D detectors are very promising detectors for use in high-radiation environments. One drawback of such devices is an increase in the complexity of the fabrication process, so that there is a need to simplify the fabrication process in order to drive down production costs. Double-sided Double Type Column (3D-DDTC) have been investigated as such an option. These sensors feature fully penetrating columnar electrodes, which have the advantage, as they do not require a support wafer for fabrication. They also exhibit better biasing than previous design, owing to an optimized punch-through biasing structure. Laser scan measurements show good alignment of the columnar electrodes, which is difficult to achieve in 3D devices.

Tests performed after proton irradiation showed good charge collection efficiency throughout the 3D unit cell, in line with previous measurements on such devices. At high fluences though, breakdown prevented full charge collection, a common problem in 3D devices owing to the high electric fields present in the device. Laser scan measurements indicate the presence of a double junction, which was not expected from TCAD simulation, so future simulations should include improved trap modelling to account for radiation damage at such high fluences.

9.2 Charge Collection Measurements on Dedicated Charge Multiplication SSDs

All sensors in this section come from the MICRON CM detector run described in the previous chapter. IV, CV and interstrip measurements were preformed prior to irradiation to measure the breakdown voltage and ensure proper processing of the sensors. Of those, only a subset of sensors having a breakdown voltage in excess of 1000 V were chosen for irradiation and subsequent charge collection measurements.

9.2.1 Measurement results

Clear signs of CM are observed for neutron irradiated sensors at a fluence of 1×10^{15} n_{eq} past 1000 V, as seen in figure 9.14, where 100% of the pre-irradiated charge is reached after 1200 V. The SNR remains relatively high (>15), as seen in figure 9.15. Proton irradiated sensors at 1×10^{15} n_{eq} showed no signs of CM up to 1100 V, shown in figure 9.16, although it is possible the signal could increase at higher voltages. The SNR stays high even at higher voltages, as seen in figure 9.17. The strip pitch is denoted by p, the width by w, sensors with intermediate biased strips by i, and floating intermediate strips by f. The number next to each are their respective values in μm.

Charge multiplication can also be observed at a neutron fluence of 5×10^{15} n_{eq}. A comparison of 2E imp. sensors can be seen in figure 9.18. A small enhancement of charge can also be seen in sensors from the extra diff. wafer, shown in figure 9.19. Although not as pronounced, the extra diff. w6, p80 sensor shows an increase of about 10-15% when compared to the std. w25, p80 sensor at high voltages.

The addition of an intermediate strips between readout electrodes is found to degrade the collected charge compared to a std. w25, p80 sensor, regardless if the strips were left biased or floating. This is seen in proton irradiated sensors at 1×10^{15} n_{eq} and in neutron irradiated sensors at 5×10^{15} n_{eq}, as seen in figures 9.20 and 9.21 respectively. Degradation is thought to be due to intermediate strips collecting charge, which does not reach the readout electronics, leading to a lower observed signal charge. When the strips are held to the same potential as the bias rail, the degradation is more pronounced compared to the situation when the strips are left floating. This is most likely due to the fact that the floating strips are at a lower bias voltage compared to the biased strips.

As expected, the w/p ratio plays an important role in enhancing charge multiplication. By taking the data at a constant bias voltage and plotting it as a

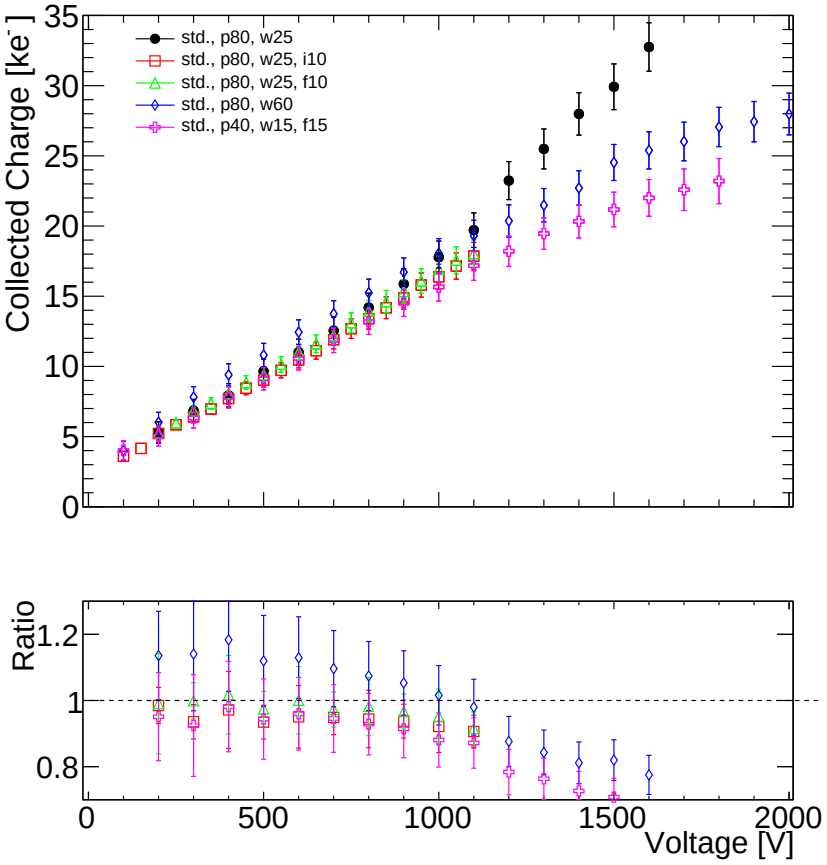

FIGURE 9.14: The collected charge (top) and the ratio compared to the standard (bottom) as a function of the bias voltage for detectors irradiated with protons to 1×10^{15} n_{eq}.

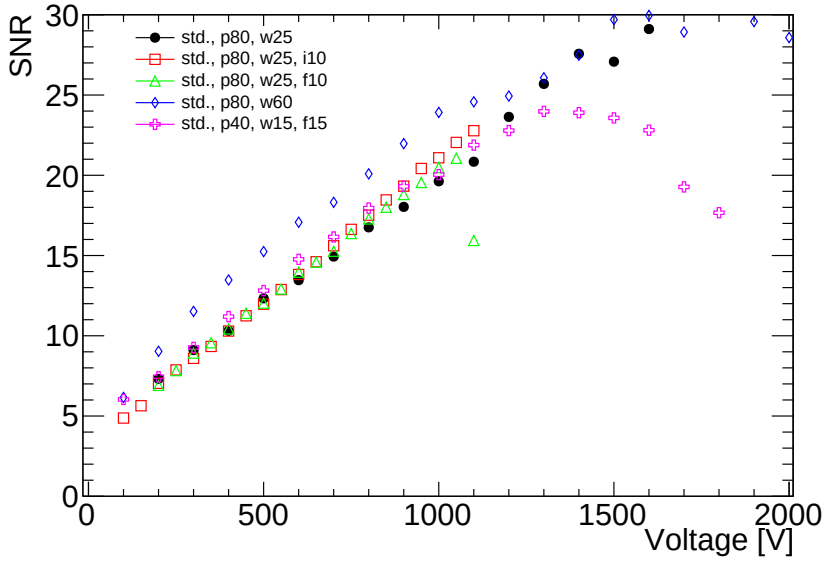

FIGURE 9.15: The signal-to-noise ratio (SNR) as a function of the bias voltage for detectors irradiated with protons to 1×10^{15} n_{eq}.

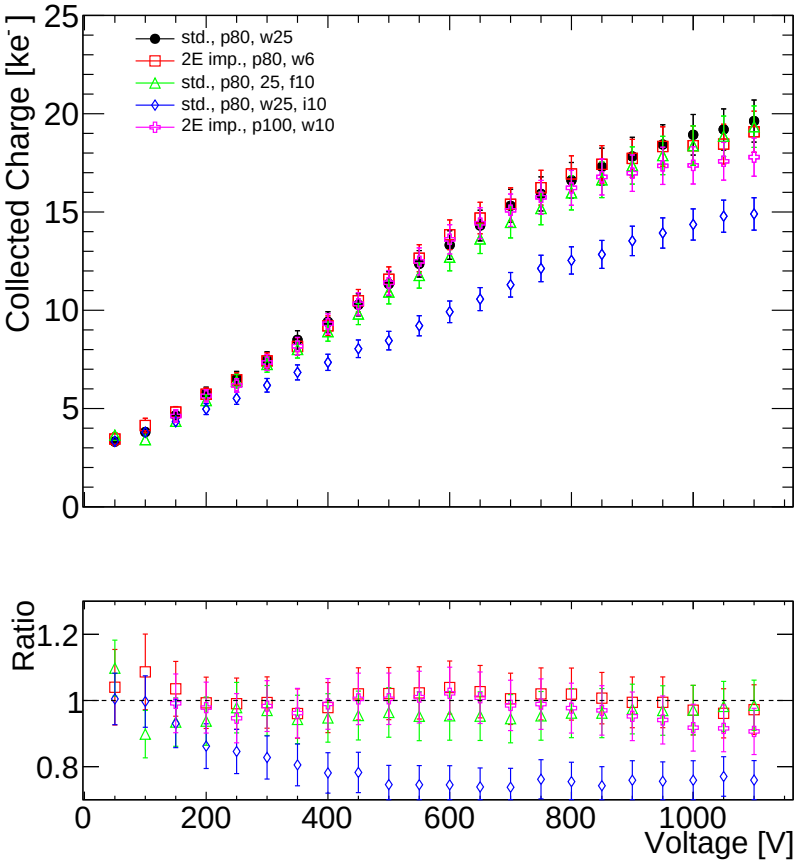

FIGURE 9.16: The collected charge (top) and the ratio compared to the standard (bottom) as a function of the bias voltage for detectors irradiated with protons to 1×10^{15} n_{eq}.

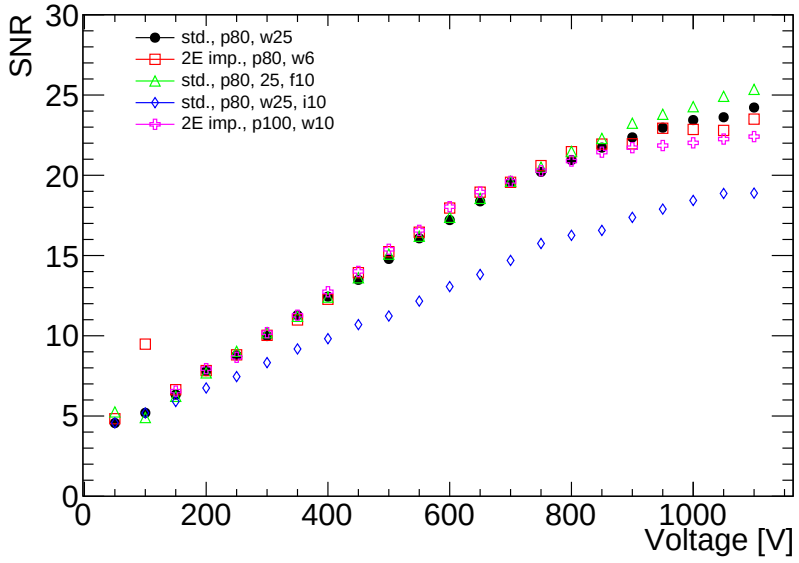

FIGURE 9.17: The signal-to-noise ratio (SNR) as a function of the bias voltage for detectors irradiated with protons to 1×10^{15} n_{eq}.

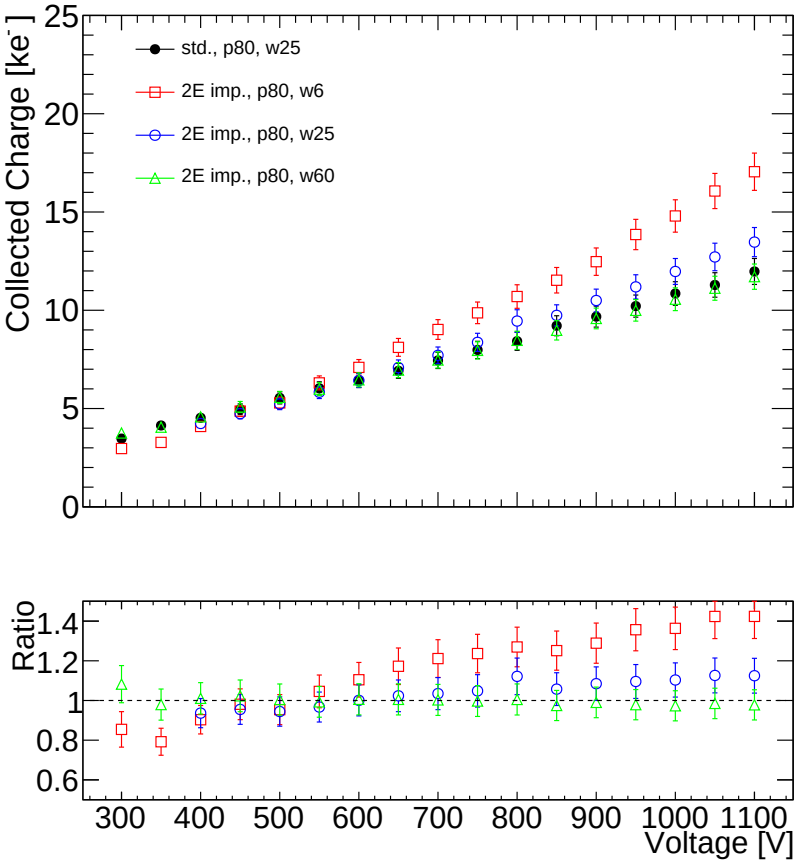

FIGURE 9.18: The collected charge (top) and the ratio compared to the standard (bottom) as a function of the bias voltage for 2E imp. sensors irradiated with neutrons to 5×10^{15} n_{eq}.

function of w/p, it is clear that lower w/p values lead to higher charge, shown in figure 9.22, for sensors irradiated with neutrons to 5×10^{15} n_{eq}. This is as expected as lower w/p values lead to a focusing of the electric field near at the strip edges [123]. Furthermore, when the data is plotted in such a fashion, a trend can be seen where not only does the wafer with twice the implant energy shows larger charge, but also the sensor from the wafer with double diffusion shows enhanced charge with respect to the standard wafer sensor. Although this enhancement is not as pronounced as the 2E imp. energy sensor, the trend is consistent for bias voltages above 600 V.

9.2.2 Discussion

Charge multiplication has been proposed as one candidate for designs in radiation hard silicon detectors. Most attempts aim at increasing the electric field near the readout electrodes past the critical value needed for impact ionization. Care must be taken to make sure the breakdown voltage and the noise do not hinder sensor performance, since impact ionization also tends to decrease the breakdown voltage while also enhancing the noise generated in the bulk.

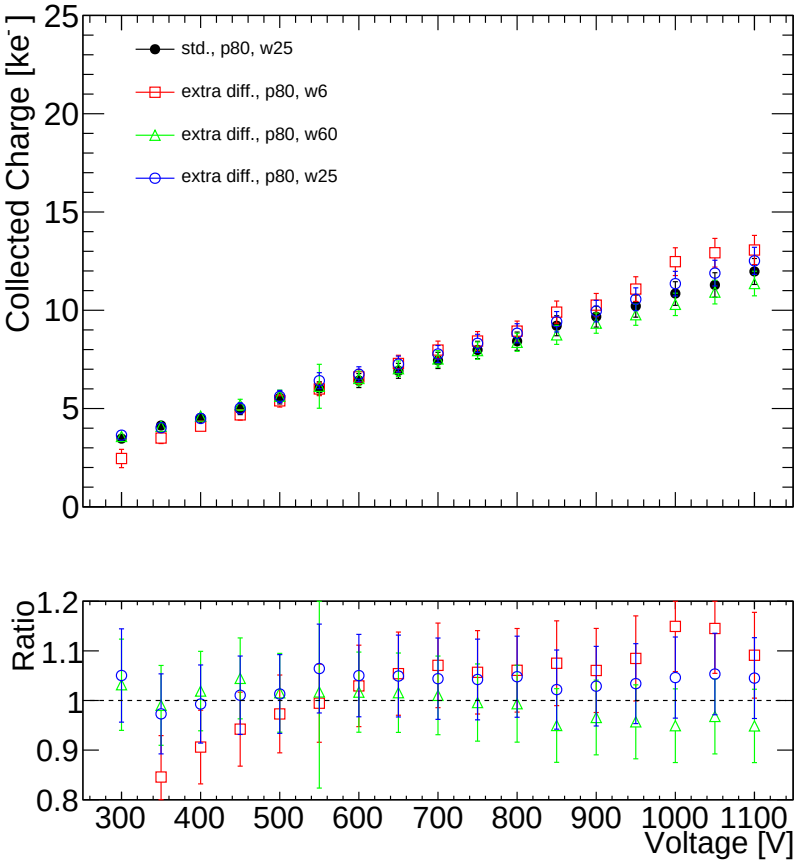

FIGURE 9.19: The collected charge (top) and the ratio compared to the standard (bottom) as a function of the bias voltage for extra diff. sensors irradiated with neutrons to 5×10^{15} n_{eq}.

Special processing of silicon sensors can lead to enhancements of the signal through the multiplication effect. Increasing both the implantation energy and diffusion time lead to increased charge after irradiation when compared to a standard processed sensor, although the increase was more pronounced in the former. The enhancement of charge is thought to be due to junctions being sharper and better defined, leading to large potential gradients and thus sufficiently large fields needed for CM.

As expected, geometry also plays a large role in signal enhancement. Of particular importance is the strip width over pitch ratio, w/p. This ratio measures how far the geometry is from a 1-D, planar diode situation, with $w/p = 1$ being a simple diode. As w/p decreases, the field lines at the strip edges become more dense, as there is less area for them to terminate on. Reducing the w/p ratio is perhaps the simplest and most effective approach to achieving charge multiplication in planar sensors.

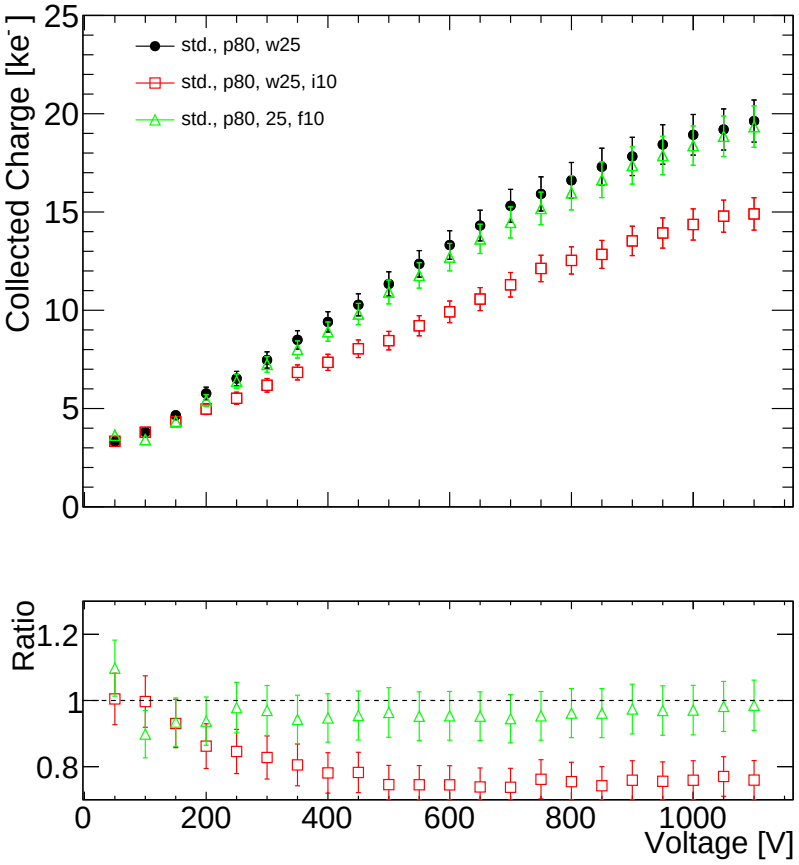

FIGURE 9.20: The collected charge (top) and the ratio compared to the standard (bottom) as a function of the bias voltage for sensors with an intermediate strip irradiated with protons to 1×10^{15} n_{eq}.

9.3 Long-term HV stability of the collected charge

9.3.1 Beta source measurements

Previous studies on unirradiated sensors have shown a drop in the detector signal over large time scales due to the Beta source used to generate signal electrons. It was shown that prolonged exposure to such a source slowly irradiates the sensor causing damage to the surface. Such a result is to be expected, as it is known that sensors suffer surface damage in the presence of ionizing radiation.

The collected charge for a pre-irradiated MICRON detector is shown in figure 9.23. The measurements were performed by holding the ^{90}Sr source in front of the sensor (as would be done during a normal test), and periodically scanning the bias voltage between 25 and 150 V. Results show no observable drop in the signal, contrary to what was observed in previous studies. A possible explanation for the discrepancy could be due to the surface isolation used during fabrication of the devices; the previous studies were on sensors containing p-stop isolation, while the MICRON sensor in this test was treated with p-spray. The p-spray could protect the whole surface of the sensor from low doses of ionizing radiation,

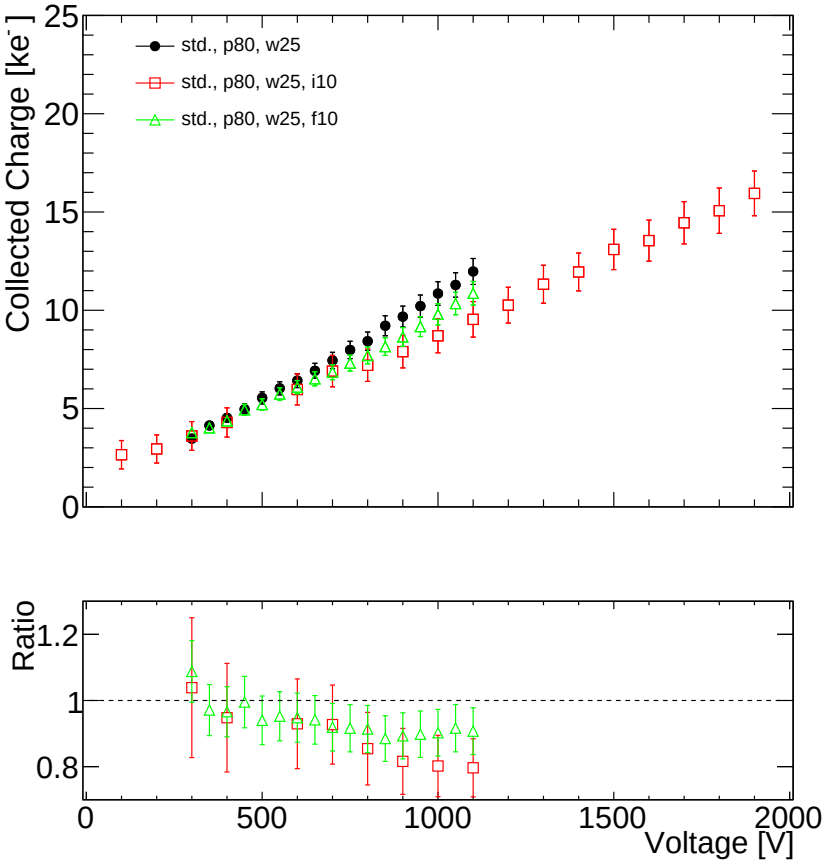

FIGURE 9.21: The collected charge (top) and the ratio compared to the standard (bottom) as a function of the bias voltage for sensors with an intermediate strip irradiated with neutrons to 5×10^{15} n_{eq}.

as it is sprayed uniformly across they entire sensor. The p-stop on the other hand consists of localized implants between readout strips, leaving much of the sensor prone to surface damage caused by ionizing radiation.

A drop in signal was observed on a few irradiated sensors held to a constant high voltage and measured with the β-source set-up. The effect is seen in neutron, proton, and mixed irradiated sensors, as well as being observed on sensors from different manufacturers, in this case MICRON and HPK.

Degradation of the collected charge for a MICRON sensor irradiated with neutrons to 5×10^{15} n_{eq} and held at 1300 V can be seen in figure 9.24. The sensor shows signs of CM, exhibiting a higher signal when compared to a standard processed sensor of the same geometry and fluence. The signal appears to drop quickly in the first day or two, with a subsequent drop in signal seen even after two weeks. After the drop was observed, the HV was removed for one day and applied again, in order to determine if the drop in signal was permanent. While a small recovery of the signal is observed, the original charge at $t = 0$ is never fully recovered. Indeed, even after removing the HV for eight months and testing

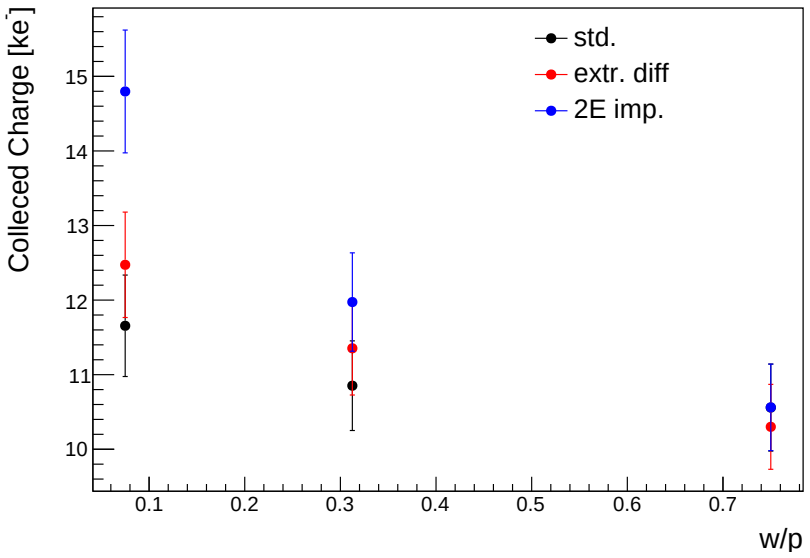

FIGURE 9.22: The collected charge as a function of w/p for sensors of different processing types irradiated with neutrons to 5×10^{15} n_{eq} and taken at $V_{bias} = 1000$ V. The trend of high charge collection for low w/p is in line with expectations.

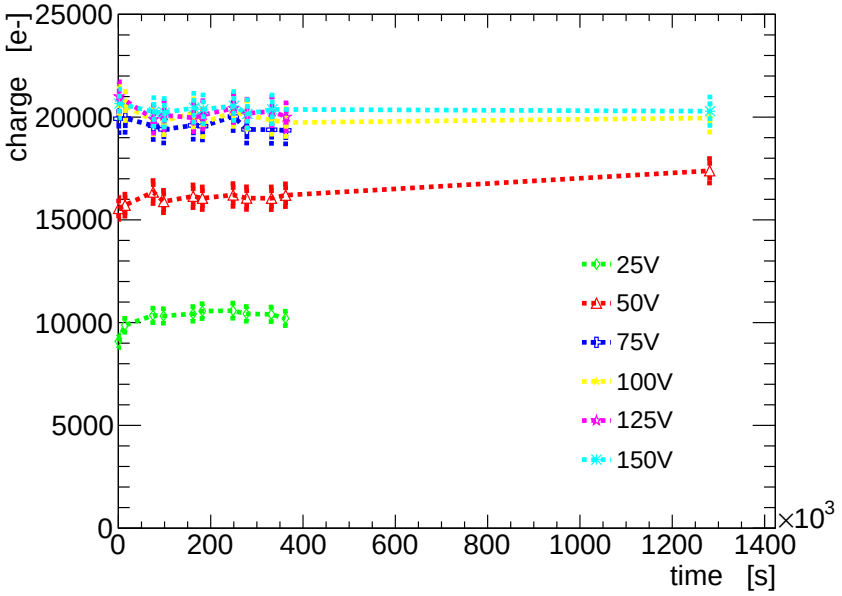

FIGURE 9.23: The collected charge as a function of time of an unirradiated MICRON sensor where the ^{90}Sr source is held in front of the sensor and the voltage is ramped periodically from 25-150 V during tests.

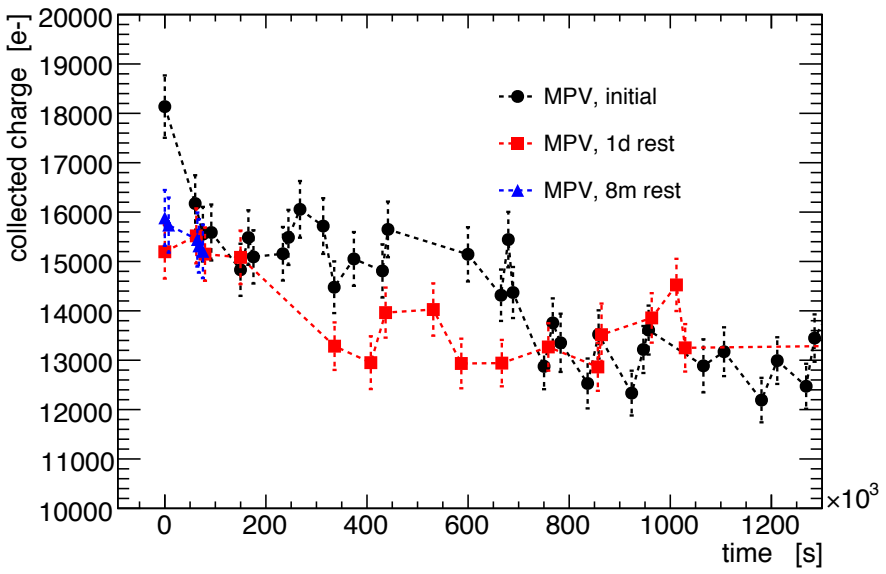

FIGURE 9.24: The collected charge as a function of time after applying a bias voltage of 1300 V for a MICRON sensor exhibiting signs of CM irradiated with neutrons to 5×10^{15} n_{eq}.

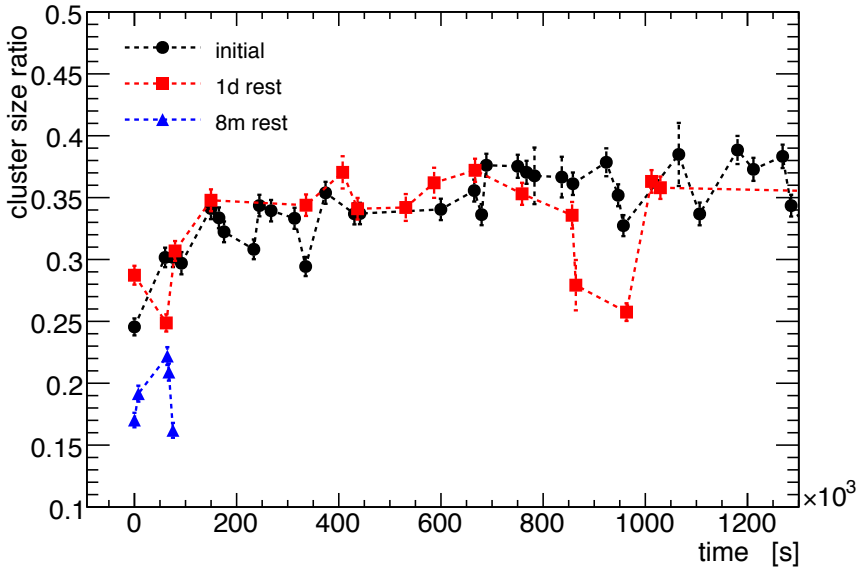

FIGURE 9.25: The ratio of 2- to 1-hit clusters as a function of time after applying a bias voltage of 1300 V for a MICRON sensor exhibiting signs of CM irradiated with neutrons to 5×10^{15} n_{eq}.

again, the original signal is not recovered, implying that a degradation of the collected charge seems to be permanent. The drop in signal is also accompanied by an increase in the cluster size, which is evident when looking at the ratio of 2- to 1-hit clusters as seen in figure 9.25. The Landau spectrum of the signal, seen in figure 9.26, also exhibits peculiar features, before and after the drop. The initial signal is seen to be broader than that of a standard sensor not exhibiting CM, and the shape of the signal appears to become double peaked.

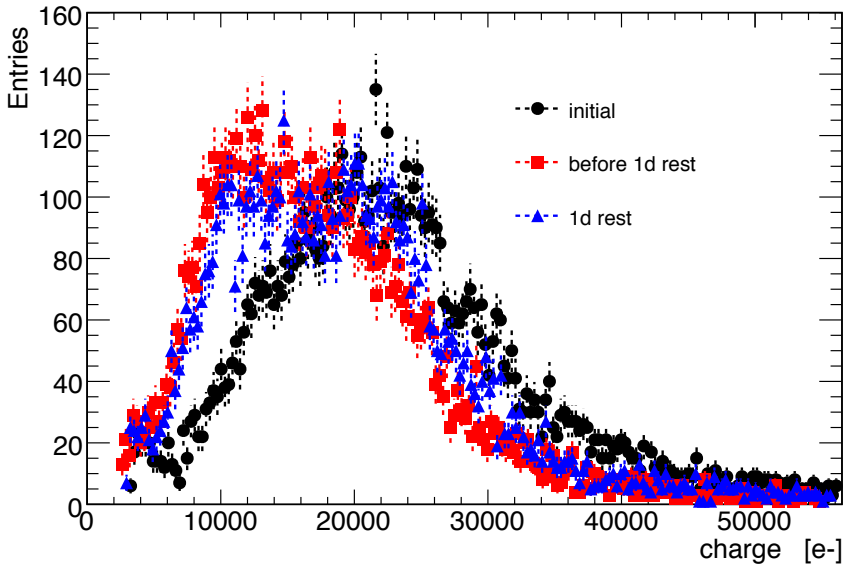

FIGURE 9.26: The signal spectra of the sensor shown in figure 9.24 before the drop (black), after the initial drop before the day of rest (red) and after the day of rest (blue).

Another MICRON sensor irradiated with neutrons to a fluence of 5×10^{15} n_{eq} and held to a reverse bias voltage of 1300 V also exhibited a drop in signal over time. While there seems to be a small increase in the collected charge at smaller times, the overall trend is that of signal loss, as seen in figure 9.27. After removing the HV for a day and retesting the sensor, the initial charge is never fully recovered, although a small increase at smaller times is still observed. The Landau spectrum of the signal is shown in figure 9.28, and a broadening of the signal is evident before the drop.

The degradation of the detector signal is also observed in proton irradiated sensors. Figure 9.30 shows the signal as a function of time for a proton irradiated MICRON sensor at a fluence of 5×10^{15} n_{eq} and held to a reverse bias voltage of 1300 V, while the Landau spectra are shown in figure 9.31. After the initial drop, the HV was removed from the sensor for one week and then repeated, where it is seen that the original signal is not recovered. The sensor was subsequently forward biased to 50 μA for one hour, in an attempt to relax any long-lived radiation-induced defect states that may have caused a drop in signal through modifications to the electric field. After no recovery of the signal was observed, the forward bias was increased to 100 μA for an additional hour, again with no recovery of the signal. Finally, in an attempt to reset any surface charges that may have caused a decrease in signal, the sensor was illuminated with UV light for one hour, which also did not show recovery the initial charge. This implies that the loss of signal is a permanent effect.

An HPK sensor from the ATLAS07 run, irradiated with a mixture of neutrons, protons and pions to 1×10^{15} n_{eq}, and previously reported on in [142], also exhibited a charge drop over time. The sensor was previously annealed to 4200 minutes at room temperature (22° C). The collected charge for this sensor held to a bias

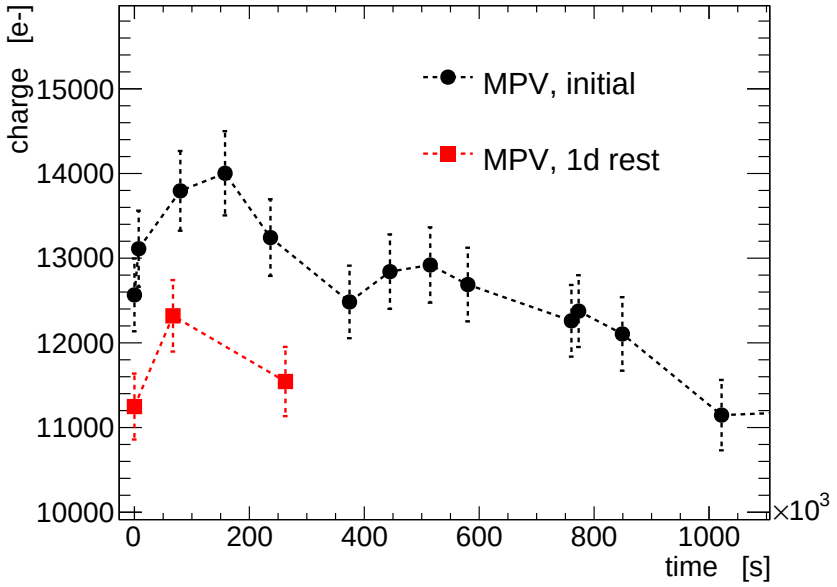

FIGURE 9.27: The collected charge as a function of time after applying a bias voltage of 1300 V for a MICRON sensor not exhibiting signs of CM irradiated with neutrons to 5×10^{15} n_{eq}.

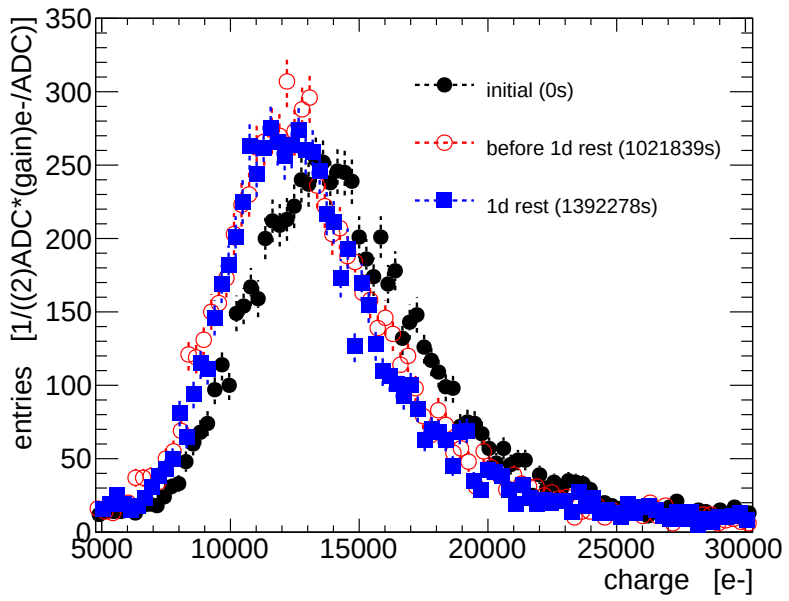

FIGURE 9.28: The signal spectra of the sensor shown in figure 9.27 before the drop (black), after the initial drop before the day of rest (red) and after the day of rest (blue).

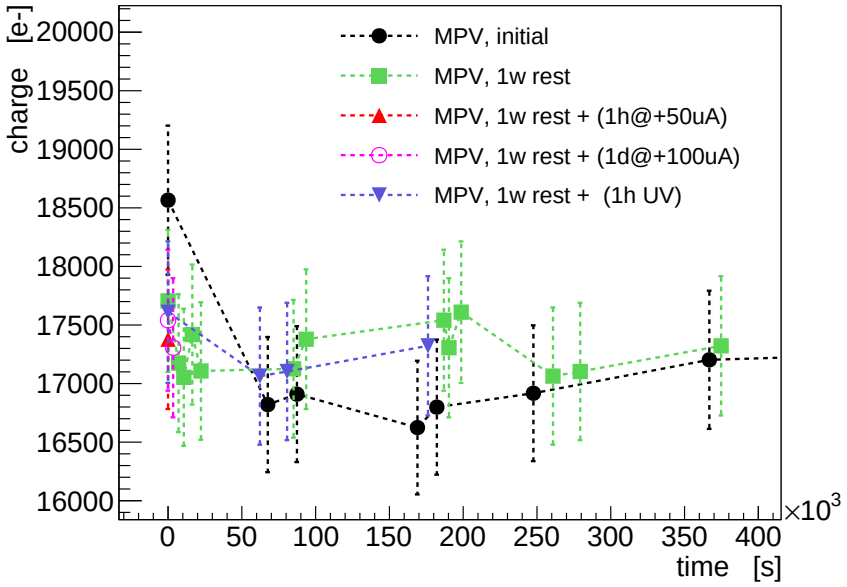

FIGURE 9.29: The collected charge as a function of time after applying a bias voltage of 1300 V for a MICRON sensor exhibiting signs of CM irradiated with protons to 1×10^{15} n_{eq}.

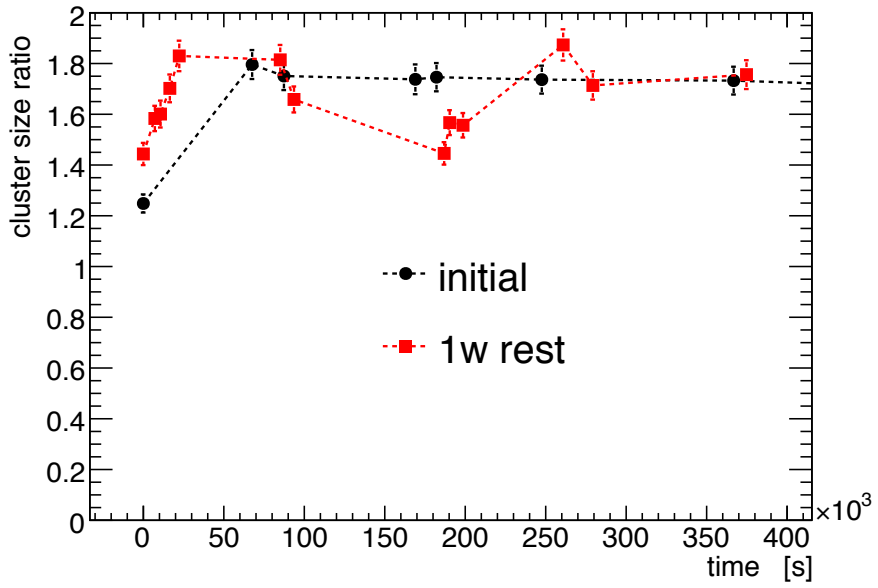

FIGURE 9.30: The ratio of 2- to 1-hit clusters as a function of time after applying a bias voltage of 1300 V for a MICRON sensor exhibiting signs of CM irradiated with protons to 1×10^{15} n_{eq}. The black curve is the initial measurement and the red is after resting for 1 week.

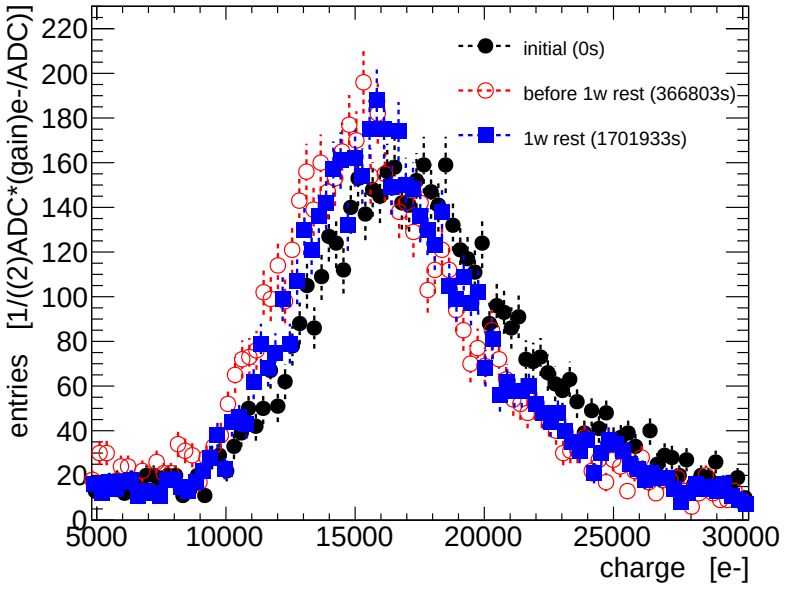

FIGURE 9.31: The signal spectra of the sensor shown in figure 9.27 before the drop (black), after the initial drop before a week of rest (red) and after a week of rest (blue).

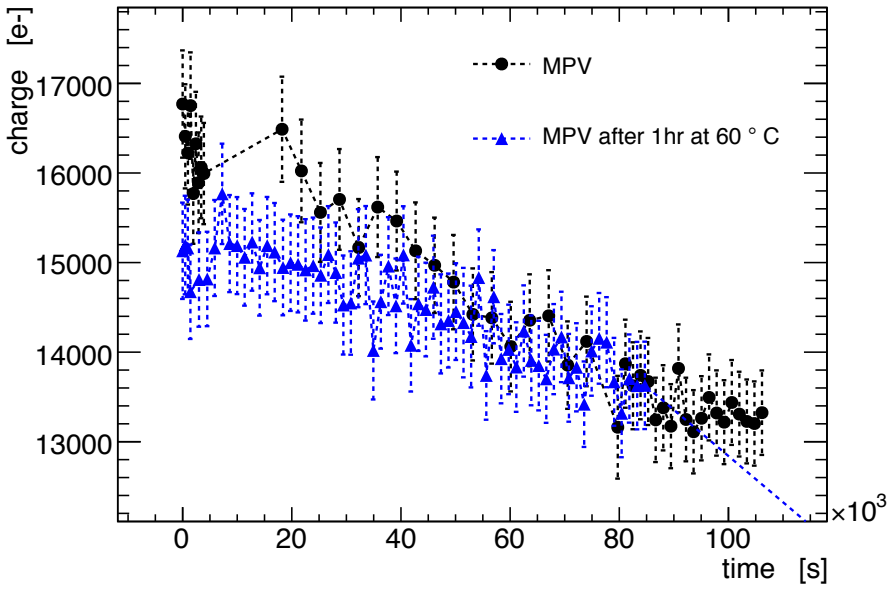

FIGURE 9.32: The collected charge as a function of time after applying a bias voltage of 1100 V for a HPK sensor irradiated with a mixture of protons, pions, and neutrons to 1×10^{15} n_{eq}. The black curve is the initial measurement and the blue is the measurement after a day of rest and accelerated annealing for one hour at 60° C.

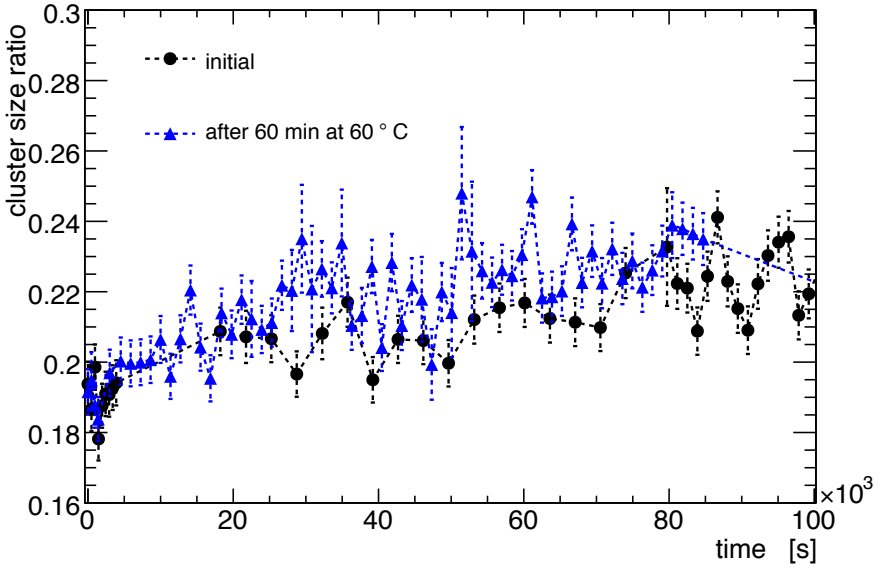

FIGURE 9.33: The ratio of 2- to 1-hit clusters for the sensor in 9.32. The black curve is the initial measurement and the blue is the measurement after a day of rest and accelerated annealing for one hour at 60° C.

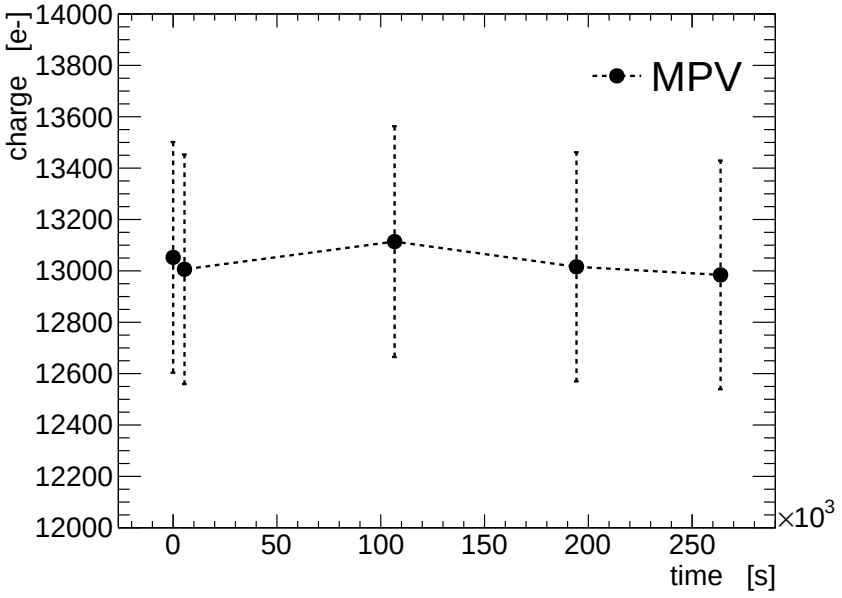

FIGURE 9.34: The collected charge as a function of time after applying a bias voltage of 700 V for a MICRON sensor not exhibiting signs of CM irradiated with neutrons to 1×10^{15} n_{eq}.

voltage of 1100 V as a function of time can be seen in figure 9.32 and the ratio of 2- to 1-hit clusters is seen in figure 9.33.

While a drop in signal was observed in irradiated detectors, this was limited to sensors at very high bias voltages. Several sensors exhibited no loss in signal when tested at lower bias voltages, although they also did not exhibit an enhancement of charge that is characteristic of charge multiplication. Figure 9.34 shows a standard processed MICRON sensor held to a bias voltage of 700 V and irradiated

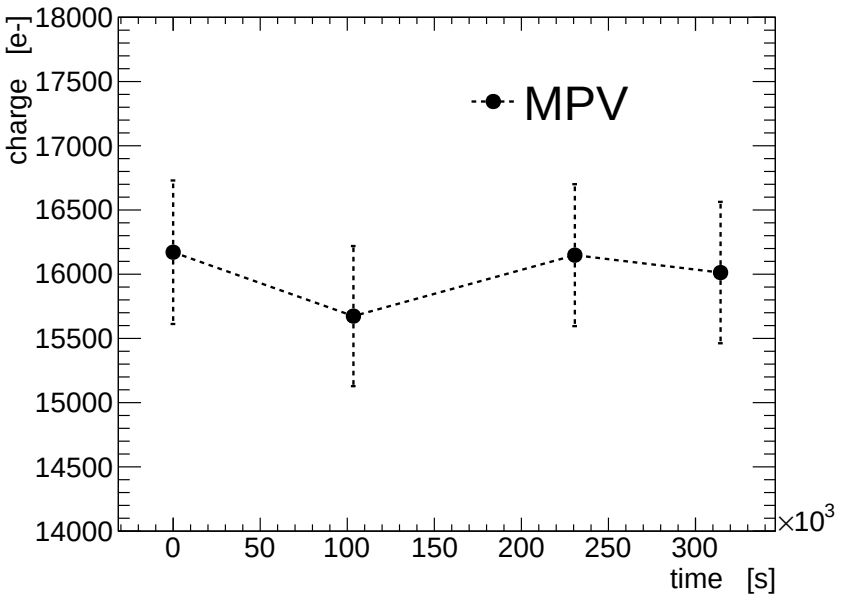

FIGURE 9.35: The collected charge as a function of time after applying a bias voltage of 820 V for a MICRON sensor not exhibiting signs of CM irradiated with protons to 1×10^{15} n_{eq}.

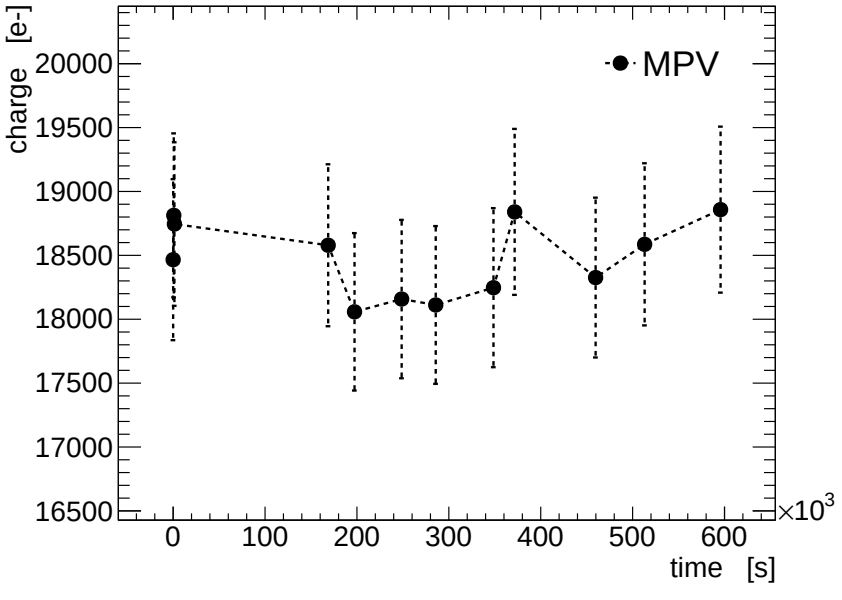

FIGURE 9.36: The collected charge as a function of time after applying a bias voltage of 1000 V for a MICRON sensor not exhibiting signs of CM irradiated with protons to 1×10^{15} n_{eq}.

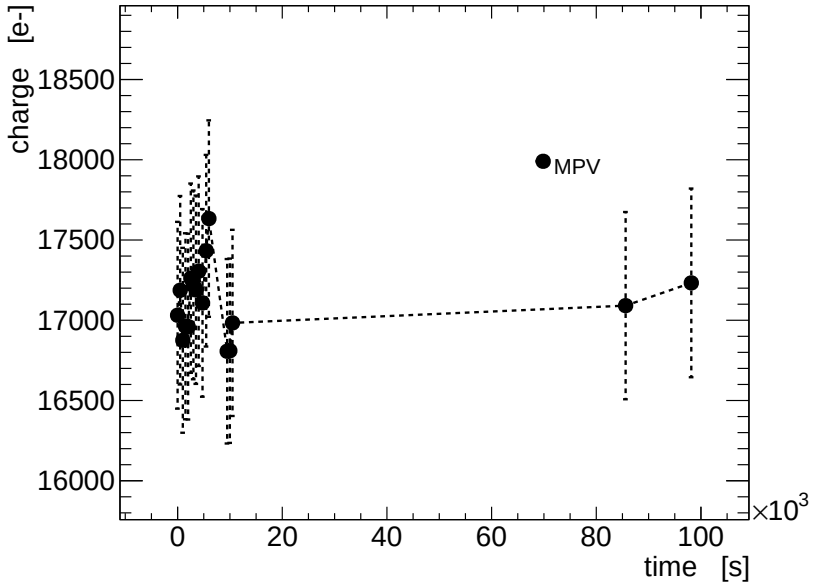

FIGURE 9.37: The collected charge as a function of time after applying a bias voltage of 1100 V for a HPK sensor not exhibiting signs of CM irradiated with protons to 2×10^{15} n_{eq}.

to a fluence of 1×10^{15} n_{eq} with neutrons. Figures 9.35 and 9.36 show a standard processed MICRON sensor held to a bias voltage 820 V and a MICRON sensor processed with twice the implantation energy held to a bias voltage of 1000 V respectively, both being irradiated with protons to a fluence of 1×10^{15} n_{eq}. Additionally, a HPK sensor irradiated to 2×10^{15} n_{eq} with protons held to a bias voltage of 1100 V did also not exhibit a decrease in signal over time, as seen in figure 9.37.

9.3.2 Laser source measurements

Laser scan measurements were also carried out in order to investigate the electric field strength near the sensor surface. Only measurements in one axis, perpendicular to the strip alignment, were performed due to the long time needed to perform the measurements in both the x and y directions (upward of a day). This ensures that the change in the signal during the individual laser scans has a minimal effect over the entire timescale investigated.

The sensor chosen for the laser scan measurements was an ATLAS07 sensor, irradiated with a mixture of protons, neutrons and pions and annealed for 4200 minutes at 60° C. The sensor had previously been tested with beta source measurements which are reported in [142] The sensor was also tested with beta source at a bias voltage 1100 V for 8 hours, in which a drop in signal was observed. The laser scan measurements, also taken at 1100 V, are shown in figure 9.38.

Measurements were carried out once a day for four days, during which the HV was continuously applied. A larger drop in the signal is seen after only one day at 1100 V, and saturates already at two days. Removing the HV for a day, and then reapplying it leads to a recovery of the charge from the beginning of the tests. This recovery does not reach the initial charge, which was lost after the

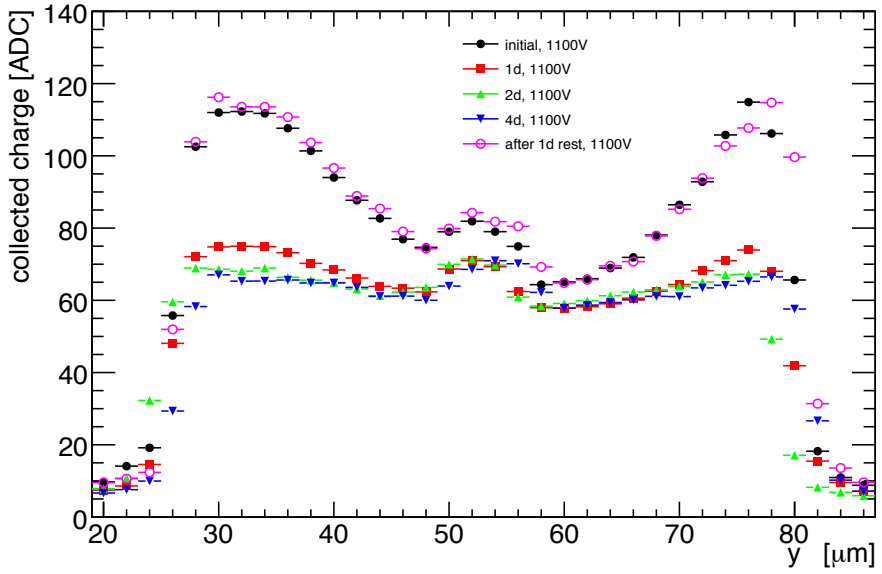

FIGURE 9.38: Laser scan measurement performed perpendicular to the strip length for an ATLAS07 sensor after mixed irradiated and accelerated annealing at 60° C for 4200 minutes and tested at 1100V. The drop in signal is seen after a couple days and the recovery is evident after removing the HV for a day and reapplying.

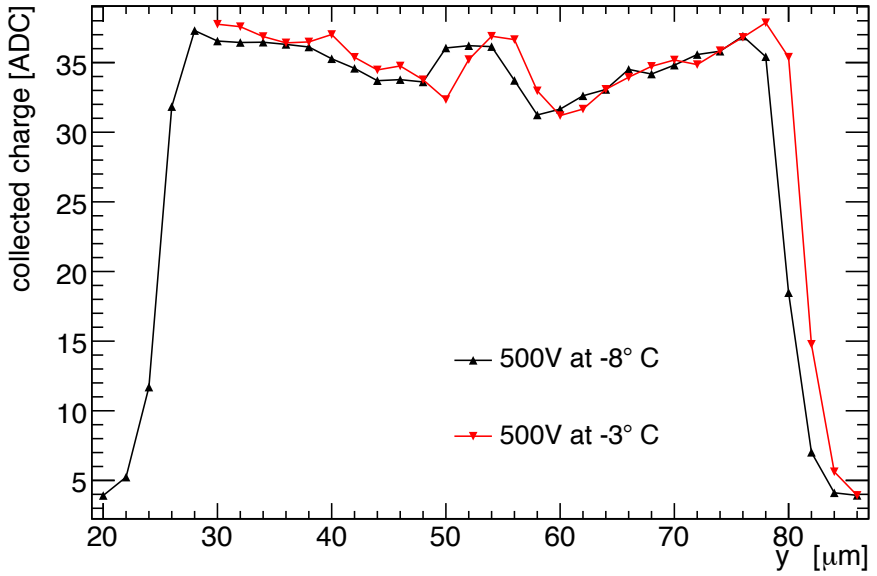

FIGURE 9.39: Laser scan measurement performed perpendicular to the strip length for an ATLAS07 sensor after mixed irradiated and accelerated annealing at 60° C for 4200 minutes and tested at 500V at two different temperatures. The charge does not depend on temperature to first order.

first beta tests. This partial recovery of the signal is consistent with what is found in beta source measurements, and implies some polarization of the electric field. Areas where the signal drops to zero represent the readout electrodes, where the laser is reflected by the AC coupled aluminum strips, and a small enhancement of charge can be seen due to the p-stop implant used for strip isolation.

Due to the long time-scales involved in the measurements, the temperature was not always constant. Refilling of the liquid nitrogen tank that was used in the cooling system caused temperatures during the test to vary by up to 10° C during a single measurement. The effect of the temperature on the signal was investigated, and can be seen in figure 9.39 for two different temperatures of -3° C and -8° C. As expected, to first order the charge is independent of the temperature during the measurement.

9.3.3 Discussion

What is evident is that the drop in signal can be broken into separate parts: a permanent non-recoverable drop of the initial charge, and a temporary drop that is recoverable after switching off the HV. Although the nature of the signal drop over large times is not well understood, there are a few possible explanations.

The ^{90}Sr source used during the measurements to create the signal will slowly irradiate the sensor, leading to surface damage that reduces the electric field near the readout electrodes. This seems to be ruled out by the source test done on the pre-irradiated sensor in figure 9.23. And the fact that the drop is seen in heavily irradiated proton sensors, where the surface damage should saturate at a relatively low dose, and on the heavily irradiated neutron sensors, where the gamma dose is already large enough to saturate the surface as well [143], seems to also rule out surface damage caused by the ^{90}Sr source. Also, the effect is seen in laser scan measurents, where no gamma source is present.

Another possible explanation would be polarization of the electric field in the sensor, which has been observed not only in large band gap materials like diamond, but also in materials with smaller band-gaps like CdTe [144, 145]. Defect states with very long lifetimes would lead to a time dependence of the space charge within the device after applying a bias voltage, which in turn leads to a reduction in the effective depleted volume of the sensor. Once the bias voltage is removed, the long-lived defect states would relax, and the sensor would return to its initial configuration. Thus, polarization could explain the the temporary, recoverable part of the signal. The drawback of such an explanation is that polarization in the silicon bulk should happen at any voltage, not just on extremely large one. Capture cross sections for such defect states in silicon which correspond to lifetimes on the scale of these measurements would also be extremely small, on the order of 10^{-21} to 10^{-22} m^2.

A polarization effect can be attributed to a bistable defect. This could lead to a bias dependent effect [146–148], as bistable defects can modify their state with the bias voltage. They can also have very long lifetimes without the need to invoke the idea of a capture cross section, *which is not a unique property of an*

interface state[1] [149].

Interface states also can be very long lived, which would account for the long time scale of the drop. They lie at the surface of the detector, where the electric fields are largest and CM is occurring, and would nonetheless be involved in the evolution of the field near the surface.

The permanent drop in signal is more puzzling, and indeed more detrimental to the use of CM devices for radiation-hard detectors. The electric field could be inducing a sort of annealing in the sensor over long time periods. High electric fields near the readout strip edges, which are needed to induce CM, could increase the temperature locally in the region where the fields are their highest. This would lead to different parts of the sensor annealing at different rates, with the regions near the strip edges with the highest field annealing faster than the rest of the sensor. This could result in a decrease of the field in these regions, reducing the effect of CM, and hence leading to less signal being collected over time. The advantage of this explanation is that the effect is permanent and should depend on the strength of the electric field, and hence the bias voltage, which is what is currently observed. The drawback of this explanation is that it is not as well documented as the other mechanisms.

The signal drop has been observed for different sensors of varying geometry and processing, coming from different manufacturers, and for different radiation flavors. Regardless of the physics of the signal degradation in CM devices at high voltages, one thing is clear; it is a real phenomena and its effects must be well understood before applying CM as a solution to radiation-hard silicon detectors. Indeed, given the current situation, the feasibility of using CM detectors in situations such as the HL-LHC seems dire.

[1] The same can be said not just of interface states, but of bulk defects as well. A cross section is a measure of the strength of an *interaction*, and thus not a unique property of a particle or defect state.

Chapter 10

Summary and Conclusions

The Large Hadron Collider is currently the most powerful particle accelerator in the world, designed to collide protons at a center-of-mass energy of $\sqrt{s} = 14$ TeV. ATLAS is one of four main experiments at the LHC. It is a general purpose detector designed to search for new physics and provide precision measurements of Standard Model processes. The determination and constraint of various parton distribution functions is included in this physics program.

Throughout its operational lifetime, the LHC is foreseen to undergo a major upgrade that will see the instantaneous luminosity increased by a factor of five and the integrated luminosity by a factor of ten. The ATLAS detector is also envisioned to undergo an upgrade, to cope with the increased data volumes and harsher radiation environment that such an increase in luminosity will bring.

The innermost layers of ATLAS consist of a large number of silicon detectors. Signal loss due to radiation damage is a primary concern for silicon detectors in ATLAS. These will be exposed to large amounts of radiation during the lifetime of ATLAS and the LHC, with the high luminosity upgrade pushing current detector technologies to the limit. An intense R&D program has been carried out in the past years aimed at finding novel ways to cope with this increased radiation dose. One option for radiation-hard detector designs has been so called charge multiplication detectors.

The work presented here is composed of two parts. In the first part, a physics analysis using the 2012 ATLAS data set was carried out, searching for events with a W boson accompanied by a charm quark. This measurement is sensitive to the strange quark content of the proton, and helps constrain the strange quark PDF. The second part of this work concentrated on detector R&D, studying the effectiveness of 3D and charge multiplication detectors as a viable candidates for radiation-hard sensors needed for the luminosity upgrade of ATLAS. Particular emphasis is put on the stability and longevity of detectors operating in the charge multiplication mode.

10.1 W+c cross-section

The production cross-section of a W boson in association with a charm quark in pp collisions has been measured using the 2012 ATLAS data set taken at $\sqrt{s} = 8$ TeV. The analysis searches in a phase space where the W boson candidate and a

charm quark, tagged by a muon from a semileptonic decay, have opposite charge sign. In particular, the difference in the number of events where the W boson and charm quark have opposite sign to those where the two have the same sign is determined. In this subtraction, many important background processes cancel out, and the W+c signal is relatively clean. Much of the analysis focuses on estimation of residual background, in particular QCD and W+light-jets, where data driven methods are employed. The measurement is carried out for events that have 1-jet, 2-jets or 1+2-jets. The 1+2-jets measurement is used to determine the 1-jet inclusive cross-section. Furthermore, the measurement of the ratio $\sigma^{fid,OS-SS}_{W^+\bar{c}}/\sigma^{fid,OS-SS}_{W^-c}$ is also carried out to investigate the possible asymmetry between the strange quark and anti-strange quark PDF. The results are compared to LO theoretical predictions, but the comparison to NLO predictions with different PDF sets would significantly improve interpretation of the results.

The measured cross-sections for a W boson accompanied by a charm quark are 59.68 ± 0.64(stat) ± 3.79(syst) pb for the 1-jet measurement, 15.74 ± 0.41(stat) ± 1.40(syst) pb for the 2-jet measurement and 77.72 ± 0.74(stat) ± 4.68(syst) pb for the 1-jet inclusive measurement. Their respective ratios for $W^+ + \bar{c}$ to $W^- + c$ production were measured to be 0.92 ± 0.02(stat) ± 0.04(syst), 0.78 ± 0.03(stat) ± 0.05(syst) and 0.89 ± 0.01(stat) ± 0.03(syst). Results are in line with the LO predictions, with the exception of the 2-jet ratio measurement, where the difference between measurement and prediction is larger than two standard deviations. More precise prediction at NLO would shed light on this result.

10.2 Charge multiplication detectors

Charge multiplication detectors, designed to increase the signal that gets partially lost after radiation damage, have been investigated. Multiplication of the signal is achieved by increasing the electric field past the critical point to induce impact ionization. Various methods are employed to achieve such large fields, from changes to the detector geometry, mainly through a decrease in the strip width over pitch ratio, to changing the processing of the strip implants, thus creating more sharply defined junctions.

This study focused on charge collection measurements, carried out with electrons coming from the decay of Sr^{90}, as well as from an infrared laser. The electrons from the Sr^{90} source closely mimic minimum ionizing particles, and are used to measure absolute charge collection of detectors to asses their performance. Measurements carried out with the IR laser serve to investigate the spatial uniformity of the electric field near the surface of the sensors, as the IR laser light does not penetrate fully through the detector thickness and is thus not useful in absolute charge collection measurements. Several sensors were tested before and after irradiation, including irradiations with protons, neutrons, pions or a combination of radiation types. Furthermore, high voltage tests were carried out over large time scales (days to weeks), where a high voltage was applied continuously to detectors once in the charge multiplication mode.

A "standard" detector having a nominal strip width of 25 μm and and pitch of 85 μm with no special processing was used as a benchmark to assess whether

sensors showed signs of charge multiplication. Several sensors exhibited signs of charge multiplication, with a pronounced effect seen in sensors with very low width over pitch ratios and sensors whose strip implants were processed with twice the normal implantation energy.

The long-term high voltage tests on irradiated devices yielded interesting results. Sensors held to a high bias voltage and initially showing signs of charge multiplication exhibited a decrease of the total collected charge, with a significant drop seen already in the first day or two of the measurement. The drop in signal was semi-permanent; there was a large permanent component, while a small recovery was seen if allowing the sensors to "rest", which means turning off the high voltage for a period of time. The time for the resting period ranged from a few hours up to many months. The recovery of signal was modest when measurements were repeated on such devices, and the original collected charge at the beginning of the measurement was never fully recovered. This was observed on sensors irradiated with different radiation species and from different detector manufacturers.

A few explanations are put forward to explain the charge drop, from polarization of the electric field due to long lived bulk or interface defect states to localized annealing of the sensor due to high electric field regions that would increase the temperature significantly in those regions. Polarization seems to be a likely candidate to explain the temporary drop in signal, as any long-lived defect states would revert to their initial state after switching off the high voltage. Electric field induced annealing could explain the permanent drop, as annealing is itself an irreversible process. More studies need to be carried out to investigate the exact nature of the signal loss. Whatever the explanation might be, it is clear that such tests call into question the viability of such sensors as radiation-hard detectors, at least in their applicability in the operational conditions of the HL-LHC.

Aside from studies on charge multiplication devices, 3D detectors were also studied. Tests focused on double sided 3D detectors, which aim to simplify the fabrication process of such devices and bring down production costs. Detectors showed good charge collection before irradiation, and laser scan measurements confirmed good alignment of the columnar electrodes, which is difficult to achieve during fabrication. Detectors were then irradiated, and showed compatible results to other sensors fabricated in the same way and tested at other institutes. An interesting discovery was the formation of a double junction in highly irradiated detectors, which was not expected from TCAD simulations.

Acknowledgements

The work in this thesis would not have been possible if it were not for the help of countless others.

First and foremost, I would like to thank Prof. Karl Jakobs for giving me the incredible opportunity to work in his group and for setting the bar so high as to never compromise one's integrity. To say this PhD would not be possible without him would be an understatement. He continually pushed me to work harder and better, and for this I am forever in his debt.

Thanks to Ulrich Parzefall, for his unwavering support, guidance and friendship. Without him I would not have been able to make it through these four years, and I consider him to be one of the most genuine, generous, honest and caring people I know.

I want to thank Christian Weiser, who always made time for me, took the care to rigorously scrutinize my work, and for his insights and countless discussions. I know I didn't make your job any easier, Christian.

Thanks to Kristin Lohwasser, who took the time to get me up to speed in my analysis and helped me every step of the way.

A special thanks to Riccardo Mori, a friend and colleague, who I have the utmost respect for. Most of the work on detector development in this thesis would not have been possible without him, and he provided countless hours of stimulating discussion and help. The insights I gained from working with him have has a tremendous impact on me as a scientist and physicist.

Thanks to Susanne Kühn for helping carry out measurements and providing useful feedback.

Marc Hauser was of extreme help, took several measurements, bonded countless detector boards, and put up with all the crap on my desk in the office we shared.

Besnik Lecini helped perform measurements on 3D detectors, and provided much needed comic relief.

I would like to thank Gian-Franco Dalla Betta for useful discussions on detectors and for procurement of many sensors tested in this thesis.

I want to thank Gianluigi Casse for fruitful discussions on detectors and helping to procure additional sensors.

I could not have managed without the help of Philip Sommer and Felix Bührer, who took the time to help me with what at times I am sure seemed like trivial computer issues, but would have taken me days or weeks to get through nonetheless.

I would also like to thank Vakhtang Tsiskaridze for helping keep my potassium levels healthy with his monthly bananas. Also because he is just a great guy who never refuses to help others.

Finally I would like to thank Christina Skorek, probably the most useful person in the world.

Appendix A

Monte Carlo Samples used in the W+c cross section measurement

A list of Monte Carlo samples used in background estimation, as well as those used in the correction from the meausred yields to the cross-section are presentes here.

Process	Sample ID	Generator
W($e\nu$)+light-jets	147025-147030	ALPGEN+PYTHIA
W($\mu\nu$)+light-jets	147033-147038	ALPGEN+PYTHIA
W($\tau\nu$)+light-jets	147041-147046	ALPGEN+PYTHIA
Z(ee)+jets	117650-117655	ALPGEN+PYTHIA
Z($\mu\mu$)+jets	117660-117665	ALPGEN+PYTHIA
Z($\tau\tau$)+jets	117670-117675	ALPGEN+PYTHIA
Z(ee)+bb+jets	110817-110820	ALPGEN+PYTHIA
Z($\mu\mu$)+bb+jets	110821-110824	ALPGEN+PYTHIA
Z($\tau\tau$)+bb+jets	110825-110828	ALPGEN+PYTHIA
WW	126928-126936	POWHEG+PYTHIA
W($e\nu$)Z	129477-129479, 129486-129488	POWHEG+PYTHIA
W($\mu\nu$)Z	129480-129482, 129489-129491	POWHEG+PYTHIA
W($\tau\nu$)Z	129483-129485, 129492-129494	POWHEG+PYTHIA
ZZ	126937-126942, 126949-126951	POWHEG+PYTHIA
$t\bar{t}$	117050	POWHEG+PYTHIA
Single Top	117360-117362	AcerMC+PYTHIA
W+$b\bar{b}$	200256-200259	ALPGEN+PYTHIA
W+$c\bar{c}$	200156-200159	ALPGEN+PYTHIA

TABLE A.1: Monte Carlo Samples used for background estimation in W+c cross-section measurement

Process	Sample ID	Generator
W+c+jets	200056-200060	ALPGEN+PYTHIA
W+$c(c \to \mu)$+jets	185900-185904	ALPGEN+PYTHIA
W+c+jets	167741	SHERPA

TABLE A.2: Monte Carlo Samples used as signal in the W+c cross-section measurement

Appendix B

Control plots for the OS and SS samples

Various kinematic distributions are checked and a comparison between data and Mone Carlo prediction are made. Here one can find the same distributions as in chapter 7, corresponding to the OS and SS samples. These samples are shown to check background distributions, since they cancel in the OS-SS plots shown in chapter 7.

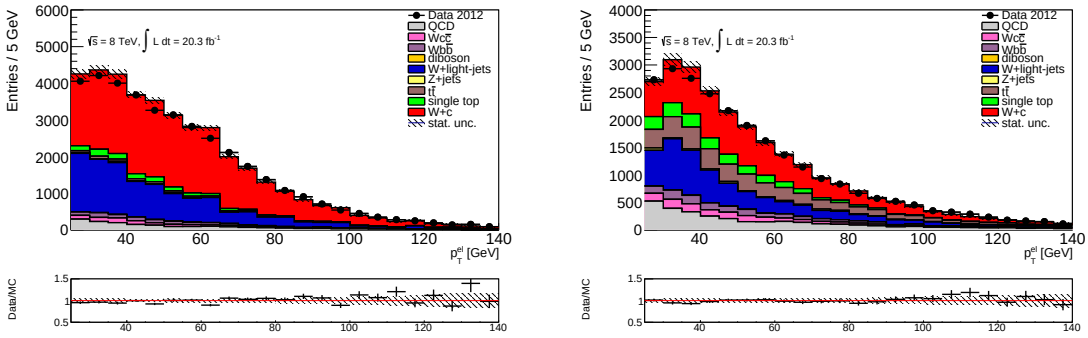

(a) (b)

FIGURE B.1: Electron p_T for the 1-jet (left) and 2-jet (right) bins in the OS sample.

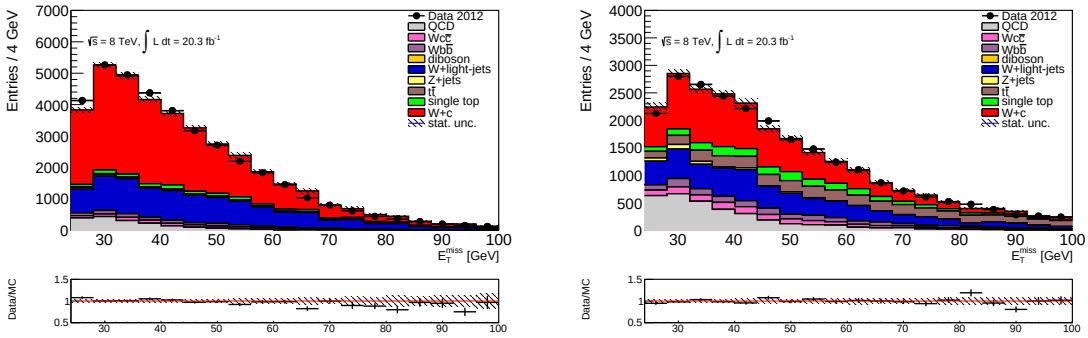

(a) (b)

FIGURE B.2: The reconstructed E_T^{miss} for the 1-jet (left) and 2-jet (right) bins in the OS sample.

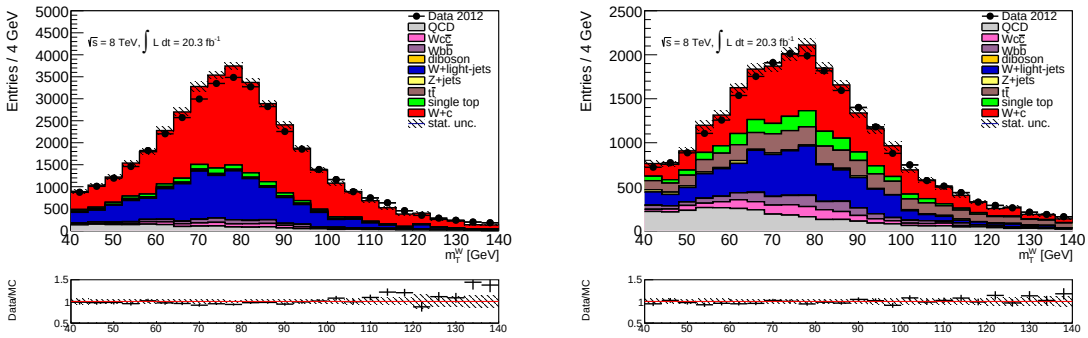

(a) (b)

FIGURE B.3: The reconstructed W boson transverse mass for the 1-jet (left) and 2-jet (right) bins in the OS sample.

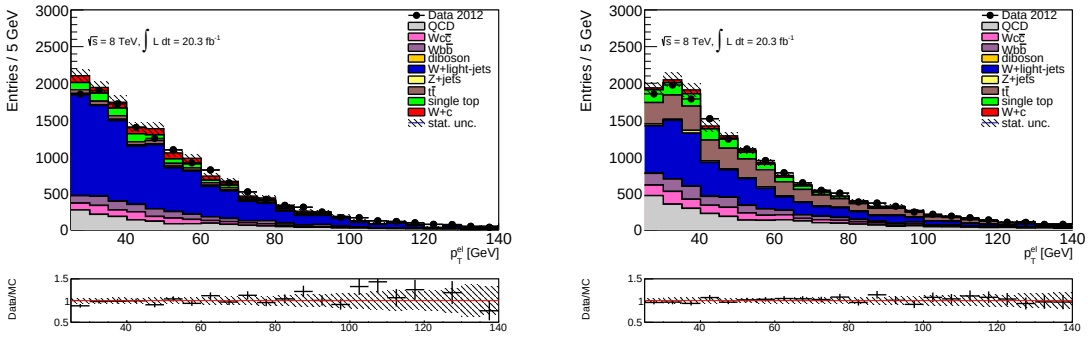

(a) (b)

FIGURE B.4: Electron p_T for the 1-jet (left) and 2-jet (right) bins in the SS sample.

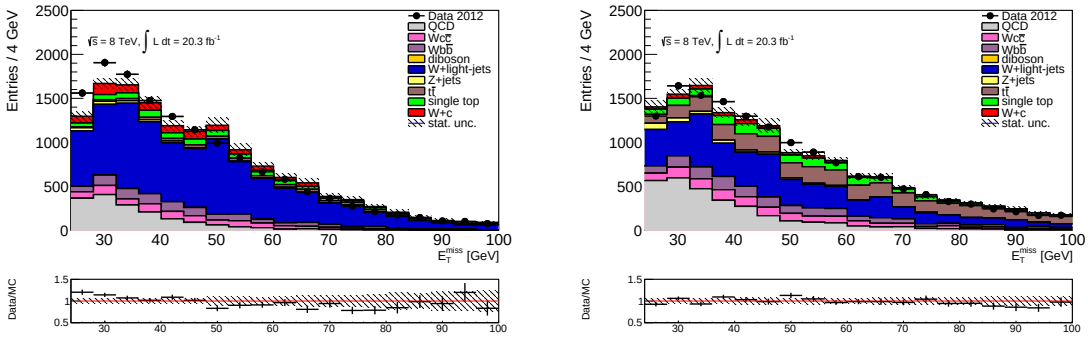

(a) (b)

FIGURE B.5: The reconstructed E_T^{miss} for the 1-jet (left) and 2-jet (right) bins in the SS sample.

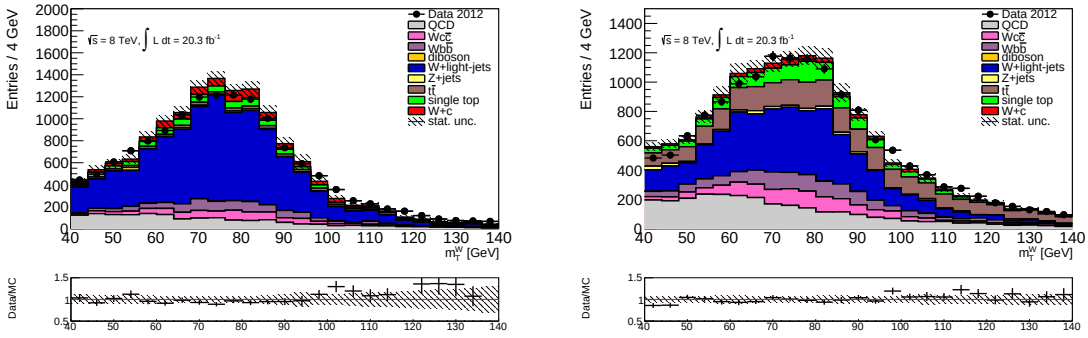

(a) (b)

FIGURE B.6: The reconstructed W boson transverse mass for the 1-jet (left) and 2-jet (right) bins in the SS sample.

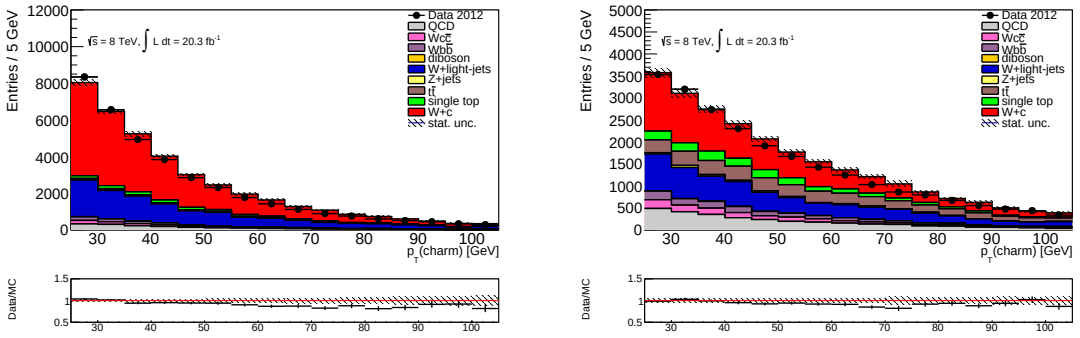

(a) (b)

FIGURE B.7: Charm-jet $p_T$for the 1-jet (left) and 2-jet (right) bins in the OS sample.

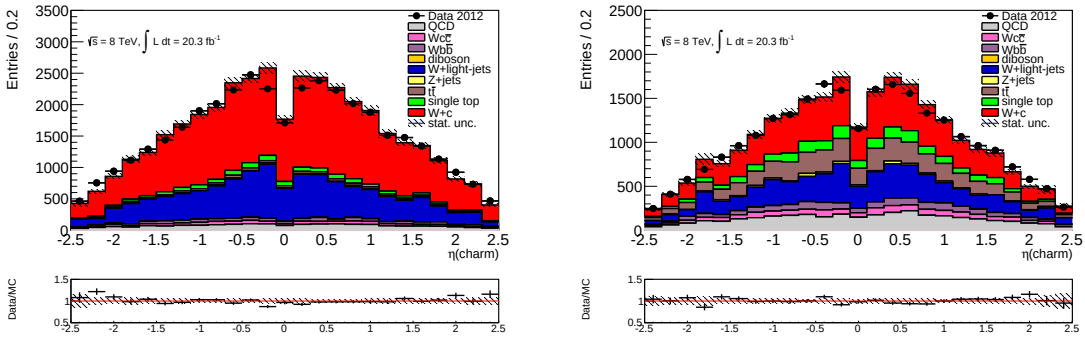

(a) (b)

FIGURE B.8: Charm-jet η for the 1-jet (left) and 2-jet (right) bins in the OS sample.

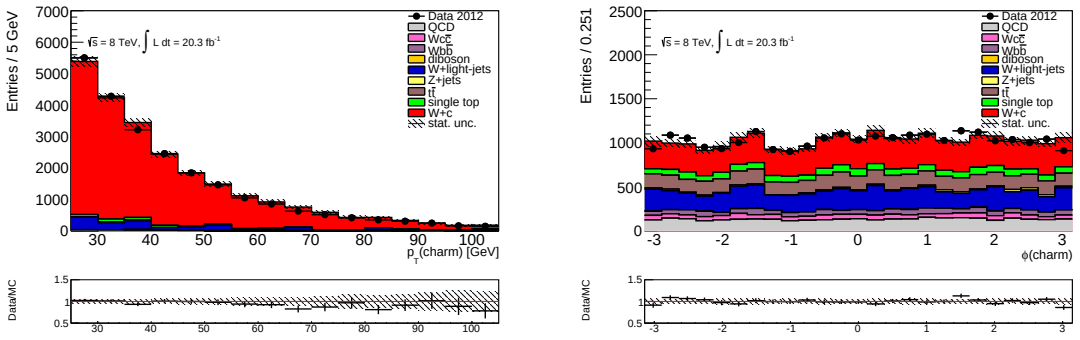

(a) (b)

FIGURE B.9: Charm-jet ϕ for the 1-jet (left) and 2-jet (right) bins in the OS sample.

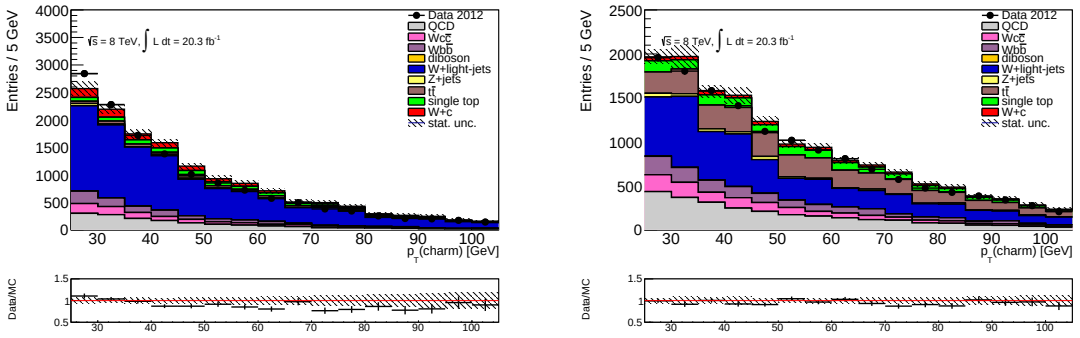

(a) (b)

FIGURE B.10: Charm-jet $p_T$for the 1-jet (left) and 2-jet (right) bins in the SS sample.

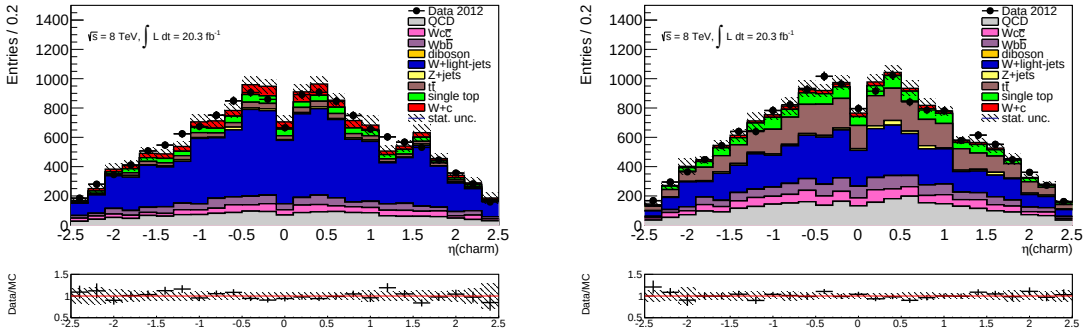

(a) (b)

FIGURE B.11: Charm-jet η for the 1-jet (left) and 2-jet (right) bins in the SS sample.

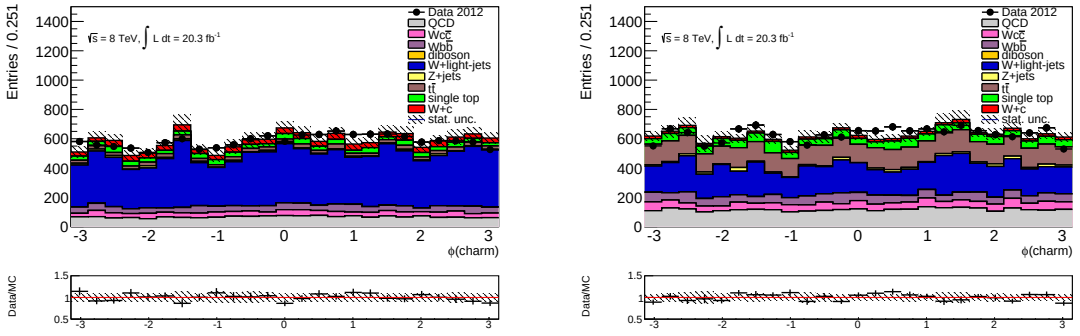

(a) (b)

FIGURE B.12: Charm-jet ϕ for the 1-jet (left) and 2-jet (right) bins in the SS sample.

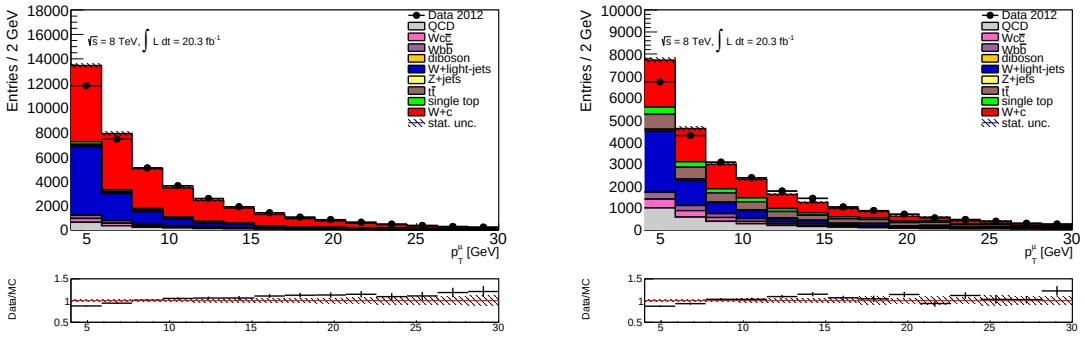

(a) (b)

FIGURE B.13: Muon p_T for the 1-jet (left) and 2-jet (right) bins in the OS sample.

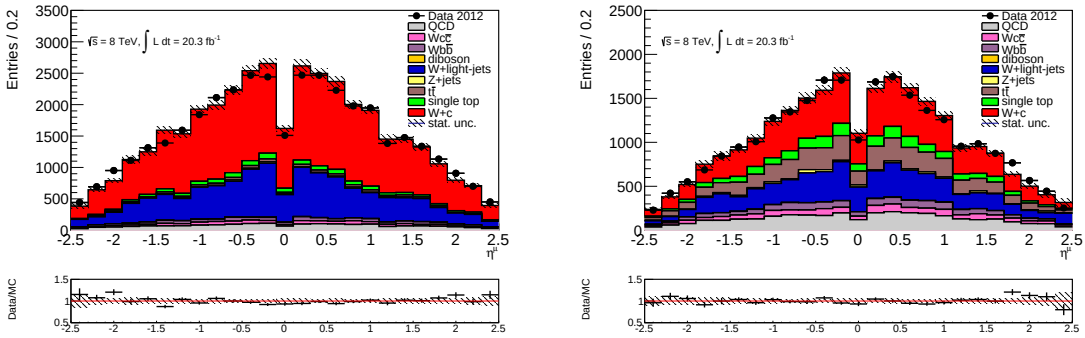

(a) (b)

FIGURE B.14: Muon η for the 1-jet (left) and 2-jet (right) bins in the OS sample.

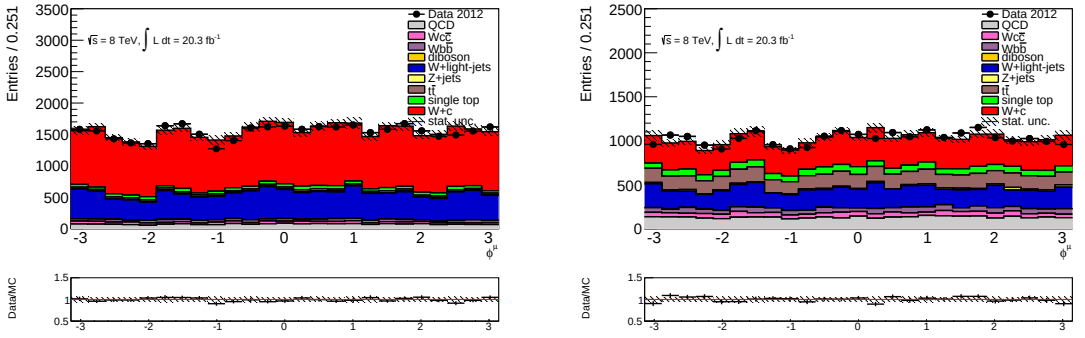

(a) (b)

FIGURE B.15: Muon ϕ for the 1-jet (left) and 2-jet (right) bins in the OS sample.

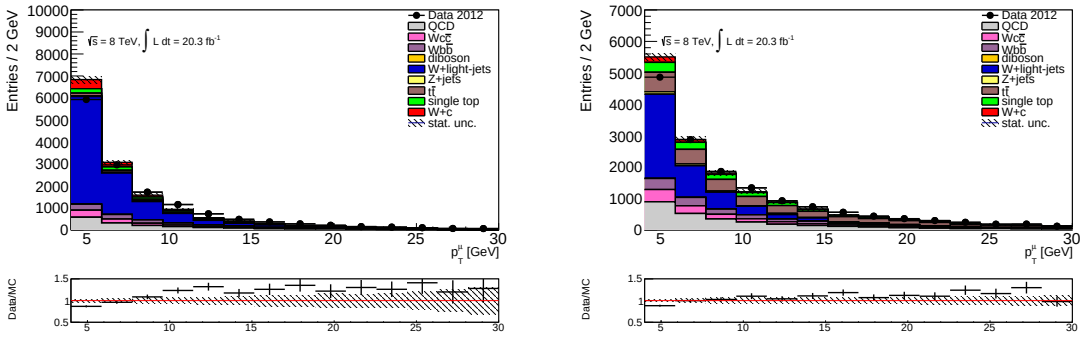

(a) (b)

FIGURE B.16: Muon p_T for the 1-jet (left) and 2-jet (right) bins in the SS sample.

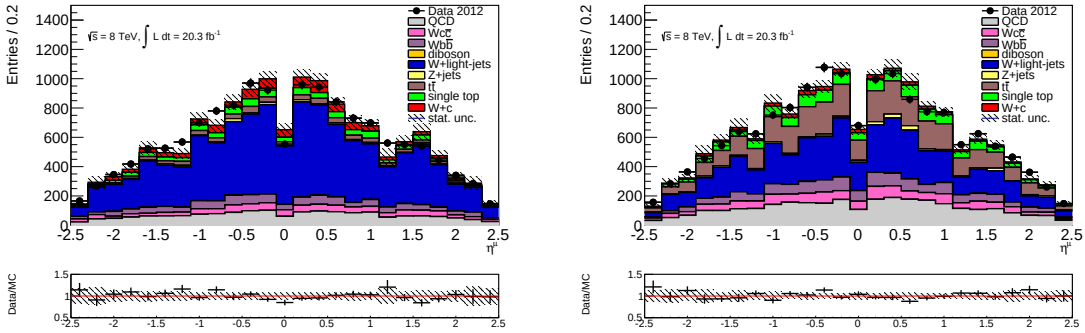

(a) (b)

FIGURE B.17: Muon η for the 1-jet (left) and 2-jet (right) bins in the SS sample.

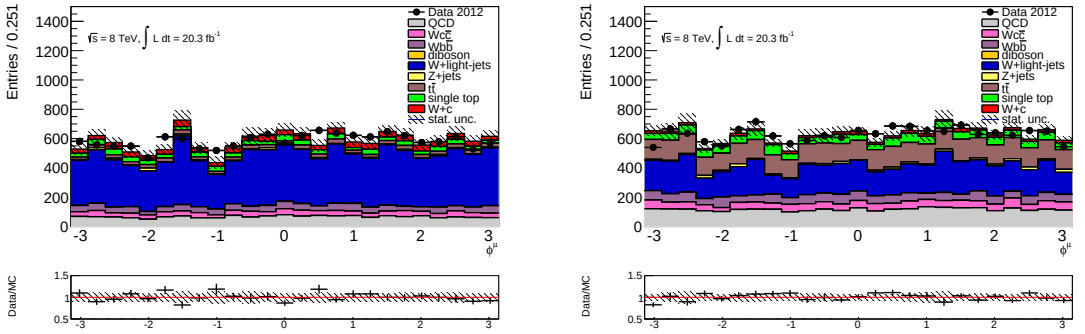

(a) (b)

FIGURE B.18: Muon ϕ for the 1-jet (left) and 2-jet (right) bins in the OS sample.

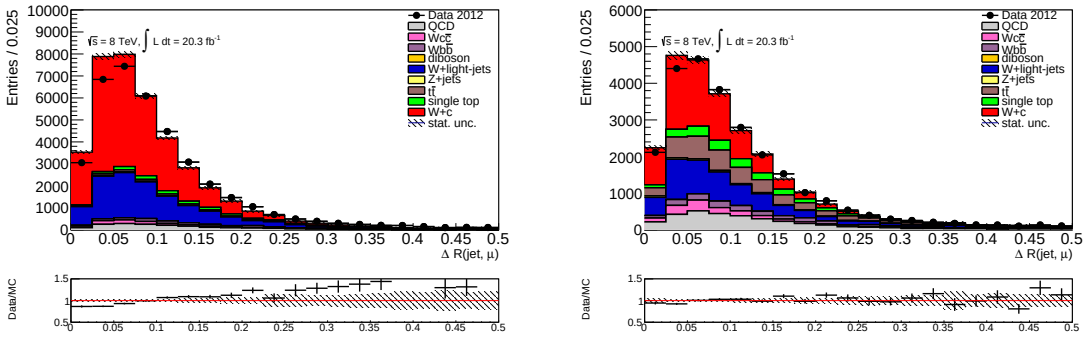

(a) (b)

FIGURE B.19: $\Delta R(jet, \mu)$ for the 1-jet (left) and 2-jet (right) bins in the OS sample.

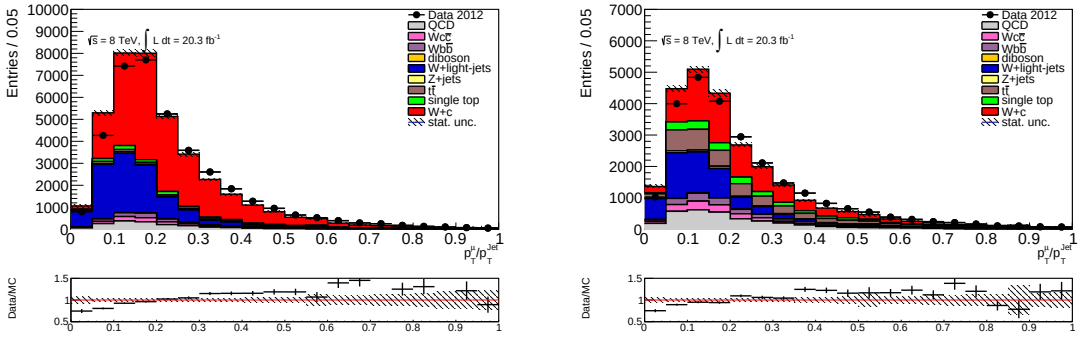

(a) (b)

FIGURE B.20: $p_T^{\mu}/p_T^{charm-jet}$ for the 1-jet (left) and 2-jet (right) bins in the OS sample.

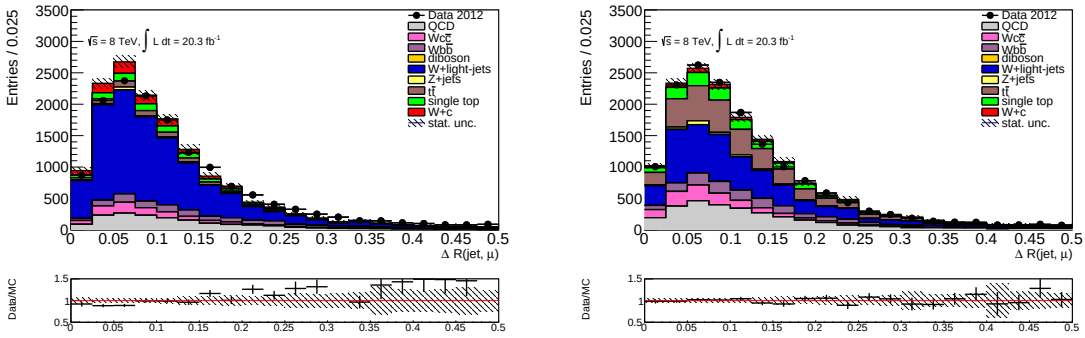

(a) (b)

FIGURE B.21: $\Delta R(jet, \mu)$ for the 1-jet (left) and 2-jet (right) bins in the SS sample.

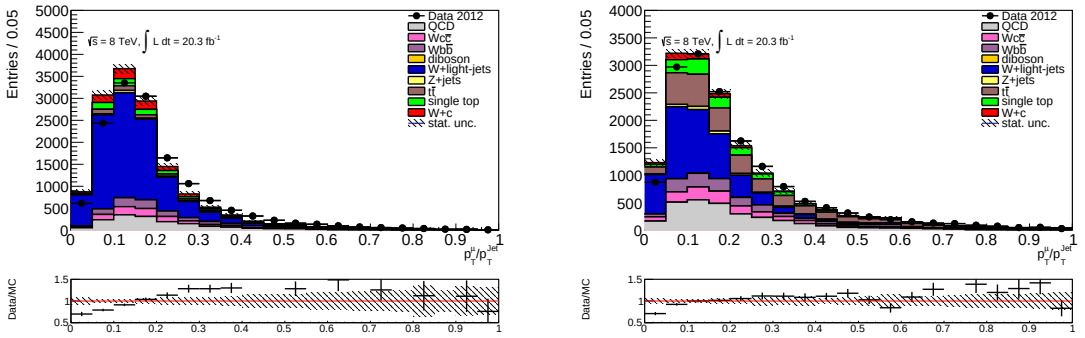

(a) (b)

FIGURE B.22: $p_T^{\mu}/p_T^{charm-jet}$ for the 1-jet (left) and 2-jet (right) bins in the SS sample.

Bibliography

[1] P. W. Higgs. Broken Symmetries and the Masses of Gauge Bosons. *Phys. Rev. Lett.*, 13(16):508–509, 1964.

[2] *Review of Particle Physics*. Particle Data Group, J. Beringer et al., 2014.

[3] M. Peskin and D. Schroeder. *An Introduction to Quantum Field Theory*. Westview Press, 1995.

[4] S. Weinberg J. Goldstone, A. Salam. Broken Symmetries. *Phys. Rev.*, 127(3):965, 1962.

[5] ATLAS Collaboration. Observation of a new particle in the search for the Standard Model Higgs boson with the ATLAS detector at the LHC. *Phys.Lett. B*, 716(1):1–29, 2012.

[6] CMS Collaboration. Observation of a new boson at a mass of 125 gev with the CMS experiment at the lhc. *Phys.Lett. B*, 716(1):30–61, 2012.

[7] ATLAS and CMS Collaborations. Combined Measurement of the Higgs Boson Mass in *pp* Collisions at $\sqrt{s} = 7$ and 8 TeV with the ATLAS and CMS Experiments. *Phys. Rev. Lett.*, 114(19):191803, 2015.

[8] F.J. Hasert et al. Observation of neutrino-like interactions without muon or electron in the gargamelle neutrino experiment. *Phys. Lett. B*, 46(1):138–140, 1973.

[9] UA1 Collaboration. Experimental Observation of Isolated Large Transverse Energy Electrons with Associated Missing Energy at $\sqrt{s} = 540$ GeV. *Phys.Lett. B*, 122(1):103–116, 1983.

[10] UA1 Collaboration. Experimental Observation of Lepton Pairs of Invariant Mass Around 95 GeV/c^2. *Phys.Lett. B*, 126(5):398–410, 1983.

[11] UA2 Collaboration. Observation of Single Isolated Electrons of High Transverse Momentum in Events with Missing Transverse Energy at the CERN *pp* Collider. *Phys.Lett. B*, 122(5-6):476–485, 1983.

[12] UA2 Collaboration. Evidence for $Z_0 \rightarrow e^+e^-$ at the CERN *pp* collider. *Phys.Lett. B*, 129(1-2):130–140, 1983.

[13] N. Cabibbo. Unitary Symmetry and Leptonic Decays. *Phys. Rev. Lett.*, 10:531, 1963.

[14] M. Kobayashi and T. Maskawa. CP-Violation in the Renormalizable Theory of Weak Interaction. *Prog. Theor. Phys.*, 49:652, 1973.

[15] M. Gell-Mann. A schematic model of baryons and mesons. *Phys.Lett.*, 8(3):214–215, 1964.

[16] G. Zweig. An SU(3) Model for Strong Interaction Symmetry and its Breaking. Report, CERN, http://cds.cern.ch/record/352337/files/CERN-TH-401.pdf, 1964.

[17] E. D. Bloom et al. High-Energy Inelastic e–p scattering at 6 ° and 10 °. *Phys. Rev. Lett.*, 23(16):930–934, 1969.

[18] M. Breidenbach et al. Observed Behavior of Highly Inelastic Electron-Proton Scattering. *Phys. Rev. Lett.*, 23(16):935–939, 1969.

[19] M. Jobes W. E. Burcham. *Nuclear and Particle Physics*. John Wiley & Sons, 1995.

[20] E.A. Paschos J. D. Bjorken. Inelastic Electron-Proton and γ-Proton Scattering and the Structure of the Nucleon. *Phys. Rev.*, 185(5):1975, 1969.

[21] R. P. Feynman. Very High-Energy Collisions of Hadrons. *Phys. Rev. Lett.*, 23(14):1415–1417, 1969.

[22] D. J. Gross C. G. Callan. High-Energy Electroproduction and the Constitution of the Electric Current. *Phys. Rev. Lett.*, 22(4):156–159, 1969.

[23] G. Parisi G. Altarelli. Asymptotic Freedom in Parton Language. *Nuclear Physics B*, 126:298–318, 1977.

[24] Y. L. Dokshitser. Calculation of structure functions of deep-inelastic scattering and e+e- annihilation by perturbation theory in quantum chromodynamics. *Sov. Phys. JETP*, 46(4):641, 1977.

[25] L. N. Lipatov V. N. Gribov. Deep inelastic e p scattering in perturbation theory. *Sov. Phys. JETP*, 15:438–450, 1972.

[26] R. S. Thorne G. Watt A. D. Martin, W. J. Stirling. Parton distributions for the LHC. *Eur. Phys. J. C.*, 63(2):189–285, 2009.

[27] T. Gleisberg et al. Sherpa 1.α, a proof-of-concept version. *Journal of High Energy Physics*, 2004(02):56, 2004.

[28] W.J. Stirling J.M. Campbell, J.W. Huston. Hard Interactions of Quarks and Gluons: a Primer for LHC Physics. *Reports on Progress in Physics*, 70(1):89–193, 2007.

[29] V. V. Sudakov. Vertex parts at very high-energies in quantum electrodynamics. *Sov. Phys. JETP*, 3:65, 1956.

[30] G. Ingelman B. Andersson, G. Gustafson and T. Sjostrand. Parton Fragmentation and String Dynamics. *Phys. Rept.*, 97(2-3):31–145, 1983.

[31] P. Skands T. Sjöstrand, S. Mrenna. PYTHIA 6.4 physics and manual. *Journal of High Energy Physics*, 2006(05):026, 2006.

[32] P. Skands T. Sjöstrand, S. Mrenna. A Brief Introduction to PYTHIA 8.1. *Computer Physics Communications*, 178(11):852–867, 2008.

[33] G.Corcella et al. HERWIG 6.5: an event generator for Hadron Emission Reactions With Interfering Gluons (including supersymmetric processes). *Journal of High Energy Physics*, 2001(1):010, 2001.

[34] ATLAS Collaboration. First tuning of HERWIG/JIMMY to ATLAS data. Technical Report ATL-PHYS-PUB-2010-014, CERN, 2010.

[35] M. Bahr et al. Herwig++ Physics and Manual. *Eur. Phys. J. C.*, 58(4):639–707, 2008.

[36] T. Gleisberg et al. Event generation with sherpa 1.1. *Journal of High Energy Physics*, 2009(02):56, 2009.

[37] M. L. Mangano et al. ALPGEN, a generator for hard multiparton processes in hadronic collisions. *Journal of High Energy Physics*, 2003(07):01, 2003.

[38] J. Alwall et al. MadGraph 5: going beyond. *Journal of High Energy Physics*, 2011(6):1–40, 2011.

[39] E. Richter-Was B. P. Kersevan. The Monte Carlo event generator AcerMC versions 2.0 to 3.8 with interfaces to PYTHIA 6.4, HERWIG 6.5 and ARIADNE 4.1. *Computer Physics Communications*, 184(3):919–985, 2013.

[40] B. R. Webber S. Frixione, P. Nason. Matching NLO QCD and parton showers in heavy flavour production. *Journal of High Energy Physics*, 2003(8):7, 2003.

[41] C. Oleari S. Frixione, P. Nason. Matching NLO QCD computations with Parton Shower simulations: the POWHEG method. *Journal of High Energy Physics*, 2007(11):70, 2007.

[42] D. J. Lange. The EvtGen particle decay simulation package. *Nucl. Instr. and Meth. A*, 462(1-2):152–155, 2001.

[43] S. M. Sze. *Physics of Semiconductor Devices*. John Wiley & Sons, 1981.

[44] F. Bloch. Über die Quantenmechanik der Elektronen in Kristallgittern. *Zeitschrift für Physik*, 52(7):555–600, 1929.

[45] A. Nathan F. Li. *CCD Image Sensors in Deep-Ultraviolet*. Springer, 2005.

[46] W. T. Read W. Shockley. Statistics of the Recombinations of Holes and Electrons. *Phys. Rev.*, 87(5):835, 1952.

[47] R. N. Hall. Electron-Hole Recombination in Germanium. *Phys. Rev.*, 87(2):387, 1952.

[48] A. Einstein. Über die von der molekularkinetischen Theorie der Wärme geforderte Bewegung von in ruhenden Flüssigkeiten suspendierten Teilchen. *Annalen der Physik*, 322(8):549–560, 1905.

[49] E. H. Hall. On a New Action of the Magnet on Electric Currents. *American Journal of Mathematics*, 2(3):287–292, 1879.

[50] W. Shockley. The Theory of p-n Junctions in Semiconductors and p-n Junction Transistors. *Bell Syst. Tech. J.*, 28(435):435–489, 1949.

[51] J.R. Brews E. H. Nicollian. *MOS (Metal Oxide Semiconductor) Physics and Technology*. John Wiley & Sons, 2003.

[52] F. Hartmann. *Evolution of Silicon Sensor Technology in Particle Physics*. Springer, 2009.

[53] C. Betancourt. Extraction of Effective Doping Concentrations in Unirradiated and Irradiated Silicon Detectors. Bachelor Thesis, 2009.

[54] C.R. Crowell M. Beguwala. Characterization of multiple deep level systems in semiconductor junctions by admittance measurements. *Solid-State Electronics*, 17(2):203–214, 1974.

[55] C. Betancourt et al. Analysis of deep level parameters in irradiated silicon detectors. *Nucl. Instr. and Meth. A*, 612(3):534–538, 2010.

[56] A. Loya S. M. Sze, D. Coleman. Current transport in metal-semiconductor-metal (MSM) structures. *Solid-State Electronics*, 14(12):1209–1218, 1971.

[57] S.M. Sze J.L. Chu, G. Persky. Thermionic injection and space-charge-limited current in reach-through p+np+ structures. *J. Appl. Phys.*, 43(8):3510–3515, 1972.

[58] J. Lohstroh et al. Punch-through currents in p+np+ and n+pn+ sandwich structures. *Solid-State Electronics*, 24(9):805–814, 1981.

[59] C. Betancourt et al. The Punch-Through Effect in Silicon Strip Detectors. *IEEE Trans. Nucl. Sci.*, 59(3):671–684, 2012.

[60] H. F.-W. Sadrozinski et al. Punch-through protection of ssds in beam accidents. *Nucl. Instr. and Meth. A*, 658(1):46–50, 2011.

[61] K. Hara et al. Beam splash effects on atlas silicon microstrip detectors evaluated using 1-w Nd:YAG laser. *Nucl. Instr. and Meth. A*, 541(1-2):15–20, 2005.

[62] T. Dubbs. Voltage on silicon microstrip detectors in high radiation fields. *IEEE Trans. Nucl. Sci.*, 46(6):1902–1906, 2000.

[63] W. N. Grant. Electron and hole ionization rates in epitaxial silicon at high electric fields. *Solid-State Electronics*, 16(10):1189–1203, 1973.

[64] R. Van Overstraeten W. Maes, K. De Meyer. Impact ionization in silicon: a review and update. *Solid-State Electronics*, 33(6):705–718, 1990.

[65] M. Köhler. *Double-Sided 3D Silicon Detectors for the High-Luminosity LHC.* PhD thesis, Albert–Ludwigs–Universität Freiburg, 2011.

[66] CERN RD50 collaboration.

[67] M. Moll. *Radiation Damage in Silicon Particle Detectors.* PhD thesis, Universität Hamburg, 1999.

[68] V. Nielsen J. Lindhard. Nuclear collisions and ionisation fluctuations in charged particle detectors. *Phys.Lett.*, 2(5):209–211, 1962.

[69] K. Hara et al. Testing of bulk radiation damage of n-in-p silicon sensors for very high radiation environments. *Nucl. Instr. and Meth. A*, 36(1):S83–S89, 2011.

[70] G. Kramberger et al. Comparison of pad detectors produced on different silicon materials after irradiation with neutrons, protons and pions. *Nucl. Instr. and Meth. A*, 612(2):288–295, 2010.

[71] S. Lindgren et al. Testing of surface properties pre-rad and post-rad of n-in-p silicon sensors for very high radiation environment. *Nucl. Instr. and Meth. A*, 636(1):S111–S117, 2011.

[72] Centro Nacional de Microelectrónica. Cnm-imc (csic).

[73] J. Segal S.I. Parker, C.J. Kenney. 3D - A proposed new architecture for solid-state radiation detectors. *Nucl. Instr. and Meth. A*, 395(3):328–343, 1997.

[74] on behalf of the ATLAS Collaboration F. Hügging. The ATLAS Pixel Insertable B-layer (IBL). *Nucl. Instr. and Meth. A*, 650(1):45–49, 2010.

[75] G. Casse et al. Enhanced efficiency of segmented silicon detectors of different thicknesses after proton irradiations up to 1×10^{16} n_{eq}/cm^2. *Nucl. Instr. and Meth. A*, 624(2):401–404, 2010.

[76] Igor Mandić et al. Observation of full charge collection efficiency in heavily irradiated n+p strip detectors irradiated up to 3×10^{15} n_{eq}/cm^2. *Nucl. Instr. and Meth. A*, 612(3):474–477, 2010.

[77] J. Lange et al. Properties of a radiation-induced charge multiplication region in epitaxial silicon diodes. *Nucl. Instr. and Meth. A*, 622(1):49–58, 2010.

[78] C. Betancourt et al. A charge collection study with dedicated RD50 charge multiplication sensors. *Nucl. Instr. and Meth. A*, 730(1):62–65, 2013.

[79] R. Mori et al. Long term performance stability of silicon sensors. *Nucl. Instr. and Meth. A*, 796(1):131–135, 2015.

[80] C. Lefèvre. The CERN accelerator complex. Complexe des accélérateurs du CERN.

[81] P. Bryant L. Evans. Lhc Machine. *Journal of Intrumentation*, 3(08):S08001, 2008.

[82] ATLAS Collaboration. The ATLAS Experiment at the CERN Large Hadron Collider. *Journal of Intrumentation*, 3(08):S08003, 2008.

[83] CMS Collaboration. The CMS experiment at the CERN LHC. *Journal of Intrumentation*, 3(08):S08004, 2008.

[84] LHCb Collaboration. LHCb Technical Design Report: Reoptimized Detector Design and Performance. Technical Report CERN-LHCC-2003-030, CERN.

[85] ALICE Collaboration. The ALICE experiment at the CERN LHC. *Journal of Intrumentation*, 3(08):S08002, 2008.

[86] ATLAS Collaboration. Tile calorimeter technical design report. Technical Report CERN-LHCC-96-042, CERN, 1996.

[87] ATLAS Collaboration. Particle counting using the lucid detector. Technical Report ATL-COM-LUM-2013-017, CERN, 2013.

[88] S. Jakobsen. Performance evaluation and optimization of the luminosity detector alfa. Master's thesis, Niels Bohr Institute, 2010.

[89] ATLAS Collaboration. Luminosity Public Results.

[90] ATLAS Collaboration. Expected Performance of the ATLAS Experiment - Detector, Trigger and Physics. arXiv:0901.0512 [hep-ex], 2009.

[91] ATLAS Collaboration. Performance of the ATLAS Inner Detector Track and Vertex Reconstruction in the High Pile-Up LHC Environment. ATLAS-CONF 2012-042, CERN, 2012.

[92] ATLAS Collaboration. Track Reconstruction Performance and Efficiency Estimation using different ID geometry samples. Technical Report ATL-COM-PHYS-2012-1541, CERN, 2012.

[93] R. Frühwirth W. Waltenberger and P. Vanlaer. Adaptive vertex fitting. *J. Phys. G*, 34(12):N343, 2007.

[94] W. Lampl et al. Calorimeter clustering algorithms: Description and performance. Technical Report ATL-LARG-PUB-2008-002, CERN.

[95] ATLAS Collaboration. Electron efficiency measurements with the ATLAS detector using the 2012 LHC proton-proton collision data. Technical Report ATLAS-CONF-2014-032, CERN, 2014.

[96] G. Soyez M. Cacciari, G. P. Salam. On the characterisation of the underlying event. *Journal of High Energy Physics*, 2010(65), 2010.

[97] ATLAS Collaboration. Measurement of the inclusive isolated prompt photon cross section in pp collisions at $\sqrt{s} = 7$ TeV with the ATLAS detector. *Phys. Rev. D.*, 83(5):052005, 2011.

[98] ATLAS Collaboration. Preliminary results on the muon reconstruction efficiency, momentum resolution, and momentum scale in ATLAS 2012 pp collision data. Technical Report ATLAS-CONF-2013-088, CERN, 2013.

[99] ATLAS Collaboration. Measurement of the muon reconstruction performance of the ATLAS detector using 2011 and 2012 LHC proton–proton collision data. *The European Physical Journal C*, 74:3130, 2014.

[100] ATLAS Collaboration. Mcp analysis guidelines for 2012 data.

[101] G. Soyez M. Cacciari, G. P. Salam. The anti-k_t jet clustering algorithm. *Journal of High Energy Physics*, 2008(04):63, 2008.

[102] ATLAS Collaboration. Combined performance studies for electrons at the 2004 ATLAS combined test-beam. *Journal of Intrumentation*, 5(11):P11006, 2010.

[103] ATLAS Collaboration. Determination of the jet energy scale and resolution at ATLAS using z/γ–jet events in data at $\sqrt{s} = 8$ tev. Technical Report ATLAS-CONF-2015-057, CERN, 2015.

[104] ATLAS Collaboration. Pile-up subtraction and suppression for jets in ATLAS. Technical Report ATLAS-CONF-2013-083, CERN, 2013.

[105] ATLAS Collaboration. Pile-up Suppression in Missing Transverse Momentum Reconstruction in the ATLAS Experiment in Proton-Proton Collisions at $\sqrt{s} = 8$ TeV. Technical Report ATLAS-CONF-2014-019, CERN, 2014.

[106] The HiLumi LHC Collaboration. HL-LHC Preliminary Design Report. Technical Report CERN-ACC-2014-0300, CERN, 2014.

[107] ATLAS Collaboration. Letter of Intent for the Phase-II Upgrade of the ATLAS Experiment. Technical Report CERN-LHCC-2012-022, CERN, 2012.

[108] B.T. Huffman on behalf of the ATLAS Collaboration. Plans for the Phase II upgrade to the ATLAS detector. *Journal of Intrumentation*, 9(02):C02033, 2014.

[109] ATLAS Collaboration. Measurement of the production of a W boson in association with a charm quark in pp collisions at $\sqrt{s} = 7$ TeV with the ATLAS detector. *Journal of High Energy Physics*, 2014(5):1, 2014.

[110] CMS Collaboration. Measurement of associated w+charm production in pp collisions at $\sqrt{s} = 7$ tev. *Journal of High Energy Physics*, 13:02, 2014.

[111] D. Mason et al. Measurement of the Nucleon Strange-Antistrange Asymmetry at Next-to-Leading Order in QCD from NuTeV Dimuon Data. *Phys. Rev. Lett.*, 99(19):192001, 2007.

[112] F. Olness et al. Neutrino Dimuon Production and the Strangeness Asymmetry of the Nucleon. *The European Physical Journal C*, 40(2):145–156, 2005.

[113] H. L. Lai et al. The Strange Parton Distribution of the Nucleon: Global Analysis and Applications. *Journal of High Energy Physics*, 2007(04):089, 2007.

[114] R. Petti S. Alekhin, S. Kulagin. Determination of strange sea distributions from νn deep inelastic scattering. *Phys. Lett. B*, 675(5):433–440, 2009.

[115] S. Alekhin et al. Determination of strange sea quark distributions from fixed-target and collider data. *Phys. Rev. D.*, 91(9):094002, 2015.

[116] O. Samoylov et al. A precision measurement of charm dimuon production in neutrino interactions from the NOMAD experiment. *Nuclear Physics B*, 876(2):339–375, 2013.

[117] A Kayis-Topaksu et al. Measurement of charm production in neutrino charged-current interactions. *New Journal of Physics*, 13(9):093002, 2011.

[118] K. Lohwasser. Private Communication.

[119] ATLAS Collaboration. Luminosity Public Results.

[120] ATLAS Collaboration. Jetetmiss CP Analysis guidlines for 2012 data.

[121] E. Lohrmann. A Summary of Charm Hadron Production Fractions. arXiv:1112.3757 [hep-ex], 2011.

[122] J. Pumplin et al. New Generation of Parton Distributions with Uncertainties from Global QCD Analysis. *Journal of High Energy Physics*, 2002(07):1, 2002.

[123] V. Eremin et al. Avalanche effect in Si heavily irradiated detectors: Physical model and perspectives for application. *Nucl. Instr. and Meth. A*, 658(1):145–151, 2011.

[124] ATLAS SCT collaboration. Supply of Silicon Microstrip Sensors of ATLAS07 specification. Technical specification, CERN, 2007.

[125] ATLAS SCT collaboration. Supply of Silicon Microstrip Sensors of ATLAS12 specification. Technical specification, CERN, 2012.

[126] C. Da Via et al. 3D silicon sensors: Design, large area production and quality assurance for the ATLAS IBL pixel detector upgrade. *Nucl. Instr. and Meth. A*, 694(1):321–330, 2012.

[127] Mara Bruzzi. Expected leakage current for the ATLAS Upgrade Si detectors. SCIPP PREPRINT SCIPP 06/16, INFN and University of Florence, Italy and SCIPP, UC Santa Cruz, USA, 2006.

[128] R. Marco-Hernandez and ALIBAVA Collaboration. A portable readout system for microstrip silicon sensors (ALIBAVA). *IEEE Trans. Nucl. Sci.*, 56(3):1642–1649, 2009.

[129] M. Schmelling S. Löchner. The Beetle Reference Manual. Technical Report LHCb-2005-105, LHCb, 2006.

[130] M. Walz. Charakterisierung von planaren Siliziumstreifendetektoren zum Einsatz am LHC-Upgrade. Diploma thesis, University of Freiburg, 2010.

[131] A. Kolšek et al. Using TRIGA Mark-II Research Reactor for Irradiation with Thermal Neutrons. *Nuclear Engineering and Design*, 283:155–161, 2015.

[132] A. Dierlamm. Irradiations in Karlsruhe. 16th RD50 Workshop, 2010.

[133] M. Povoli et al. Impact of the layout on the electrical characteristics of double-sided silicon 3D sensors fabricated at FBK. *Nucl. Instr. and Meth. A*, 699:22–26, 2013.

[134] G. Giacomini et al. Development of Double-Sided Full-Passing-Column 3D sensors at FBK. *IEEE Trans. Nucl. Sci.*, 60(3), 2013.

[135] G.-F. Dalla Betta. Performance evaluation of 3D-DDTC detectors on p-type substrates. *Nucl. Instr. and Meth. A*, 624(2), 2010.

[136] G. Giacomini et al. Noise Characterization of Double-Sided Silicon Microstrip Detectors With Punch-Through Biasing. *IEEE Trans. Nucl. Sci.*, 58(2):569–576, 2011.

[137] C. Da Via et al. 3D active edge silicon sensors: Device processing, yield and QA for the ATLAS-IBL production.

[138] M. Petasecca et al. Numerical Simulation of Radiation Damage Effects in p-Type and n-Type FZ Silicon Detectors. *IEEE Trans. Nucl. Sci.*, 53(5):2971–2976, 2006.

[139] D. Pennicard et al. Simulations of radiation-damaged 3D detectors for the Super-LHC. *Nucl. Instr. and Meth. A*, 592(1-2):16–25, 2008.

[140] E. Vianello et al. Optimization of double-side 3D detector technology for first productions at FBK. 2011.

[141] M. Köhler et al. Comparative measurements of highly irradiated n-in-p and p-in-n 3D silicon strip detectors. *Nucl. Instr. and Meth. A*, 659(1):272–281, 2011.

[142] S. Kuehn et al. Signal and charge collection efficiency of n-in-p strip detectors after mixed irradiation to HL-LHC fluences. *Nucl. Instr. and Meth. A*, 730(1):58–61, 2013.

[143] G. Kramberger. Private Communication.

[144] F. V. Wald R. O. Bell, H. B. Serreze. Polarization in Cadmium Telluride Nuclear Radiation Detectors. *IEEE Trans. Nucl. Sci.*, NS-23(1):159–170, 1976.

[145] H. Toyama et al. Quantitative Analysis of Polarization in CdTe Radiation Detectors. *Japanese Journal of Applied Physics*, 45(11):8842–8847, 2006.

[146] V. Cindro. Bistable damage in neutron-irradiated silicon diodes. *Nucl. Instr. and Meth. A*, 476(1):565–568, 2002.

[147] L. C. Kimerling A. Chantre. Configurationally multistable defect in silicon. *Appl. Phys. Lett.*, 44:1000, 1986.

[148] M. Mikuž et al. Bias dependence and bistability of radiation defects in silicon. *Nucl. Instr. and Meth. A*, 466(2):345–352, 2001.

[149] J. T. Ryan et al. Interface-state capture cross section-Why does it vary so much? *Appl. Phys. Lett.*, 106:163503, 2015.